Contribution to real-time air system modeling dedicated to trapped mass estimation

Farouq Meddahi

UNIVERSITÉ D'ORLÉANS

ÉCOLE DOCTORALE ENERGIE, MATERIAUX, SCIENCES DE LA TERRE ET DE L'UNIVERS

LABORATOIRE PRISME

THÈSE présentée par :

Farouq MEDDAHI

Soutenue le : **[12 décembre 2016]**

Pour obtenir le grade de : **Docteur de l'université d'Orléans**

Discipline/ Spécialité : MECANIQUE ET ENERGETIQUE

Contribution à la Modélisation Temps-Réel de la Chaîne d'Air dédiée à l'Estimation du Remplissage

THÈSE dirigée par :

Mr Yann CHAMAILLARD	Professeur, Université d'Orléans
Mr Alain CHARLET	Maître de conférences, Université d'Orléans

RAPPORTEURS :

Mr David Chalet	Professeur des Universités, Ecole Centrale de Nantes
Mr Antonio Sciarretta	Maître de conférences- IFP EN

JURY

Mr Pascal Higelin	Professeur, Université d'Orléans - Président du jury
Mr Yann CHAMAILLARD	Professeur, Université d'Orléans
Mr Pierre Melchior	Maître de conférences, Université Bordeaux 1
Mr Alain CHARLET	Maître de conférences, Université d'Orléans

All models are wrong. Some are useful.
George E. P. Box,
Professor of Statistics,
University of Wisconsin

TABLE OF CONTENTS

LIST OF TABLES

LIST OF FIGURES

ACKNOWLEDGEMENT

This dissertation is the result of three years of research as a PhD student at the control engineering group of the Robert-Bosch GmbH in Germany, with collaboration with the Institut PRISME from the Orléans University in France.

The present accomplishment was made possible thanks to the excellent supervision of Dr. Alain Charlet, who encouraged new ideas and approaches and constructively filtered the bad ones. His work ethic and personal commitment are amongst many values I will certainly try to adopt. I also want to thank Pr. Yann Chamaillard, for his trust and guidance throughout the present research work.

A special thank goes to Mr. Christian Fleck without whom I probably would have never started this adventure. He also defined the subject and provided me with technical inspiration during the last three years.

I would like to thank my colleagues at Robert Bosch GmbH. I am indebted to Steffan Grödde, Thomas Machowicki, Bastian Reineke and Felix Rützel for the discussions and time they sacrificed to allow me to clarify ideas with them. All the thanks also go to Mr. Wolfgang Fischer for giving me the possibility to be part of the project. I am in many ways grateful to Franz Raichle for his engagement, values and principles.

I would like to express my thanks and gratitude to Mr. David Chalet and Mr. Antonio Sciaretta for having agreed to review this thesis report, and to Mr. Pascal Higelin and Mr. Pierre Melchior for being members of the thesis committee.

In Orléans, I thank the Internal Combustion Engine team for the help and the great atmosphere. Unfortunately I have spent only a few time in Orléans, however I enjoyed the company and fruitful discussions with Amine, Pierre, Sokratis, Salim, Antoine.

On a personal level, I would like to thank my parents for their patience and their forgiveness during the time I committed myself this work. My deepest affection goes to them, for the love, support, encouragement and inspiration.I am deeply grateful to my wife, without whom, this document would have probably not seen the light.

INTRODUCTION

Nowadays the world counts more than 1.2 billion cars. This figure is likely to double and reach 2.5 billion by the year 2050. This large fleet has an enormous impact on the environment. It is the main user of energy in the world. In fact, it consumes the most of world's petroleum which leads to air pollution creation and makes the fleet of cars a significant contributor to the global warming phenomena due to the high emissions of CO_2. Indeed, the transportation has the fastest growing carbon emissions of any economic sector.

The estimation of engine breathing is the step towards a cost effective emission reduction. The trapped mass in the cylinder is the major factor in combustion control, and hence its products. For this reason, the scope of this work is the estimation of the gas dynamics along the engine air system with the aim of a better modeling engine breathing.

Several models and tools have been developed for internal combustion engines modeling. Figure I summaries the current state of art in terms of accuracy, computation time and number of states, taking into consideration a maximum of only one space dimension.

At one hand, full 1D models considers mass, energy and momentum conservation in both time and space to determine the system states at every instant. Commercial softwares are based on these models, with a dedicated solver, and the need to a minimum amount of experience to build and to calibrate a full model. On the other hand, real-time ECU functions are based on lumped parameter models. They use mass and enthalpy conservation to estimate pressure and temperature in plenums and then coupled to orifices to estimate a mass and energy flow. These require a very low computational power but neglect inherently important phenomena such as waves and gas dynamics.

To bridge the gap between the two approaches, several reduced order models have been developed [1, 2, 3, 4, 5, 6].

The work presented in [7] have shown that the Quasi-Propagatory Model is a very promising approach. It offers a good compromise between accuracy and computational power. This modeling principal relies on the observation of pressure oscillations at a given point along the duct. The pressure will oscillate according to the boundary condition across the duct until steady state is reached. This can be simulated using simple ordinary differential equations, thus, avoiding the fine space discretization.

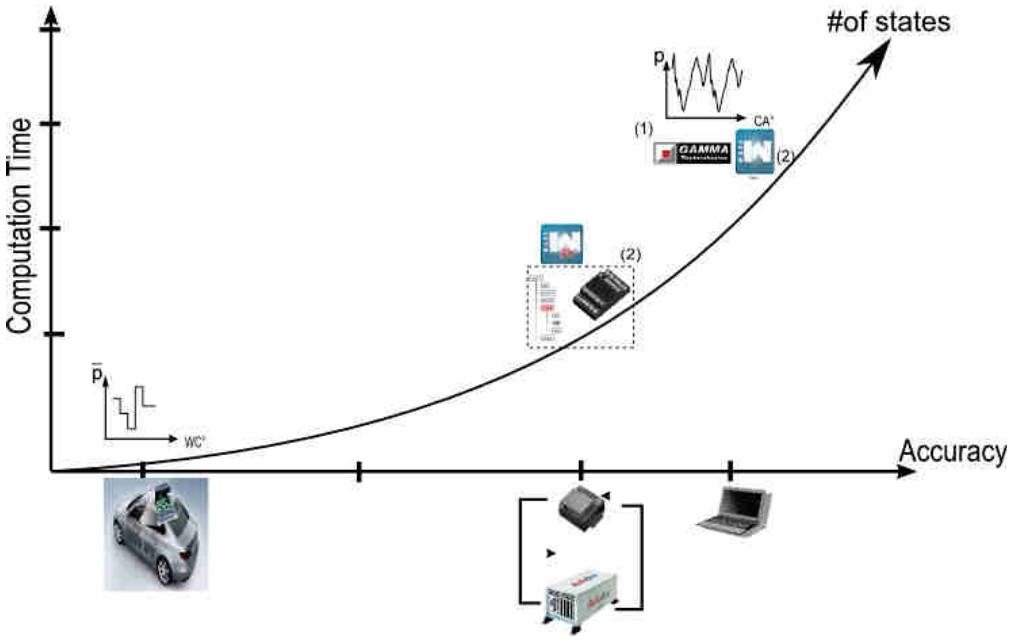

Fig. I.: Modeling state of the Art

Unfortunately, the reduced order models are still not real-time. Some tools such as Wave-RT® have been developed [8] which require a dedicated hardware and mathematical libraries to speed up the calculations.

This work focuses on building a hybrid model for the air-system taking into consideration only 0D and quasi-1D models. This will lead to a better accuracy (compared to lumped parameter models)since gas dynamics will be taken into consideration. At the same time, the calculation time will be decreased compared to 1D models, as the quasi-1D models will be used only along ducts observing very apparent phenomena such as the intake manifold. For the exhaust manifold, it will be shown that filling and emptying effects are dominant, and lumped models are sufficient.

To illustrate the existing trade-offs, various criterion are used such as accuracy, calibration effort and computation time.

The present document is structured as follows:

- Chapter 1 will go briefly through the evolution of diesel and gasoline emissions and their control strategies progression. Then, two important test drive cycles,

namely the NEDC and its successor the WLTC are compared to each other.

- Chapter 2 will go through the full 1D modeling of gas dynamics, and will analyze some numerical schemes to solve the conservative partial differential equations. Boundary conditions treatment is briefly stated, and coupled with duct models. Based on the accuracy and the minimum calculation effort compromise, a reference scheme is selected to serve later for the first numerical validation of the low order models. For comparison and validation, the shock tube and the acoustic test benches are used.
- Chapter 3 will present the quasi-propagation modeling approach. This modeling methodology, despite its simplicity, manages to take momentum phenomena resulting from the gas movement inside engine ducts due to valves movement. Numerical validation is presented taking results from the previous chapter as a reference.
- Chapter 4 will present remaining component in the air system to be used later in an overall air system simulation.
- To provide accurate boost pressure estimation, chapter 5 presents an extended approach to compress data-maps modeling to provide reliable denser look up tables.
- Chapter 6 combines the models from the previous chapters to perform an overall air-path simulation. A combination of quasy-1D and lumped parameter models was then used based on system characteristics to efficiently model gas dynamics.

  This offered an even faster simulation, while taking wave phenomena at the entry of the intake valves into consideration. The over all simulation is validated with respect to measurements for the complete engine operation points.

Publications

- Meddahi, F., Charlet, A., Chamaillard, Y., Fleck, C., and Groedde, S. ”Modeling waves in ICE ducts: Comparison of 1D and Low OrderModels”. SAE International, (2015-24-2386), 2015. doi: 10.4271/2015-24-2386.
- Meddahi, F., Charlet, A., Chamaillard, Y., Fleck, C. ”Incorporating Thermo- and Aerodynamic Losses into Compressor Models for Real-Time Applications”. SAE International, (2015-01-1715), 2015. doi: 10.4271/2015-01-1715.

Patent(submitted)

- Meddahi, F., Groedde, S., Fischer, W., Gaenzle, D., and Bleile, T. ”Frischluftmassenbestimmung mit schnellem Temperatursensor nach Verdichter”.

INTRODUCTION(FRENCH)

De nos jours, le nombre de voiture présente dans le parc roulant mondial est estimé à 1,2 milliard de voitures. Ce chiffre, même très important devra doubler pour atteindre les 2,5 milliard d'ici 2050. Cette augmentation est loin d'être sans danger pour l'environnement et les êtres vivants, en effet, cela conduit à l'augmentation de la consommation des énergies fossiles par le secteur des transports et du coup conduits à l'explosion des émissions polluantes responsable de la dégradation de la santé du réchauffement climatique par le biais des émissions de CO_2.

L'estimation de la quantité d'air admise dans le moteur est une étape cruciale pour la course à la diminution des émissions polluantes et à moindre coûts. En effet, la masse de l'air emprisonnée dans le cylindre est un facteur important pour le contrôle de la combustion et par ce biais sur les produits de cette réaction chimique (polluants). À l'ombre de ce qui a été présenté ci-dessus, ce travail de thèse se focalise sur l'estimation de la dynamique de l'air dans la conduite d'admission afin de mieux modéliser le processus d'admission dans le moteur automobile.

Plusieurs outils et modèles de simulation numérique ont été développés afin de modéliser au mieux le comportement du moteur à combustion interne. La figure II représente un résumé de l'évolution de la modélisation 1D en termes de précision, temps de calcul et nombre d'étapes. D'après la figure II, on peut remarquer que d'une part, la modélisation 1D dite "complète" tient compte de la conservation de la masse, de l'énergie et du moment en fonction du temps et de l'espace pour déterminer l'état du système à chaque instant. Ceci est le cas des logiciels de simulation commerciaux qui incluent un solveur dédié et aussi demande une certaine connaissance de l'utilisateur pour la construction et la calibration des modèles.

D'autre part, la modélisation temps réel est basée sur des modèles à paramètres concentrés. Ces modèles utilisent la conservation de la masse et d'enthalpie pour estimer la pression et la température dans les plénums, puis les couplent à des orifices afin d'estimer le flux de masse et d'énergie. ils exigent très peu de puissance de

calcul mais négligent intrinsèquement des phénomènes importants tels que les ondes et la dynamique des gaz. Pour combler l'écart entre les deux approches, plusieurs modèles Ainsi les deux approches énoncées précédemment démontrent les avantages à combiner les deux concepts. Pour se faire, plusieurs modèles ont été développés avec comme caractéristique des ordres de complexité moins important [1, 2, 3, 4, 5, 6].

L'étude faite par Meddahi et al. [7] a montré que le modèle "Quasi-Propagatif" représente une approche prometteuse en offrant un bon compromis entre précision et puissance de calcul. Le principe de ce modèle repose sur l'observation des variations (oscillations) de la pression à un point donné sur la ligne d'admission. En effet, la pression subit des oscillations en fonction des conditions aux limites présentent dans la conduite d'admission jusqu'à atteindre l'équilibre. Ce comportement peut être simulé à l'aide d'équations différentielles ordinaires toute en évitant la discrétisation de l'espace.

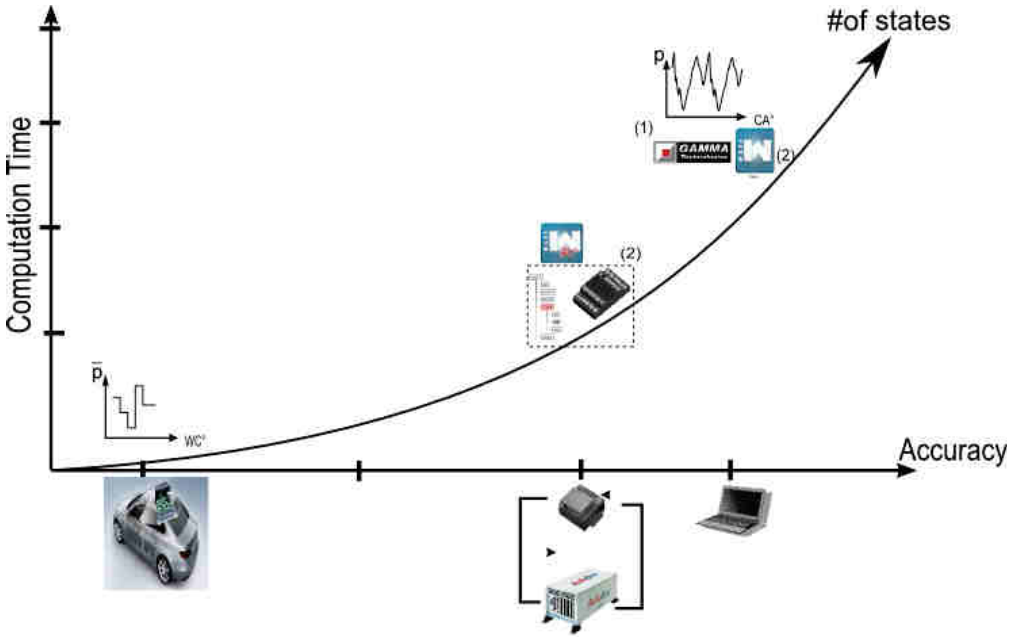

Fig. II.: Modélisaation de l'état de l'art

Malheureusement, les modèles à ordre réduit sont limités par le faite qu'ils ne sont pas des modèles "temps réelles", Cette limitation peut être contournée avec une certaine configuration comme dans le cas de Wave-RT® [8] mais nécessite un hardware spécifique et des bibliothèques mathématiques dédiées.

Ce travail de thèse présente le développement d'un modèle "hybride" 0D et quasi 1D pour le système d'admission. Cette approche permet l'obtention d'une meilleure précision puisque la dynamique des gaz est prise en compte. Et ceci, tout en réduisant le temps de calcul par rapport aux modèles 1D ; rendu possible en utilisant les modèles quasi-1D uniquement pour l'étude des phénomènes très spécifiques tel que sur le collecteur d'admission. Pour ce dernier, il sera démontré que les effets de décharge

et remplissage sont dominants, et que les modèles à paramètres concentrés sont suffisants. Afin d'illustrer les compromis existant dans ce type d'approche, diffèrents critères de sélection ont été utilisés comme par l'exemple la précision, la complexité de l'effort de calibration et le temps de calcul.

À l'ombre de ce qui a été énoncé précédemment, ce rapport de thèse sera structuré comme suite

- Chapitre 1 : Présente une brève introduction de l'évolution de la réglementation des émissions polluantes des moteurs à allumage par compression et commandé et les améliorations apportées aux stratégies de control mises en place afin d'épouser ces limites d'émissions. Ensuite deux cycles de conduite seront présentés à savoir le NEDC et son successeur, le WLTC ainsi que leur comparaison.
- Chapitre 2 : Décrit la modélisation 1D de la dynamique des gaz, et l'analyse de certains schémas numériques afin de résoudre les équations aux dérivées partielles. Le traitement des conditions limites y sera mentionné, et couplé avec des modèles de la conduite d'admission. Un schéma de référence y est choisi en se basant sur les critères de sélection mentionnés dans le chapitre 1 (haute précision et minimum de calcul). Un modèle de référence y est sélectionné pour les pré-essais de validation numérique, et cela par le biais d'un tube à choc et un banc d'essais acoustique.
- Chapitre 3 : Ce chapitre est consacré à l'approche du modèle "quasi-préparative", il y sera présenté la méthodologie associée à ce modèle, mais aussi les points forts ; tel que son aptitude à prendre en considération les phénoménes d'inertie, résultants du mouvement des gaz à l'intérieur des conduites du moteur (mouvements des soupapes). La validation numérique est aussi incluse dans ce chapitre en prenant comme référence les résultats obtenus dans le chapitre précédent.
- Chapitre 4 : Présente les composants résiduels qui seront utilisés plus tard dans une simulation globale du système d'air.
- chapitre 5 : Fournit une estimation précise de la pression de suralimentation, il y est aussi présenté une approche étendue pour modéliser le compresseur afin de fournir des cartographies fiables et plus complètes.
- Chapitre 6 : Ce dernier chapitre combine les résultats des chapitres précédents pour effectuer une simulation "globale" de la chaine d'air. Il y sera montré que pour la configuration du moteur à allumage par compression utilisée, les effets 1D sont plus présents le long de la conduite et du collecteur d'admission. D'après ce résultat, le QPM sera choisi pour modéliser le sous système précèdent.

CHAPTER 1

MOTIVATION

The main objectives of car manufacturers nowadays are more performing, cost effective and clean autos. On one hand, emissions regulations are mandatory and imposed by major governments of countries and regions. On the other hand, fuel economy and better performing engines are the crucial criteria for drivers.

Enhancements in engine design as well as more sophisticated management have continuously contributed to the progress of engine performance and reduction of exhaust gas toxicity. However, advances in engine technology have been proved insufficient and automotive engines were and still are a major source of urban air pollution. Necessitating thus the introduction of exhaust gas after-treatment systems and exhaust gas recirculation.

To highlight the upcoming challenges, we will first see how emissions regulations and fuel economy evolved during the last two decades.

1. Emissions

Emissions are being regulated by several governments with large auto markets which cover around 80 % of global passenger vehicles. These regulations set quantitative limits on specific air pollutants. They consist of emissions proven to be harmful for public health such as nitrogen dioxide (NO_2), partially burned hydrocarbon (HC) and carbon monoxide (CO). The following chart in fig. 1.1, summarizes the European emissions standards.

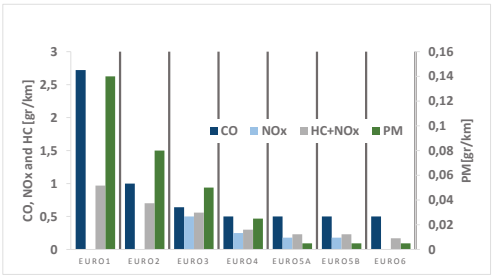

(a) Diesel Engines

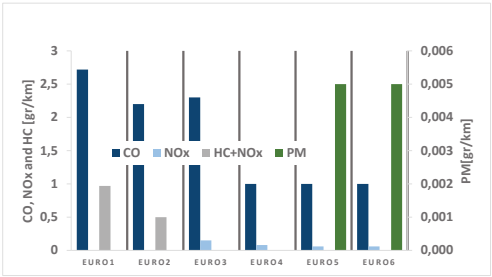

(b) Gasoline Engines

Fig. 1.1.: History of diesel and gasoline EU emissions standards[9]

The low operating costs, efficiency and durability made diesel engines have a wide range of applicability. At the same time, compression ignition engines have significant impact on environmental pollution problems. Figure 1.1a gives a history of the changing landscape of European diesel emission legislations over the past twenty years.

Euro 1 limited CO, HC and NO_x. Back then engines were certified on the assembly line before being mounted on the vehicle. Starting from Euro 2 (1996), all engines were required to meet the same limit levels immediately after production and the certification was no longer based on individual test samples. Technologies such as the rotary injection pump, IDI combustion, low pressure injection (700-800 bar) and low pressure EGR (Exhaust Gas Recirculation) were used to comply with the regulations [10]. In 2001, Euro 3, a test cycle was introduced to mimic on-road operations. Common rail systems, 1D combustion, and Diesel Oxidation Catalyst (DOC) for PM reduction were used. Five years later, Euro 4 made mandatory exhaust after treatment systems. On Board Diagnostics (OBD) was also introduced to monitor the engine's emission control. Euro 4 also introduced Air to Fuel ratio (A/F) management, electric control of fuel injection, engine tuning and turbocharger with inter-cooler. Euro 5 (2009) further reduced NO_X and PM levels. At that time, improved versions of previous technologies, variable geometry turbine, Diesel Particulate Filter (DPF) and variable valve timing made it possible to fulfill the regulations while maintaining fuel consumption levels. In 2014, Euro 6 set the lowest emission levels for diesel engines. In this case, the exhaust after-treatment system was augmented with a rail pressure higher than 2100 bar to fulfill the regulations.

As shown in fig. 1.1b, gasoline engines were exempted from PM standards until Euro 5. At the same time, diesel engines are allowed more NO_x emissions, but require producing less CO (starting from Euro 2).
These regulations dealt specifically with gaseous emissions like NO_X, HC and CO. CO_2 emissions are on the other hand, defined according to vehicle mass and manufacturers

sales. For example, Those selling less than a 1000 car/year or special vehicles can be excluded from the legislation. Manufacturers selling between 1000 and 10000 cars/year can propose their own reduction targets whereas those selling between 10 and 300 thousand cars/year, can apply to a given percentage reduction. For larger OEMs, If the average manufacturer's fleet exceeds the limits, the latter have to pay excess emissions penalties for each car registered (From 2019, 95 €from the first gram of exceedance) [10].

2. Fuel Economy

CO_2 emissions are directly proportional to fuel consumption. They both have known a large decrease in the last two decades. Figure 1.2 gives the historical fleet CO_2 emissions performance and current or proposed passenger vehicle standards. The data is obtained from *The International Council On Clean Transportation* [11] where differences between the test cycles[1] have already been accounted for.

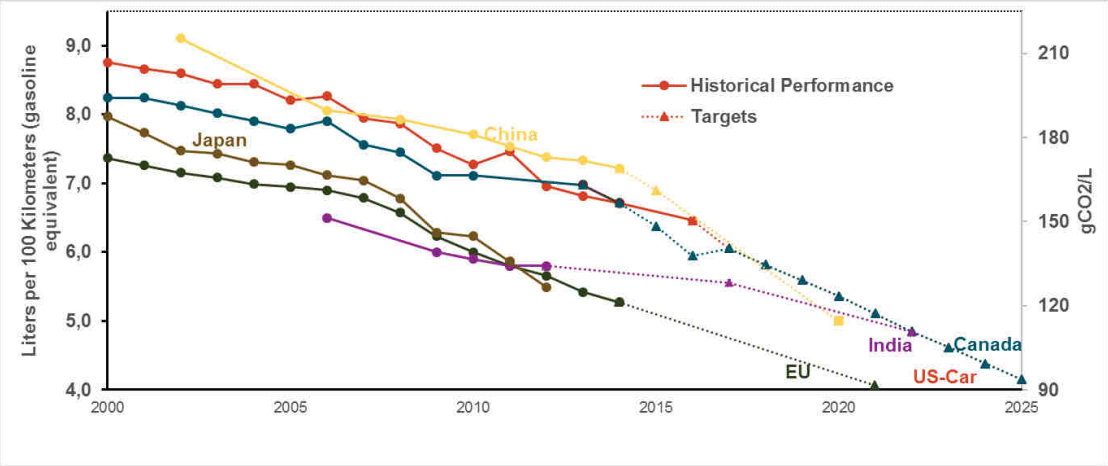

Fig. 1.2.: Passenger car CO_2 emissions and fuel consumption, normalized to NEDC Global passenger vehicle standards[12]

For comparison reasons, all the regulations have been converted to the New European Driving Cycle (NEDC). The EU passenger car standard of 95 g/km for 2020 (effectively 2021) can be compared to similar targets for the US (93 g/km for 2025 passenger cars), Japan (105 g/km by 2020), and China (117 g/km by 2020). The chart does not take into account any credits (such as super-credits or Eco-innovations) or differences in (real-world) enforcement.

Despite the tremendous reduction in fuel consumption, further cut is still to be achieved.

[1] Specific tests conducted to ensure adherence to emissions standards. See section 4

3. Overall and Annual Required Fuel and CO2 Reduction

Figure 1.3 gives the overall and annual required fuel economy and CO_2 improvements. Significant and more challenging stringent regulations will be soon effective. Hence, improvements are still required by automobile car makers.

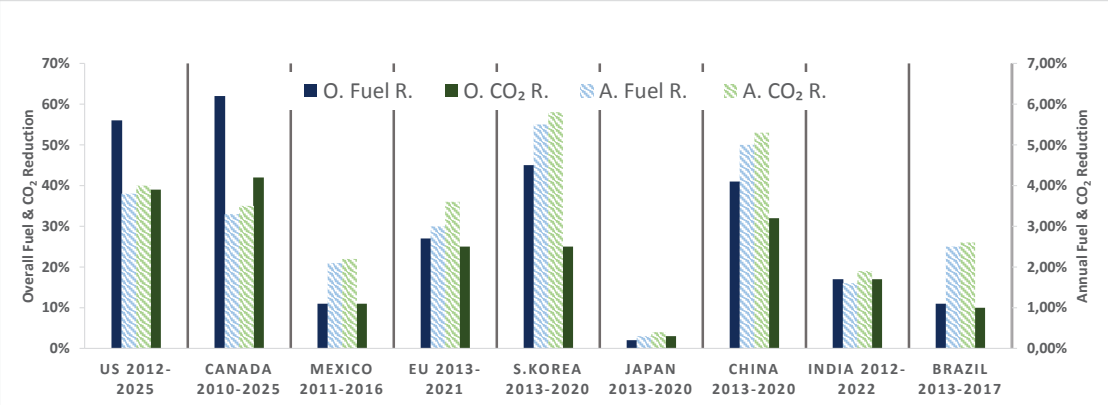

Fig. 1.3.: Overall (O) and annual(A) required(R) fuel and CO_2 reduction [12]

The challenges are not only in the emissions legislations, but also in the test cycles defined to quantify the emissions. These have been criticized for not being really representative for Real Driving Emissions (RDE). The following section gives a brief comparison between the current NEDC and the new proposed WLTC test cycles.

4. Test Drive Cycles- A Comparison Between the NEDC and WLTC

During the last decade, several harmonized engine dynamo-meter cycles have been developed for emissions certification for heavy and light duty engines, non-road engines as well as motorcycles. If for instance, we consider Light-Duty Vehicles (LDVs), governments have developed their own test cycles such as the European (NEDC), the American Federal Test Procedure (FTP-75) and the Japanese Cycle (JC 08). These cycles differ mainly in their representativeness and completeness, or in other words, in their ability to represent statistically real-world conditions.

Despite the tremendous reduction in cars emissions, Light-Duty vehicles remain an important source of nitrogen oxides and carbon monoxide and play a major role in the persisting air quality problems in many urban areas. Weiss et al. [13] have shown that the NEDC used for Type Approval (TA) fails to reproduce Real Driving Emissions (RDE). The result is higher emissions under real driving conditions. Although nitrogen oxides for gasoline vehicles, carbon monoxide and total hydrocarbon emissions for both diesel and gasoline engines generally remain below the threshold limit, nitrogen oxides for diesel engines, including modern Euro 5 cars exceed emissions limit by

320±90 %. At the same time, on-road carbon dioxide emissions surpass laboratory emissions by 21±9%.

Emission measurements are conducted in laboratories for a good reason that is the ability to control influencing variables in such environment. However, not only emissions were different from real world ones, but even fuel consumption. ICCT has reported that differences between official laboratories and real-world fuel consumption and CO_2 values were around 7% in 2011 and 30% in 2013 [14].

These discrepancies not only affect society due to emissions health related issues and consumers who will spend more on fuel, but also governments and manufacturers who are losing credibility.

This motivated the development of new test cycles such as the WLTC. The main difference is the dynamics contained in the WLTC compared to its predecessor, the NEDC, as it is shown in fig. 1.4.

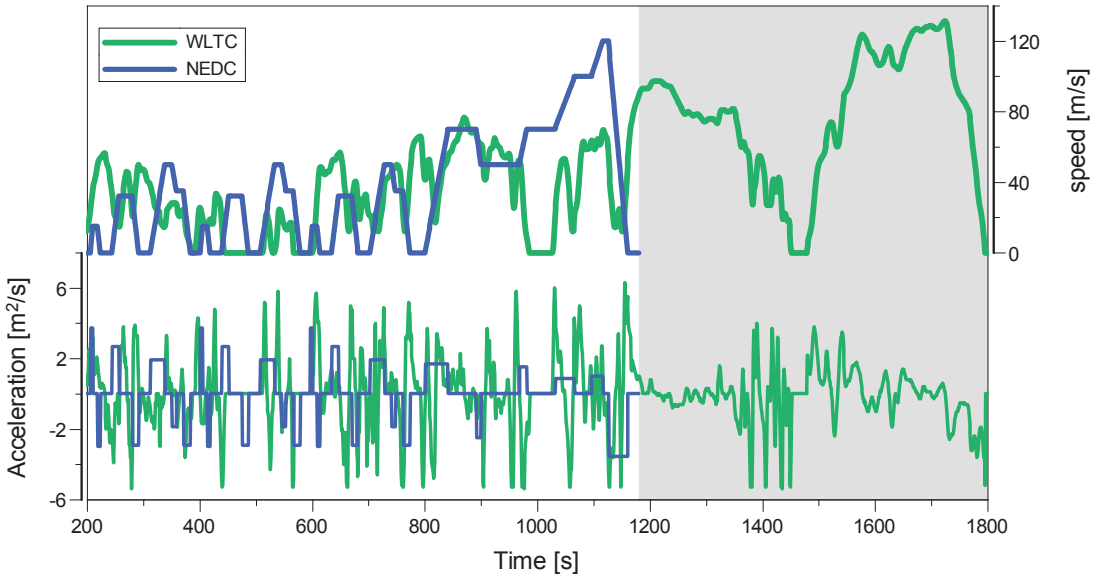

Fig. 1.4.: Velocity and acceleration profiles for the NEDC and WLTC test cycles

In contrast to the NEDC, the WLTC covers a wider band of acceleration, speed combinations and is more dynamic. It has denser data in regions less than 80 km/hr as it covers more short trips which occur in real world conditions.

Figure 1.5 shows that the NEDC clearly has only some constant accelerations and decelerations. The WLTC, on the other hand, covers a wider range of combinations but there are some zones left at very low speeds around 70-110 km/hrs.

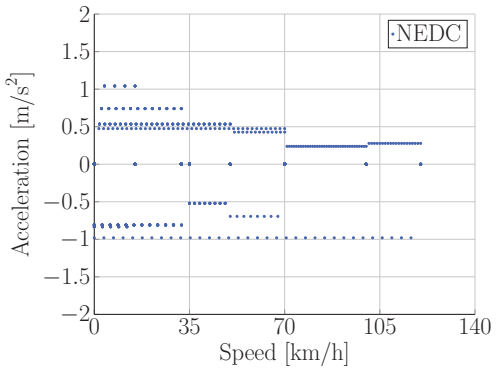

(a) Acceleration vs. Speed of the NEDC

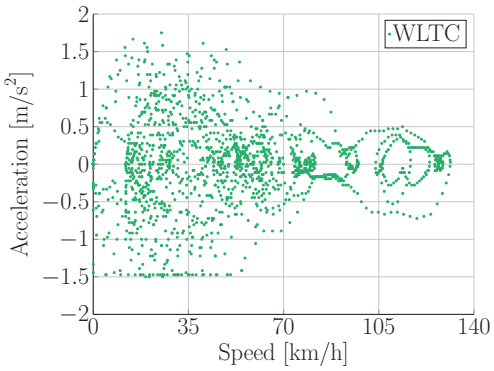

(b) Acceleration vs. Speed of the WLTC

Fig. 1.5.: Comparison between NEDC and WLTC cycles: Acceleration-Speed Combinations

Essentially, the main difference between the two cycles is the amount of higher dynamics considered in the WLTC as shown in fig. 1.6. This will make transient phenomena in engines more apparent and stationary maps less effective when it comes to engine transient performance and transient emissions. More accurate models will be required to complete slow sensors and support engine management strategies.

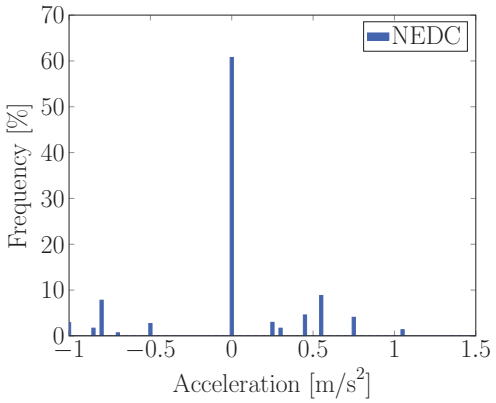

(a) Histogram of the NEDC Acceleration

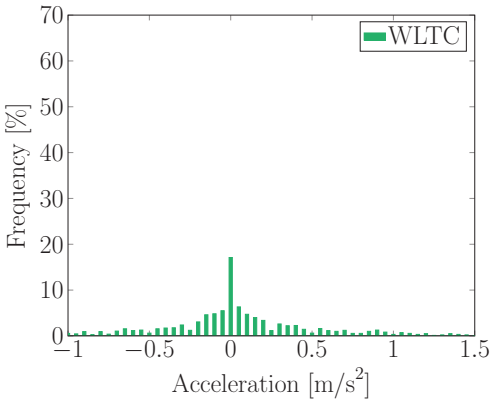

(b) Histogram of the WLTC Acceleration

Fig. 1.6.: Comparison between NEDC and WLTC cycles: Acceleration Histogram

In the next section, current modeling and control strategies will be generically explained. The impact of the new emission regulations will be then highlighted, and the role of this thesis is underlined.

5. Key Factors for Legislations Achievement

The fulfillment of the legislations requires improvement in both engine actuators and ECU-functions. Both the vehicle body, components design as well as estimation and control of key system states (such as gas concentrations) are crucial corner stones.

Figure 1.7 summaries the interaction of estimation and control functions on the ECU with the air and combustion systems as a reaction to driver demand while satisfying system and emission constraints. System states are estimated by means of implemented models or measured using series sensors. Along with driver request, actuators such as throttle valve, EGR and waste valves, injectors are actuated to attain the required response.

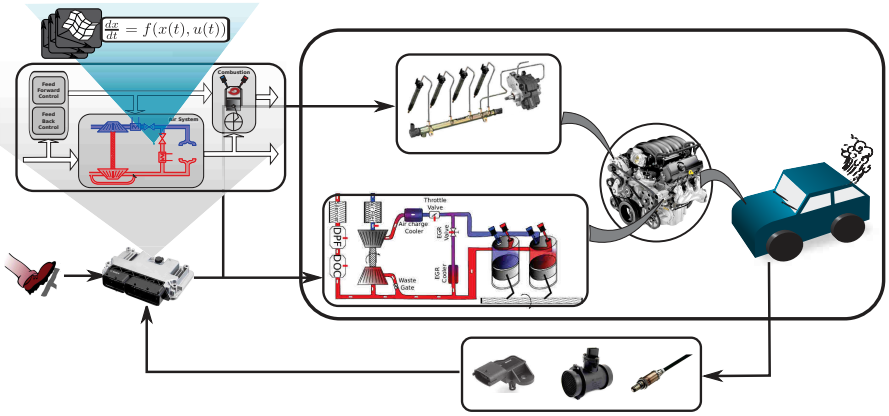

Fig. 1.7.: Simplified Control structure

As shown in fig. 1.7, there are many operating variables that affect engine performance, efficiency and emissions. The *air system* is the first set of actuators which will induce the proper amount of air into the combustion chamber to respond to the driver's demand and provide the required power output while staying within emissions limitations.

Hence, the first step consists of inducing the necessary mass (fresh air + recirculated exhaust gas) into the cylinders to provide the required power output with the minimum fuel consumption, consistent with smooth reliable operation. This being not always possible, it is then necessary to inject the proper fuel quantity depending on the actual trapped mass. For the time being, there are no available techniques to measure the trapped mass and species proportions on series engines. It is thus necessary to estimate them.

However constraints from the emissions legislations may dictate different air/fuel ratio values as it is indicated in fig. 1.8.

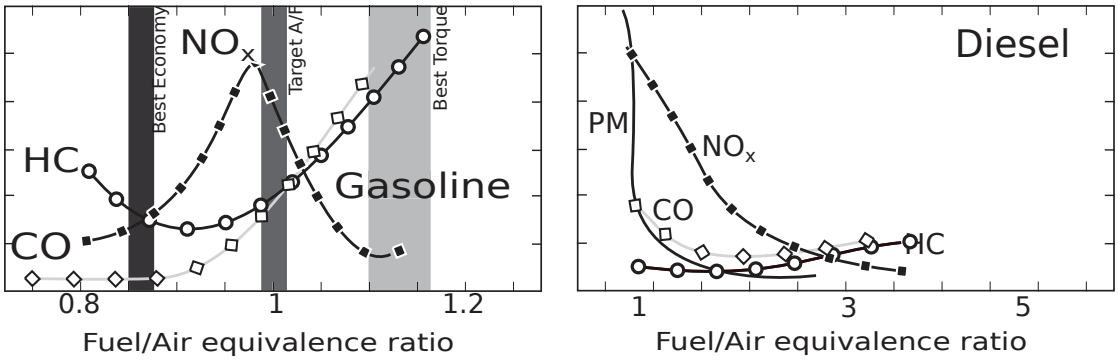

Fig. 1.8.: Fuel/Air impact on emissions and performance[15]

Diesel and gasoline engines differ in resulting emissions. These discrepancies are due to the differences in the combustion process (excess air, concentration, compression ratio, fuel,...). Diesel engines have high particulate and nitrogen dioxide (NO_x) emissions, whereas spark-ignition engines have higher oxides of nitrogen(NO), carbon monoxide (CO) and partially burned hydrocarbons (HC) emissions.

Figure 1.8 shows qualitatively how NO_x, CO and HC vary for diesel and gasoline engines as a function of the air/fuel ratio. Spark-ignition engines are generally operated close to stoichiometric for lower emissions, under a rich mixture for a maximum power and under lean mixture for a minimum consumption. Leaner mixtures in gasoline engines give fewer emissions until misfire takes place which eventually results in higher HC emissions.

Figure 1.8 clearly shows that there is no optimum A/F ratio for minimum emissions. This is the main reason for exhaust gas after-treatment systems such as The Three Way Catalyst (TWC) which also requires a precise control of the A/F ratio for maximum conversion efficiency as shown in fig. 1.9

On the other hand, compression ignition engines always operate under lean mixtures approaching stoichiometric conditions. However, lean mixtures degrade the DOC efficiency and result in higher particulates emissions.

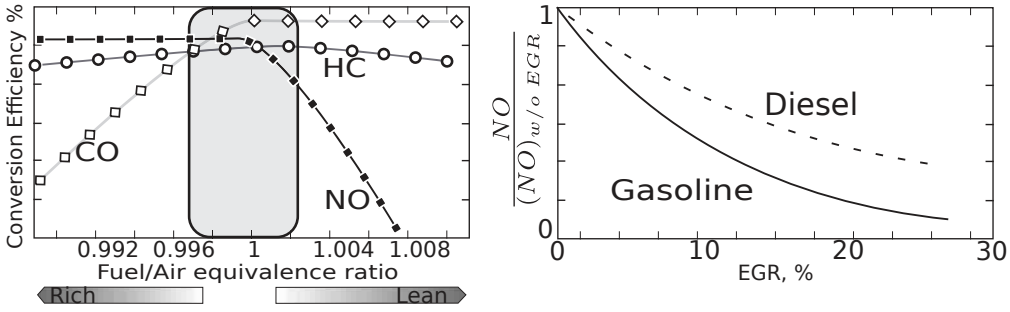

Fig. 1.9.: Effect of Fuel/Air on catalyst efficiency (left) and sensitivity of NO emissions on EGR concentrations (right)

6. Scope of the Thesis: Why Air System Modeling

It is clear that both trapped mass and fuel play a role in the combustion process. However, common rail injection systems can be set very accurately for every working cycle. Which means the main difficulty is to estimate and control species flowing in and out from the cylinder.

In addition, and as highlighted earlier, test cycles will contain more dynamics and less steady-state operation. This means the steady or quasy-steady hypothesis errors will be more apparent. Gas dynamics effects (inertia, mixture, transport) will have a higher impact, and data based models will require denser maps (which means more measurements costs) or result in higher dynamic errors.

Gas dynamics have a great influence on the emissions and performances of an engine. For example, engine volumetric efficiency is mainly dependent on the instantaneous pressure across the intake and exhaust valves. When both intake and exhaust valves are open, instantaneous pressure differences will control the internal EGR flow, which is very difficult to take into consideration using simple steady state maps, especially with complex technologies such as Variable Valve Timing (VVT).

CHAPTER 2

1D FLOW MODELING IN INTERNAL COMBUSTION ENGINES

As long as the transient operation of Internal Combustion Engines (ICE) is concerned, the 1D[1] Flow Simulation Models will be, for many coming years, the only useful applicable tool, which can provide a good compromise between accurate information, computational power and complexity [16].

In addition, the prediction of transient phenomena in ICE manifolds is also of crucial importance for real-time application. Many relevant aspects influencing engine performance (especially during transient) such as the estimated trapped mass and air-to-fuel ratio (A/F) control can be optimized if pressure waves are considered. For this purpose, several reduced models have been developed [1, 2, 3, 17, 18, 4, 5, 6] to overcome the high computational cost of 1D models. These issues will be discussed in the next chapter. In this chapter, we will discuss several full 1D modeling approaches of flow through engine ducts and their qualities will be assessed. Accuracy and stability are also briefly discussed. Methods under the scoop are the Graphical and Numerical Method of Characteristics, the Lax-Wendroff based-schemes and the recent Conservation Element-Solution Element (CE-SE) method.

The goal behind using these methods, is to provide a reliable reference for model reduction methods presented in the next chapter. They also offer access to unmeasured quantities such as local concentrations, or overcome slow measurements such as temperature sensors.

1. Introduction

It is clear that the Internal combustion Engine (ICE) emissions have known a massive reduction, as they become a major political and research topic. On the other hand, the

[1] Only one space dimension is considered

performance of ICE is being made better through the use of turbochargers and more sophisticated control strategies. Yet, the efficiency of ICE used in passenger cars is no more than 40% [19]. In addition, emissions' legislations will always become stricter, hence the need to a further improvement will always exist.

The flow in the ICE intake manifold determines the flow in the cylinder prior to the combustion, which helps to better control the combustion through a better estimation of reactants taking part in the combustion process, hence a control of emissions. Similarly, the flow in the exhaust manifold determines the flow into the turbine, and thereby the efficiency of the turbo-charging system. This simply highlights the importance of an understanding and modeling of flow along the engine ducts, as this is one of the key factors to a better performance and lower emissions.

The most detailed models of fluid and gas flow are based on the *first principles*, such as the conservation of mass, momentum and energy[2]. Arnau et al. [21] Classified the calculation models on the basis of their complexity as mean value(MV) or quasi-steady models, filling and emptying models, one dimensional (1D) wave-action models and the three dimensional calculation codes.

Mean Value Engine Models (MVEM)offer dynamic and steady information within a given accuracy, and have to be corrected to overcome the simplifications' error. They however offer a good compromise between simplicity and accuracy. These models have been widely used for controllers design [22, 23].

The reasonable computational cost of 1D codes allows the calculation of whole internal combustion engines with all their components, and play a major role in engine design and development. 1D wave action models simplify the engine by means of ducts, where only one dimension is considered and plenum, where the gas is stopped and their properties are constant in the entire element. Finally, quasi-steady models are used to solve the junctions between the different elements. Many professional tools have been developed based on this modeling approach such as Gt-Power® from GTISoft and Wave from Riccardo.

CFD codes, which consider the three spatial dimensions, are only used to model single engine components in spite of their accuracy in compared to 1D codes. They are mainly used in co-simulation with 1D tools to increase the overall model accuracy along given components such as the combustion chamber.

Figure 2.1 shows the hierarchy of simulation models. In this section, we restrict our selves to inviscid flows with a focus on the nonlinear Euler Equation.

[2]A set of conservation laws is a collection of statements of *flux conservation* in space-time. Mathematically, these laws are represented by a set of integral equations. The differential form of these laws is obtained from the integral form, with the assumption that the *physical solution is smooth*[20]

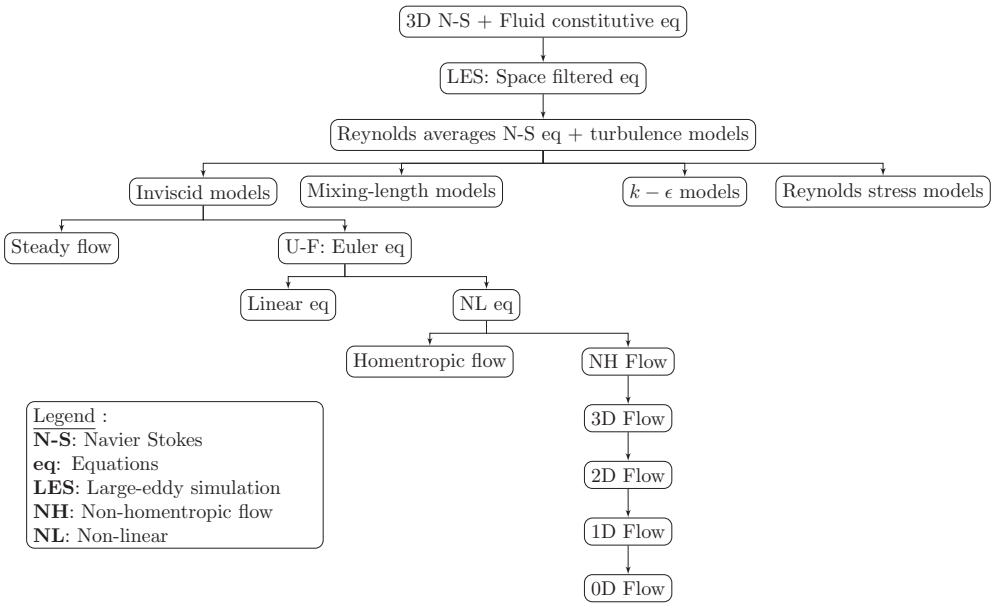

Fig. 2.1.: Hierarchy of simulation methods[24]

Figure 2.2a shows the viscous stress components applied to the faces of a control volume by the surrounding fluid. In ICE ducts, we make the assumption that variations in the y- and z- axis can be neglected, and we end up with a 1-D fluid representation. Figure 2.2b shows conservative quantities' variation along a variable area duct.

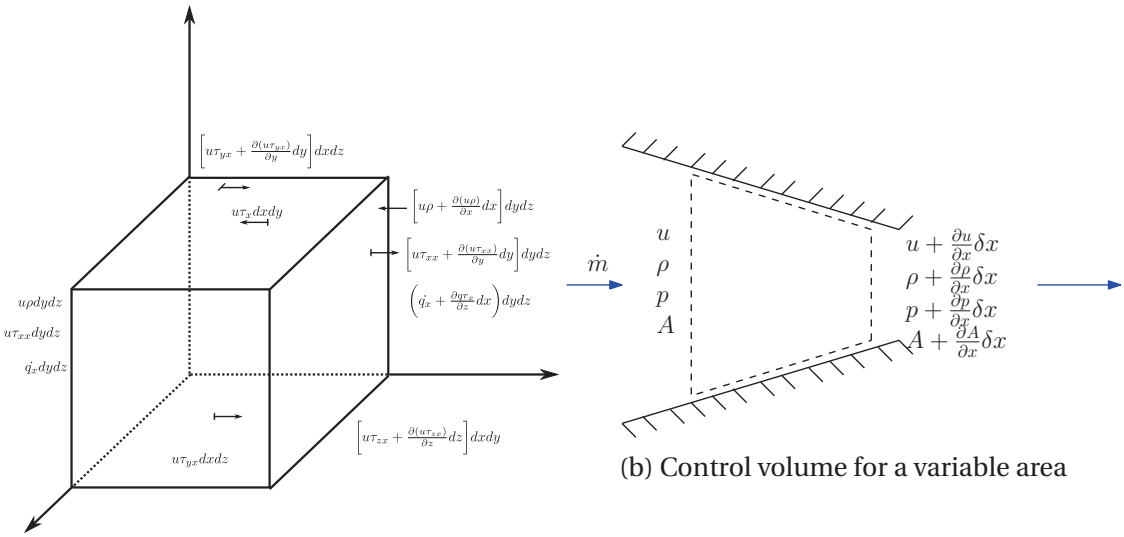

(a) Control volume with viscous stress components

(b) Control volume for a variable area

Fig. 2.2.: Comparison between 3D and 1D Modeling

In the following, the 1D flow Equations (also called as Euler Equation when the source terms are neglected) will be developed in accordance with fig. 2.2b.

1.1. Mass Conservation Equation

The mass conservation states that the rate of variation of mass within the closed control volume, is equal to the net mass flow. This can be written in the following integral form:

$$\int_V \frac{\partial \rho}{\partial t} dV + \int_A \rho \vec{u} d\vec{A} = 0 \tag{2.1}$$

In term of a one-dimensional flow, the velocity $\vec{u}$ can be substituted by the average velocity at the cross-section A.

$$\frac{\partial \rho}{\partial t} A dx + (\rho + \frac{\partial \rho}{\partial x} dx)(u + \frac{\partial u}{\partial x} dx)(A + \frac{\partial A}{\partial x} dx) - \rho u A = 0 \tag{2.2}$$

Neglecting all 2^{nd} or much higher-order terms of dx, then the continuity equation is expressed in form of:

$$\frac{\partial \rho}{\partial t} + u \frac{\partial \rho}{\partial x} + \rho \frac{\partial u}{\partial x} = -\frac{\rho u}{A} \frac{dA}{dx} \tag{2.3}$$

or equivalently

$$\frac{\partial \rho}{\partial t} + \frac{\partial (\rho u)}{\partial x} + \frac{\rho u}{A} \frac{dA}{dx} = 0 \tag{2.4}$$

- $\frac{\partial \rho}{\partial t} A dx$: the rate of variation of the mass within the control volume.
- $\frac{\partial \rho u A}{\partial x}$: variation of the mass flow rate per unit length
- or $\frac{\partial \rho u A}{\partial x} dx$: the net mass flow rate across the volume

1.2. Momentum Equation

The momentum equation imposes the Newton's second law on the control volume, which states that any change in momentum of the fluid within a control volume must result from the net flow of fluid into the volume and the action of external forces on the fluid within the volume. The one-dimensional integral form of the momentum

equation is:

$$\int_V \frac{\partial(\rho\vec{u})}{\partial t} dV + \int_A \vec{u} \cdot (\rho\vec{u}) \cdot d\vec{A} = \int_A p d\vec{A} + \vec{F}_f \tag{2.5}$$

The magnitude of shear forces $\vec{F}_f$ on the control volume should be proportional to the shear stress τ_w as well as the area of the contact surface $\pi D dx$ (in case of a cylindrical tube).

$$F_f = -\frac{u}{|u|} \tau_w \pi D dx \tag{2.6}$$

With respect to the friction factor f, the shear stress τ_w can be expressed as:

$$\tau_w = \frac{1}{2} \rho u^2 f \tag{2.7}$$

In the meanwhile, the area of the contact surface $\pi D dx$ is equivalent to (by multiplying and dividing by $(D/4)$

$$\pi D dx = \frac{1}{4} \pi D^2 \frac{4}{D} dx = \frac{4}{D} A dx \tag{2.8}$$

Hence, the shear forces F_f will become

$$F_f = -\frac{u}{|u|} \frac{1}{2} \rho u^2 f \pi D dx = -\frac{u}{|u|} \frac{4f}{D} \frac{\rho u^2}{2} A dx \tag{2.9}$$

Integrating the eq. (2.5) over the control volume:

$$\begin{aligned} \frac{\partial(\rho u)}{\partial t} A dx + (\rho + \frac{\partial \rho}{\partial x} dx)(u + \frac{\partial u}{\partial x} dx)^2 (A + \frac{\partial A}{\partial x} dx) - \rho u^2 A = \\ [p - (p + \frac{\partial p}{\partial x} dx)] A - \frac{u}{|u|} \frac{4f}{D} \frac{\rho u^2}{2} A dx \end{aligned} \tag{2.10}$$

Similarly, neglecting all 2^{nd} or higher-order terms of dx and using eq. (2.4), eq. (2.10)

becomes:

$$\rho\frac{\partial u}{\partial t}+\rho u\frac{\partial u}{\partial x}+\frac{\partial p}{\partial x}+\frac{\rho u^2}{A}\frac{dA}{dx}+sgn(u)\frac{4f}{D}\frac{\rho u^2}{2}=0 \tag{2.11}$$

The symbol $sgn(u)$ denotes the sign of the velocity. It implies that the resistance force is unconditionally opposite to the direction of the flow. Defining the coefficient of frictional resistance G,

$$G=sgn(u)\frac{4f}{D}\frac{u^2}{2} \tag{2.12}$$

the momentum equation can now be written as:

$$\frac{\partial(\rho u)}{\partial t}+\frac{\partial(\rho u^2+p)}{\partial x}+\frac{\rho u^2}{A}\frac{dA}{dx}+\rho G=0 \tag{2.13}$$

1.3. Energy Equation

The equation of energy applies the first law of thermodynamics. It states that the variation in the internal energy of the control volume is equal to the amount of the external heat supplied to it, subtracting the amount of work done on its surroundings. The mathematical description for the integral of the energy conservation is:

$$-\delta\dot{Q}+\int_V\frac{\partial}{\partial t}[\rho(h-\frac{p}{\rho}+\frac{v^2}{2}+gz)]dV+\int_A(h+\frac{v^2}{2}+gz)(\rho\vec{v}\cdot d\vec{A})=0 \tag{2.14}$$

where $\delta\dot{Q}$ indicates the heat inflow per unit time through the borders of the control volume. The value of gz equals the potential energy per unit mass initiated by the volume force. Supposing the contribution of volume force is relatively smaller than the other terms, integrate the eq. (2.14) and neglecting the term gz:

$$\begin{aligned}-\delta\dot{Q}+\frac{\partial}{\partial t}[\rho A(h-\frac{p}{\rho}+\frac{u^2}{2})dx]+\rho uA(h+\frac{u^2}{2})+\\ \frac{\partial}{\partial x}[(\rho uA(h+\frac{u^2}{2})]dx-\rho uA(h+\frac{u^2}{2})=0\end{aligned} \tag{2.15}$$

Equation (2.4), (**??**),and (2.15) contain four unknowns (ρ, u, p, and h) thus the set of equations is not enough for solving.

In the theory of fluid dynamics, an additional relation among the gas states is required for building a completely closed system of governing equations together. A proper supplement for closing this system is based on the hypothesis of a perfect gas, which is on one hand subjected to the law of ideal gas, and on the other hand, indicates the specific heat c_v and c_p can be considered as constant. Along with the definition of a perfect gas, there are

$$\begin{cases} p = \rho R_{spec} T \\ h = c_p T \\ e = c_v T \end{cases} \quad \text{and} \quad \begin{cases} R_{spec} = c_p - c_v \\ \gamma = \dfrac{c_p}{c_v} \end{cases} \tag{2.16}$$

where the variable p, T, ρ, h and e stand for respectively the pressure, temperature, density, specific enthalpy and specific internal energy of the gas. Besides that, the parameters R_{spec}, c_p, c_v and γ gained from the gas properties, denote separately the specific gas constant, specific heat capacity at constant pressure, specific heat capacity at constant volume and specific heat capacity ratio, remaining invariable during the flow process.

Substituting the expression of gas states in eq. (2.15) with eq. (2.16):

$$\frac{\partial}{\partial t}[\rho A(c_v T + \frac{u^2}{2})dx] + \frac{\partial}{\partial x}[\rho u A(c_v T + R_{spec} T + \frac{u^2}{2})]dx = \delta\dot{Q} \tag{2.17}$$

Introducing the rule of perfect gas from eq. (2.16) gives

$$\frac{\partial(\rho u A R_{spec} T)}{\partial x} = \frac{\partial(puA)}{\partial x} \tag{2.18}$$

Expanding the equation and eliminating the terms involving the partial derivative $\partial A/\partial t$:

$$\begin{aligned} \rho u A \frac{\partial}{\partial x}(c_v T + \frac{u^2}{2}) + \frac{\partial(puA)}{\partial x} + (c_v T + \frac{u^2}{2})\frac{\partial(\rho u A)}{\partial x} \\ + A\rho\frac{\partial}{\partial t}(c_v T + \frac{u^2}{2}) + (c_v T + \frac{u^2}{2})A\frac{\partial \rho}{\partial t} = \delta\dot{Q} \end{aligned} \tag{2.19}$$

Without doubt, the derivation based on the energy equation must be always in compliance with the law of mass conversation. On the basis of this continuity equation, which is referred in eq. (2.3), the 3^{rd} and 5^{th} terms from eq. (2.19) can vanish together.

After elimination, the equation turns out to be

$$\frac{\partial}{\partial t}(c_vT+\frac{u^2}{2})+u\frac{\partial}{\partial x}(c_vT+\frac{u^2}{2})=\frac{\delta\dot{Q}}{\rho A\delta x}-\frac{1}{\rho A}\frac{\partial(pAu)}{\partial x} \tag{2.20}$$

The mathematical statement for total derivative of the stagnation internal energy $c_vT+u^2/2$ can be proposed in this case intending to simplify the expression above

$$\begin{aligned}\frac{d}{dt}(c_vT+\frac{u^2}{2})&=\frac{\partial}{\partial t}(c_vT+\frac{u^2}{2})+u\frac{\partial}{\partial x}(c_vT+\frac{u^2}{2})\\&=\frac{\delta\dot{Q}}{\rho A\delta x}-\frac{1}{\rho A}\frac{\partial(pAu)}{\partial x}\\&=\frac{\delta\dot{Q}}{\rho A\delta x}-\frac{u}{\rho}\frac{\partial p}{\partial x}-\frac{p}{\rho A}\frac{\partial(Au)}{\partial x}\end{aligned} \tag{2.21}$$

To be obedient to the law of ideal gas, the derivative of stagnation internal energy can be expressed as:

$$\begin{aligned}\frac{d(c_vT)}{dt}&=\frac{d}{dt}(\frac{c_v}{R_{spec}}\frac{p}{\rho})\\&=\frac{d}{dt}(\frac{1}{(\gamma-1)}\frac{p}{\rho})\\&=\frac{1}{(\gamma-1)\rho}[(\frac{\partial p}{\partial t}+u\frac{\partial p}{\partial x})-\frac{p}{\rho}(\frac{\partial\rho}{\partial t}+u\frac{\partial\rho}{\partial x})]\end{aligned} \tag{2.22}$$

Manipulating the other partial differential of stagnation internal energy with the momentum **??**, the total derivative of the kinetic energy can be reformulated as follows:

$$\begin{aligned}\frac{d}{dt}(\frac{u^2}{2})&=u\frac{du}{dt}\\&=u(\frac{\partial u}{\partial t}+u\frac{\partial u}{\partial x})\\&=u(-\frac{1}{\rho}\frac{\partial p}{\partial x}-G)\end{aligned} \tag{2.23}$$

On the other hand, the term $\partial(Au)/\partial(x)$ in eq. (2.20) can be extracted from the continuity eq. (2.4):

$$\frac{\partial(Au)}{\partial x}=-\frac{A}{\rho}(\frac{\partial\rho}{\partial t}+u\frac{\partial\rho}{\partial x}) \tag{2.24}$$

Manipulating the eq. (2.20) by replacing the corresponding terms with the equations from (2.21) to (2.23) and multiplying by $(\gamma-1)\rho$:

$$\begin{aligned}&\frac{\partial p}{\partial t}+u\frac{\partial p}{\partial x}-\frac{p}{\rho}\left(\frac{\partial \rho}{\partial t}+u\frac{\partial \rho}{\partial x}\right)+(\gamma-1)\,\rho u\left(-\frac{1}{\rho}\frac{\partial p}{\partial x}-G\right)\\&=(\gamma-1)\rho\left[\frac{\delta\dot{Q}}{\rho A\delta x}-\frac{u}{\rho}\frac{\partial p}{\partial x}-\frac{p}{\rho A}\left(-\frac{A}{\rho}\right)\left(\frac{\partial \rho}{\partial t}+u\frac{\partial \rho}{\partial x}\right)\right]\end{aligned} \tag{2.25}$$

Rearranging the statement of the equation gives:

$$\frac{\partial p}{\partial t}+u\frac{\partial p}{\partial x}-\gamma\frac{p}{\rho}\left(\frac{\partial \rho}{\partial t}+u\frac{\partial \rho}{\partial x}\right)=(\gamma-1)\,\rho\left(\frac{\delta\dot{Q}}{\rho A\delta x}+uG\right) \tag{2.26}$$

The speed of sound for an ideal gas is given as:

$$a^2=\gamma\frac{p}{\rho} \tag{2.27}$$

Furthermore, representing the heat transfer term on the right side of eq. (2.26) and defining $\dot{q}$ as being the heat flux density across the boundary of the control volume.

$$\dot{q}=\frac{\delta\dot{Q}}{\rho A\delta x} \tag{2.28}$$

Consequently, all the simplifications above lead to the final form of energy conservation:

$$\frac{\partial p}{\partial t}+u\frac{\partial p}{\partial x}-a^2(\frac{\partial \rho}{\partial t}+u\frac{\partial \rho}{\partial t})=(\gamma-1)\rho(\dot{q}+uG) \tag{2.29}$$

Introducing the stagnation internal energy and stagnation enthalpy of the fluid as:

$$\begin{aligned}e_0&=e+\frac{u^2}{2}=h-\frac{p}{\rho}+\frac{u^2}{2}\\h_0&=h+\frac{u^2}{2}\end{aligned} \tag{2.30}$$

Then the energy equation in (2.17) can be reformulated as:

$$\frac{\partial(\rho e_0)}{\partial t}+\frac{\partial(\rho u h_0)}{\partial x}+\frac{\rho u h_0}{A}\frac{dA}{dx}-\rho\dot{q}=0 \tag{2.31}$$

$$\begin{pmatrix}\text{Rate of change}\\ \text{of internal}\\ \text{energy}\end{pmatrix}=-\begin{pmatrix}\text{Net}\\ \text{Energy}\\ \text{Flow}\end{pmatrix}+\begin{pmatrix}\text{Net}\\ \text{heat}\\ \text{flux}\end{pmatrix}$$

Gathering the previous non-conservative equations (2.3), (**??**) and (2.29) for mass, momentum and energy for a *one-dimensional, unsteady, compressible, variable-cross-section-area and viscous flow* can give rise to a new tightly coupled system of partial differential equations:

$$\begin{cases}\dfrac{\partial\rho}{\partial t}+\rho\dfrac{\partial u}{\partial x}+u\dfrac{\partial\rho}{\partial x}+\dfrac{\rho u}{A}\dfrac{dA}{dx}=0\\ \dfrac{\partial u}{\partial t}+u\dfrac{\partial u}{\partial x}+\dfrac{1}{\rho}\dfrac{\partial p}{\partial x}+G=0\\ \dfrac{\partial p}{\partial t}+u\dfrac{\partial p}{\partial x}-a^2\left(\dfrac{\partial\rho}{\partial t}+u\dfrac{\partial\rho}{\partial x}\right)-(\gamma-1)\,\rho\,(\dot{q}+uG)=0\end{cases} \tag{2.32}$$

Commonly, the governing equations are written in terms of conserved quantities ρ, ρu, ρe_0:

$$\begin{cases}\dfrac{\partial\rho}{\partial t}+\dfrac{\partial(\rho u)}{\partial x}+\dfrac{\rho u}{A}\dfrac{dA}{dx} & =0\\ \dfrac{\partial(\rho u)}{\partial t}+\dfrac{\partial(\rho u^2+p)}{\partial x}+\dfrac{\rho u^2}{A}\dfrac{\partial A}{\partial x}+\rho G & =0\\ \dfrac{\partial(\rho e_0)}{\partial t}+\dfrac{\partial(\rho u h_0)}{\partial x}+\dfrac{\rho u h_0}{A}\dfrac{dA}{dx}-\rho\dot{q} & =0\end{cases} \tag{2.33}$$

Thus, the governing equations (2.33) can be considered as an algebraic sum of the unsteady term $\partial/\partial t$, the convection term $\partial/\partial x$ and the source term, which contain all the rest terms that cannot be integrated into the first two terms.

With respect to the theory of partial differential equations, the complete characterization eq. (2.32) or eq. (2.33) for the dynamics of the investigated flow can be mathematically identified as a system of quasi-linear non-homogeneous hyperbolic partial differential equations (abbr. H-PDEs).

Since this system contains three independent governing equations and an identical

number of independent variables, the closure condition of this problem has been fully satisfied. In this sense, the uniqueness and certainty of the solution for this H-PDEs can be mathematically guaranteed.

Equation (2.33) is known as the *Euler Equation*. This is a system of three equations with four unknowns p,u,ρ,T. The system is most of the time written in vector notation, which makes it easier to carry the equations set.

$$\mathbf{W} = \begin{bmatrix} \rho \\ \rho u \\ \rho e_0 \end{bmatrix}, \mathbf{F}(\mathbf{W}) = \begin{bmatrix} \rho u \\ (\rho u^2 + p) \\ \rho u h_o \end{bmatrix}, \mathbf{S}(\mathbf{W}) = \begin{bmatrix} \rho u \\ \rho u^2 \\ \rho u h_0 \end{bmatrix} \frac{d\,(lnA)}{dx} + \begin{bmatrix} 0 \\ \rho G \\ -\rho \dot{q} \end{bmatrix} \tag{2.34}$$

$$\frac{\partial \mathbf{W}}{\partial t} + \frac{\partial \mathbf{F}(\mathbf{W})}{\partial x} + \mathbf{S}(\mathbf{W}) = 0 \tag{2.35}$$

Thus, when dealing with an ideal gas, which can be true almost always in the case of ICE, the system can be augmented using ideal gas law, which enables to solve for the unknown variables. Any other flow property such as enthalpy, energy and speed of sound can be calculated using the independent state variables. As no analytical solution exist, the flow properties at every node of the duct and time instant can be obtained by means of different numerical methods. Additionally, it is possible to consider the inclusion of the chemical species transport, by augmenting the system of equations. Serrano et al. [25] stated that this later action will not cause any changes, neither in the solution procedure, nor in the order of accuracy of the numerical method.

For a homentropic flow (constant cross section, no heat transfer or friction), eq. (2.33) can also be written as follows:

$$\frac{\partial \mathbf{W}}{\partial t} + \mathbf{A}\frac{\partial \mathbf{W}}{\partial x} = 0 \tag{2.36}$$

where $\mathbf{W}$ is a vector whose components, say m in number, are the independent variables and $\mathbf{A}$ is an m x m matrix, whose elements depend generally on the components of U and on x and t.The system is called hyperbolic [3] if A has all real eigenvalues and m linearly independent eigenvectors. $\mathbf{A}$ is not usually a symmetric matrix.

[3]The system is called hyperbolic if $\mathbf{A}$ in the PDE $\frac{\partial \mathbf{W}}{\partial t} + \mathbf{A}\frac{\partial \mathbf{W}}{\partial x} = 0$ has all real eigenvalues and m linearly independent eigenvectors. For proof see appendix A.

2. Solution of the Conservation Equations

2.1. Initial and Boundary Conditions

The system of equations, eq. (2.35) can be applied to gas flowing into or from the duct, initially moving or stationary gas. Hence, initial and boundary conditions are required to have a defined problem. In practical applications, the processes to be investigated take place in a concrete geometry (e.g., in turbines, exhaust and intake manifolds, after treatment systems etc.) during a finite interval of time. Once the geometry is specified, boundary conditions can then be properly taken into consideration. These are usually modeled using steady state models as the variation in space is considered to be more apparent with respect to states variation with respect to time. A summary of boundary conditions treatment in I.C.E is given in section 7.

The choice of the time interval to be considered is dictated by the nature of the problem at hand (for example gas temperature, concentrations and duct geometry), by the objectives of the analytical or numerical study, and by the available computational power.

2.2. Numerical Constraints

The continuous conservation equations can be said to be practically worthless without numerical methods. This is a branch of applied mathematics that deals with numerical simulation of fluid flow. Discretization schemes play a crucial role in the implementation of flow models, but they, themselves, cause many problems, and are not always straightforward implementable. A deep understanding is necessary to be able to avoid any instabilities and numerical errors which will make the solution drift away from the real one (or appear as non-physical simulation results).

Symmetric or upwind shock capturing numerical schemes have overtaken in the last decade the Method of Characteristics (MOC) [26] to model transport phenomena in engine ducts. However, they still rely on the MOC when it comes to quasi-steady boundary conditions. Upwind time marching schemes use the flow characteristics to define the time step size (for a fixed space mesh), whereas symmetric schemes are independent of the flow characteristics.

Consistency, stability[4], and convergence are the three cornerstones of numerical approximation. A discretization that meets all of these requirements is guaranteed to produce an accurate solution provided that Δx and ΔT are sufficiently small. However, the definition of *sufficiently small* is highly problem-dependent. If a numerical scheme fails to resolve a small-scale feature properly on a given mesh, it typically reacts by generating large numerical errors and/or nonphysical side effects, such as a spontaneous loss or gain of mass or spurious oscillations, also known as 'wiggles'. Discontinuities

[4] A numerical method is said to be stable if numerical errors, e.g., due to round off, are not amplified, and the approximate solution remains bounded.

such as shocks and intra-pipe boundaries are the main source of violation of physical constraints. Sometimes, very small discontinuities can be neglected, such as very small pressure or temperature differences but there are cases, where they result in completely wrong unstable calculations. Therefore, certain physical constraints, such as conservation and boundedness, may need to be enforced at the discrete level [27].

In the case of 1D flow simulation, the system is most of the time subject to the well-known stability condition observed by Courant, Friedrichs, and Lewy in [28] , which takes the form

$$\frac{c\Delta T}{\Delta x} < 1 \tag{2.37}$$

and says that the distance traveled by a sound wave relative to the fluid must not exceed the distance $x_{j+l} - x_j = \Delta x$ between neighboring points. In other words, waves or perturbations cannot travel more than one mesh length in one calculation time increment. Otherwise, the gas dynamics will not be captured by the numerical scheme continuously which leads to wrong calculations and even instabilities.

2.3. Physical Constraints

They are conservation, boundedness and causality. Conservation dictates that the diffusive or convective numerical effect resulting from the discretization cannot create or destroy the mass inside the duct. They can alter the local density for example, but at most distribute the mass improperly. Finite volume and discontinuous Galerkin methods are conservative by construction, both globally and locally. The continuous Galerkin FEM provides global conservation and is claimed to be locally conservative by some authors [29, 30]. Conservation may be lost if inaccurate quadrature rules or nonstandard approximations are employed [27].

3. Schemes for Hyperbolic Systems in One Space Variables

Unsteady flows with ICE ducts can be considered to be essentially one-dimensional in the inlet and exhaust systems [31]. Hence, in this document, we will restrict our selves only to one dimensional models. On the other hand, The 0D elements are those which are able to accumulate flow. In this case, flow conditions are constant over the volume at each calculation instant. This is the case of the cylinders, turbine or other volumes in inter-coolers, after-treatment devices, etc. These kinds of elements are solved by means of a filling and emptying model that include the mass and energy conservation equations for open systems combined with the ideal gas state equation. The chemical species transport across 0D elements involves the addition of $n-1$ mass conservation equations to calculate the mass fraction of n chemical species [25].

The basic methods of modeling one-dimensional compressible flow in inlet and exhaust systems can be classified into four major groups; namely wave theory, method of characteristics, finite difference and finite volume techniques [24]:

3.1. Wave Theroy

In some references, also called *linear wave theory*. It can only be applied to short pipes with neglected friction or heat transfer (homentropic[5] flows.), or to naturally aspirated engines, which have small pressure disturbances.

3.2. Method of Characteristics

This approach has been already used for the solution of partial differential equations. Benson [26] has then applied this method graphically for the simulation of homentropic and non-homentropic flow in the ICE ducts using a graphical approach. He then soon noticed the complexity even for very simple cases such as single cylinder engines and developed a numerical approach.

3.3. Finite Difference and Finite Volume Methods

In these methods, the duct is subdivided into small increments of length by a computational mesh whose nodes define the location at which the flow variables are calculated. Their values are obtained by algebraic equations which approximate the differential equations and connect the node variables to each other.

Various techniques are used in the discretization and solution stages [32].

In the following, we will present briefly the MOC and some finite difference methods. The MOC will be used later as a base for boundary conditions treatment, whereas finite difference methods, will be evaluated in terms of accuracy and calculation effort to be used later as reference for reduced order models.

4. The Method of Characteristics

The first contribution to the calculation of the one-dimensional non-stationary flow in the ducts of the combustion engines are derived from the graphical and numerical applications of the classical method of characteristics [33, 34]. This approach has the merit of reproducing numerically wave propagation that is at the basis of phenomena of non-stationary flow, and to allow a simple and natural treatment of all types of boundary conditions of practical interest.

[5] Homentropic flow is a flow without temperature discontinuities such as those occurring in exhaust pipes, which involve changes of entropy level and produce non-homentropic flow fields [26]

Starting from the Euler Equation, and considering[6] a homentropic flow (no friction, no heat transfer), and no section variation:

Continuity

$$\frac{\partial(\rho u)}{\partial x} = -\frac{\partial \rho}{\partial t} \Rightarrow \frac{1}{\rho}\frac{\partial \rho}{\partial t} + \frac{u}{\rho}\frac{\partial \rho}{\partial x} + \frac{\partial u}{\partial x} = 0 \tag{2.38}$$

Momentum

$$\frac{\partial(\rho)}{\partial x} = \rho\frac{D\rho}{Dt} \Rightarrow \frac{1}{\rho}\frac{\partial p}{\partial t} + \frac{\partial u}{\partial t} + u\frac{\partial u}{\partial x} = 0 \tag{2.39}$$

Assuming a reference state, the Third conservation equation. i.e. constant entropy (isentropic flow) is expressed as:

$$\frac{p}{p_{ref}} = \left(\frac{a}{a_{ref}}\right)^{2\gamma/(\gamma-1)} \tag{2.40}$$

or

$$\frac{\rho}{\rho_{ref}} = \left(\frac{a}{a_{ref}}\right)^{2/(\gamma-1)} \tag{2.41}$$

For isentropic flow ρ_{ref}, p_{ref} and a_{ref} are constant, hence, equations 2.40 and 2.41 can be written in differential form as:

$$\frac{dp}{p} = \frac{2\gamma}{\gamma-1}\frac{da}{a} \tag{2.42}$$

$$\frac{d\rho}{\rho} = \frac{2}{\gamma-1}\frac{da}{a} \tag{2.43}$$

Writting in terms of partial derivatives in x and t yields:

$$\frac{1}{p}\frac{\partial p}{\partial x} = \frac{2\gamma}{\gamma-1}\frac{1}{a}\frac{\partial a}{\partial x} \tag{2.44}$$

$$\frac{1}{\rho}\frac{\partial \rho}{\partial t} = \frac{2}{\gamma-1}\frac{1}{a}\frac{\partial a}{\partial t} \tag{2.45}$$

[6]The same approach can be used for non-homentropic flow [26]

$$\frac{1}{\rho}\frac{\partial \rho}{\partial x} = \frac{2}{\gamma - 1}\frac{1}{a}\frac{\partial a}{\partial x} \tag{2.46}$$

Substituting eq. (2.45) and eq. (2.46) into the original continuity equation 2.38 yields:

$$\frac{2}{\gamma - 1}\frac{\partial a}{\partial x} + \frac{2}{\gamma - 1}u\frac{\partial a}{\partial x} + a\frac{\partial u}{\partial x} = 0 \tag{2.47}$$

Similarly, using eq. (2.44) , the momentum equation can be rewritten as:

$$\frac{2}{\gamma - 1}a\frac{\partial a}{\partial x} + \frac{\partial u}{\partial t} + u\frac{\partial u}{\partial x} = 0 \tag{2.48}$$

Hence, two conservation equations were obtained in terms of the local speed of sound a and the particle velocity u for the special case of constant entropy throughout the whole fluid flow. The objective now is to evaluate a and u for $\forall x$ and t

eq. (2.47) and eq. (2.48) are manipulated as follows:

eq. (2.47)$+\frac{\gamma-1}{2}$eq. (2.48)

$$\Rightarrow \left[\frac{\partial a}{\partial t} + (u + a)\frac{\partial a}{\partial x}\right] + \frac{\gamma - 1}{2}\left[\frac{\partial u}{\partial t} + (u + a)\frac{\partial u}{\partial x}\right] = 0 \tag{2.49}$$

eq. (2.47)$-\frac{\gamma-1}{2}$eq. (2.48)

$$\Rightarrow \left[\frac{\partial a}{\partial t} + (u + a)\frac{\partial a}{\partial x}\right] - \frac{\gamma - 1}{2}\left[\frac{\partial u}{\partial t} + (u + a)\frac{\partial u}{\partial x}\right] = 0 \tag{2.50}$$

In order to obtain the characteristic equations, it is assumed that a and u are uniquely related by the expression $c = c(a, u)$.

Hence, the solution of eq. (2.49) and eq. (2.50) will be of the form

$$c = c(x, t) \tag{2.51}$$

Thus,

$$(da)_{char} = \left(\frac{\partial a}{\partial t}dt + \frac{\partial a}{\partial x}dx\right)_{char}$$
$$(du)_{char} = \left(\frac{\partial u}{\partial t}dt + \frac{\partial u}{\partial x}dx\right)_{char}$$

the total derivatives along a characteristic are then:

$$\left(\frac{da}{dt}\right)_{char} = \left(\frac{\partial a}{\partial t} + \frac{\partial a}{\partial x}\frac{dx}{dt}\right)_{char}$$
$$\left(\frac{du}{dt}\right)_{char} = \left(\frac{\partial u}{\partial t} + \frac{\partial u}{\partial x}\frac{dx}{dt}\right)_{char}$$

or

$$\left(\frac{da}{dt}\right)_{char} = \left(\frac{\partial a}{\partial t} + c\frac{dx}{dt}\right)_{char}$$
$$\left(\frac{du}{dt}\right)_{char} = \left(\frac{\partial u}{\partial t} + c\frac{dx}{dt}\right)_{char}$$

then, the following conditions are then hold along a characteristic:

$$\left(\frac{dx}{dt}\right)_{char} = c \tag{2.52}$$
$$\left(\frac{da}{dt}\right)_{char} = \frac{\partial a}{\partial t} + c\frac{\partial a}{\partial x} \tag{2.53}$$
$$\left(\frac{du}{dt}\right)_{char} = \frac{\partial u}{\partial t} + c\frac{\partial u}{\partial x} \tag{2.54}$$

These equations represent the changes in a and u with respect to x and t along specifically defined curves called the characteristics. The function $c = c(a,u)$ now has to be determined to satisfy, along the characteristics, the last equations as well as basic equations 2.49 and 2.50

Now, we will see how equations 2.52,2.53 and 2.54 or combinations will produce normal differential equations.

$$c = \frac{dx}{dt} = u + a \tag{2.55}$$

$$\frac{da}{dt} + \frac{\gamma - 1}{2}\frac{du}{dt} = 0 \Rightarrow \frac{da}{du} = -\frac{\gamma - 1}{2} \tag{2.56}$$

and

$$c = \frac{dx}{dt} = u - a \tag{2.57}$$

$$\frac{da}{dt} - \frac{\gamma-1}{2}\frac{du}{dt} = 0 \Rightarrow \frac{da}{du} = \frac{\gamma-1}{2} \tag{2.58}$$

eqs. (2.55) and (2.56) and eqs. (2.57) and (2.58) can be grouped and written as:

$$\frac{dx}{dt} = u \pm a$$
$$\frac{da}{du} = \mp\frac{\gamma-1}{2}$$

and the Riemann Invariants are:

$$\lambda = a + \frac{\gamma-1}{2}u \tag{2.59}$$
$$\beta = a - \frac{\gamma-1}{2}u \tag{2.60}$$

The method of characteristics is a first order method. It is not able to identify and correctly propagate the discontinuities of flow, whether they are shock waves or contact discontinuities [7]. A first order accurate numerical scheme is inadequate to meet the needs of current applications, because it generates an excessive amount of numerical viscosity, which has the effect to reduce significantly the resolution of steep gradients and high frequency disturbances that characterize the non-stationary flow in the ducts of the fast motors. The inability to capture discontinuity in flow is a serious limitation, since the contact surfaces [8] are always present in persistent intake and exhaust of engines, while the bumps may occur sometimes in the diverging sections of the ducts [35].

4.1. Illustrating Example

Consider two volumes with different pressures attached to a duct. The high-pressure border of the duct is assumed as upstream boundary, whereas the other one is considered as downstream boundary.The duct is initially open to the downstream volume as shown in the following figure.

[7] Contact discontinuity is the interface of two gases of different composition, or different temperature:an example is the intake valve, forward and back flow of combustion products in the exhaust and intake paths respectively

[8] Contact surfaces also occur in systems of constant composition in the form of abrupt changes in density and temperature–negative density values are the main danger in this case.

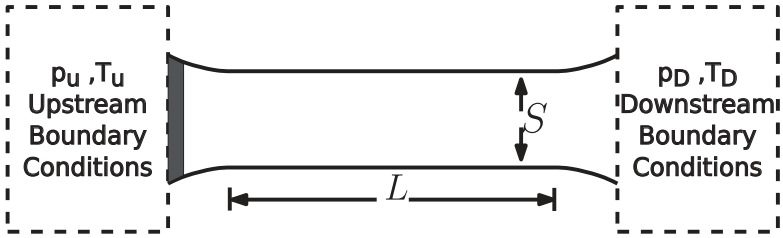

Fig. 2.3.: A generic QPM Branch

Simulating this situation using the full 1D CE-SE scheme (validated in the previous chapter using the shock tube numerical test), and the open boundary condition (given in section 7), the following pressure and gas velocity profiles at position (L/2) is obtained:

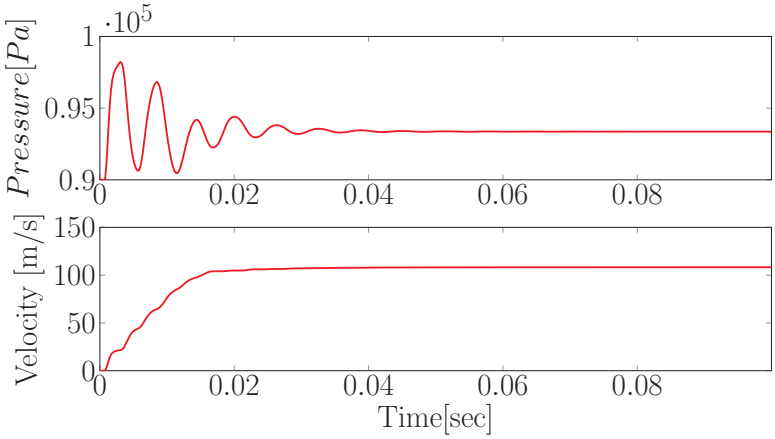

Fig. 2.4.: Pressure and Gas Velocity Mid-Point the Tube

- If the duct has initially the downstream conditions, the pressure at the mid-point will oscillate until stationarity. Similarly, the flow velocity will gradually increase until a constant velocity is reached. This is represented in fig. 2.4. The first increase in the mid-point pressure is due to the compression wave moving from left to right ($p_U > p_D$). When this compression wave reaches the downstream open end, it will be reflected and inverted, which appears as a decrease in the pressure signal.
- When the flow reaches stationarity, the duct will act as a simple restriction between the two volumes. Hence, regardless of the initial state of the duct, the steady state velocity u_∞, is a function of the boundary conditions and the geometry only. Even if in the case of an ICE, stationary states are not reached due to the continuous opening and closure of the valves, this approach remains valid as steady states are calculated at the beginning of each iteration.

To explain this behavior in terms of the characteristics, consider the *position diagram*

shown in fig. 2.5b and the *state diagram* in fig. 2.5a.

The position diagram gives the possibility to track waves propagation, whereas the state diagram is used to calculate particles velocity and sound speed at a given position. These two diagrams can be used solely to calculate a full solution (also known as the graphical solution [26]), except that the procedure will become a tedious task even for simple problems.

According to fig. 2.3:

- Initially, the tube has the same downstream conditions. The gas is at rest, hence $u_0 = 0$, and $p = p_0$ or a_0
- These are shown in the state diagram as an initial state.
- Both λ_0 (eq. (2.59)) and β_0 (eq. (2.60)) are shown on the position and state diagram.
- Once the separation is removed, there is a perturbation which will travel from left to right.
- This perturbation is the λ_1 characteristic. It is drawn in the position diagram automatically. In the state diagram, we know that the fluid velocity will increase, which means λ_1 will be drawn to the right of λ_0.
- The transition between $(0, a_0)$ to (u_1, a_1) is done along the β_0 characteristic. This will lead to an increase in both local fluid velocity and speed of sound.
- Once the perturbation will reach the right boundary condition, a β_1 characteristic will be generated.
- a_1 speed of sound will now decrease along λ_1, and the fluid velocity will increase.
- The process will continue until stationarity is reached.

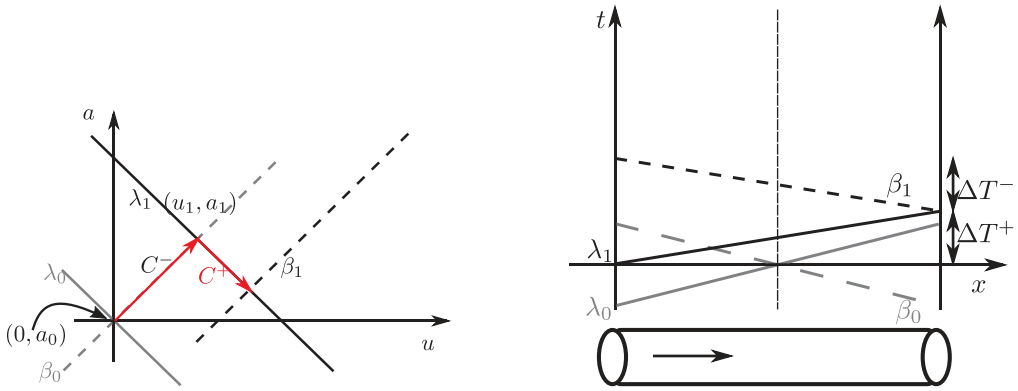

(a) The state diagram

(b) The position diagram

Fig. 2.5.: Illustration of the QPM idea using characteristics (The initial characteristics are shown in gray)

Physically, the characteristic curves can propagate from the upstream boundary with speed $c^+ = a + u$ and from the downstream boundary with speed $c^- = u - a$. Thus, it takes respectively $\Delta t^+ = L/(a+u)$ and $\Delta t^- = L/(a-u)$ for the propagation from one end of the pipe to the other, if the variation of the velocity c can be neglected in these short periods. The trace of the characteristics is recorded in the $t - x$ plane.

5. Finite Difference Discretization Schemes

As an alternative to the method of characteristics, Winterbone and Pearson [36] propose the use of a finite difference scheme accurate to the second order [37] for the calculation of the evolution of non-stationary flow in the engine ducts. The finite difference methods are generally much more efficient than the method of characteristics.

Because these numerical schemes use the conservative form of the equations, they allow building the shock-capturing schemes, which can be taken into account in a natural discontinuity. The limit of such an approach, is the spurious oscillations which will corrupt the numerical solution of order higher than two. These oscillations are only removed by means of an artificial viscosity.

The Lax-wendroff Scheme with one and two steps is presented for the case of homentropic flow with no cross section variation. These two assumptions do not alter the algorithm, and are here avoided for clarification sake.

5.1. Lax-Wendroff 1-Step

The simplest scheme is the one known as the Lax-Wendroff 1 step [37]. It basically states that the new state at a given position depends on the previous state at that same position and also the first adjacent positions.

The equations are simple to derive and straightforward to implement. Figure 2.6a shows a representation of the Lax-wendroff scheme with one step in the x-t plane.

$$W_i^{n+1} = W_i^n - \frac{\Delta T}{2\Delta x}\left[A\left(W_{i+1}^n - A\left(W_{i-1}^n\right)\right)\right] \tag{2.61}$$

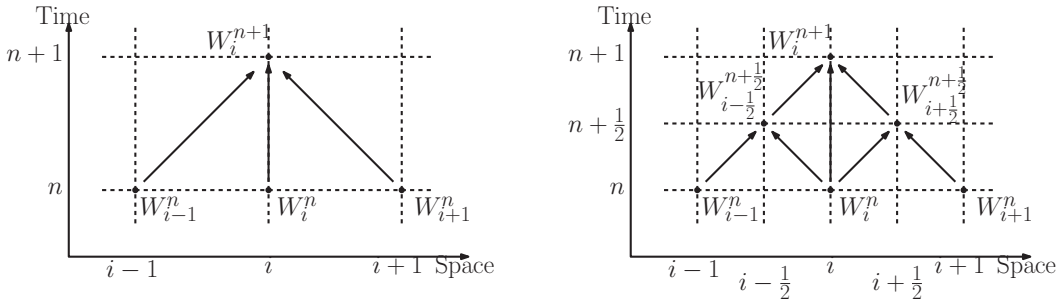

(a) The One Step Lax-Wendroff scheme

(b) The Two Steps Lax-Wendroff scheme

Fig. 2.6.: The Lax-Wendroff schemes

5.2. Lax-Wendroff 2-Steps

The second scheme, was an extension of the Lax-wendroff one step. This time, the new state is based on information from two steps backward (or one extra intermediate step is used), and it involves four adjacent cells. Figure 2.6b shows a representation of this scheme in the x-t domain.

The new state at instant $(n+1)$ and position (i) can be calculated as:

$$\begin{aligned} W_{i+1/2}^{n+1/2} &= \frac{1}{2}\left(W_{i+1}^n + W_i^n\right) - \frac{\Delta t}{2\Delta x}\left(\mathbf{F}_{i+1}^n - \mathbf{F}_i^n\right) \\ W_{i-1/2}^{n+1/2} &= \frac{1}{2}\left(W_i^n + W_{i-1}^n\right) - \frac{\Delta t}{2\Delta x}\left(\mathbf{F}_i^n - \mathbf{F}_{i-1}^n\right) \\ W_i^{n+1} &= W_i^n - \frac{\Delta t}{\Delta x}\left(\mathbf{F}_{i+1/2}^{n+1/2} - \mathbf{F}_{i-1/2}^{n+1/2}\right) \end{aligned} \tag{2.62}$$

5.3. Conclusion on Difference Methods

For a physical solution in a region of rapid change, the smoothness assumption is difficult to realize by a numerical approximation that can use only a limited set of discrete variables. This difficulty becomes even worst in the presence of discontinuities, such as shocks. [20]

Onorati et al. [38] have compared the results obtained with symmetric finite difference schemes and with a discontinuous finite-element method in the solution of classical test cases for one-dimensional unsteady flows in ducts. They have considered the second-order accurate two-step Lax-Wendroff method and the MacCormack predictor-corrector method with the addition of the FCT (Flux-Corrected Transport) or the TVD (Total Variation Diminishing) techniques, and a second- and third-order accurate discontinuous Galerkin finite-element method. The shock-tube calculations show that the second-order accurate finite-difference and finite element results have a very similar accuracy, whilst the third-order accurate FEM gives significant improvements

in the resolution of the discontinuities. In the case of the shock-turbulence interaction problem, in which the solution is characterized by shocks as well as by high-frequency oscillations, the gain in accuracy of the third-order FEM was more evident. It was found that the FEM is computationally more demanding than finite difference schemes. In addition, the FEM is well suited to model flow regions characterized by strong variation of the cross-sectional area and of friction and heat transfer at duct walls, since this method allows a more flexible local refinement of the mesh. This makes adjacent ducts with very different mesh size may be easily treated. Moreover, hybrid FEM models coupling 1D calculations of flows in ducts with 3D direct modeling of flow boundary regions could be naturally developed. In fact, the greater geometrical flexibility and the straightforward treatment of boundary conditions allowed by the FEM could be crucial advantage in these cases over the more commonly adopted finite-difference techniques. This is especially true in multidimensional applications since the FEM is ideally suited to be used on unstructured grids.

Corberán and Gascón [39] have tried to adapt the FCT techniques and the original TVD scheme proposed by Harten [40] to the calculation of cases with variable cross section. The most serious difficulty has been found in the treatment of the differences expressed on the variation of the conserved state variables W. The terms concerning those W differences always led to excessive diffusion in the points in which the rate of cross-section variation is high, or even to problems in the global conservation along the pipe. This difficulty disappears when all the differences in the scheme can be expressed as flux differences. The proposed scheme has been derived following this idea, but this has been only possible for a TVD scheme and not for the FCT techniques.

6. The Conservation Element-Solution Element Scheme

Chang and To [41] described a new numerical method for solving conservation laws. lt is much simpler than a typical high resolution method. No flux limiter or any characteristics based technique is involved. No artificial viscosity or smoothing is introduced, and no moving mesh is used. Yet this method is capable of generating highly accurate shock tube solutions.

The idea is to divide the x-t space into two types of regions: A region where an approximation of the solution is to be used, through a Fourier transform, the new approximation is to be used within a region where the solution is said to be conservative: Which means , that for this numerical scheme, a condition is set from the beginning to impose conservation.

This scheme has a stencil containing only two points. This minimization of stencil has the effect of reducing numerical diffusion. It is achieved by including α_j and β_j as numerical variables. The fluxes at an interface separating two Conservation Elements (CE) are evaluated with no interpolation or extrapolation. Accuracy of flux evaluation is enhanced by requiring that the solution given in eq. (2.67) satisfies the Euler equations at the center of every Solution Element (SE). This makes all use of characteristics-based

techniques less necessary. The above key features can contribute to the simplicity, generality and accuracy of the current scheme. They all owe their existence to the use of staggered SEs and CEs [41].

The first step of the numerical scheme used is the approximation of the solution in each SE (j, n) by a Taylor series expansion of 2.35 truncated after the terms of the 1st order:

$$\widetilde{w}_m\left(x,t;j,n\right)=\left(\sigma_m\right)_j^n+\left(\alpha_m\right)_j^n\left(x-x_j\right)+\left(\beta_m\right)_j^n\left(t-t^n\right) \tag{2.63}$$

where:

$$\left(\sigma_m\right)_j^n=\left(w_m\right)_j^n \tag{2.64}$$

$$\left(\alpha_m\right)_j^n=\left(\frac{\partial\widetilde{w}_m}{\partial x}\right)_j^n \tag{2.65}$$

$$\left(\beta_m\right)_j^n=\left(\frac{\partial\widetilde{w}_m}{\partial t}\right)_j^n \tag{2.66}$$

and the subscript m refers to the m^{th} element of the vector. Similarly:

$$\widetilde{f}_m\left(x,t;j,n\right)=\left(f_m\right)_j^n+\left(\frac{\partial\widetilde{f}_m}{\partial x}\right)_j^n\left(x-x_j\right)+\left(\frac{\partial\widetilde{f}_m}{\partial t}\right)_j^n\left(t-t^n\right) \tag{2.67}$$

We may denote the approximation vectors of f and S, in each SE(j,n), by $\tilde{f}$ and $\tilde{S}$, respectively and are calculated as follows:

$$\tilde{f}_m=[\tilde{f}_1,\tilde{f}_2,\tilde{f}_3,....\tilde{f}_{L+3}]$$
$$\tilde{s}=[\tilde{s}_1,\tilde{s}_2,\tilde{s}_3,...,\tilde{s}_{L+3}]$$

such that

$$\tilde{f}(x,t;j,n)\approx f(\tilde{w}(x,t;j,n)) \qquad \tilde{s}(x,t;j,n)\approx s(\tilde{w}(x,t;j,n)) \tag{2.68}$$

Where the subscript L referes to the number of species to be considered.

To obtain the numerical solution, it is necessary to know the coefficients $(\sigma_m)_j^n$, $(\alpha_m)_j^n$, $(\beta_m)_j^n$, $\forall j,n$.

Assuming that these coefficients at the time step n are known and we seek to compute the coefficients of the next step, $n+1/2$.

For the calculation of $(\sigma_m)_j^{n+1/2}, m=1,2,3,...,L+3$ we use the resolution of the

integral form of the system of eq. (2.33), in each $CE(j, n+1/2)$ with reference to figs. 2.7a and 2.7b

$$\underbrace{\iint\limits_{CE(j,n+1/2)} \frac{\partial \tilde{w}_m}{\partial t} + \frac{\partial \tilde{f}_m}{\partial x} dxdt}_{\text{I}} + \underbrace{\iint\limits_{CE(j,n+1/2)} \tilde{s}_m dxdt}_{\text{II}} = 0, \quad k = 1, 2, ..., L+3. \tag{2.69}$$

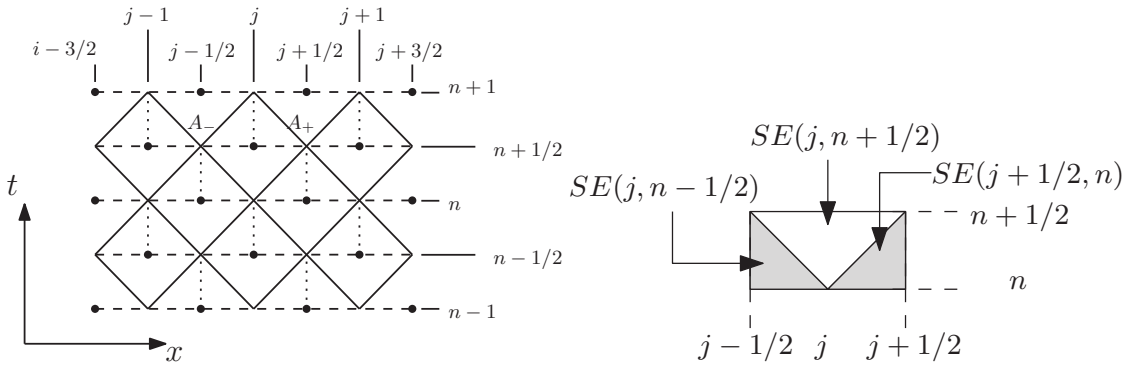

(a) The CE-SE stencil (b) The CE-SE Element

Fig. 2.7.: The CE-SE Method

Applying *Green's theorem* to eq. (2.69), we obtain the following path integral defined along the boundary of CE$(j, n+1/2)$ for $m = 1, 2, 3, .., L+3$:

$$\begin{aligned}(\sigma_m)_j^{n+1/2} =& \frac{(\sigma_m)_{j-1/2}^n + \sigma_m)_{j+1/2}^n}{2} + g_m(j-1/2, n) - g_m(j+1/2, n) \\ &- \frac{\Delta t}{4}[\tilde{s_m}(j-1/2, n) + \tilde{s}(j+1/2, n)]\end{aligned} \tag{2.70}$$

where,

$$g_1 = \frac{\Delta x}{8}\alpha_1 + \frac{\Delta t}{2\Delta x}(\sigma_2 + \frac{\Delta t}{4}\beta_2) \tag{2.71}$$

$$g_2 = \frac{\Delta x}{8}\alpha_2 + \frac{\Delta t}{2\Delta x}\sigma_2[(\gamma-1)\frac{\sigma_3}{\sigma_2} + \frac{3-\gamma}{2}\frac{\sigma_2}{\sigma_1}] + \frac{\Delta t^2}{8\Delta x}[(\gamma-1)\beta_3 + \frac{3-\gamma}{2}\frac{\sigma_2^2}{\sigma_1}(2\frac{\beta_2}{\sigma_2} - \frac{\beta_1}{\sigma_1})] \tag{2.72}$$

$$g_3 = \frac{\Delta x}{8}\alpha_3 + \frac{\Delta t}{2\Delta x}\frac{\sigma_2^2}{\sigma_1}(\gamma\frac{\sigma_3}{\sigma_2} - \frac{\gamma-1}{2}\frac{\sigma_2}{\sigma_1}) + \frac{\Delta t^2}{8\Delta x}\frac{\sigma_2}{\sigma_1}[\gamma\sigma_3(\frac{\beta_3}{\sigma_3} + \frac{\beta_2}{\sigma_2} - \frac{\beta_1}{\sigma_1}) + \frac{\gamma-1}{2}\frac{\sigma_2^2}{\sigma_1}(2\frac{\beta_1}{\sigma_1} - 3\frac{\beta_2}{\sigma_2})] \tag{2.73}$$

$$\vdots$$

$$g_{L+3} = \frac{\Delta x}{4}\alpha_{L+3} + \frac{\Delta t}{2\Delta x}[\frac{\sigma_{L+3}\sigma_2}{\sigma_1}] + \frac{\Delta t^2}{8\Delta x}[\frac{\sigma_{L+3}}{\sigma_1}\beta_2 + \frac{\sigma_2}{\sigma_1}\beta_{L+3} - \frac{\sigma_{L+3}\sigma_2}{\sigma_1^2}\beta_1] \tag{2.74}$$

with L, being the number of species considered and $\sigma_m = (\sigma)^n_{j+1/2}$, $\alpha_m = (\alpha_m)^n_{j+1/2}$ and $\beta_m = (\beta_m)^n_{j+1/2}$ for $m = 1, 2, 3, ..., L+3$.

To obtain $g_m(x_{j-1/2}, t; j-1/2, n)$, σ_m is replaced in eqs. (2.71) to (2.74) by $(\sigma)^n_{j-1/2}$, $\alpha_m = (\alpha_m)^n_{j-1/2}$ and $\beta_m = (\beta_m)^n_{j-1/2}$

We now decompose the integral source terms **II** in eq. (2.69) as the sum of three integrals defined in each SE, (refer to fig. 2.7) and approximate each one of these integrals using the *mean value theorem* for integrals, using the value of the integrand in the center of the rhombus,

$$\iint\limits_{CE(j,n+1/2)} \tilde{s_m} dx dt \cong \frac{(\Delta x)(\Delta t)}{4}[\frac{\tilde{s_m}(j+1/2, n) + \tilde{s_m}(j-1/2, n)}{2} + \tilde{s_m}(j, n+1/2)] \tag{2.75}$$

where,

$$\tilde{S_1}(j, n+1/2) = \delta_j \sigma_2 \tag{2.76a}$$

$$\tilde{S_2}(j, n+1/2) = \frac{\sigma_2^2}{\sigma_1}(\frac{2f}{d_j}\frac{\sigma_2}{|\sigma_2|} + \delta_j) \tag{2.76b}$$

$$\tilde{s_3}(j, n+1/2) = \frac{\sigma_2^2}{\sigma_1}(\gamma\frac{\sigma_3}{\sigma_2} - \frac{\gamma-1}{2}\frac{\sigma_2}{\sigma_1})\delta_j - \frac{4q_j^n}{d_j} \tag{2.76c}$$

$$\vdots$$

$$\tilde{S_{L+3}}(j, n+1/2) = \delta_j \frac{\sigma_{L+3}\sigma_2}{\sigma_1} \tag{2.76d}$$

For $\sigma_m = (\sigma_m)_j^{n+1/2}$, $m = 1, 2, 3, ..., L+3$ With the following approximation:

$$\tilde{s_m}(j, n+1/2) = \frac{\tilde{s_m}(j-1/2, n) + \tilde{s_m}(j+1/2, n)}{2}, \qquad m = 1, 2, 3..L+3, \tag{2.77}$$

Which is an explicit system.

In order to obtain the coefficients $(\alpha)_j^{n+1/2}, m = 1, 2, 3, ...L+3$ we define 3 points in $CE(j, n+1/2), P_+, P$ and P_-, corresponding to the coordinates $(x_{j+1/2}, t^{n+1/2})$ $(x_j, t^{n+1/2})$ and $(x_{j-1/2}, t^{n+1/2})$, respectively as shown in fig. 2.7.

Since $A_\pm$ does not belong to $SE(j \pm 1/2, n)$ the value of $\tilde{w_m}(A_\pm)$ is calculated in the point that is below A_+ and P_- in each corresponding SE. In case that a discontinuity of solution occurs between A_+ and P but not between A and A_-, one would expect that $|(\alpha_{k+})_j^{n+1/2}| \gg |(\alpha_{k-})_j^{n+1/2}|$, where

$$(\alpha_{m\pm})_j^{n+1/2} = \pm \frac{\tilde{w_m}(P_\pm) - \sigma_{m_j}^{n+1/2}}{(\Delta x/2)} \tag{2.78}$$

are the lateral differences. As P and P_- are on the same side of the discontinuity, $(\alpha_m)_j^{n+1/2}$ should be closer to $(\alpha_{m-})_j^{n+1/2}$ than $(\alpha_{m+})_j^{n+1/2}$. This suggests that $(\alpha_m)_j^{n+1/2}$ should be a weighted average between $(\alpha_{m+})_j^{n+1/2}$ and $(\alpha_{k-})_j^{n+1/2}$, which gives more weight to the term with the smallest module,

$$\alpha_{m\pm} = \begin{cases} \frac{|\alpha_{m+}|^c \alpha_{m-} + |\alpha_{m-}|^c \alpha_{m+}}{|\alpha_{m+}|^c + |\alpha_{m-}|^c}, & |\alpha_{m+}|^c + |\alpha_{m-}|^c \neq 0, \\ 0, & |\alpha_{m+}|^c + |\alpha_{m-}|^c = 0, m = 1, 2, 3, ..., L+3 \end{cases} \tag{2.79}$$

where c is positive real constant. In the boundary of the domain we calculate the $(\alpha_m)_0^{n+1/2}$ using forward differences, $(\alpha_m+)_0^{n+1/2}$, and $(\alpha_m)_M^{n+1/2}$ by means of backward differences, $(\alpha_m-)_0^{n+1/2}$, both defined in eq. (2.78). Finally, the coefficients, $(\beta_m)_j^{n+1/2}$,

$m = 1, 2, 3, ..., L+3$ are obtained by replacing $\frac{\partial \tilde{f}_m}{\partial x}(j, n+1/2)$ and eq. (2.76) in eq. (2.35)

$$(\beta_1)_j^{n+1/2} = -\alpha_2 - \delta_j \sigma_2 \tag{2.80a}$$

$$(\beta_2)_j^{n+1/2} = -(\gamma-1)\alpha_3 + \frac{\sigma_2^2}{\sigma_1}[\frac{(3-\gamma)}{2}(\frac{\alpha_1}{\sigma_1} - 2\frac{\alpha_2}{\sigma_2}) - \frac{2f}{d_j}\frac{\sigma_2}{|\sigma_2|} - \delta_j] \tag{2.80b}$$

$$(\beta_3)_j^{n+1/2} = -\frac{\sigma_2}{\sigma_1}[\gamma\sigma_3(\frac{\alpha_3}{\sigma_3} + \frac{\alpha_2}{\sigma_2} - \frac{\alpha_1}{\sigma_1} + \delta_j) + \frac{\gamma-1}{2}\frac{\sigma_2^2}{\sigma_1}(2\frac{\alpha_1}{\sigma_1} - 3\frac{\alpha_2}{\sigma_2} - \delta_j)] + \frac{4h}{d_j}[T_{w,j} - \frac{\gamma-1}{2}(2\frac{\sigma_3}{\sigma_1} - \frac{\sigma_2^2}{\sigma_1^2})] \tag{2.80c}$$

$$\vdots$$

$$(\beta_{L+3})_j^{n+1/2} = -[\frac{\sigma_{L+3}}{\sigma_1}\alpha_2 + \frac{\sigma_2}{\sigma_1}\alpha_{L+3} - \frac{\sigma_{L+3}\sigma_2}{\sigma_1^2}\alpha_1] - \delta_j\frac{\sigma_{L+3}\sigma_2}{\sigma_1} \tag{2.80d}$$

Onorati and Ferrari [42] applied this method to the tracking of the chemical species along the intake and exhaust duct systems, introducing the species continuity equations in the numerical model. In particular, the back-flow of combustion products in the intake pipe and the through-flow of air in the exhaust duct during the valve overlap have been simulated.The fluid dynamic model is based on the numerical solution of the fundamental conservation equations for one-dimensional, unsteady, compressible flows in ducts with variable cross-sectional area. Three approaches can be considered when taking gas concentration into consideration:

- Perfect gas with constant specific heats
- Ideal gas with specific heats depending on the gas chemical composition
- The specific heats depend on the gas chemical composition and temperature

In CE SE, parameters and their derivatives are considered as independent variables and are computed simultaneously at each time-step that leads to local and global flux conservation [43]. It also proved its efficiency for multi-dimensional problems [44].

Earlier in this chapter, several methods for solving unsteady compressible 1-D flow were discussed, and their qualities assessed. The next chapter will explain some boundary conditions treatment. Finally, simulation results for both duct simulations and boundary conditions will be presented.

7. Boundary Conditions Treatment

The numerical methods applied to know the fluid conditions in 1D elements allow obtaining them only in the internal nodes. Hence, one can say that these models

and numerical methods previously discussed are worthless if they are not coupled to accurate models of boundary conditions. The boundary conditions in the ICE field include turbines, compressors, throttle valves, EGR-valves, intake and exhaust valves and any other restriction or complex geometry. The Method of Characteristics is the most used in the treatment of these boundaries.

Different boundaries can be encountered on an ICE such as, open and closed ends, throttle valves, compressors, turbines ... The similarity between the models for these boundaries is the quasy-steady assumption. This hypothesis can be less true for a turbine (the wave can propagate through the turbine large volume) compared to a simple boundary such as a closed end.

Until 1982, Boundary conditions and jump conditions should be applied by fitting procedures of second-order accuracy on all surfaces of singularity (shocks, interfaces, slip surfaces, contact discontinuities, and boundaries of rarefaction fans) [45]. Later on, Benson [26] presented a detailed approach on how to use the *Riemann Variables*[9] to treat boundary Conditions in an appropriate way.

Onorati et al. [46] stated that the simple junction boundary condition assuming negligible pressure losses (constant pressure models by Benson [26], Winterbone and Pearson [24] is generally not satisfactory in the case of complex junctions of high performances engines, since it can provide misleading predictions of pressure pulses reaching the cylinder intake and exhaust valves, with unreliable prediction of the engine volumetric efficiency. The required junction model in this case must account for pressure losses and directionality effects. Onorati et al. [46] developed then a new model which allow estimating the pressure loss coefficients by means of analytical expressions.

7.1. Modeling Principal

Typical boundaries for which models exist are open and closed ends, in flow boundaries, valve boundaries, junctions, orifices, throttle valves, turbines and compressors.

Mainly the following hypothesis are the corner stones for the various models:

- Quasi Static Models [Winterbone and Pearson [24]]
- Use of Mass and energy conservation
- The system can be augmented using the momentum equation
- Use of different hypotheses (depending also on flow nature) to solve the system
- The flow is considered compressible

Despite the above assumptions, singularities modeling within the ICE remains challenging, as the propagation of pressure waves through junctions are inherently multidimensional phenomenon [47].

For this reason, mass and energy balance are made considering that the flow is stationary at each time step [31], which justifies the first hypothesis. However, the flow is

[9] The reader is invited to refer to the Appendix D for a detailed treatment of the boundaries.

continuously distributed by valves opening and closing, which contradicts the same hypothesis. Some authors justify the quasy-stationarity choice by the fact that the variation in space is more dominant as the one in time, and hence, the PDE will reduce to an ODE in space, thus the quasy-stationarity assumption.

7.2. Typical Boundary Conditions in the ICE

The basic boundary conditions for ICE are:

- Completely closed end such as a closed valve
- A partially open end, such as an open intake valve
- A completely open end, such as ducts ending up to the atmosphere

Any other boundary condition, can be modeled as a combination or based on the previous boundaries. Figure 2.10 gives a representation of the boundaries stated above, with a superposition of the CIR's stencil.

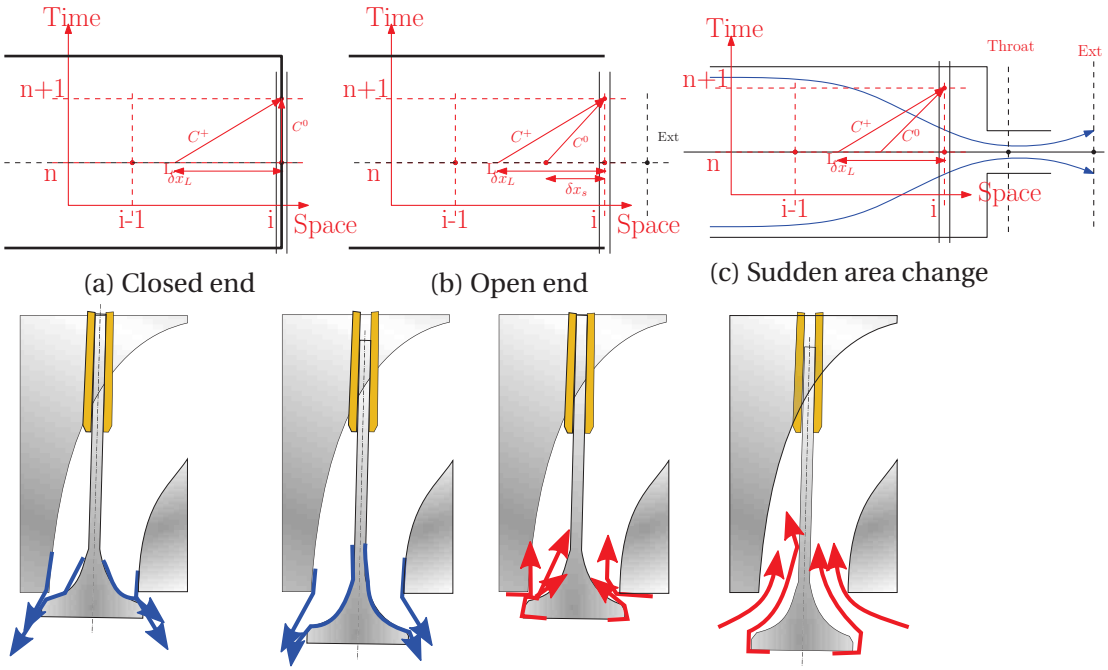

(a) Closed end (b) Open end (c) Sudden area change

(d) Flow through valves in ICE

Fig. 2.8.: Typical boundary conditions with C.I.R[10]

[10]CIR: is a finite difference method named after Courant, Isaacson and Rees. It is a direct discretization in an upwind manner of the characteristic computability equations.

7.3. Main Modeling Approaches for Boundary Conditions

The gas flows in ICE are non-steady and changes in the fluid properties take place in space, x, and time, t. However, for the boundary conditions, the spatial rates of change of fluid properties are far greater then the temporal one. These conditions are known as *quasi-steady flow conditions* and steady flow gas relationships maybe used in this case [26].

As earlier stated, the MOC is the corner stone in the boundary conditions treatment. Zuecrow and Hoffman [48] on the concept of MOC said that it can be introduced from several points of view:

- From a physical point of view, a characteristic is defined as the path of propagation of a physical disturbance. An example is when disturbances for a supersonic flow propagate on the Mach lines, which are the characteristics for the supersonic flow
- From a purely heuristic point of view, a characteristic is defined as a curve along which the governing partial differential equations can be manipulated into total differential equations.
- From a more rigorous mathematical point of view, a characteristic is a curve across which the derivatives of a physical property may be discontinuous, while the property itself remains continuous.
- From the most rigorous mathematical point of view, a characteristic is defined as a curve along which the governing partial differential equations reduce to an interior operator, that is, a total differential equation. That interior operator is known as the compatibility equation.

A brief resume on how to obtain the characteristics equations is available in the Appendix. In the following, we shall present a very basic explanation, on how the MOC can be extremely useful to visually track the waves.

7.3.1. Graphical Example with the MOC

The idea behind this subsection, is to bring in front the beauty of the MOC. However, in real applications, other numerical methods are more efficient.

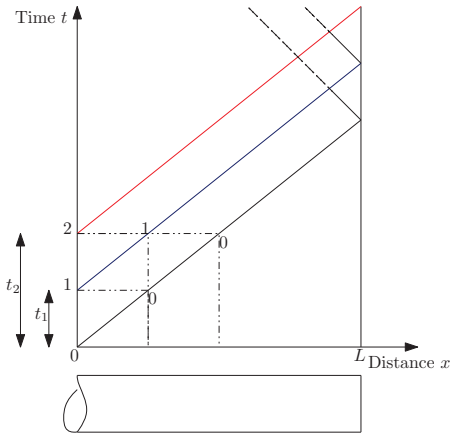

Consider the pipe content to be initially at rest. A disturbance is then initialized at the left end of the pipe, this will cause the pressure, sound speed as well as the flow speed change values. The first initialization of the disturbance will be represented by the right moving characteristic.

Fig. 2.9.: Closed end boundary condition

- The black line is drawn first, as the disturbance is at the lower left corner. We know that due to the transport phenomena, the initial condition 0 will be transported along the line.
- At $t = t_1$, the blue line is drawn parallel to the first line. The lines are parallel as the characteristic will be conserved. However, the new state 1 will be now transported along the new characteristic.
- At $t = t_2$, the same procedure is repeated.
- One has to keep in mind that the states (represented as $0, 1, 2...$ in the graph) have to propagate on the characteristic line. this will enable the reconstruction of the pressure profile all along the duct, at any instant, and so is the propagation of the waves visualized.

7.3.2. Flow Interaction at Standard Boundary Conditions

Whether for the closed end or the open end boundary conditions, calculate the Riemann Invariants along the neighboring characteristics to the boundary condition. Once these are available, the C.I.R is used to calculate the new characteristics at the boundary conditions. To calculate the flow properties, the system of equations is then closed by considering extra hypothesis depending on the flow and boundary nature.

In fig. 2.10a, a 3-D plot to illustrate an initialized wave transported towards to the closed end.

When the wave is initialized with moving speed toward the closed end, it can suffer some decay in amplitude due to friction and heat transfer. In this simulation, we discarded both effects to consider a homentropic flow. The wave arrives at the closed end and then mounts on itself, to get back. This is actually due to momentum and mass conservation. Since the end is closed, the flow will have to get back in the other

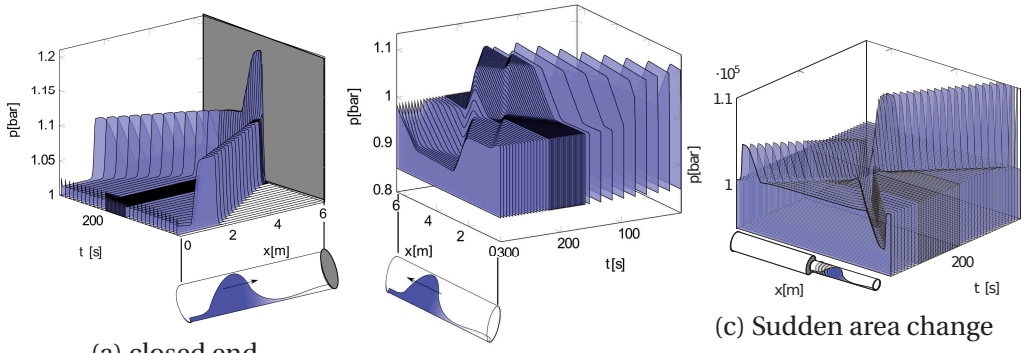

(a) closed end

(b) Open end

(c) Sudden area change

Fig. 2.10.: Isometric illustration of standard boundary conditions in the time-distance plane

direction, but first, come to rest first due to continuity. This will cause an increase in the local pressure and hence, the wave looks like it's mounting on itself. For the closed end boundary conditions, a straightforward simplification is taking the local fluid speed at the boundary to be *zero*, hence one unknown state is directly estimated.

For an open end, the behavior is completely different, and relatively more complex. Pressure changes due to interaction with an open end are driven by the pressure gradient itself, and hence the flow nature. The main property of the open end, is the phase shift of the wave, which we see in fig. 2.10b. In the considered example, the positive wave approaches the open end, and gets inverted there. The reason for this, is that once the wave arrives to the open end, it will see a different pressure (in this case, it was the ambient pressure, which was smaller), particles flow will be accelerated instantly, whereas flow still in the tube will have a lower speed, and hence the fall in pressure magnitude. This pressure wave now will naturally travel in the negative direction.

The partially open end modeling resembles to the open end boundary condition modeling, but augmented through the use of a loss factor which characterizes the section variation.

7.4. Chemical Species Transport in Boundary Conditions and 0D Elements

The inclusion of the chemical species transport does not affect the solution procedure of the MOC but can modify the value of the Riemann variables and the entropy level. The transport of chemical species in 1D elements can be performed by solving the governing equations system by means of finite difference numerical methods. However, wave action models consider other types of elements that can be found in internal combustion engine: cylinders, turbine, compressor, diesel particulate filters, intercoolers, volumes, etc. All this kind of systems are modeled as boundary conditions, 0D elements or a combination of these with 1D elements [25].

7.5. Conclusion on Boundary Condition Modeling

The above models where developed for homentropic flows, to simplify explanation and implementation. However, the entropy levels in the various parts of the flow may have significant effects. The entropy levels may not be uniform, and the flow will then be *non-homentropic*. In this case, special care has to be taken to correct the above algorithms. The idea is based on correcting the Riemann Invariants , which will be called, for the non-homentropic flow, Riemann Variants, as they change value along the characteristic line. Unfortunately, there is no analytic expression to calculate the amount of variation, and the problem can only be solved iteratively

8. Validation

8.1. Validation Using Numerical Shock Tube Test Bench

For the sake of an intuitive illustration of the importance of a good and proper choice of the numerical scheme, a 1D flow simulation using the different stencils seen earlier is performed.

8.1.1. The Shock Tube Test

The Sod shock tube problem, named after Gary A. Sod, is a common test for the accuracy of computational fluid codes . The test form a discontinuity of the pressure and density. For this special case, an analytical solution has also been developed and is used as a reference for comparison and validation of 1D numerical schemes.

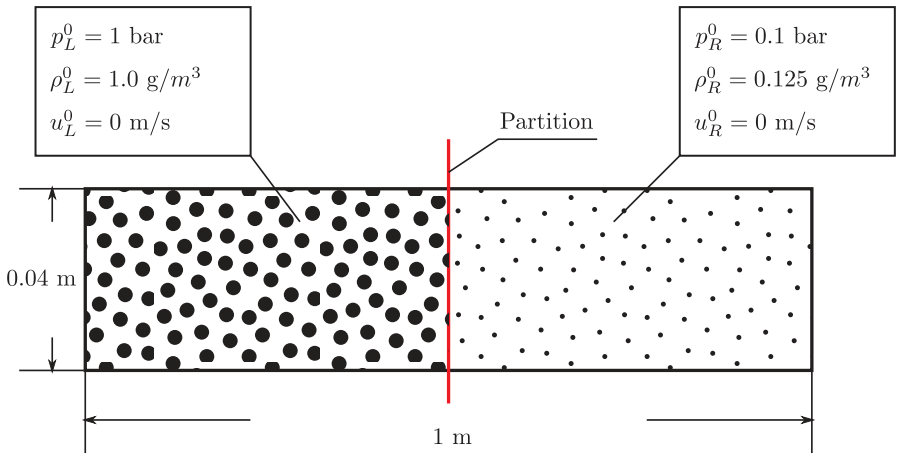

Fig. 2.11.: Initial conditions of the shock tube experiment

A duct of length 1 m and a diameter of 0.04 m with both ends being closed is considered. The tube is divided into two tubes having the same length and different gas conditions

as shown in fig. 2.11. Since the purpose of this section is the comparison of 1D numerical schemes, boundary conditions are kept out of the scope. It will be noticed from the simulation results that no wave interaction with boundaries is presented.

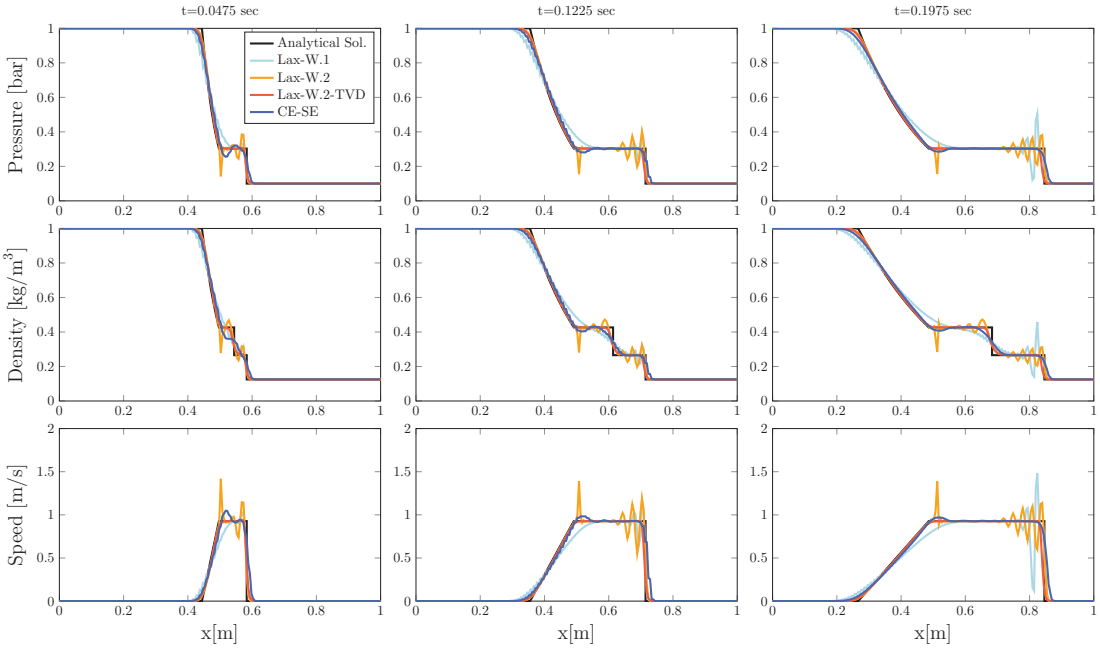

Fig. 2.12.: Shock tube comparison results

Initially, the two tubes are separated. The gas is stationary and has initial states (1 bar, 1 kg/m^3) to the right whereas the conditions to the left are (0.1 bar and $0.125\ kg/m^3$).

To avoid any complex flow, we assume that the separation is completely removed in $\Delta T = 0$ seconds. This will initiate a flow from the left to the right and a shock wave traveling in the same direction.

For this simulation, the space discretization was the same for all methods and taken as $\Delta\, x = 0.005$

Then, at the end of every iteration, the CFL condition is used to calculate the maximum time step size. This way, it is possible to assess and compare the accuracy and computational performance of the schemes.

Figure 2.12 and 2.13 shows the simulated fluid states using the analytical approach as well as the finite difference methods seen earlier in this chapter.

It is clear that severe oscillations have corrupted the shock tube simulation results using the Lax-Wendroff one and two steps. The two schemes lead to a better accuracy on the rarefaction waves as on the compression wave. Notice also that the amplitude of the oscillations is continuously increasing.

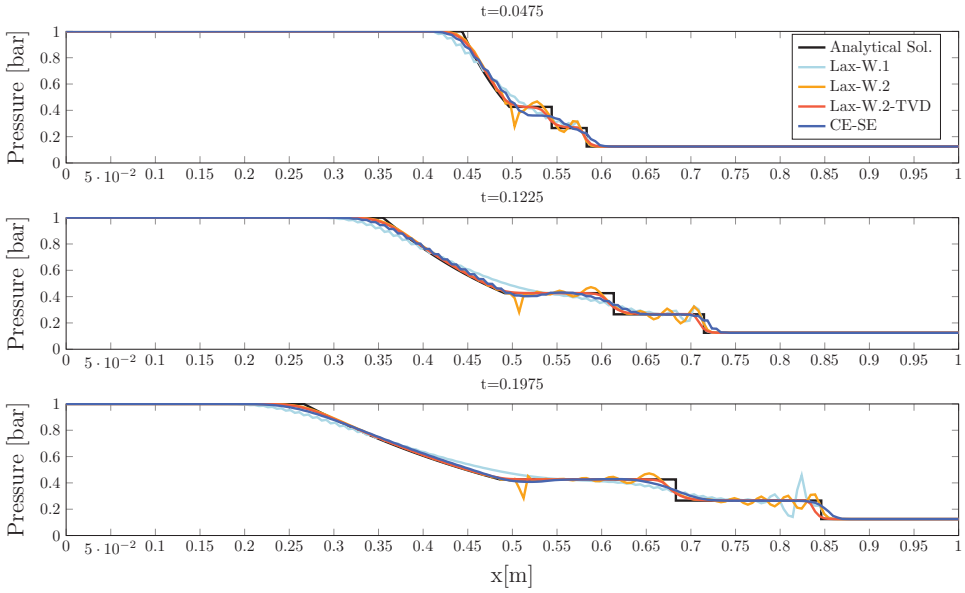

Fig. 2.13.: Shock tube at t=0.0475 s

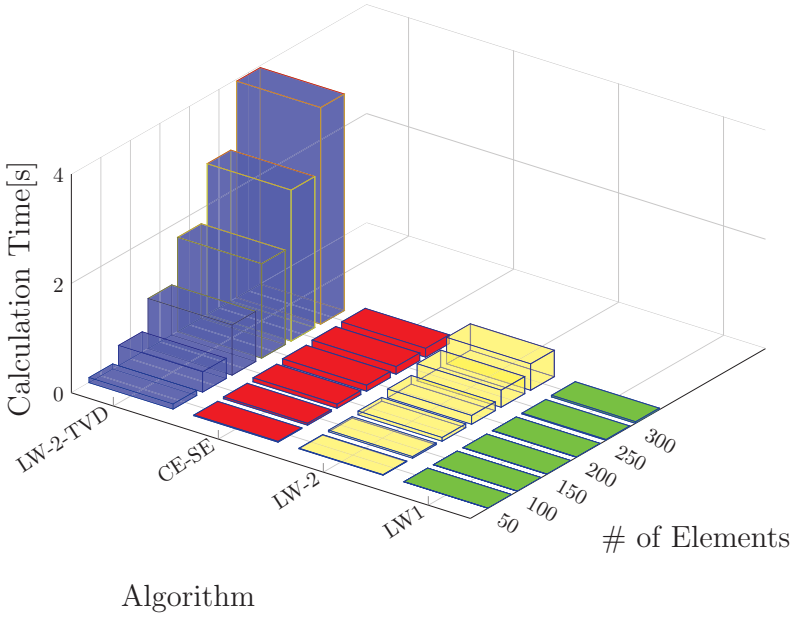

Fig. 2.14.: Effect of space discretization size

These oscillations are successfully removed using the symmetrical Total Variation Diminishing (TVD) method. In addition, then discontinuities are also well resolved.

It is also noticeable that the CE-SE handles properly the discontinuities and that the

simulated gas states are accurate and oscillations free.

This makes the two last schemes represent the best candidates simulating gas dynamics in ICE ducts. However, fig. 2.14 shows that the calculation time of the Lax-Wendroff with TVD increases exponentially as the space discretization decreases. This is of course expected as the CE-SE by nature requires no additional flux limiters or artificial viscosity.

In addition, the conservation of physical quantities is often altered as it suffers from the inevitable numerical errors due to discretization. The next figure shows an investigation of mass conservation during the shock tube simulation. According to mass conservation, the total amount of mass inside the tube is supposed to be constant over the simulation, as the system is considered to be completely closed.

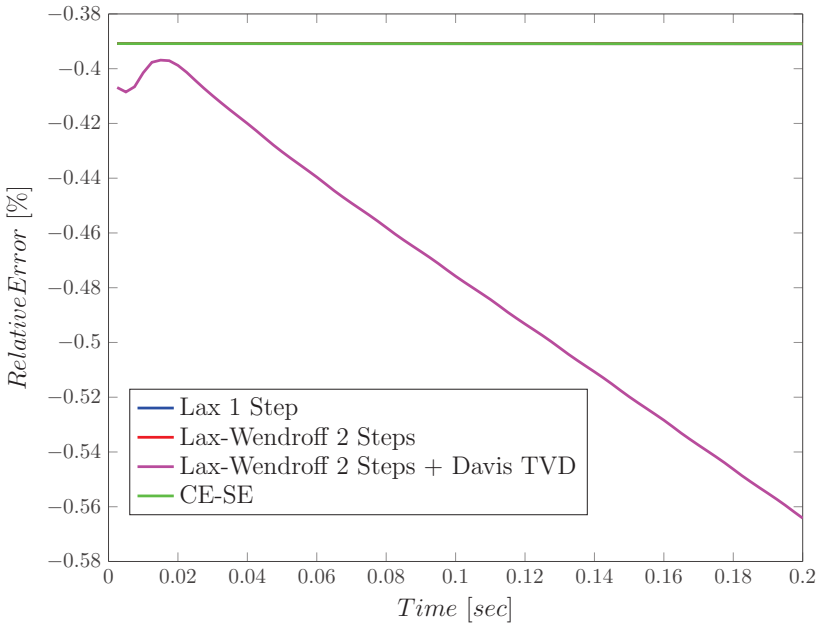

Fig. 2.15.: Mass relative error of shock tube simulation

Once again, the CE-SE outperforms the other numerical stencils as shown on the figure. The CE-SE owes its conservation to the use of the integral form of conservation equations, which completes the PDE. The main advantage of the integral form is its validity even across discontinuities. The remaining numerical schemes are based on the PDE only which lose validity across discontinuities.

8.1.2. Concentrations Transport

Once again, the shock tube test has been used to test the transport of different concentrations. If we assume the left and right parts of the tube have different concentrations

of the species X_1, X_2 and X_3, the following concentrations transport is obtained.

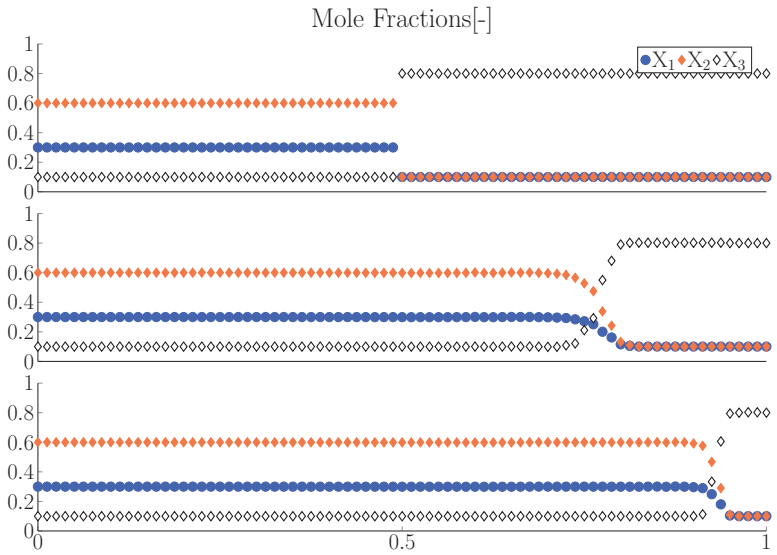

Fig. 2.16.: Concentrations Transport at different instants

Concentrations transport is defined by the gas velocity. This is why the compression and rarefaction waves are not apparent on fig. 2.16.

It can be seen that using this two test cases, the validation of the CE-SE open and closed end as well as moving valve boundary conditions has been performed

8.2. Validation at the Acoustic Test Bench

Before validating the models on a real ICE air system, it was decided to assess the accuracy of these schemes and boundary conditions on the acoustics test bench available at the PRISME laboratory. The test bench fig. 2.17 gives the possibility to decouple transport phenomena along the ducts and wave interaction at complex boundaries. This is a very useful advantage as it helps better understand the physics behind and validate the signal models.

8.2.1. Experimental Set Up

The shock tube in fig. 2.17 is a widely used experiment to validate transport models for engine ducts. It offers the possibility to isolate the effect of ducts and restrictions on wave propagation. This gives a possibility to understand phenomena and validate specific model parts.

The test bench consists of a real engine cylinder head with a valve actuated to generate one pressure pulse. The valve connected to a variable length pipe (1m to 12 m) which

can be open to the atmosphere or a 50 L volume. The pressures in the cylinder and the volume can be controlled up to values of 20 and 4 bars respectively. The pressure difference across the valve will then define the flow direction (inflow or outflow) as well as flow nature (subsonic or sonic). The valve is actuated by a simple mechanical system instead of the actual camshaft. Using a free sliding weight moving vertically with respect to the valve which is brought to a given height, then left free to hit the valve. After the carriage bounces back away from the valve, it is held to prevent further successive valve openings. The momentum transfer from the weight to the valve will push the valve down to a certain opening position, then the valve spring will bring it back to its closed position.

The amount of momentum transfer is only controlled by the mass height (always starts with zero velocity). This gives a good repeatability of the experiments in terms of valve opening profile and initial mass height.

Fast-response pressure transducers dispersed along the duct have been used to record the wave propagation. A no-contact transducer based on Foucault currents is used to measure the valve opening. If the pipe is long enough, the first wave will pass completely the first sensors before the reflected wave reaches the same sensors.

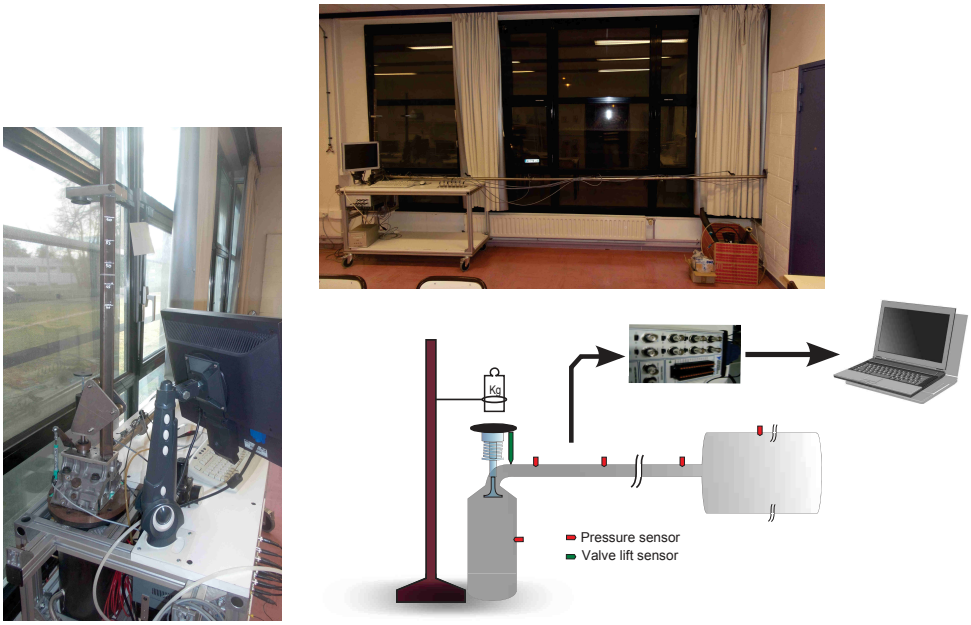

Fig. 2.17.: Acoustic Test Bench

Sensor Type	Manufacturer	Model	Scale
Pipe pressure	Bosch	0-261-230-049	0-2.5 bar
Cylinder pressure	Kistler	4045A5	0-10 bar
Valve lift	Gefran	P212A25	-
Acquisition Card	National Instruments	NI DAQPad-6070E	

Table 2.1.: Test Bench Specifications

8.2.2. Results

Using an atmospheric pressure in the cylinder and a 1.5 bar in the tube, it was possible to generate a rarefaction wave through the tube and a flow into the cylinder. This rarefaction wave is transported from the left to the right in an opposite direction with respect to mass flow. This case hase been simulated using the CE-SE and boundary conditions.Results are given in 2.19.

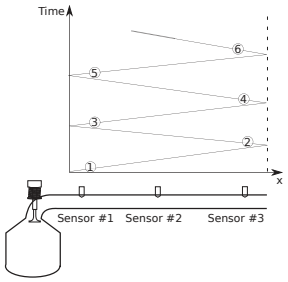

Fig. 2.18.: Waves and sensors distribution

The time delays between the three sensors are due to their distribution. Sensor at position 1 lies closer to the valve. This is why the perturbation (wave #1 in fig. 2.18) is first sensed by sensor #1, sensor #2 then #3.

Once the rarefaction wave arrives at the left open end, it will be inverted and reflected. Now, the wave travels from the right to the left. This inverted wave is now seen first by sensor #3, #2 and then #1. Because the valve is now completely closed, it will behave as a closed end. As seen previously, the wave will be reflected only. This wave will pass through sensor 1 while the rarefaction wave is still not completely through. The superposition of these two waves results in the second peak at sensor # 1. The same phenomena will also happen but at the trailing edge of the previous wave. Thus, the very small peak is measured at sensor #2. The same behavior of the open end boundary is observed at sensor #3, but now inverting the compression wave and generating a rarefaction wave.

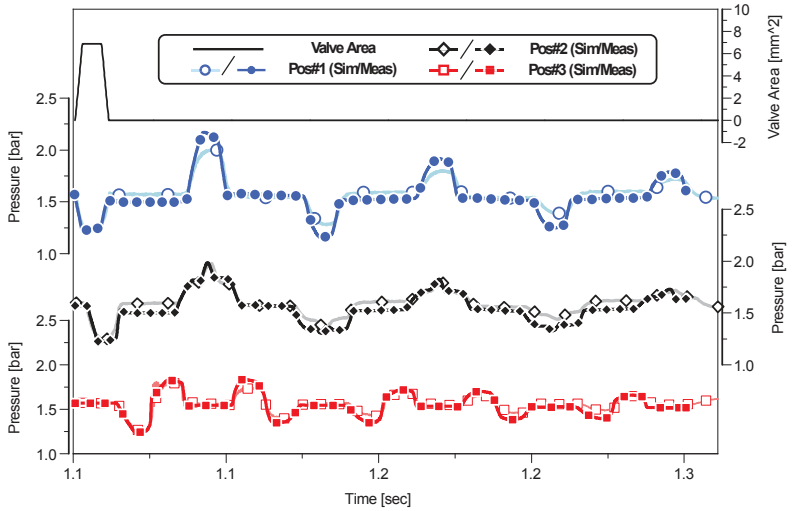

Fig. 2.19.: Intake At the Acoustic Test Bench

To simulate an exhaust case (flow from the cylinder to the pipe), we increased the pressure in the cylinder and kept the pressure in the tube equal to the atmospheric pressure. In this case, a compression wave is generated due to the valve opening fig. 2.20.

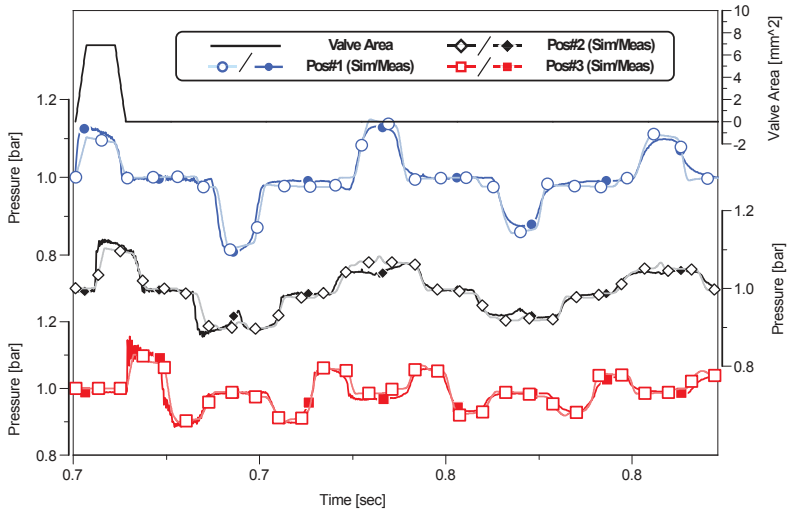

Fig. 2.20.: Exhaust At the Acoustic Test Bench

For both the intake and the exhaust cases, the simulation matches well with the experiment. Waves reflection is properly reproduced, and waves superposition is respected.

Some differences between the measurements and the simulation can be observed, and are mainly due to the boundary conditions modeling.

9. Conclusion

In this chapter, the governing equations of 1D gas dynamics have been stated. Afterwards, a detailed investigation of existing 1D numerical schemes for the simulation of gas dynamics within the engine ducts have been performed.

Four numerical schemes that differs in complexity have been considered. The Lax-Wendeoff with one and two steps have proved to be very simple but became quickly inefficient in a region of rapid change or discontinuities. This can be improved using the Total Variation Diminishing (TVD) treatment. However, this extra treatment results in an additional computational penalty.

The CE-SE proved to be the candidate offering the best compromise between accuracy and computational effort.

In the second part of this chapter, standard boundary conditions have been presented. Without going into a detailed modeling, the boundary conditions were used to feed the duct model for the sake of validation under the acoustic test bench. This special test bench gave the possibility to isolate wave propagation phenomena for a better understanding.

As mentioned earlier, the achievement of an efficient calculation and sufficient accuracy are of great importance. Unfortunately, the CE-SE is still far from being implementable on current ECUs.

In the next chapter, we will see how some reduced models can be used to model wave phenomena in engine ducts.

CHAPTER 3

REDUCED ORDER MODELS

The simulation of flow dynamics has been an essential stone in the design and development of engines. The appropriate solution of the 1D-Euler Equations simulates waves propagation in the ICE ducts, which is then used to evaluate their impact on engine efficiency. Various schemes have been formulated based on the Method of Characteristics (MOC) [49, 26], upwind and symmetric finite-difference schemes [41, 35, 50, 38] or finite volume shock-capturing methods [32]. In the previous chapter, discrepancies in the accuracy, stability and calculation time have been discussed, to shed the light on the importance of the numerical scheme choice.

These models (also called 1D codes) offer an accurate description of the gas dynamics in intake and exhaust paths. This plays a dominant role in the cylinder filling estimation which is a major factor for emissions, performance and fuel consumption optimization. However, they are still not real-time compatible for current ECUs due to their calculation costs.

The computational power required by the 1D models is the major obstacle in front of their boarding on series ECUs. The numerical speed in the simulation of internal combustion engine ducts, is mainly restricted by the amount of calculation required per cell as well as the number of cells.

To overcome this problem, considerable work has been done to develop models which bridge the gap between the 1D and pure lumped parameter models. Mainly two approaches can be noticed:

- Up-Down Approach: are reduced order models derived from the conservation laws without oversimplifying the topology of the engine air-path system [1, 2, 3]
- A Bottom-Up Approach: are models obtained through an input-output relationship [17, 18] or an extension of the lumped parameters [4, 5, 6]

In this work, we will concentrate on the quasi-propagatory modeling approach.

1. The Quasi Propagatory Model

Lumped parameter models pattern the mass flow as a function of the pressure difference only. This will result in an error in the transient phenomena inside the intake and exhaust manifolds, which is crucial for the model-based air-fuel ratio control. On the other hand, 1D models consider inertial effects by means of the momentum conservation law, but are computationally expensive due to the space discretization and the numerical treatment.

To bridge the gap between the lumped parameter and 1D models, Cipollone and Sciarretta [4] presented a novel relationship obtained by observing the solution offered by the MOC for a duct branch connecting two reservoirs at different pressures.

The basic idea is to separate the inertial properties of the fluid from the capacitive ones. Because the final model is an ordinary differential equation, the calculation along the complete duct is no more explicitly required, which reduces intrinsically the calculation time.

The partial differential over space and time are always coupled in the three governing equations. If one of these two differentials can be mathematically decoupled from the other one, the equation can be easily reformulated into a couple of ordinary partial differential equations, which significantly reduces the complexity and expense by solving only the differential equations.

In the following, the MOC is used to transform the conservation partial differential equations into ordinary differential equations. Afterwards, an illustration example and the development of the QPM dynamic model are established.

The three governing conservation equations from eq. (2.32) are restated here:

$$\frac{\partial \rho}{\partial t} + \rho \frac{\partial u}{\partial x} + u \frac{\partial \rho}{\partial x} + \frac{\rho u}{A} \frac{dA}{dx} = 0 \tag{3.1}$$

$$\frac{\partial u}{\partial t} + u \frac{\partial u}{\partial x} + \frac{1}{\rho} \frac{\partial p}{\partial x} + G = 0 \tag{3.2}$$

$$\frac{\partial p}{\partial t} + u \frac{\partial p}{\partial x} - a^2 \left(\frac{\partial \rho}{\partial t} + u \frac{\partial \rho}{\partial x} \right) - (\gamma - 1)\, \rho\, (\dot{q} + uG) = 0 \tag{3.3}$$

with

$$G = sgn(u) \frac{4f}{D} \frac{u^2}{2}$$

Manipulating eqs. (3.1) to (3.3) as follows:

$a^2 \cdot eq.\ (3.1) + \rho a \cdot eq.\ (3.2) + eq.\ (3.3) \Rightarrow$

$$\left[\frac{\partial p}{\partial t} + (u+a)\frac{\partial p}{\partial x}\right] + \rho a \left[\frac{\partial u}{\partial t} + (u+a)\frac{\partial u}{\partial x}\right] - (\gamma - 1)\rho(\dot{q} + uG) + \frac{\rho u a^2}{A}\frac{dA}{dx} + \rho a G = 0 \tag{3.4}$$

$a^2 \cdot eq.\ (3.1) - \rho a \cdot eq.\ (3.2) + eq.\ (3.3) \Rightarrow$

$$\left[\frac{\partial p}{\partial t} + (u-a)\frac{\partial p}{\partial x}\right] + \rho a \left[\frac{\partial u}{\partial t} + (u-a)\frac{\partial u}{\partial x}\right] - (\gamma - 1)\rho(\dot{q} + uG) + \frac{\rho u a^2}{A}\frac{dA}{dx} + \rho a G = 0 \tag{3.5}$$

Along the particular characteristic given by eq. (2.55) which involves the condition

$$\frac{dx}{dt} = u + a \tag{3.6}$$

the total derivative of the pressure p and the fluid velocity u can be rewritten as

$$\begin{cases} \dfrac{dp}{dt} = \dfrac{\partial p}{\partial t} + \dfrac{dx}{dt}\dfrac{\partial p}{\partial x} & \Rightarrow \quad \dfrac{dp}{dt} = \dfrac{\partial p}{\partial t} + (u+a)\dfrac{\partial p}{\partial x} \\ \dfrac{du}{dt} = \dfrac{\partial u}{\partial t} + \dfrac{dx}{dt}\dfrac{\partial u}{\partial x} & \Rightarrow \quad \dfrac{du}{dt} = \dfrac{\partial u}{\partial t} + (u+a)\dfrac{\partial u}{\partial x} \end{cases} \tag{3.7}$$

Substituting (3.7) into (3.4) and rearranging:

$$\frac{1}{\rho a}\frac{dp}{dt} + \frac{du}{dt} - \frac{\gamma - 1}{a}(\dot{q} + uG) + \frac{au}{A}\frac{dA}{dx} + G = 0 \tag{3.8}$$

Similarly, along the regressive characteristic eq. (2.57)

$$\frac{dx}{dt} = u - a \tag{3.9}$$

The total derivatives can be written as:

$$\begin{cases} \dfrac{dp}{dt} = \dfrac{\partial p}{\partial t} + \dfrac{dx}{dt}\dfrac{\partial p}{\partial x} & \Rightarrow \quad \dfrac{dp}{dt} = \dfrac{\partial p}{\partial t} + (u-a)\dfrac{\partial p}{\partial x} \\ \dfrac{du}{dt} = \dfrac{\partial u}{\partial t} + \dfrac{dx}{dt}\dfrac{\partial u}{\partial x} & \Rightarrow \quad \dfrac{du}{dt} = \dfrac{\partial u}{\partial t} + (u-a)\dfrac{\partial u}{\partial x} \end{cases} \tag{3.10}$$

Substituting into (3.5) and rearranging:

$$\frac{1}{\rho a}\frac{dp}{dt} - \frac{du}{dt} - \frac{\gamma-1}{a}(\dot{q} + uG) + \frac{au}{A}\frac{dA}{dx} - G = 0 \tag{3.11}$$

Equations (3.8) and (3.11) are said to be mathematically equivalent , *along the characteristic curves eqs.* (3.6) *and* (3.9) to the partial differential equations set of eqs. (3.1) to (3.3).

It is evident that along the curves defined by eq. (3.6) and eq. (3.9), the set of PDEs in eqs. (3.4) and (3.5) can be formally reduced to a set of ODEs. Mathematically, these curves are called *Characteristics* or *Characteristic Curves* and the set of reduced ODEs are named as *Compatibility Conditions*[1].

For a homentropic flow, the non-homentropic terms ($\dot{q}, G, \frac{dA}{dx}$) in eqs. (3.8) and (3.11) are ought to disappear, hence:

$$\frac{dp}{dt} = -\rho a\frac{du}{dt} \qquad \text{along } c^+ : \frac{dx}{dt} = u + a \tag{3.12a}$$

$$\frac{dp}{dt} = \rho a\frac{du}{dt} \qquad \text{along } c^- : \frac{dx}{dt} = u - a \tag{3.12b}$$

These two expressions state that along the characteristic given by eq. (3.12a) , the velocity is increasing while the pressure is decreasing. At the same time, along eq. (3.12b), both the velocity and pressure are increasing.

To visualize this, consider a homentropic flow exists in a duct connecting two volumes, there will be eventually a steady state at which the velocity and pressure will not vary anymore (see figure 3.1) depending on the duct initialization.

[1] Compatibility conditions state that p (or a) and u cannot change arbitrarily, but have to satisfy eqs. (3.8) and (3.11)

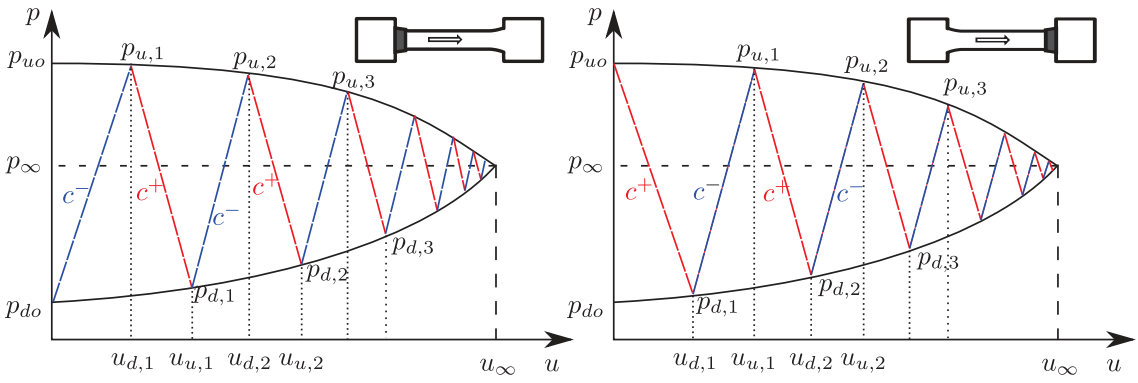

(a) Right traveling perturbation

(b) Left traveling perturbation

Fig. 3.1.: Illustration of the QPM using characteristics[2]

Considering that the left volume has a higher pressure compared to the right volume, the gas is flowing from left to right. Perturbations are also initiated first at the left boundary then transported across the duct.

Depending on whether the tube has initially right or left conditions, Figures 3.1a and 3.1b are used respectively to visualize the gas state at a given point until the gas reaches stationarity. The case in fig. 3.1a will be next illustrated in detail. The same holds for fig. 3.1b.

1.1. The Dynamic Model

The fundamental physics of QPM is based on the MOC theory, which has been illustrated in the previous section and is restated here for clarity:

$$\frac{1}{C}\frac{dp}{dt} + \frac{du}{dt} + \sigma_1 + \sigma_2 + \sigma_3 = 0 \qquad \text{at} \frac{dx}{dt} = u + a \tag{3.13a}$$

$$\frac{1}{C}\frac{dp}{dt} - \frac{du}{dt} + \sigma_1 + \sigma_2 - \sigma_3 = 0 \qquad \text{at} \frac{dx}{dt} = u - a \tag{3.13b}$$

where in the equations, $C = \rho a$ denotes the characteristic slope of $p-u$ curves (fig. 3.2),

[2] In this case, the boundary conditions steady states coincide because it is a homentropic flow.

while the non-homentropic terms σ_i are:

$$\begin{cases} \sigma_1 = -\dfrac{\gamma - 1}{a}(\dot{q} + uG) \\ \sigma_2 = \dfrac{au}{A}\dfrac{dA}{dx} \\ \sigma_3 = G \end{cases} \tag{3.14}$$

The theory of MOC can now be applied to analyze the flow in the duct. Integrating the corresponding conditions eqs. (3.13a) and (3.13b) respectively over the time interval Δt^+, during which the characteristics propagates with the velocity c^+ as well as over the Δt^-, during which it propagates with the velocity c^-:

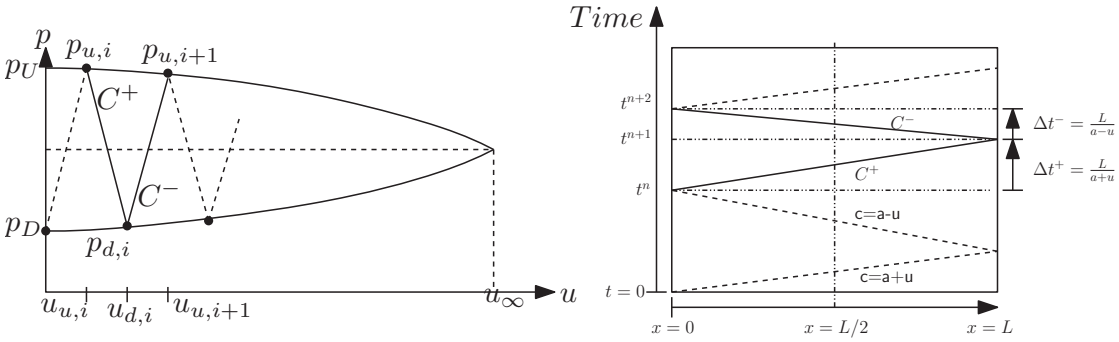

Fig. 3.2.: The Quasi-Propagatory Model

Integrating eq. (3.13a) between two successive time instants t_n and t_{n+1} for the progressive wave as shown in fig. 3.2:

$$\int_{t_n}^{t_{n+1}} \left[\frac{1}{C}\frac{dp}{dt} + \frac{du}{dt} + \sigma_1 + \sigma_2 + \sigma_3\right] dt = 0 \qquad \text{Along } C^+ \tag{3.15}$$

where $(\Delta t^+ = t_{n+1} - t_n)$ is the time required by the progressive wave to travel from one pipe end to the other:

$$p_{d,i} - p_{u,i} + Cu_{d,i} - Cu_{u,i} + \alpha_1 = 0 \tag{3.16}$$

with:

$$\alpha_1 = (\sigma_1 + \sigma_2 + \sigma_3)C\Delta t^+ \tag{3.17}$$

Similarly, integrating eq. (3.13b) between two successive time instants $t_n + 1$ and t_{n+2} for the regressive wave:

$$\int_{t_{n+1}}^{t_{n+2}} \left[\frac{1}{C} \frac{dp}{dt} - \frac{du}{dt} + \sigma_1 + \sigma_2 - \sigma_3 \right] dt = 0 \qquad \text{Along } C^- \tag{3.18}$$

$$p_{u,i+1} - p_{d,i} - C u_{u,i+1} + C u_{d,i} + \alpha_2 = 0 \tag{3.19}$$

Where α_2 denote

$$\alpha_2 = (\sigma_1 + \sigma_2 - \sigma_3) C \Delta t^- \tag{3.20}$$

To supply proper exact boundary conditions, non-linear physical models are required, which results in the high calculation effort. To avoid this, a linearization of the boundaries profile can be considered as shown in the $p - u$ plane in fig. 3.3.

Using a homentropic flow, the boundary conditions will converge to the same steady state value:

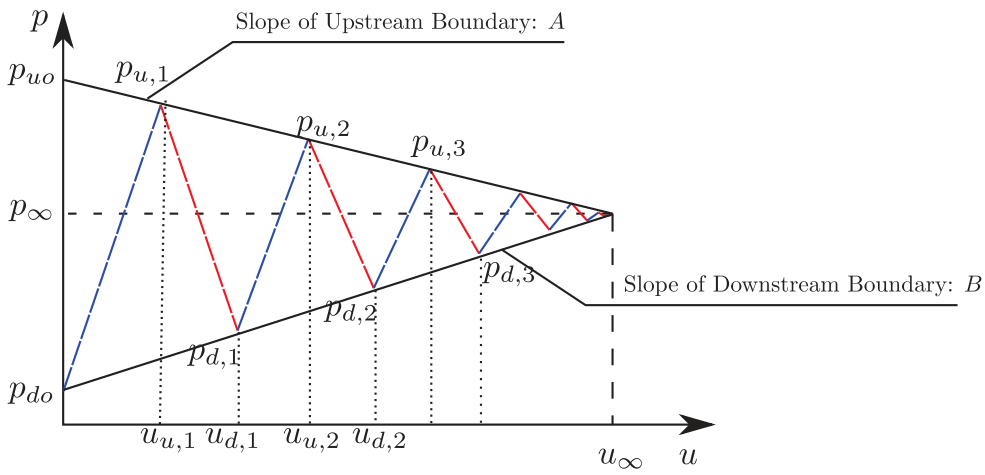

Fig. 3.3.: Linearized p-u plane

Suppose the pressure variation at a given boundary is given as:

$$p = f(u)$$

where f is a nonlinear function.

Linearizing around a given fluid velocity u^*

$$p = f(u^*) + \left.\frac{df}{du}\right|_{u^*} (u - u^*) \tag{3.21}$$

Thus, applying the previous approximation in accordance with fig. 3.3:

$$p_{u,i} = p_{uo} - A u_{u,i} \tag{3.22a}$$
$$p_{d,i} = p_{do} + B u_{d,i} \tag{3.22b}$$

Such that p_{uo} and p_{do} can be regarded as the pressures on the borders of the duct, where the fluid is stationary, i.e.

$$\begin{cases} p_{uo} = p_{u,j}\,|_{u_{u,j}=0} \\ p_{do} = p_{d,j}\,|_{u_{d,j}=0} \end{cases} \tag{3.23}$$

A and B are the coefficients representing the slope of the straight lines between the stationary state $(u = 0)$ and steady state $(u = u_\infty)$

Substituting eq. (3.22a) into eq. (3.16):

$$(p_{d,0} + B \cdot u_{d,i}) - (p_{u,0} - A \cdot u_{u,i}) + C\,(u_{d,i} - u_{u,i}) + \alpha_1 = 0 \tag{3.24}$$

Solving for $u_{d,i}$, yields:

$$u_{d,i} = \frac{-1}{C + B}\left[(p_{d,0} - p_{u,0}) + (A - C) \cdot u_{u,i} + \alpha_1\right] \tag{3.25}$$

Similarly, Substituting eq. (3.22b) into eq. (3.19):

$$(p_{u,0} - A \cdot u_{u,i+1}) - (p_{d,0} + B \cdot u_{d,i}) - C\,(u_{u,i+1} - u_{d,i}) + \alpha_2 = 0 \tag{3.26}$$

Solving for $u_{u,i+1}$, yields:

$$u_{u,i+1} = \frac{1}{C + A}\left[(p_{u,0} - p_{d,0}) + (C - B) \cdot u_{d,i} + \alpha_2\right] \tag{3.27}$$

Substitution of eq. (3.25) into eq. (3.27), yields:

$$\begin{aligned} u_{u,i+1} = & \frac{(C-B)(C-A)}{(C+B)(C+A)} u_{u,i} + \frac{2C}{(C+B)(C+A)}(p_{uo} - p_{do}) \\ & - \frac{1}{C+A}\left(\alpha_1 \frac{C-B}{C+B} - \alpha_2\right) \end{aligned} \tag{3.28}$$

and equivalently:

$$\begin{aligned} u_{d,i+1} = & \frac{(C-B)(C-A)}{(C+B)(C+A)} u_{d,i} + \frac{2C}{(C+B)(C+A)}(p_{uo} - p_{do}) \\ & - \frac{1}{C+B}\left(\alpha_1 - \alpha_2 \frac{C-A}{C+A}\right) \end{aligned} \tag{3.29}$$

The velocities at the upstream and downstream boundaries reach a steady state as long as no variation with time can be seen, i.e. $u_{u,i+1} = u_{u,i}$ and $u_{d,i+1} = u_{d,i}$. Thus, one can write:

$$\begin{cases} u_{u,\infty} = u_{u,i} = u_{u,i+1} \\ u_{d,\infty} = u_{d,i} = u_{d,i+1} \end{cases}$$

Hence, solving eqs. (3.28) and (3.29) with the above constraints yields the explicit expressions for $u_{u,\infty}$ and $u_{d,\infty}$ as follows:

$$\begin{cases} u_{u,\infty} = \dfrac{p_{uo} - p_{do}}{A+B} - \dfrac{C+B}{2C(A+B)}\left(\alpha_1 \dfrac{C-B}{C+B} - \alpha_2\right) \\ u_{d,\infty} = \dfrac{p_{uo} - p_{do}}{A+B} - \dfrac{C+A}{2C(A+B)}\left(\alpha_1 - \alpha_2 \dfrac{C-A}{C+A}\right) \end{cases} \tag{3.30}$$

Notice that $u_{u,\infty} = u_{d,\infty}$ in the case of homoentropic flow, where the assumption $\alpha_1 = \alpha_2 = 0$ is given.

Thus, eqs. (3.28) and (3.29) can be simplified in terms of the steady values of both velocities:

$$\begin{cases} u_{u,i+1} = \lambda u_{u,i} + (1-\lambda) u_{u,\infty} \\ u_{d,i+1} = \lambda u_{d,i} + (1-\lambda) u_{d,\infty} \end{cases} \tag{3.31}$$

where the coefficient λ denotes

$$\lambda = \frac{(C-B)(C-A)}{(C+B)(C+A)} \tag{3.32}$$

The QPM approximates gas dynamics while taking inertial effects in a lumped parameter way. To ease the calculation, solely the gas states at the midpoint of the duct are desired to be investigated. Approximating the value of velocity at the midpoint with their averages of them from upstream and downstream gives

$$u_{i+1} = \lambda u_i + (1-\lambda)u_\infty \tag{3.33}$$

where

$$u_i = \frac{1}{2}(u_{u,i} + u_{d,i}) \text{ and } u_\infty = \frac{1}{2}(u_{u,\infty} + u_{d,\infty}) \tag{3.34}$$

Because these equations are obtained using the integral along Δt^+ and Δt^-, this recursive scheme requires a fixed time step dependent on the wave speed and gas velocity. To overcome this, a dynamic model is obtained as follows:

eq. (3.33) $\Rightarrow$

$$\begin{cases} u_{i+1} = \lambda u_i + (1-\lambda)u_\infty \\ u_i = \lambda u_{i-1} + (1-\lambda)u_\infty \end{cases} \Rightarrow \begin{cases} u_{i+1} - \lambda u_i = (1-\lambda)u_\infty \\ u_i - \lambda u_{i-1} = (1-\lambda)u_\infty \end{cases}$$

Subtracting the previous two equations yields:

$$u_{i+1} - (\lambda+1)u_i + \lambda u_{i-1} = 0 \Rightarrow u_{i+1} = (\lambda+1)u_i - \lambda u_{i-1} \tag{3.35}$$

using eqs. (3.33) and (3.35), the following vector equation is obtained:

$$\begin{bmatrix} u_{i+1} \\ u_i \end{bmatrix} = \begin{bmatrix} \lambda+1 & -1 \\ 1 & 0 \end{bmatrix} \cdot \begin{bmatrix} u_i \\ u_{i-1} \end{bmatrix} \tag{3.36}$$

For $i = 1$:

$$\begin{bmatrix} u_2 \\ u_1 \end{bmatrix} = \begin{bmatrix} \lambda+1 & -1 \\ 1 & 0 \end{bmatrix} \cdot \begin{bmatrix} u_1 \\ u_0 \end{bmatrix}$$

Similarly, for $i = 2$:

$$\begin{bmatrix} u_3 \\ u_2 \end{bmatrix} = \begin{bmatrix} \lambda+1 & -1 \\ 1 & 0 \end{bmatrix} \cdot \begin{bmatrix} u_2 \\ u_1 \end{bmatrix} = \begin{bmatrix} \lambda+1 & -1 \\ 1 & 0 \end{bmatrix} \cdot \overbrace{\begin{bmatrix} \lambda+1 & -1 \\ 1 & 0 \end{bmatrix} \cdot \begin{bmatrix} u_1 \\ u_0 \end{bmatrix}}^{\begin{bmatrix} u_2 \\ u_1 \end{bmatrix}} = \begin{bmatrix} \lambda+1 & -1 \\ 1 & 0 \end{bmatrix}^2 \cdot \begin{bmatrix} u_1 \\ u_0 \end{bmatrix}$$

Which iteratively leads to:

$$\begin{bmatrix} u_{i+1} \\ u_i \end{bmatrix} = \begin{bmatrix} \lambda+1 & -1 \\ 1 & 0 \end{bmatrix}^i \cdot \begin{bmatrix} u_1 \\ u_0 \end{bmatrix} = M^i \cdot \begin{bmatrix} u_1 \\ u_0 \end{bmatrix}$$

the matrix M can be diagonalized as:

$$M = \begin{bmatrix} 1 & 1 \\ 1/\lambda & 1 \end{bmatrix} \cdot \begin{bmatrix} \lambda & 0 \\ 0 & \lambda \end{bmatrix} \cdot \begin{bmatrix} 1 & 1 \\ 1/\lambda & 1 \end{bmatrix}^{-1} = \begin{bmatrix} 1 & 1 \\ 1/\lambda & 1 \end{bmatrix} \cdot \begin{bmatrix} \lambda & 0 \\ 0 & 1 \end{bmatrix} \cdot \frac{\lambda-1}{\lambda} \begin{bmatrix} 1 & -1 \\ -1/\lambda & 1 \end{bmatrix}$$

Finally,

$$\begin{bmatrix} u_{i+1} \\ u_i \end{bmatrix} = \frac{\lambda-1}{\lambda} \cdot \begin{bmatrix} 1 & 1 \\ 1/\lambda & 1 \end{bmatrix} \cdot \begin{bmatrix} \lambda^i & 0 \\ 0 & 1 \end{bmatrix} \cdot \begin{bmatrix} 1 & -1 \\ -1/\lambda & 1 \end{bmatrix} \cdot \begin{bmatrix} u_1 \\ u_0 \end{bmatrix} \tag{3.37}$$

Simplifying and keeping the second raw only:

$$u_i = \frac{1}{\lambda-1} \lambda^i (u_1 - u_0) - u_1 + \lambda u_0$$

Knowing that

$$u_1 = \lambda u_0 + (1-\lambda) u_\infty$$

Thus:

$$u_i = \left(1 - \lambda^i\right) u_\infty + \lambda^i u_0 = \left(1 - \lambda^i\right) u_\infty \tag{3.38}$$

The model stability depends on the parameter λ as follows [3]:

- if $|\lambda| > 1$

$$\Rightarrow \lim_{i \to +\infty} \lambda^i = +\infty$$
$$\Rightarrow \lim_{i \to +\infty} u_i = +\infty$$

- if $\lambda = -1$

$$\Rightarrow u_i = \begin{cases} 0 & i = 0, 2, 4, 6, ... \\ 2u_\infty & i = 1, 3, 5, 7, ... \end{cases}$$

- if $\lambda = 1 \Rightarrow u_i = 0 \; \forall i$
- if $\lambda = 0$, the system has reached stationarity
- The system is stable elsewhere

Using the change of variable $\tau = \frac{-\Delta T}{ln\lambda}$ or $\lambda = e^{\frac{-\Delta T}{\tau}}$ for $0 < \lambda < 1$:

$$eq.\ (3.38) \Rightarrow u_i = \left(1 - e^{\frac{-i\Delta T}{\tau}}\right) u_\infty \tag{3.39}$$

or, for a general time instant:

$$u = u_\infty (1 - e^{-t/\tau}) \tag{3.40}$$

where the time constant τ is

$$\tau = -\frac{\Delta T}{\ln \lambda} \tag{3.41}$$

where Δt denotes the time interval between the emergence of two successive velocity

[3] This analysis hold in case different boundary conditions are applied

states. According to the $t-x$ plane of characteristics curve, it can be calculated as:

$$\Delta t = \frac{L}{a+u} + \frac{L}{a-u} \tag{3.42}$$

In case $-1 < \lambda < 0$, the change of variable $\tau = \frac{-\Delta T}{ln(-\lambda)}$ or $\lambda = -e^{\frac{-\Delta T}{\tau}}$ is used:

$$eq.\ (3.38) \Rightarrow u_i = \left(1-(-1)^i e^{\frac{-i\Delta T}{\tau}}\right) u_\infty = \left(1 - cos(i\pi)\cdot e^{\frac{-i\Delta T}{\tau}}\right) u_\infty \tag{3.43}$$

Or:

$$u = u_\infty(1-\cos(\omega t)\cdot e^{-t/\tau}) \tag{3.44}$$

where the subscript i has been removed and:

$$\begin{cases} \tau = -\dfrac{\Delta T s}{\ln\lambda} \\ \omega = -\dfrac{\pi}{\Delta t} \end{cases} \tag{3.45}$$

Although eqs. (3.40) and (3.44) supply a simple approach to calculate the midpoint velocity explicitly, the involved coefficients such as Δt_{mid}, τ and ω are, however, time-dependent values. Additionally, a plausible prediction for the steady velocity is often not available except for some specific cases. Last but not least, this discrete model is not a fixed-time-step approach so that the specification of the variable time step $\Delta_{t,\mathrm{mid}}$ is necessary for every iteration. A more effective way to use these deductions is to transform the explicit equations into a continuous-time model constructed on the non-linear ODEs.

Differentiating eq. (3.40):

$$\begin{aligned} \frac{du}{dt} &= u_\infty \cdot \frac{1}{\tau} \cdot e^{-t/\tau} \\ &= u_\infty \cdot \frac{1}{\tau} \cdot \left(1 - \frac{u_{\mathrm{mid}}}{u_\infty}\right) \end{aligned}$$

Or:

$$\frac{du}{dt} + \frac{u - u_\infty}{\tau} = 0 \qquad \text{for} \lambda > 0 \tag{3.46}$$

Similarly, differentiating eq. (3.44) twice, yields:

$$\frac{du}{dt} = u_\infty e^{-t/\tau} \left(\frac{cos(\omega t)}{\tau} + \omega sin(\omega t) \right) \tag{3.47a}$$

$$\frac{d^2u}{dt^2} = u_\infty e^{-t/\tau} \left[\left(\omega^2 - \frac{1}{\tau^2} \right) cos(\omega t) - \frac{2\omega}{\tau} sin(\omega t) \right] \tag{3.47b}$$

Or:

$$\frac{d^2u}{dt^2} + \frac{2}{\tau}\frac{du}{dt} + \left(\omega^2 + \frac{1}{\tau^2} \right) (u - u_\infty) = 0 \qquad \text{for} \lambda < 0 \tag{3.48}$$

Otherwise, when $\lambda = 0$, the current midpoint velocity will be equalized to the one in the steady state.

$$\lambda = 0 : \quad u_{\text{mid,i+1}} = u_\infty \tag{3.49}$$

After the reformulation of the solutions, it is possible to convert the continuous model back into a discrete one with assigning a new uniform iteration step ΔT. The explicit discretization for the both derivatives stated in eqs. (3.40) and (3.44) is expressed as:

$$\begin{cases} \dfrac{du}{dt} = \dfrac{u_{i+1} - u_i}{\Delta T} \\ \dfrac{d^2u}{dt^2} = \dfrac{u_{i+1} + u_{i-1} - 2u_i}{\Delta T^2} \end{cases} \tag{3.50}$$

Then, eq. (3.50) can be reformulated into:

$$\begin{cases} \lambda > 0 : & \dfrac{u_{i+1} - u_i}{\Delta T} + \dfrac{u_i - u_\infty}{\tau} = 0 \\ \lambda < 0 : & \dfrac{u_{i+1} + u_{i-1} - 2u_i}{\Delta T^2} + \dfrac{2}{\tau}\dfrac{u_{i+1} - u_i}{\Delta T} + \left(\omega^2 + \dfrac{1}{\tau^2} \right) (u_i - u_\infty) = 0 \end{cases} \tag{3.51}$$

Reorganizing the equations gives

$$\begin{cases} \lambda > 0: & u_{i+1} = \left(1 - \dfrac{\Delta T}{\tau}\right) u_i + \dfrac{\Delta T}{\tau} u_\infty \\ \lambda < 0: & u_{i+1} = \dfrac{(2-\omega^2)\tau^2 + 2\Delta T\tau - 1}{\tau^2 + 2\Delta T\tau} u_i - \dfrac{\tau}{\tau + 2\Delta T} u_{i-1} + \dfrac{\omega^2\tau^2 + 1}{\tau^2 + 2\Delta T\tau} u_\infty \end{cases} \tag{3.52}$$

thus presenting a method to solve the velocity field at the midpoint iteratively.

2. Boundary Conditions Treatment

So far, both the characteristic slopes A and B as well as the pressure constant p_{uo} and p_{do} have not been specified. These parameters are dependent on the boundary condition, geometry and the current gas state in the pipe.

Different models are used to treat the boundary conditions, depending on the geometry and flow nature (sonic or subsonic). Thus, to derive these parameters, the different flow situations has to be treated separately. Once again, the MOC is used for the boundary treatment.

In computational fluid dynamics, two boundary conditions exist referred as static or stagnation pressure conditions. In terms of numerical simulation, stagnation condition assumes a zero velocity at the boundary (atmosphere). A Pressure drop is required for the fluid to enter the computational region.

On the other hand, static conditions are used in the case of a continuous pressure profile across the boundary (such as simulation within one single pipe).

Based on this, the following cases exist for the simulation of the air system path:

- Either the gas is entering the tube from the atmosphere, which means $u_{atm} = 0$, and only stagnation conditions are existent at upstream
- The gas is entering the tube from an adjacent volume and static conditions are considered
- For downstream conditions, static conditions are considered for capacities within adjacent pipes. For the exhaust case, it is found to be a common assumption to consider that kinetic energy after the end throttle is not recovered. Hence, exhaust pressure is equal to static pressure.

Every single branch will comprise half of the adjacent capacities. This makes the boundary conditions of the branch set by the lumped parameters of the capacities (i.e p,T).

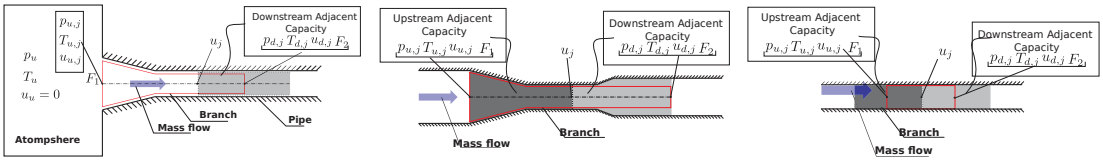

(a) Stagnation-Static (b) General Static-Static (c) Same duct Static-Static

Fig. 3.4.: Illustration of the QPM boundary conditions combinations

Hence, the following two combinations can take place:

- Total-Static
- Static-Static

To calculate now the slopes A and B defined by eqs. (3.22a) and (3.22b), an explicit expression of $p_{u,i}$ as a function of $u_{u,i}$ and $p_{d,i}$ as a function of $u_{d,i}$ has to be obtained. This represents the variation of the boundary pressure as a function of the local flow speed and is to be detailed in the following.

2.1. Situation 1: *Total-Static*

In this case, flow is considered to be flowing from a reservoir at stagnation conditions to a capacity at static conditions through a restriction defined by ψ which represents the ratio of the partially open end diameter to the pipe diameter.

2.1.1. Flow Leaving the Branch to the Reservoir i.e $u < 0$

In this case, the pressure at the upstream boundary conditions is by definition equal to the outside pressure, i.e $p_{u,i} = p_{ext}\ \forall u_{u,i}$.

Hence,

$$\frac{\partial p_{u,i}}{\partial u_{u,i}} = 0 \quad \forall u \Rightarrow A = 0 \quad \forall u_{u,i} \tag{3.53}$$

$$p_{uo} = p_{u,i} + A \cdot u_{u,i} \Rightarrow p_{uo} = p_{u,i} \tag{3.54}$$

As for the downstream boundary, the downstream pressure will always be equivalent to the given boundary conditions, thus:

$$p_{d,i} = p_{d,0} = p_d \qquad \forall t \Rightarrow B = 0 \tag{3.55}$$

2.1.2. Subsonic Flow Entering the Branch From the Reservoir i.e $0 < u < u_d^*$

In this case, the upstream boundary pressure is not anymore defined only by the external pressure, but also by the branch mid-point velocity.

First, we calculate the critical flow speed, to differentiate a chocked flow.

when the flow is chocked downstream, we have:

$$\frac{a_d}{a_u} = \frac{p_d}{p_u}^{\frac{2\gamma}{\gamma-1}} \Rightarrow \frac{u_d^*}{a_u} = \frac{p_d}{p_u}^{\frac{2\gamma}{\gamma-1}} \Rightarrow u_d^* = a_u \cdot \frac{p_d}{p_u}^{\frac{2\gamma}{\gamma-1}} \tag{3.56}$$

With the superscript $*$ referring to the critical flow speed.

Enthalpy conservation between the reservoir and the duct entry can be written as:

$$c_p T_u + \frac{u_u^2}{2} = c_p T_{u,i} + \frac{u_{u,i}^2}{2} \tag{3.57}$$

The reservoir is considered to be large enough (such that the contribution of the kinetic energy to the total pressure can be neglected), eq. (3.57) can be rewritten as:

$$c_p \cdot (T_{u,i} - T_u) = \frac{1}{2}\left(u_u^2 - u_{u,i}^2\right) \approx -\frac{1}{2}u_{u,i}^2 \tag{3.58}$$

Or:

$$\begin{aligned} \frac{T_{u,i} - T_u}{T_u} = \frac{-u_{u,i}^2}{2c_p T_u} = -\frac{(\gamma-1)u_{u,i}^2}{2\gamma R_{spec} T_u} = -\frac{(\gamma-1)u_{u,i}^2}{2a_u^2} \\ \Rightarrow \frac{T_{u,i}}{T_u} = 1 - \frac{(\gamma-1)u_{u,i}^2}{2a_u^2} \end{aligned} \tag{3.59}$$

Using the conservation of volumetric flow (or mass flow, since the density is considered to be constant) between the pipe entry and pipe mid-point:

$$A_1 \cdot u_{u,i} = A_{pipe} \cdot u_i \Rightarrow u_{u,i} = \frac{A_{pipe}}{A_1} \cdot u_i = \frac{u_i}{\psi} \tag{3.60}$$

Assuming an isentropic expansion between the reservoir and the throat, one can write:

$$\frac{p_{u,i}}{p_u} = \left(\frac{T_{u,i}}{T_u}\right)^{\frac{\gamma}{\gamma-1}} \Rightarrow p_{u,i} = p_u \cdot \left(\frac{T_{u,i}}{T_u}\right)^{\frac{\gamma}{\gamma-1}} \tag{3.61}$$

Then, substituting eq. (3.59) and eq. (3.60) into eq. (3.61)

$$\begin{aligned} p_{u,i} &= p_u \left(1 - \frac{(\gamma-1)u_{u,i}^2}{2a_u^2}\right)^{\frac{\gamma}{\gamma-1}} \\ &= p_u \left(1 - \frac{(\gamma-1)u_i^2}{2\psi a_u^2}\right)^{\frac{\gamma}{\gamma-1}} \end{aligned} \tag{3.62}$$

Using the definition of the parameter A from eq. (3.22a):

$$\begin{aligned} A &= \lim_{\Delta u_{u,i}\to 0} \frac{\Delta p_{u,i}}{\Delta u_{u,i}} = \frac{\partial p_{u,i}}{\partial u_{u,i}} = \frac{\gamma p_u u_{u,i}}{a_u^2}\left(1 - \frac{(\gamma-1)u_{u,i}^2}{2a_u^2}\right)^{\frac{1}{\gamma-1}} \\ &= \frac{\gamma p_u u_i}{\psi a_u^2}\left(1 - \frac{(\gamma-1)u_i^2}{2\psi^2 a_u^2}\right)^{\frac{1}{\gamma-1}} \end{aligned} \tag{3.63}$$

Substituting eq. (3.62) into eq. (3.22a):

$$p_{uo} = p_{u,i} + Au_{u,i} = p_u \left(1 - \frac{(\gamma-1)u_i^2}{2\psi a_u^2}\right)^{\frac{\gamma}{\gamma-1}} + Au_{u,i} \tag{3.64}$$

The downstream pressure will always be consistent with the downstream pressure, thus $B = 0$.

2.1.3. Sonic Flow Entering the Branch from the Reservoir i.e $u > u_d^*$

For the upstream condition, the parameters A and p_{u0} are the same as for the subsonic case, and are given by eqs. (3.64) and (3.65) respectively.

$$A = \frac{\gamma p_u u_i}{\psi a_u^2}\left(1 - \frac{(\gamma-1)u_i^2}{2\psi^2 a_u^2}\right)^{\frac{1}{\gamma-1}} \tag{3.65}$$

and

$$p_{uo} = p_u \left(1 - \frac{(\gamma-1)u_i^2}{2\psi a_u^2}\right)^{\frac{\gamma}{\gamma-1}} + Au_{u,i}$$

For a sonic flow in a convergent duct, the maximum velocity achieved in the duct is exactly the local sonic speed.

$$u_i = u_{d,i} = a_{d,i} \tag{3.66}$$

Considering an isentropic process between the two capacities enclosing the branch:

$$p_{d,i} = p_u \left(\frac{a_{d,i}}{a_u}\right)^{\frac{2\gamma}{\gamma-1}} = p_u \left(\frac{u_i}{a_u}\right)^{\frac{2\gamma}{\gamma-1}} \tag{3.67}$$

The parameter B can be evaluated as:

$$B = \frac{\partial p_{d,i}}{\partial u_{d,i}} = \frac{2\gamma}{\gamma-1}\frac{p_u}{a_u}\left(\frac{u_{d,i}}{a_u}\right)^{\frac{\gamma+1}{\gamma-1}} = \frac{2\gamma}{\gamma-1}\frac{p_u}{a_u}\left(\frac{u_i}{a_u}\right)^{\frac{\gamma+1}{\gamma-1}} \tag{3.68}$$

Eventually, the pressure parameter from the downstream end p_{do} will take the form

$$p_{do} = p_u \left(\frac{a_{d0}}{a_u}\right)^{\frac{2\gamma}{\gamma-1}} = p_u \left(\frac{u_i}{a_u}\right)^{\frac{2\gamma}{\gamma-1}} \tag{3.69}$$

2.2. Situation 2: Static-Static

This is mainly for the simulation of a pipe section, where the convergence or divergence exist only at the downstream boundary.

Thus, independently of the flow nature and direction, because there exist no contraction or enlargement, the static upstream conditions will result in:

$$A = 0 \Rightarrow p_{u0} = p_u \qquad \forall u \tag{3.70}$$

For the downstream conditions, three cases has to be differentiated because kinetic energy after the restriction is not recovered, thus $p_{d0} \neq p_d$.

2.2.1. Negative Flow i.e $u < 0$

For a back flow, the downstream condition be similar to the previous downstream case for a back flow, thus:

$$B = 0 \tag{3.71}$$

2.2.2. Subsonic Flow i.e $0 < u < a$

2.2.2.1 $p_u/p_d < \pi_{crit}$

To obtain an expression of B following the definition given by eq. (3.22b), an expression relating the downstream pressure to the downstream boundary velocity is required. However, below the critical pressure ratio (upstream to downstream), the flow is subsonic and is defined by the upstream conditions as well as the downstream conditions.

In this case, such an explicit relation cannot be defined, and B is simply approximated as:

$$B = \frac{p_u - p_d}{u_d} \tag{3.72}$$

Where u_i is the current gas velocity at the branch mid-point.

To calculate the throat velocity, consider the enthalpy conservation and continuity between the upstream and downstream branch boundaries given by:

$$\rho_u u_u A_u = \rho_d u_d A_d \tag{3.73a}$$

$$c_p T_u + \frac{u_u^2}{2} = c_p T_d + \frac{u_d^2}{2} \tag{3.73b}$$

Considering an isentropic process along the downstream restriction:

$$\frac{p_d}{p_u} = \left(\frac{\rho_d}{\rho_u}\right)^{\frac{1}{\gamma}} = \left(\frac{T_d}{T_u}\right)^{\frac{\gamma}{\gamma-1}} \tag{3.74}$$

then:

$$
\begin{aligned}
eq.\ (3.73b) \Rightarrow \frac{1}{2}u_d^2 &= c_p\left(T_u - T_d\right) + \frac{u_u^2}{2} \\
&= c_p T_u\left(1 - \frac{T_d}{T_u}\right) + \frac{u_u^2}{2} \\
&= c_p T_u\left(1 - \left(\frac{p_d}{p_u}\right)^{\frac{\gamma-1}{\gamma}}\right) + \frac{u_u^2}{2}
\end{aligned} \tag{3.75}
$$

at the same time:

$$
\begin{aligned}
eq.\ (3.73a) \Rightarrow u_u &= \frac{\rho_d}{\rho_u}\cdot\frac{F_d}{F_u}\cdot u_d \\
&= \frac{\rho_d}{\rho_u}\cdot\phi\cdot u_d
\end{aligned} \tag{3.76}
$$

Substituting into eq. (3.75) yields:

$$
\frac{1}{2}u_d^2 = c_p T_u\left(1 - \left(\frac{p_d}{p_u}\right)^{\frac{\gamma-1}{\gamma}}\right) + \frac{1}{2}\left[\frac{\rho_d}{\rho_u}\cdot\frac{1}{\phi}\cdot u_d\right]^2
$$

Solving for u_d:

$$
u_d^2 = 2\cdot\frac{a_u^2}{\gamma-1}\left[1 - \left(\frac{p_d}{p_u}\right)^{\frac{\gamma-1}{\gamma}}\right]\left[1 - \frac{1}{\phi}\left(\frac{p_d}{p_u}\right)^{2/\gamma}\right]^{-1} \tag{3.77}
$$

and the downstream boundary slope B can be calculated as:

$$
B = \frac{p_u - p_d}{u_d} = \frac{p_u - p_d}{a_u\phi}\sqrt{\frac{(\gamma-1)\left(1 - \frac{1}{\phi}\left(\frac{p_d}{p_u}\right)^{2/\gamma}\right)}{2\left[1 - \left(\frac{p_d}{p_u}\right)^{\frac{\gamma-1}{\gamma}}\right]}} \tag{3.78}
$$

2.2.2.2 Case $p_u/p_d > \pi_{crit}$

This case demonstrates the specific condition for a flow phenomenon in a convergent duct, in which a transition process from the subsonic flow to sonic flow can take place,

whereas the branch velocity still did not reach the sound speed, the throat flow can reach the sonic speed.

From a physical point of view, with the gradual contraction of the flow cross-section area, the pressure of the fluid falls considerably. The loss of static pressure head is mostly converted to the accumulation of fluid kinetic energy. Thus, if the pressure drop happens to exceed the critical case, i.e. the pressure ratio is greater than the critical value, the fluid flowing with a subsonic speed can be eventually accelerated to the local sonic speed at the outlet profile of the duct. Nevertheless, owing to the geometrical constraint[4], the fluid is not capable of traveling beyond the sonic limit.

It is now necessary to calculate the critical pressure where the transition to sonic flow takes place:

The critical pressure p_u^* is defined as:

$$\frac{p_u^*}{p_d} = \left(\frac{a_u}{a_d}\right)^{\frac{2\gamma}{\gamma-1}} \Rightarrow p_u^* = p_d \cdot \left(\frac{a_u}{a_d}\right)^{\frac{2\gamma}{\gamma-1}} \tag{3.79}$$

Using the ellipse of energy and considering sonic flow downstream the restriction only:

$$\begin{aligned} a_u^2 + \frac{\gamma-1}{2}u_u^2 = a_d^2 + \frac{\gamma-1}{2}u_d^2 = \frac{\gamma+1}{2}a_d^2 \\ \Rightarrow \left(\frac{a_u}{a_d}\right)^2 + \frac{\gamma-1}{2}\left(\frac{u_u}{a_d}\right)^2 = \frac{\gamma+1}{2} \end{aligned} \tag{3.80}$$

Combining the mass conservation and isentropic process between the upstream and downstream, one can write:

$$\begin{aligned} \rho_u \cdot A_u \cdot u_u = \rho_d \cdot A_d \cdot u_d \Rightarrow u_u = \frac{A_d}{A_u} \cdot \frac{\rho_d}{\rho_u} \cdot u_d \\ \Rightarrow u_u = \phi \cdot \left(\frac{a_u}{a_d}\right)^{\frac{-2}{\gamma-1}} \cdot a_d \Rightarrow \frac{u_u}{a_d} = \phi \cdot \left(\frac{a_u}{a_d}\right)^{\frac{-2}{\gamma-1}} \end{aligned} \tag{3.81}$$

[4]According to the differential form of continuum equation, i.e. $\frac{d\rho}{\rho} + \frac{du}{u} + \frac{dA}{A} = 0$, and the definition of sonic speed, i.e. $a = dp/d\rho$, it can be inferred that $\frac{du}{dA} = \frac{u}{A(Ma^2-1)}$. If the fluid accelerates over the sound speed, i.e. $du > 0$ and Mach number $Ma > 1$, then there must exist dA>0 to satisfy the conservation of mass. However, it does not conform to the geometry of a convergent pipe

Substituting into eq. (3.80) yields:

$$\left(\frac{a_u}{a_d}\right)^2 + \frac{\gamma-1}{2}\phi\left(\frac{a_u}{a_d}\right)^{\frac{-4}{\gamma-1}} = \frac{\gamma+1}{2} \tag{3.82}$$

which using the change of variable $\alpha = \frac{a_u}{a_d}$, can be written as:

$$\alpha^2 + \frac{\gamma-1}{2}\phi^2\alpha^{\frac{-4}{\gamma-1}} - \frac{\gamma+1}{2} = 0 \tag{3.83}$$

The evaluation of α involves the solution of a high-order polynomial[5]. To ease the solution process, the first-order Taylor series is used to expand the term $\alpha^{\frac{-4}{\gamma-1}}$ at the point $\alpha = 1$:

$$\alpha^{\frac{-4}{\gamma-1}} = 1 + \frac{-4}{\gamma-1}(\alpha-1) \tag{3.84}$$

Imposing the expansion back to the equation (3.83) gives the approximate solution of a second-order equation for α

$$\alpha = 1 \pm \frac{\gamma-1}{4}\sqrt{1-\phi^2} \tag{3.85}$$

thus verifying the prerequisite for transition from subsonic to sonic flow mathematically, which is $\phi < 1$. However, the solution $\alpha = 1 - \frac{\gamma-1}{4}\sqrt{1-\phi^2}$ is not consistent with the condition $\alpha = \frac{a_u}{a_d} = \left(\frac{p_u^*}{p_d}\right)^{\frac{\gamma-1}{2\gamma}} > 1$.
Hence, the critical downstream pressure at the sonic state will be:

$$p_u^* = p_d\left(1 + \frac{\gamma-1}{4}\sqrt{1-\phi^2}\right)^{\frac{2\gamma}{\gamma-1}} \tag{3.86}$$

Thus, the flow velocity at the upstream end u_u^* can be calculated using the mass conservation as:

[5]For example, an ideal diatom gas, such as N_2, O_2, owns the specific gas ratio $\gamma = 7/5 = 1.4$, which makes the function become $\alpha^2 + 0.2\phi^2\alpha^{-10} - 1.2 = 0$. Which can be solved only numerically.

$$u_u^* = \frac{\rho_d}{\rho_u} \cdot \frac{F_d}{F_u} \cdot u_d \Rightarrow u_u^* = \left(\frac{p_d}{p_u^*}\right)^{\frac{\gamma-1}{2\gamma}} \cdot \phi \cdot \alpha \cdot a_u$$

$$u_u^* = \left(\frac{p_d}{p_u^*}\right)^{\frac{\gamma-1}{2\gamma}} \cdot \phi \cdot \left(1 + \frac{\gamma-1}{4}\sqrt{1-\phi^2}\right)^{\frac{-2}{\gamma-1}} \cdot a_u \tag{3.87}$$

and the parameter B can be approximated as:

$$B = \frac{p_u^* - p_d}{u^*} \tag{3.88}$$

2.2.3. Sonic Flow at the Throat i.e $u_t = a_t$

The critical pressure ratio can now be written as:

$$\left(\frac{p_d}{p_t}\right)_{cr} = \left(\frac{p_d}{p_t}\right)_{cr}^{\frac{2\gamma}{\gamma-1}} \Rightarrow \left(\frac{p_d}{p_t}\right)_{cr} = \left(\frac{p_d}{p_t}\right)_{cr}^{\frac{\gamma-1}{2\gamma}} \tag{3.89}$$

The mass conservation between the upstream and the throat will result into:

$$\rho_d \cdot A_d \cdot u_d = \rho_t \cdot A_t \cdot u_t \Rightarrow u_d = \left(\frac{a_t}{a_d}\right)^{\frac{2}{\gamma-1}} \cdot \phi \cdot u_t \tag{3.90}$$

Because the throat is chocked, $u_t = a_t$, hence:

$$\begin{aligned} u_d = \left(\frac{a_t}{a_d}\right)^{\frac{2}{\gamma-1}} \cdot \phi \cdot a_t \Rightarrow u_d &= \left(\frac{a_t}{a_d}\right)^{\frac{2}{\gamma-1}} \cdot \phi \cdot \frac{a_t}{a_d} \cdot a_d \\ \Rightarrow u_d &= \left(\frac{a_t}{a_d}\right)^{\frac{\gamma+1}{\gamma-1}} \cdot \phi \cdot a_d \end{aligned} \tag{3.91}$$

Or:

$$a_d = \alpha^{+\frac{\gamma+1}{\gamma-1}} \cdot \frac{u_d}{\phi} \tag{3.92}$$

Then, the pressure at the downstream end $p_{d,i}$ will be

$$p_{d,i} = p_u \left(\frac{a_{d,i}}{a_u} \right)^{\frac{2\gamma}{\gamma-1}} = p_u \left(\frac{u_i \cdot \alpha^{\frac{\gamma+1}{\gamma-1}}}{\phi \cdot a_u} \right)^{\frac{2\gamma}{\gamma-1}} \tag{3.93}$$

According to the definition of B and p_{do}:

$$\begin{aligned} B = \frac{\partial p_{d,i}}{\partial u_{d,i}} &= \frac{2\gamma}{\gamma-1} p_u \left(\frac{\alpha^{\frac{\gamma+1}{\gamma-1}}}{\phi a_u} \right)^{\frac{2\gamma}{\gamma-1}} u_i^{\frac{\gamma+1}{\gamma-1}} \\ p_{do} &= p_u \left(\frac{u_i \alpha^{\frac{\gamma+1}{\gamma-1}}}{\phi a_u} \right)^{\frac{2\gamma}{\gamma-1}} - B u_i \end{aligned} \tag{3.94}$$

3. Emptying-Filling Model

As discussed from the previous section, the dynamics of the duct flow inside the engine intake and exhaust manifold is associated with the upstream and downstream boundary conditions imposed on its borders.

By using a lumped-parameter model, these flow behaviors are only concerned and recorded at the midpoint of the pipe. However, in most cases of investigation, it is also desired to gather these significant flow characteristics in other places of the duct. In order to obtain the data from those positions, the duct must be subdivided into a limited number of branches. It ensures the midpoints of some of them are exactly located on the positions which needs to be investigated. Then, gas states in those places are calculable by applying the midpoint Quasi-Propagatory method.

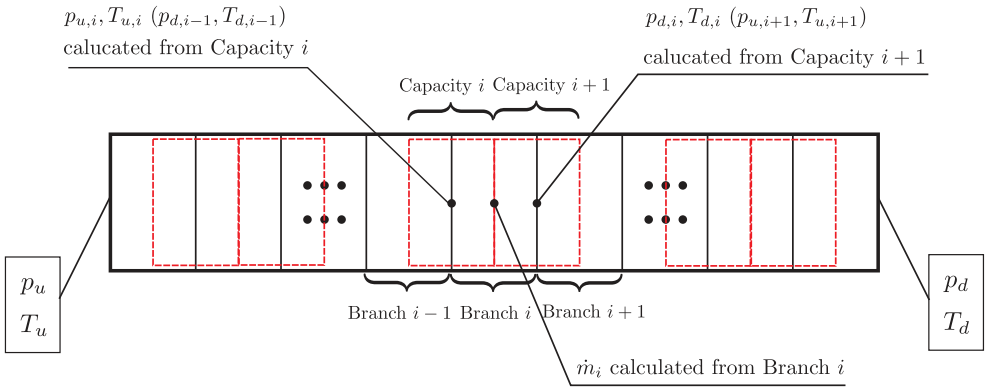

Fig. 3.5.: Connection of the Branch Models and Capacity Models in a Duct

However, the couple of boundary conditions p_u and p_d from each branch are not available. Thus, an intermediate flow model, the so-called **Empty-Filling Capacity Model**, is introduced to supply the missing information. The model connects the branches by means of involving the half volume of each branch so that the midpoints of them are exactly the boundaries of the capacity (see figure 3.5). Considering the mass and energy equilibrium for the control volume of the capacity gives

$$\begin{cases} \dfrac{dm_{cap}}{dt} = \displaystyle\sum_{i=1}^{N} \dot{m}_i \\ \dfrac{dE_{cap}}{dt} = \displaystyle\sum_{i=1}^{N} \dot{m}_i h_i + \dot{q} \end{cases} \tag{3.95}$$

where the left side of equality denotes the time variation of mass and energy in the capacity whereas the right side refers to the sum of net mass and energy flux from the branch $i-1$ and i into the capacity. For a fixed-geometry capacity i, its volume remains unchanged during the flow process so that

$$\begin{aligned} \frac{dm_{cap}}{dt} &= \frac{d(\rho_{cap} V_{cap})}{dt} = V_{cap}\frac{d\rho_{cap}}{dt} + \rho_{cap}\frac{dV_{cap}}{dt} = V_{cap}\frac{d\rho_{cap}}{dt} \\ \frac{dE_{cap}}{dt} &= \frac{d(m_{cap} e_{cap})}{dt} = \frac{d(\rho_{cap} V_{cap} c_v T_{cap})}{dt} = V_{cap}\frac{c_v}{R_{spec}}\frac{dp_{cap}}{dt} = \frac{V_{cap}}{\gamma - 1}\frac{dp_{cap}}{dt} \end{aligned} \tag{3.96}$$

Combing the equation (3.95) and (3.96) and discretizing it explicitly in time interval ΔT obtains the new gas state of the fluid in capacity

$$\begin{cases} \rho_{cap}^{n+1} = \rho_{cap}^{n} + \left(\dfrac{1}{V_{cap}} \displaystyle\sum_{i=1}^{N} \dot{m}_i^n \right) \Delta T \\ p_{cap}^{n+1} = p_{cap}^{n} + \left(\dfrac{\gamma - 1}{V_{cap}} \displaystyle\sum_{i=1}^{N} \dot{m}_i^n h_i^n + \dot{q}^n \right) \Delta T \\ T_{cap}^{n+1} = \dfrac{p_{cap}^{n+1}}{R_{spec} \rho_{cap}^{n+1}} \end{cases} \tag{3.97}$$

For a lumped-parameter model, the gas states at the midpoint of the capacity can be represented by these unified values, i.e. ρ_{cap}^{n+1}, p_{cap}^{n+1} and T_{cap}^{n+1}. Thus, since the midpoint of the capacity lies on either the upstream or the downstream end of the involved branches, their boundary conditions p_u, T_u or p_d, T_d can be determined.

4. Numerical Validation

Before validating the QPM approach on an ICE air system, it will first be compared to the full 1D CE-SE. The CE-SE was already validated and proved being advantageous from an accuracy and calculation point of view compared to other numerical schemes.

We will consider the flow scenario given by fig. 2.3 for an upstream pressure equal to 1 bar and downstream pressure equal to 0.9 bar. The tube having initially the downstream conditions.

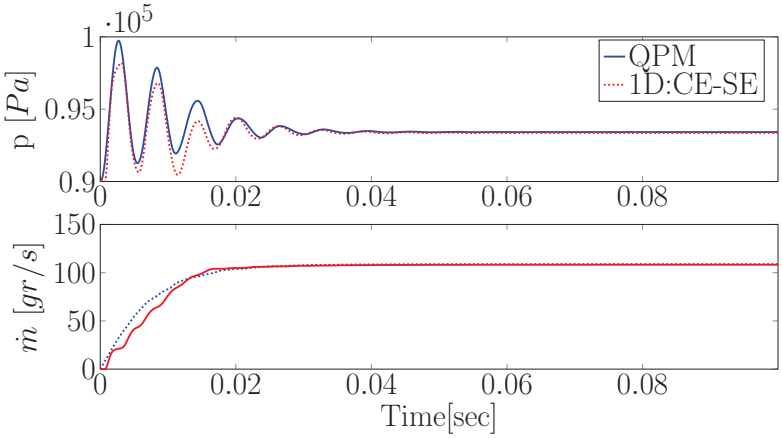

Fig. 3.6.: QPM Vs 1D Modeling

It is clear that, despite its simplicity, the QPM captures properly the pressure and mass flow profiles. Taking into consideration that only geometrical characteristics are used to parameterize the QPM, the amplitude accuracy is considered satisfactory since the reference in this case are also simulation results.

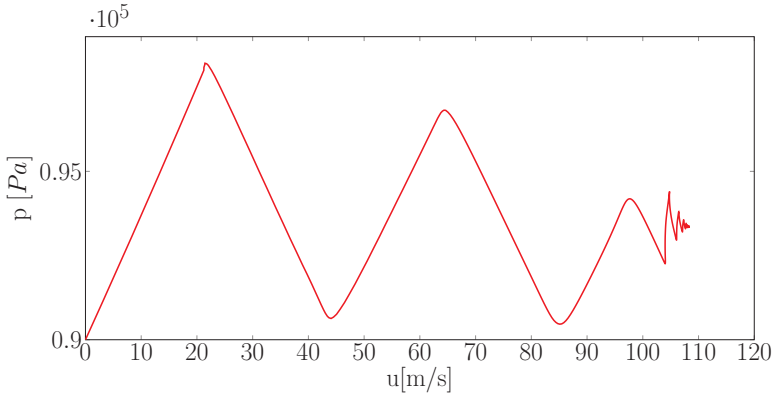

Fig. 3.7.: QPM Idea

	CE-SE	QPM
Ellapsed Time	$\approx$ 665s	1.5s
Number of States	300	5

5. Conclusion

This chapter presented the Quasi-Propagatory Model to model the unsteady-one dimensional gas flow using a low order modeling principle. As it is clearly seen in section 1, this approach overcomes the schemes from previous chapter due to the smaller number of states and the reduced amount of calculation effort.

The QPM is based on observing waves propagation in a duct connecting two large volumes. it is then noticed that the pressure and the velocity profiles can be related to duct boundary conditions directly without necessarily considering explicitly direct adjust modes.

Using initial and approximated steady states, the envelop enclosing the pressure profile can be approximated. The Method of Characteristics can then be used to provide progressive and regressive waves speeds, which will be used to calculate pressure and velocity profiles at every time steps.

For the numerical validation of the QPM, the CE-SE was considered as a reference. Without any complex tuning, the QPM produced accurate results with respect to the reference while offering a huge reduction in the calculation effort.

In the following chapter, the remaining components of the air system will be presented, to be used for an overall system simulation in chapter 6. Chapter 4 will present an amelioration of the compressor data-based modeling algorithm, to ensure a good estimation of the boost pressure.

CHAPTER 4

0D ENGINE MODELING

The air system is mainly a network of volumes such as the intake and exhaust manifolds interconnected using valves, turbine, compressor, filters and coolers.

0D Engines models have essentially evolved as emissions and On-Board Diagnosis[1] evolved [51]. They are also known as control-oriented models as they provide an input-output relationship with reasonable precision and affordable computational complexity [22].

This chapter will present briefly the common equations used to model the air system components. The reader is referred to [22] for detailed analysis.

1. Manifolds

Volume along the engine air system are modeled as open thermodynamic systems. These have already been discussed in the capacity sub model of the QPM, and the states equations based on the governing equations of mass and energy are restated here.

Considering the system shown in fig. 6.12, the pressure inside the intake manifold, exhaust manifold (with high pressure EGR) and a simple volume can be calculated as follows:

[1] OBD should detect any malfunctioning in engine system or if any exhaust emissions are beyond the standard limits

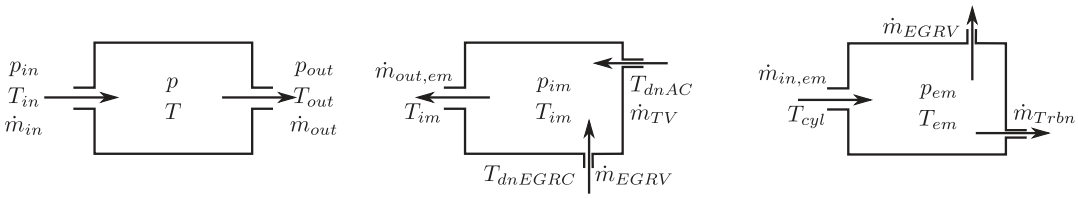

(a) General volume (b) Intake manifold (c) Exhaust manifold

Fig. 4.1.: Volumes representation

$$\frac{dp}{dt} = \frac{\gamma R}{V} \cdot (\dot{m}_{in} T_{in} - \dot{m}_{out} T) \tag{4.1}$$

$$\frac{dp_{im}}{dt} = \frac{\gamma R}{V_{im}} \cdot (\dot{m}_{TV} T_{dnAC} + \dot{m}_{EGRV} T_{em} - \dot{m}_{out,im} T_{im}) \tag{4.2}$$

$$\frac{dp_{em}}{dt} = \frac{\gamma R}{V_{em}} \cdot (\dot{m}_{in,em} T_{Cyl} - (\dot{m}_{EGRV} + \dot{m}_{Turb}) \cdot T_{em}) \tag{4.3}$$

as for the temperatures, the following differential equations hold:

$$\frac{dT}{dt} = \frac{T \cdot R}{p \cdot V \cdot c_v} \left[c_p \cdot \dot{m}_{in} \cdot T_{in} - c_p \cdot \dot{m}_{out} \cdot T - c_v \left(\dot{m}_{in} - \dot{m}_{out} \right) \right] \tag{4.4a}$$

$$\begin{aligned} \frac{dT_{im}}{dt} = \frac{T_{im} \cdot R}{p_{im} \cdot V_{im} \cdot c_v} \left[c_p \cdot \dot{m}_{TV} \cdot T_{dnAC} + c_p \cdot \dot{m}_{EGRsV} \cdot T_{dnEGRC} \right. \\ \left. - c_p \cdot \dot{m}_{out,im} \cdot T_{im} - c_v \left(\dot{m}_{TV} - \dot{m}_{out,im} \right) \right] \end{aligned} \tag{4.4b}$$

$$\begin{aligned} \frac{dT_{em}}{dt} = \frac{T_{em} \cdot R}{p_{em} \cdot V_{em} \cdot c_v} \left[c_p \cdot \dot{m}_{in,em} \cdot T_{Cyl} \right. \\ \left. - c_p \cdot (\dot{m}_{EGRV} + \dot{m}_{Trbn}) \cdot T_{em} - c_v \left(\dot{m}_{in,em} - \dot{m}_{EGRV} - \dot{m}_{Trbn} \right) \right] \end{aligned} \tag{4.4c}$$

The differential equations have to be adapted in case of back flow.

2. Throttle Valve

This element allows controlling mass and thus enthalpy flow based on the pressure and temperature differences across the valve. The modeling for the control has been well established and can be found in details [22]. It will be here briefly stated.

Considering an ideal gas flowing adiabatically across the valve, the internal energy conservation can be written as:

$$\dot{m} = c_d \cdot A_{goe} \frac{p_{up}}{\sqrt{RT_{up}}} \cdot \begin{cases} \sqrt{\gamma \cdot \left(\frac{2}{\gamma+1}\right)^{\frac{\gamma+1}{\gamma-1}}} & \text{for } \frac{p_{dn}}{p_{up}} > \left(\frac{p_{dn}}{p_{up}}\right)_{cr} \\ \left(\frac{p_{dn}}{p_{up}}\right)^{\frac{1}{\gamma}} \cdot \sqrt{\frac{2\gamma}{\gamma-1} \cdot \left(1 - \left(\frac{p_{dn}}{p_{up}}\right)^{\frac{\gamma-1}{\gamma}}\right)} & \text{for } \frac{p_{dn}}{p_{up}} < \left(\frac{p_{dn}}{p_{up}}\right)_{cr} \end{cases} \tag{4.5}$$

Where $\left(\frac{p_{dn}}{p_{up}}\right)_{cr}$ represents the critical ratio for which the flow reaches sonic conditions (in the narrowest part).

fig. 4.2 shows the variation of geometrical area of the valve as a function of the angle α (right) and the variation of the flow function Ψ as a function of the pressure ratio across the valve (left).

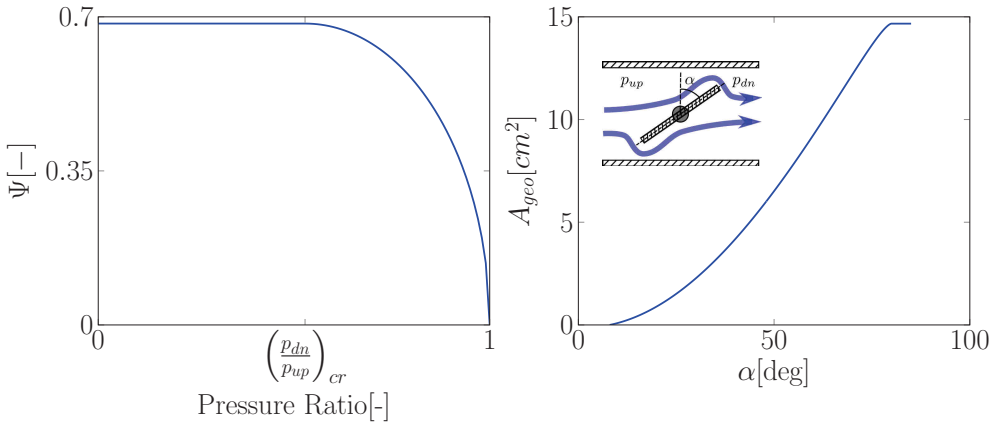

Fig. 4.2.: Throttle Valve

3. EGR Valve

The idea of the Exhaust-Gas Recirculation (EGR) is to reintroduce a portion of the exhaust gases into the cylinder. This will decrease the amount of oxygen available in the cylinder and increase the heat capacity due to the larger quantity of CO_2. This will reduce the flame temperature which will slow down the NO_x formation mechanism [15]. Nevertheless, an excess EGR can have a detrimental effect on engine breathing, since less exhaust gas flowing through the turbine means instantly a slower turbocharger speed, and hence, less bossing pressure. Simultaneously, exhaust gas recirculation can deteriorate the Air/Fuel Ratio which have a direct impact on tail-pipe emissions.

4. Thermal Exchangers

Compressors are used to increase the boosting pressure, but also lead to a higher fresh air temperature. Which will decrease the air density and affect the engine breathing. Heat exchangers are used to have a lower temperature with the same pressure, which will increase even more the density.

Heat exchangers are also used in with high and low pressure EGRs.

To obtain the temperature downstream the heat exchanger, a simple effectiveness coefficient is considered, such that:

$$T_{dn} = \eta_{he} \cdot T_{coolant} + (1 - \eta_{he}) \cdot T_{up} \tag{4.6}$$

5. Turbocharger

The exhaust enthalpy is used to power the turbine which drive the compressor through the shaft. This will help increase the intake manifold pressure. This will result in a higher air density within the cylinders allowing for more fuel injection and engine downsizing.

The waste-gate and variable geometry turbines are the two actuators attached to the turbocharger to provide a fast dynamic air flow response and/or avoid over-boosting.

The modeling of the turbocharger is common for all modeling approached (distributed and lumped parameters models). It is base on the manufacturer data maps obtained from hot-gas test benches.

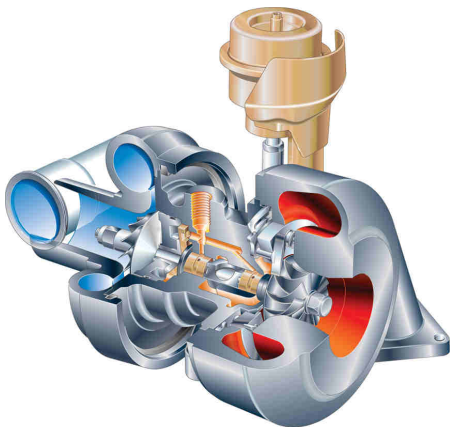

Fig. 4.3.: Turbocharger

5.1. Turbine

Whether for 0D or 1D models, the turbine and compressor are usually modeled based on the manufacturer data maps obtained on a stationary hot gas stand. These data maps relate four variables which are the mass flow, pressure ratio (or temperature), rotational speed and efficiency. Depending on the application, and whether it is an off-line simulation or series engine with available sensors, the input/output sets may differ. For an off-line simulation, the variable geometry turbine is:

$$\dot{m}_{t,corr} = \left(pos, N_{t,corr}, \frac{p_{up}}{p_{dn}} \right) \tag{4.7}$$

$$\eta_t = \left(pos, N_{t,corr}, \frac{p_{up}}{p_{dn}} \right) \tag{4.8}$$

The turbine mass flow will then contribute into the mass and enthalpy conservation of exhaust manifold, whereas the efficiency is used to calculate the turbine real power used to drive the compressor. The pos variable represents the nozzle position.

Usually, the data map of each fixed position is approximated using any of the available algorithms [52, 53, 54, 55, 56], and then the resulting model parameters are interpolated as a function of the valves geometry.

It is also necessary that temperature and pressure corrected quantities are used. This correction accounts for ambient differences between the hot gas test bench and the real engine operation conditions. Corrected quantities are calculated as:

$$N_{t,corr} = \frac{\sqrt{T_{ref}}}{\sqrt{T_{up}}} \qquad \dot{m_{t,corr}} = \dot{m} \cdot \frac{\sqrt{T_{up}}}{\sqrt{T_{ref}}} \cdot \frac{p_{ref}}{p_{up}} \tag{4.9}$$

Once these quantities are available, the available power from the turbine can be calculated as:

$$P_t = \dot{m}_t \cdot T_{up} \cdot \eta_T \left[1 - \left(\frac{p_{dn}}{p_{up}} \right)^{\gamma} \right] \tag{4.10}$$

The turbine discharge temperature can then be calculated as:

$$T_{dn} = T_{up} - \frac{P_t}{c_p \cdot \dot{m}_t} \tag{4.11}$$

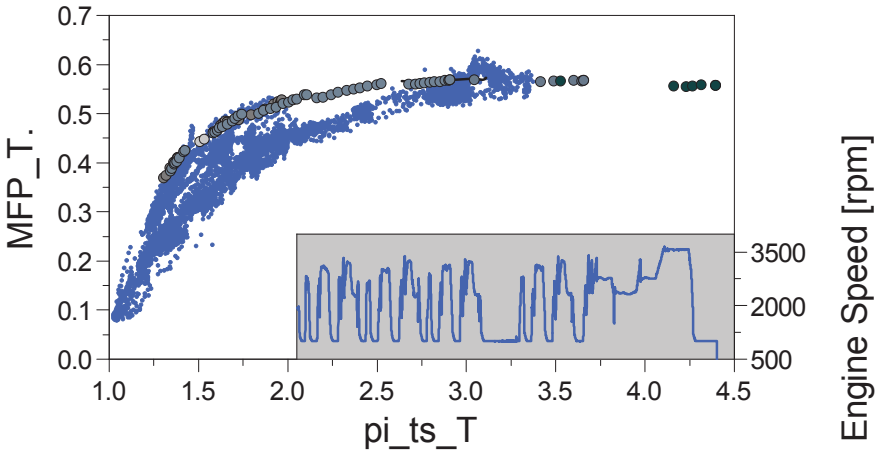

Fig. 4.4.: NEDC On turbine data map

Figure 4.4 shows a superposition of measured quantities and manufacturer data map of Mass Flow Parameter (MFP) and pressure ratio across the turbine. It is clear that data maps are not sufficient, and that it is necessary to interpolate and extrapolate these data maps. The following figure shows a possible interpolation and extrapolation using the algorithm proposed by Jensen et al. [52].

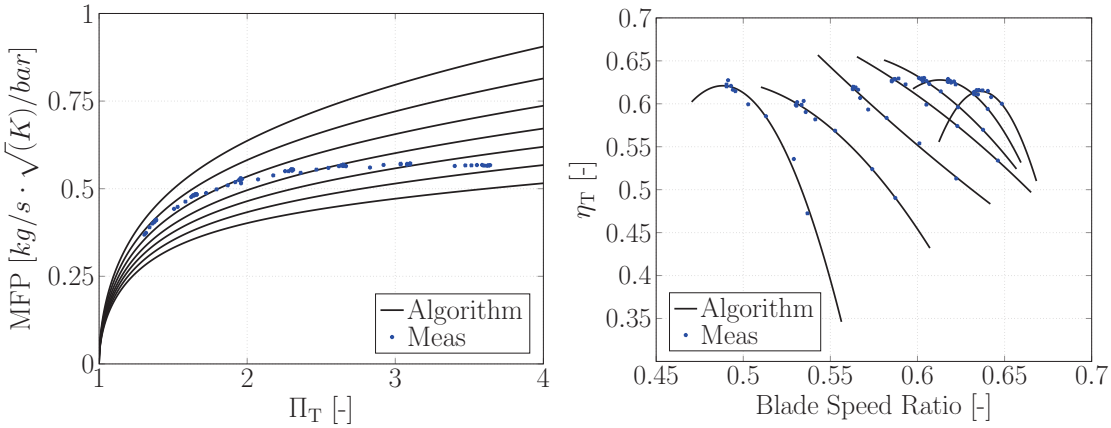

(a) Pressure Ratio Inter- and Extrapolation

(b) Efficiency Inter- and Extrapolation

Fig. 4.5.: Turbine data maps inter- and extrapolation

5.2. Turbocharger Shaft

The turbocharger shaft is defined by the power difference between the turbine, the compressor and any other mechanical and thermal losses. These losses are usually very difficult to account for using physical models and are taken into consideration

through an efficiency variable.

The turbocharger rotation speed is thus calculated as:

$$\frac{dN_{tc}}{dt} = K_I \frac{\eta_{tc} \cdot P_t - P_c}{J_{tc} \cdot N_{tc}} \tag{4.12}$$

Where K_I is a constant, and J_{tc} turbocharger inertia.

5.3. Compressor

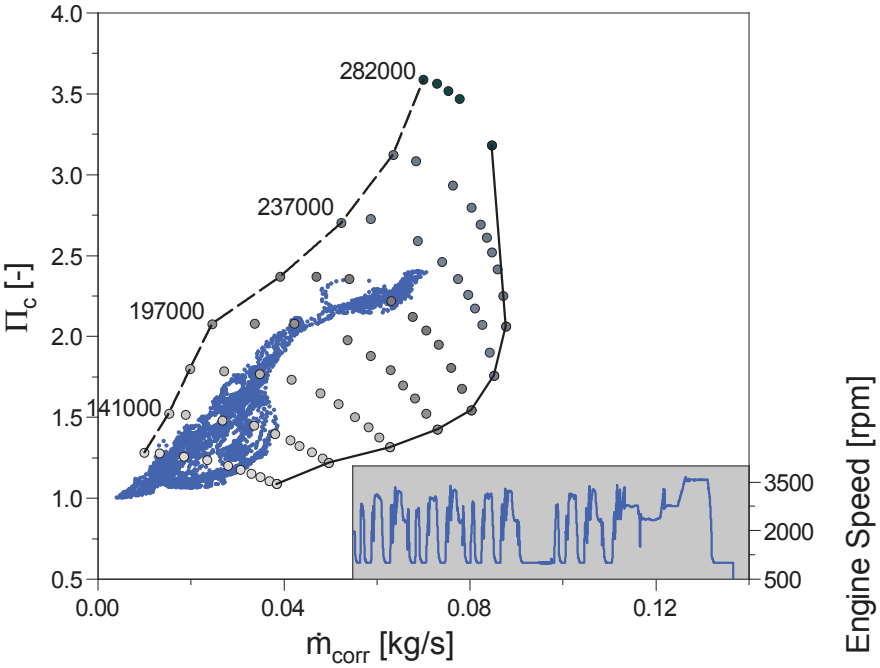

Fig. 4.6.: NEDC On compressor data map

The compressor is a very crucial component in engine modeling, as it provides one boundary which will define engine breathing efficiency. It is a very complicated component due to the complexity of the compression process taking place along the compressor stages. Hence, the compressor data maps has been widely used to model the compressor as full physical accurate model can only be obtained using 3D modeling.

Most of engine simulation models are based on performance maps provided by the manufacturer. These maps cover only a limited TC operating range by:

- The central area is the stable operating zone. This area is separated from the unstable area on its left by the surge line. When the mass flow rate through a compressor is reduced while maintaining a constant pressure ratio, a point arises at which local flow reversal occurs in the boundary layers. This should result in a low efficiency but not necessary in instability. If the flow rate is further reduced, complete reversal occurs. This will relieve the adverse pressure gradient until a new flow regime at a lower pressure ratio is established. The flow will then build up again to the initial condition and thus flow instability will continue at a fixed frequency.
- Surge line at low flow rate: this line represents the limits of the compressor stable operation. This limit depends on the compressor and its ducting
- Minimum measurable rotational speed: which is governed by poor measuring accuracy at low rotational speed. This is because compressor total pressure ratio, temperature difference and compressor mass flow rate decrease with decreasing rotational flow rate. This results in an increase in the measuring error
- Maximum measurable rotational speed which is restricted by the TC maximum allowable speed.
- Test rig resistance curve and/or compressor choking at high flow rate: represents the characteristics of the compressor ducting with a fully opened throttle valve.The area to the right of the compressor map is associated with the very high gas velocity. It is the result of shocking of the limiting flow area in the machine. Extra mass flow through the compressor can only be gained by higher speeds. This additional mass flow will certainly be limited by the ability of the diffuser area to accept the flow. When diffuser choking occurs, compressor speed may rise substantially with little increase in mass flow rate.
- The area of maximum efficiency naturally falls in the central stable operating zone. In practice, it tends to lie in an area roughly parallel to the surge line with vaneless-type diffusers and very close to the surge line in the case of vaned-type diffusers.

Similar to the turbine, the compressor modeling is also based on manufacturer data maps. This will be treated in detail in the next chapter.

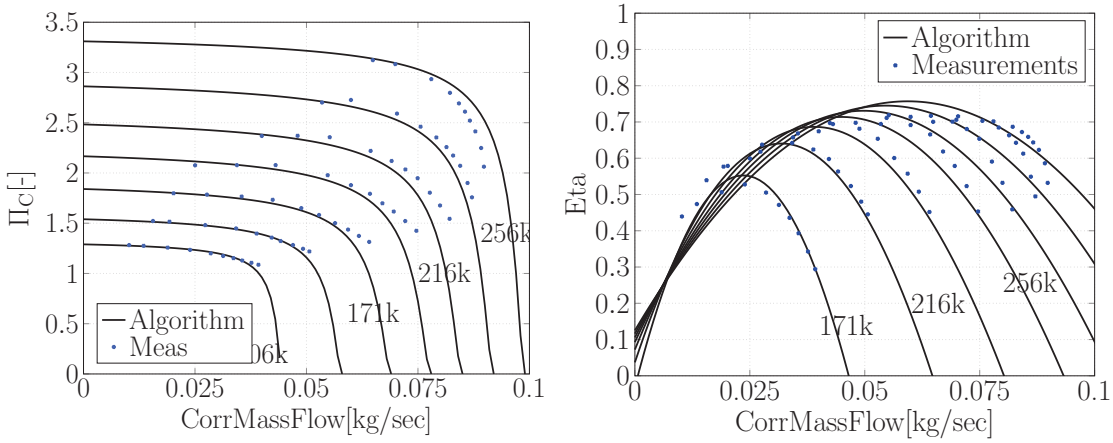

(a) Pressure ratio inter- and extrapolation

(b) Efficiency inter- and extrapolation

Fig. 4.7.: Compressor data maps inter- and extrapolation

6. Conclusion

In this chapter, various components of two air system have been presented and their models described. These models have been used for controllers design and on-line engine breathing estimation [52, 57, 53, 51]. These models are based on a decomposition of the engine air system into a network of control volumes (Lumped parameters models), modeled based on a mass and energy conservation. Due to this inherently simplistic approach, the high-frequency wave dynamics are neglected. Except the Manifold model, the remaining models are common between 0D and 1D modeling approaches.

These models will be assembled to provide an overall air system simulation in chapter

CHAPTER 5

COMPRESSOR MODEL OPTIMIZATION

Compressor models play a major role as they define the boost pressure in the intake manifold. These models have to be suitable for real-time applications such as control and diagnosis and for that, they need to be both accurate and computationally inexpensive. However, the models available in the literature usually fulfill only one of these two competing requirements. On the one hand, physics-based models are often too complex to be evaluated on line. On the other hand, data-based models generally suffer insufficient extrapolation features.

To combine the merits of these two types of models, this chapter presents an extended approach to compressor modeling with respect to thermo- and aerodynamic losses. In particular, the model developed by Martin et al. [55] is augmented to explicitly incorporate friction, incidence and heat transfer losses. The resulting model surpasses the extrapolation properties of data-based models and facilitates the generation of extended lookup tables.

In conclusion, the three main advantages of the developed approach are first, a high fitting quality resulting in accurate lookup tables for the real-time application, second, little measurement data are required and third, the identification process supports the high model accuracy.

1. Literature Overview

In the automotive industry, there is a certain consciousness that downsizing the internal combustion engine is one of the most effective means for reducing its carbon dioxide emissions and boost fuel efficiency. Downsized engines with a lower number of cylinders and displacement are lighter and have a low fuel consumption.

Legislation must be satisfied, but not at the expense of engine performance. Hence, with a lower displacement, the performance of the engine can be maintained by making

sure that more air will be aspirated into the combustion chamber to burn additional fuel. This is made possible by the turbocharger.

The overall engine modeling has evolved all along the engine development. Grondin et al. [51] presented a resume explaining that evolution. In order to understand, design and control the turbocharger, several models have been developed with different complexities. The turbocharger models can vary from simple data maps, up to 1D, 2D and 3D models, which can be heuristic or data-driven physical models [58, 59, 60, 61, 62, 63, 64]. In this paper, we focus on models dedicated to control design.

In Mean Value Engine Models (MVEM) as well as commercial 1D simulation tools, the compressor and turbine models rely basically on data maps supplied by the manufacturer. These data maps are used by interpolation and extrapolation algorithms, to generate more condense lookup tables by means of fitting either pure mathematical or physics based models. In the case of control strategies design, the turbocharger model is incorporated into a mean value engine model which have shown a great compromise between system dynamics prediction, computation complexity as well as memory costs. In [52], a complete MVEM is developed for a small Turbocharged Diesel Engine. Eight years later, Moraal and Kolmanovsky [54] presented a new interpolation technique which can be used to interpolate and extrapolate the manufacturer lookup tables. Dowell and Akehurst [65] suggested a faster mapping approach through the combination of spline and parametric methods.

In a recent work, Martin et al. [55] and then El Hadef et al. [66] incorporated the physics of the turbocharger into the modeling, as well as the interpolation/extrapolation methods. This is supposed to give a better guarantee for the quality of the fitted data, likewise the extrapolated one. However, and based on the measurements, it is observed that the fitting quality is not at its optimum due to the model linearity. Also, the treatment of the iso-speed lines is done individually (during model identification), and then, the identified parameters are interpolated. This identification strategy will automatically reduce the model accuracy.

The work presented here, will basically rely on Martin et al. [55] results and extend the current model, to also consider the main losses taking place over the compressor stages, mainly the inducer and the volute. This will result in a nonlinear model and a one-step identification for all iso-speed lines, which will enhance model fidelity.

This chapter is organized as follows: First, a brief explanation of compressor background is given, then reference compressor modeling algorithms are summarized. The new modeling approach is then explained, and finally comparison results between the reference and new model are stated.

2. Compressor Background

Compressor data maps usually come in the form of maps. The characteristics are often mapped at far greater speeds than would be run on engines (fig. 5.1: colored

region). The data are also taken at constant speeds. This implies that the data has to be extrapolated, to calculate the low speeds data (blue triangles), and interpolated, to calculate the non-supplied speeds (red circles). Figure 5.1 is a standard compressor data map, with real data from engine test bench superimposed.

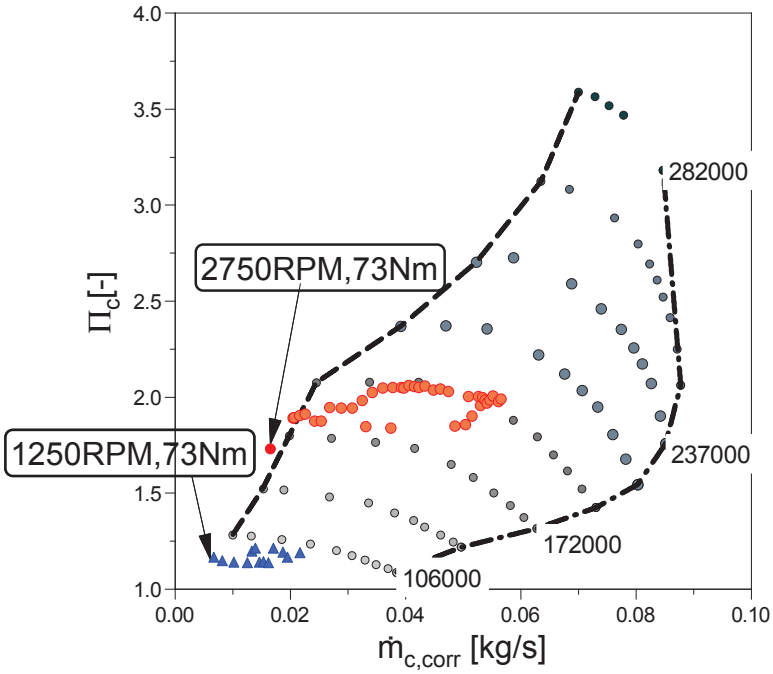

Fig. 5.1.: Superposition of two operating points measurements from a 2-cylinder diesel engine on the compressor data map

The transition between the engine operation points will automatically bring the need to interpolation, as the measured iso-speed lines are not dense enough. In addition, the overall volume between the compressor and the engine (valves, ducts and the intake manifold) is often not sufficient to damp the pressure fluctuations resulting from the intake valves movement. As for the low speed extrapolation, the mass flow and turbocharger speed will always start from zero to reach the measured zone. The lowest measured speed is imposed by the poor measuring accuracy as the mass flow, pressure ratio and temperature decrease as the rotational speed decreases [67], hence the need to extrapolation.

The ideal compression process is usually taken as a reversible adiabatic compression, whereas, in real compressors, the process is neither reversible nor adiabatic. This can be noticed through the compressor power (eq. (5.1) and eq. (5.2)), and is mainly due to the losses.

$$-\dot{W}_c = \frac{\dot{m}_c c_p T_{01}}{\eta_c}\left[\left(\frac{p_{02}}{p_{01}}\right)^{\frac{\gamma-1}{\gamma}} - 1\right] \tag{5.1}$$

$$\eta_c = \frac{\left(\frac{p_{02}}{p_{01}}\right)^{\frac{\gamma-1}{\gamma}} - 1}{\frac{T_{02}}{T_{01}} - 1} \tag{5.2}$$

3. Compressor Reference Modeling

In this section, the compressor fitting algorithm from Jensen et al. [52] and El Hadef et al. [66] are restated, as it will be used as a reference for comparison.

For the pressure ratio, the same model presented in [52] is used, where the modeling principle is as follows:

- The compressor work is expressed in terms of a dimensionless head parameter which is the ratio of the energy required to raise the pressure, and the kinetic energy of the compressor

$$\psi_c = \frac{c_p \cdot T_{01} \cdot \left((p_{02}/p_{01})^{\frac{\gamma-1}{\gamma}} - 1\right)}{1/2u_c^2} \tag{5.3}$$

- A dimensionless flow rate is calculated from the measured mass flow and a theoretical flow rate through the compressor

$$\phi_c = \frac{\dot{m}_{c,corr}}{\rho_a \pi r_c^2 u_c} \tag{5.4}$$

- Equation (5.5) is used to relate the above two dimensionless parameters:

$$\psi_c = \frac{A + B \cdot \phi_c}{C - \phi_c} \tag{5.5}$$

- The models can be improved when the parameters in eq. (5.5) are taken function of the rotational speed.
- Once the parameters in eq. (5.5) are fitted, it can be interpolated and extrapolated to get the pressure ratio as a function of mass flow and rotational speed.

Simulation results for the pressure fitting are given in this section in fig. 5.2 as no comparison is performed for the pressure ratio, and the same model is partially used by the improved and base algorithms. Simulation results for the enthalpy and efficiency are presented in the Results section.

3.1. Discussion

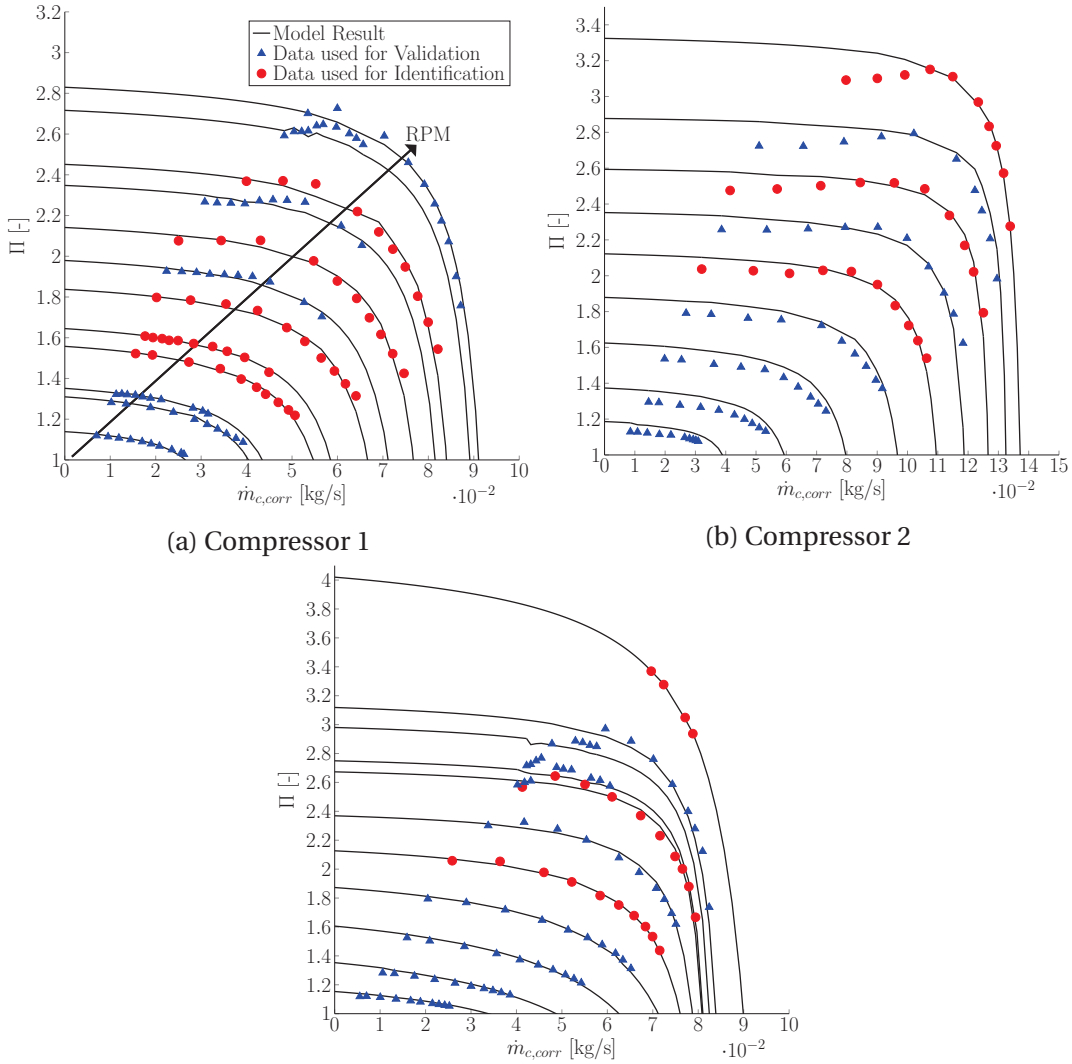

(a) Compressor 1

(b) Compressor 2

(c) Compressor 3

Fig. 5.2.: Pressure ratio approximation

- The model accuracy degrades for high speeds in the extrapolated area. This can be due to the fact that eq. (5.5) is based on observation and the lack of physics.
- The current work scope is the enthalpy model. Hence, this pressure ratio method is kept as it is used by Martin et al. [55] as well.

The efficiency fitting algorithm is resumed in fig. 5.3

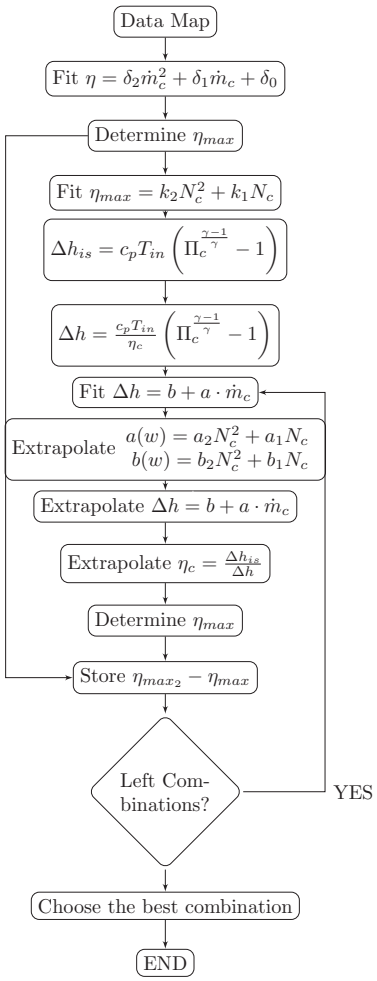

Fig. 5.3.: Compressor efficiency algorithm from [66]

In Δh calculation, it is suggested in [66] that the parameters a and b are second order polynomials function of the turbocharger speed:

$$a, b = k_2 N_{tc}^2 + k_1 N_{tc} + k_0 \tag{5.6}$$

One can also notice that the flowchart in fig. 5.3 is based on an iterative procedure to identify the enthalpy model parameters. This will be overcome in the new algorithm.

The reader is referred to [52, 66] for details on the previous algorithms and to section 5 for the linear enthalpy model.

4. Euler Equation for Turbo-machines

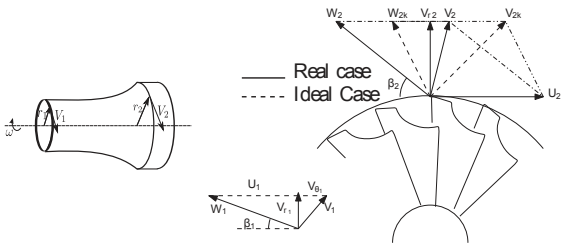

Fig. 5.4.: Euler equation for turbo-machines

With reference to Fig. 5.4, Hanlon [68] consider a rotor belonging to a generic turbo-machine, taking into examination the conditions existing in section 1 (inlet) and section 2 (discharge). Utilizing the equation of balance of momentum for the stationary flow between two sections, it is possible to obtain:

$$\tau = m\left(r_2 \cdot V_2 - r_1 \cdot V_1\right) \tag{5.7}$$

The work transferred through the blades per mass unit of fluid processed is thus given by:

$$W = \tau\omega/m = \omega\left(r_2 \cdot V_2 - r_1 \cdot V_1\right) \tag{5.8}$$

The 1^{st} principle of thermodynamics establishes that the work per mass unit is equal to, for an adiabatic flow, the variation in total enthalpy.

$$\begin{aligned}\Delta h_{0,1-2} &= h_2 - h_1 \\ &= \omega\left(r_2 \cdot V_2 - r_1 \cdot V_1\right) \\ &= U_2 \cdot V_2 - U_1 \cdot V_1\end{aligned}$$

5. Enthalpy Linear Model

Using the vector triangle equality, we get:

$$\Delta h = U_2^2 - U_2 V_{r2} cot\left(\beta_2\right) \tag{5.9}$$

and since

$$V_{r2} = \frac{\dot{m}_c}{\rho \cdot S_{rot}} \tag{5.10}$$

with S_{rot} being the effective area through which mass flows.
Then:

$$\begin{aligned}\Delta h &= U_2^2 - U_2 \frac{\dot{m}_c}{\rho \cdot S_{rot}} cotan\,(\beta 2) \\ &= U_2^2 \left[1 - \frac{\dot{m}_c}{\rho \cdot S_{rot} \cdot U_2} cotan\,(\beta 2)\right] \\ &= U_2^2 \left[a' + b' \cdot \dot{m}_c\right]\end{aligned}$$

hence, for a constant rotational speed, one can write:

$$\Delta h = a + b \cdot \dot{m}_c \tag{5.11}$$

6. New Model Basic Equations

In this section, the main hypothesis and development steps of the extended model are presented. As previously mentioned, the main extension is based on losses. Hanlon [68] stated that the dominant losses for the compressor are those due to friction and incidence. These are the main losses taken into consideration in the developed new model and are stated in the following subsections.

6.1. Pressure Drop Due to Friction

Hanlon [68] defines it as being the dissipation terms associated with friction phenomena between the walls of the machine ports (both rotor and stationary) and fluid flowing through it. In general, the flow in compressors is characterized by turbulence, so it can be considered that the energy dissipated is proportional, in first approximation, to the square of the fluid velocity and thus to the square of the volume flow in inlet conditions. This energy is not transferred to the gas under the form of potential energy, but only as heat. In [68], Hanlon stated that the work per mass unit associated with dissipation due to friction can be given by:

$$W_f = k_f {\dot{m}_c}^2 \tag{5.12}$$

where k_f represents a suitable constant that takes account of the specific fluid dynamic characteristics.

In [69], the friction work is given by:

$$W_f = 4f\frac{l}{D}\frac{\dot{m_c}^2}{2} \tag{5.13}$$

which reduces to eq. (5.12) if one defines a hydraulic diameter and an equivalent length.

In [63], Bozza and De Bellis developed a 1D model to simulate the compressor. The authors took into account the friction losses directly in the flow equation through the definition of a friction coefficient f, depending on the local velocity based Reynolds Number. The factor f is calculated as:

$$f = x_f \cdot 0.01 \cdot \left(\frac{1.8e5}{Re_L}\right)^{0.2} \tag{5.14}$$

x_f being a tuning constant, and Re the Reynolds Number.

The use of the above expression requires local Re estimation, and hence the consideration of the space dimension. In our case, we can only use a global expression, as we do not have access to any local flow characteristics, and so, we will be using eq. (5.12):

$$\Delta h_f = k_f \dot{m_c}^2 \tag{5.15}$$

6.2. Pressure Drop Due to Incidence

In [68], Hanlon stated that pressure losses due to incidence depend merely on the geometry of the blade, and on the speed triangle immediately upstream of the blade leading edge. These losses can be approximated by eq. (5.16).

$$\Delta h_I = k_2 \left(\dot{m_c} - \dot{m_c}^*\right)^2 + k_0 \tag{5.16}$$

where the constants k_2 and k_0 are once again related to the particular problem treated.

6.3. Heat Losses

If we consider the overall compressor as a simple pipe then, the convective heat transfer between the gas and the compressor material can be approximated in stationary state using :

$$\dot{q} = \dot{m_c} \cdot c_p \cdot dT = \alpha \cdot \pi \cdot D \left(T_{gas,init} - T_{wall}\right) dx \tag{5.17}$$

Integrating and solving for the gas exit temperature:

$$T_{gas,out} = T_{wall} + (T_{gas,init} - T_{wall}) \cdot e^{-(\alpha \cdot \pi \cdot D \cdot L)/(c_p \cdot \dot{m}_c)} \tag{5.18}$$

Setting:

$$\begin{cases} Cst = -\frac{\alpha \cdot \pi \cdot D \cdot L}{c_p} \\ x = \frac{1}{\dot{m}_c} \\ (T_{gas,init} - T_{wall}) = \Delta T_{init} \end{cases}$$

yields:

$$T_{gas,out}(x) = T_{wall} + \Delta T_{init} \cdot e^{Cst \cdot x} \tag{5.19}$$

A Taylor's series expansion around $x = 0$ of the eq. (5.19) is:

$$\begin{aligned} \tilde{T}_{gas,out}(x) &= T_{wall} + \sum_{n=1}^{+\infty} \frac{T_{gas}^{(n)}(x)}{n!} x^n \\ &= T_{wall} + Cst \cdot \Delta T_{init} \cdot x + Cst^2 \cdot \frac{\Delta T_{init}}{2} \cdot x^2 + ... \\ &= T_{wall} + Cst \cdot \Delta T_{init} \cdot \frac{1}{\dot{m}_c} + Cst^2 \cdot \frac{\Delta T_{init}}{2} \cdot \frac{1}{\dot{m}_c^2} + ... \end{aligned}$$

Since the overall enthalpy variation due to heat transfer is given by:

$$\Delta h_{HL} = c_p \cdot \Delta T_{HL} \tag{5.20}$$

where the subscript HL stands for $Heat\ Loss$, the change in enthalpy due to heat transfer is approximated as:

$$\begin{aligned} \Delta h_{HL} = c_p \cdot \Big[& T_{wall} - T_{gas,Init} + Cst \cdot \Delta T_{init} \cdot \frac{1}{\dot{m}_c} \\ & + Cst^2 \cdot \frac{\Delta T_{init}}{2} \cdot \frac{1}{\dot{m}_c^2} + ... \Big] \end{aligned} \tag{5.21}$$

It will be shown in the Results section that truncating eq. (5.21) at $\frac{1}{\dot{m}_c}$ is sufficient for model accuracy within the compressor operating range. Thus, we suggest to take the

heat transfer into account using eq. (5.22)

$$\Delta h_{HL} = k_{HL,0} + k_{HL,-1} \cdot \frac{1}{\dot{m}_c} \tag{5.22}$$

The term $\frac{1}{\dot{m}_c}$ can be explained through the entropy-enthalpy diagram as well. This diagram is given in fig. 5.5 where the contribution of each stage in the centrifugal compressor to the pressure raise is shown. The stages numbering is given in fig. 5.6. Along the impeller stage, kinetic energy is added to the air by means of the work performed. This energy will then be partially converted to pressure by decelerating the air along the volute and collector. The amount of energy transfer by the impeller wheels to the air will depend on the rotational speed, however, the pressure raise along the volute and collector will merely depend on the flow nature. Ideally, one aims at a minimum entropy variation Δs so the Δh is higher, and so is the exit pressure. This is shown in fig. 5.5.

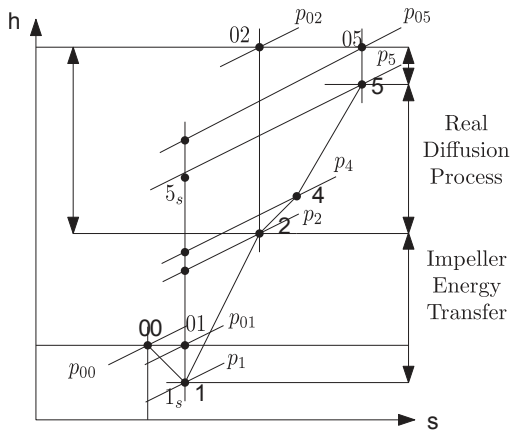

Fig. 5.5.: h-s diagram for a centrifugal compressor.The stages numbering is given in fig. 5.6.

6.3.1. Note on Losses Consideration

The Euler Turbo-machinery Equation is given in eq. (5.23).

$$\Delta h = U_2 V_{\theta 2} - U_1 V_{\theta 1} \tag{5.23}$$

Equation (5.23) considers the fluid states at the entry and exit of the impeller. It gives an estimation of the work done on the fluid by the shaft in an ideal situation without any losses. For automotive turbocharger compressor, it can be seen that the dimensions of diffuser and the volute are greater then the impeller size. This can be seen in the fig. 5.6

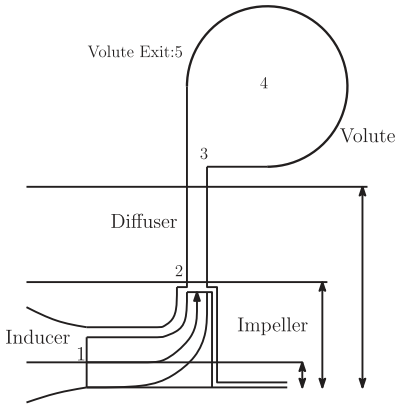

Fig. 5.6.: Main compressor stations

This makes the contribution of the two last stages (diffuser and volute) also significant in the final air state at the compressor exit. In addition, the developed model is an overall model comprising all compressor stages; hence, it is not very sensitive to local phenomena as long as the overall compressor behavior is simulated correctly.

7. Overall Model

The overall losses model can be obtained by summing eqs. (5.12), (5.16) and (5.22) and it resumes to :

$$\begin{aligned}\Delta h_{OL} &= \Delta h_f + \Delta h_I + \Delta h_{HL} \\ &= k_A \dot{m_c}^2 + k_U \left(\dot{m_c} - \dot{m_c}^*\right)^2 + k_0 \\ &+ k_{HL,0} + k_{HL,-1} \cdot \frac{1}{\dot{m_c}}\end{aligned} \tag{5.24}$$

Where Δh_{OL} represents the enthalpy variation due to the overall losses. Regrouping terms, yields:

$$\Rightarrow \Delta h_{OL} = k_2 \dot{m_c}^2 + k_1 \dot{m_c} + k_0 + k_{-1} \cdot \frac{1}{\dot{m_c}} \tag{5.25}$$

hence, the real specific enthalpy can be obtained through the combination of equations 5.11 and 5.25 and is given by:

$$\Delta h = a_2 \cdot \dot{m_c}^2 + a_1 \cdot \dot{m_c} + a_0 + a_{-1} \cdot \frac{1}{\dot{m_c}} \tag{5.26}$$

The parameters a_2 , a_1 , a_0 , a_{-1} are given by:

$$a_2 = a_{12}N_{tc}^2 + a_{11}N_{tc} \tag{5.27}$$
$$a_1 = a_{23}N_{tc}^3 + a_{22}N_{tc}^2 + a_{21}N_{tc} \tag{5.28}$$
$$a_0 = a_{32}N_{tc}^2 + a_{31}N_{tc} \tag{5.29}$$
$$a_{-1} = a_{42}N_{tc}^2 + a_{41}N_{tc} + a_{40} \tag{5.30}$$

The above parameters dependency on the rotational speed is pure data-based. The polynomials order is obtained using trial and error from one compressor data, and then kept constant for all compressors. It is very important to consider this dependency, as the rotational speed defines the flow nature and vector triangles as well. The advantage of physics-based models with respect to data based model is the accuracy even for extrapolation. This can be seen in the results in the comparison between the model from [66] and the new model in fig. 5.7.

7.1. Note on the Model Identification

The parameters a_{ij} in the model can be identified using any optimization algorithm for a least square method. If we consider P the vector of parameters a_{ij} and X the vector with entries $(N_{tc}^i \cdot \dot{m}_c^j)$, we can formulate the model as:

$$\Delta h = X \cdot P \Rightarrow P = \left(X^T \cdot X\right)^{-1} \cdot X^T \cdot \Delta h \tag{5.31}$$

Care must be taken to avoid the use of badly conditioned matrices.

8. Results

A comparison between the new and old models is presented in fig. 5.7. For the model identification and validation, three different compressors have been used for the model validation. The main compressors characteristics are given in table 5.1

Table 5.1.: Geometric characteristics of the compressors used for model identification and validation

	Blades #	diameter [mm]	Engine
Compressor 1	12	38	Diesel
Compressor 2	8	37	Gasoline
Compressor 3	12	40	Gasoline

Compressor 1 will be used as an example to study the dependency of the model on the selected iso-speed lines for the parameters identification, where different combinations are selected.

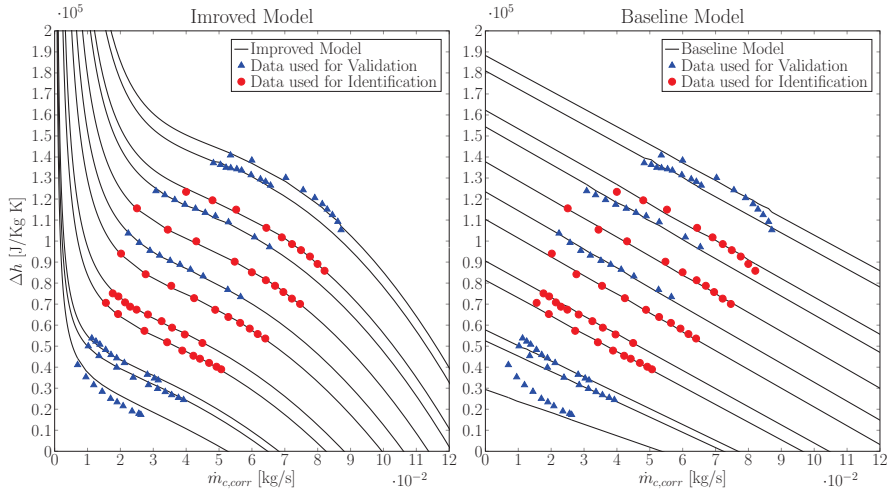

(a) Compressor 1

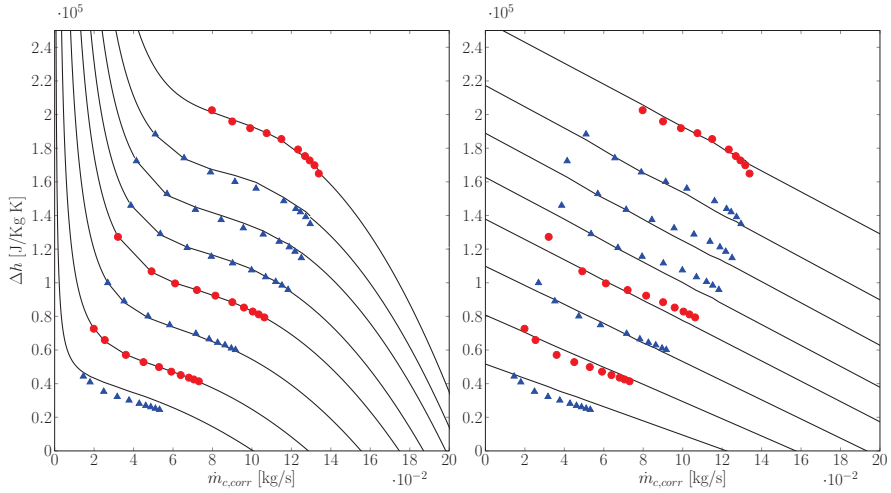

(b) Compressor 2

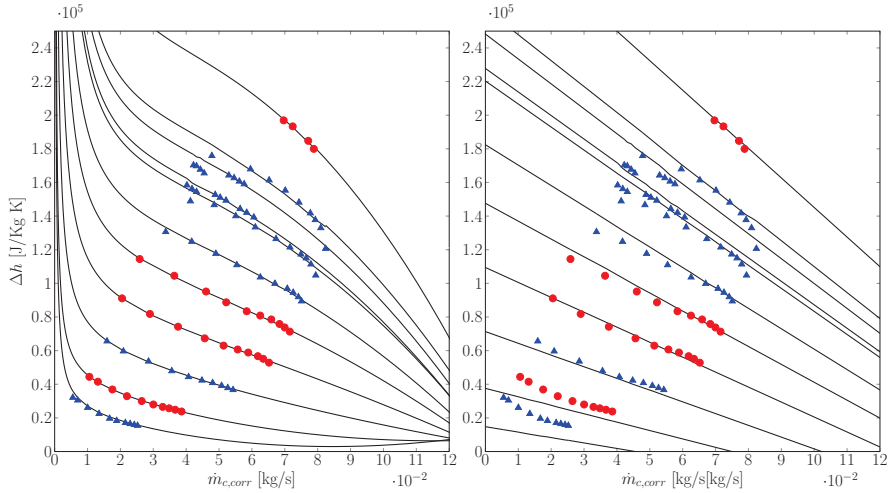

(c) Compressor 3

Fig. 5.7.: Comparison between the new and old models approximation: despite the use of a partial set of the measurements for the identification, the new model shows a better fitting quality for both interpolation and extrapolation

8.1. Remark

It is important to point out that less then half of the available data was used for the parameters identification ($\approx 30\%\_only$) (scattered data in red circles). Data in the lower speeds are completely extrapolated and validated as well as interpolated data (filled blue triangles). This can be considered as an additional constraint to test the model validity, as pure-data based models will most of the time give a wrong approximation once tested outside the data used for identification, whereas for physics-based models, they can still be accurate in the extrapolation area, as long as the physics used in the model development is still applicable.

8.2. Discussion

The model parameters were identified for the available compressors and are given in the following table:

Table 5.2.: Identified model parameters for the three test case compressors

Parameter	Compressor 1	Compressor 2	Compressor 3
a_{12}	$-2.2527e-07$	-0.0018	-0.0063
a_{11}	-0.2256	-4.3208	16.3108
a_{23}	$-7.9340e-12$	$-1.9912e-06$	$7.6284e-07$
a_{22}	$7.3315e-06$	0.0304	0.0068
a_{21}	-0.7406	-46.2380	-34.4675
a_{32}	$-1.5237e-06$	-0.0191	0.0049
a_{31}	0.5127	54.6206	13.5556
a_{42}	$1.6221e-06$	0.0205	0.0020
a_{41}	-0.2766	-60.3805	-5.4679
a_{40}	$1.3629e+04$	$4.6175e+04$	$5.0907e+03$

eqs. (5.27) to (5.30)are restated here for clarity:

$$a_2 = a_{12}N_{tc}^2 + a_{11}N_{tc} \tag{5.32}$$
$$a_1 = a_{23}N_{tc}^3 + a_{22}N_{tc}^2 + a_{21}N_{tc} \tag{5.33}$$
$$a_0 = a_{32}N_{tc}^2 + a_{31}N_{tc} \tag{5.34}$$
$$a_{-1} = a_{42}N_{tc}^2 + a_{41}N_{tc} + a_{40} \tag{5.35}$$

It can be seen that the parameters of compressors 2 and 3 can be considered close to each other, however, parameters from compressor 1 are very different. This can be due to the fact that both compressors 2 and 3 are for a gasoline engine; however, compressor

1 is for a diesel. This similarity is also observed in fig. 5.7.The main comparison results are listed below:

- By taking a minimum amount of data for the model parameters identification, it is clear that the extended model shows a higher flexibility and a better fitting.
- Once the mass flow tends towards zero, there is an increase in the extrapolated enthalpy. The same behavior was obtained by a 1D simulation performed by Bozza and De Bellis [64] and published in 2011. This can be, in this current work, due to the truncation of the Taylor Series approximation of the exponential term in the gas temperature variation due to heat transfer between the gas and the material. An increase of the enthalpy variation can still be expected, as the residence time will increase due to the decrease of the mass flow. This will allow a maximum heat transfer between the gas and the material.
- The enthalpy variation for higher mass flows tends toward zero. This can be due to choking where the maximum mass flow is reached and a rapid, abrupt decrease in the performance of the compressor will take place.
- The main difference between the two models and algorithms lies in the model structure as well as the parameters identification. In the algorithm presented by El Hadef et al. [66], the iso-speeds are treated separately, and then the model parameters are identified. If a minimum amount of data is selected, it can be insufficient to capture the shape of the measured iso-speed data. In the new algorithm however, the model parameters are identified once and only once, for the complete data set.
- It is known that heat flux from the turbine to the compressor can be negligible for high compressor speeds. This makes heat losses along the compressor dominating for those speeds, and this can be seen through the nonlinear shape of the high iso-speed enthalpy lines.

9. Overall Algorithm

The final algorithm is resumed in the flowchart in fig. 5.8 and the simulation results are shown in fig. 5.9

9.1. Discussion

- Because the pressure ratio estimation is the same for both algorithms, all differences between the models simulation results are reported to the enthalpy estimation models.
- Results based on the new model show a minimum error compared to the model from El Hadef et al. [66] especially for the low speeds.

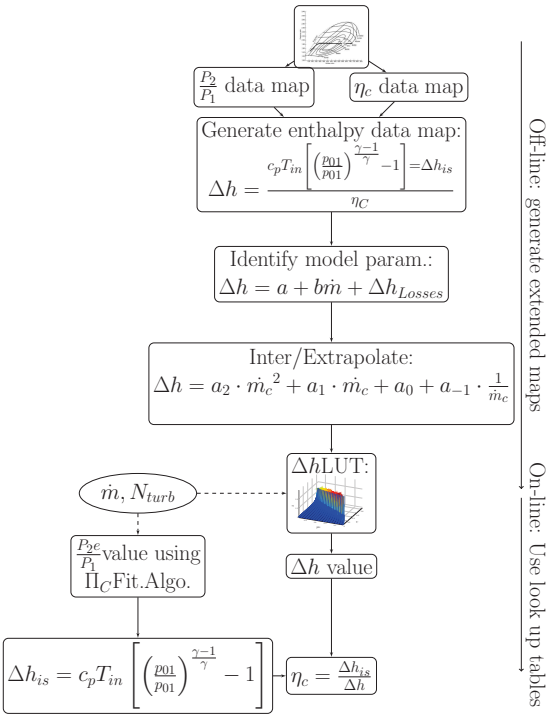

Fig. 5.8.: Overall Interpolation and Extrapolation Algorithm

- Although the new model showed a good fitting for the enthalpy estimation, one can still notice an error in the efficiency (this error is present in both models). This is mainly due to the pressure estimation, as the model used by Jensen et al. [52] is not physically based, but rather on observation.

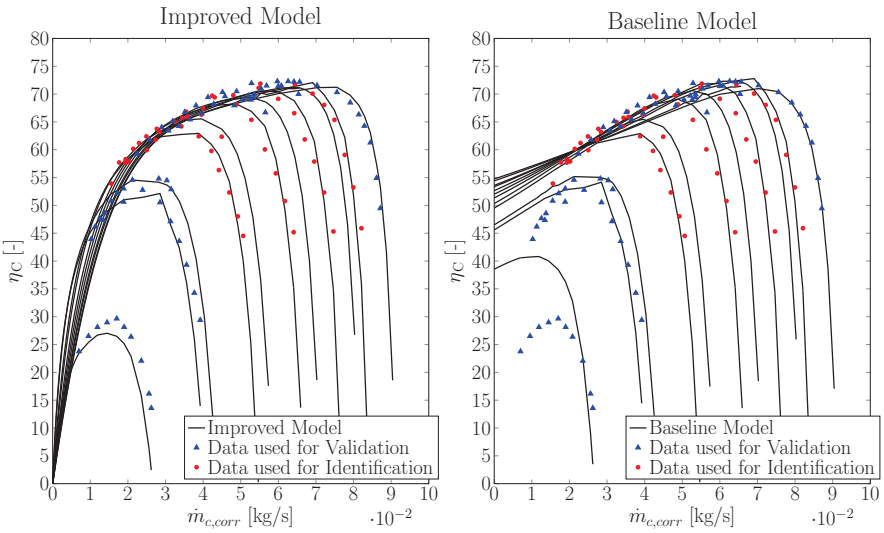

(a) Compressor 1

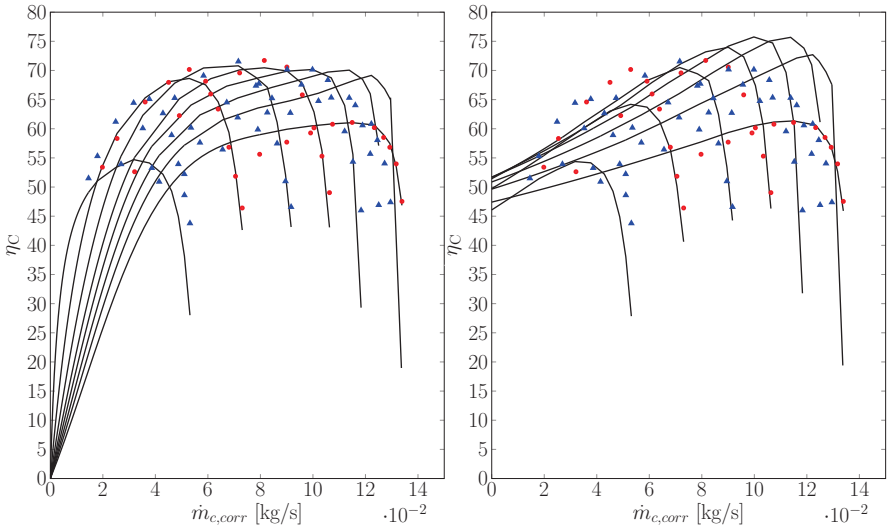

(b) Compressor 2

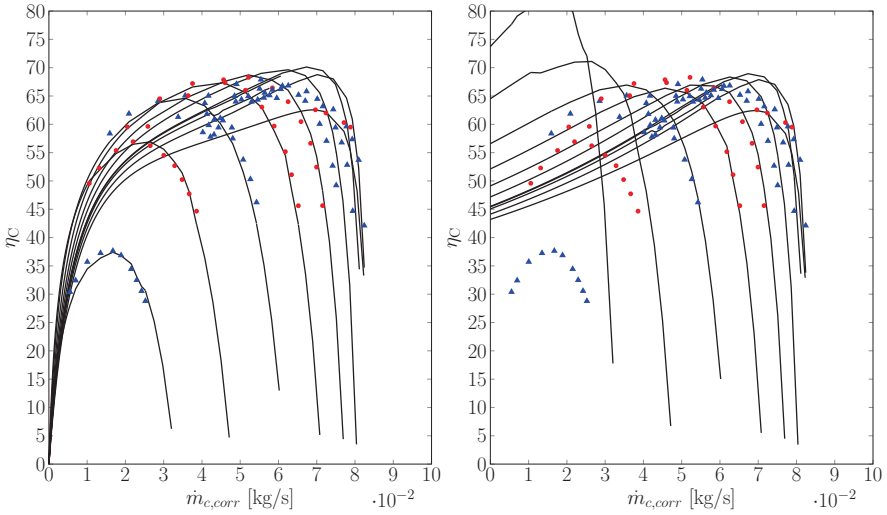

(c) Compressor 3

Fig. 5.9.: Comparison between the new and old models approximation: Manufacturer data is split into data used for identification (circles), and the rest for model validation (filled triangles). Left: New Model, Right: Linear Model

10. Conclusion

A new enthalpy model for the turbocharger compressor has been developed and validated in the current work. The model showed a better accuracy, even when strict constraints are imposed on the parameters' identification. The model can predict data outside the identification field, provide more accuracy for control models and reduce the measurements time. Sensitivity analysis was also performed to show the model dependency on the data considered for identification.

Slight deviations are still observed, and are reported to the following aspects:

- Lack of physics in the pressure estimation model.
- The mathematical approximation of the enthalpy variation due to heat transfer.
- The use of simple polynomials to consider the parameters' dependency on the rotational speed.

CHAPTER 6

EXPERIMENTAL VALIDATION

The previous chapters have presented the full 1D continuous models, some numerical schemes as well as low order models. The 1D models have been validated using the numerical shock tube test bench and the acoustics test bench. They then were used as a reference for the validation of the low order models.

It is now necessary to test the validity and accuracy of these models on the combustion engine. To test under engine-like conditions, the intake path of a virtual one cylinder engine implemented in GT-Power® and a production two cylinder engine are used.

Before performing a complete air system simulation, only a duct along the intake path will be implemented using the different approaches. This will give the possibility to correlate all the differences to these models. Based on the results, the air-system is completely simulated and compared finally to reference measurements.

The difference in the geometry of the two engines and the different number of cylinders will result in different acoustic effects. This will give the possibility to better assess the modeling approaches.

1. Validation on the Virtual 1-Cylinder Engine

First, a virtual engine implemented using GT-Power® was used to assess the previous models in the modeling of the air flow in the intake path. The simple geometry will enable a better assessment for the capacitive and inertial properties of the different approaches.

Results in this section will compare reference results using GT-Power® to the CE-SE, QPM and MTF (Method of Transfer Function) methods. The latter is presented in the Appendix.

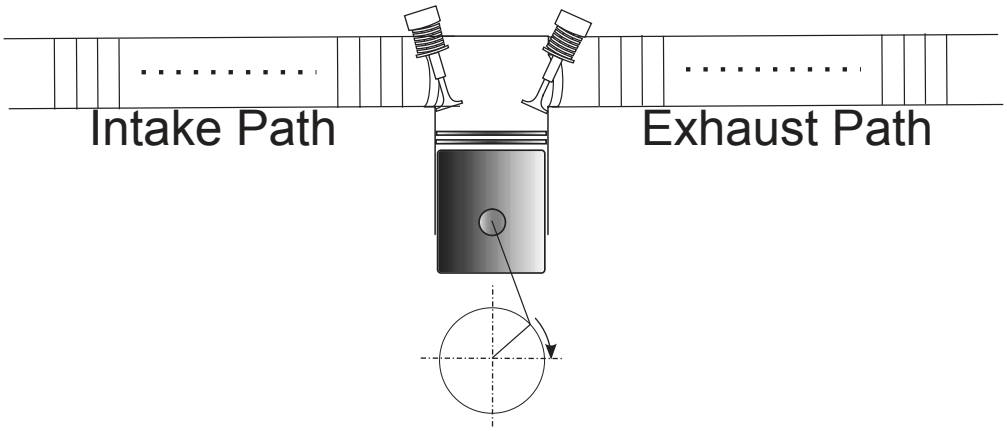

Fig. 6.1.: Schematic of the virtual 1-cylinder engine

To properly assess the previous ducts models, we will simulate only the intake duct using the previous methods. The rest of the system (intake valve + cylinder+ Exhaust path) will be simulated using GT-Power®.

A Co-simulation is performed where the intake path will be simulated by the previous methods under Simulink®. In the case of the CE-SE, a routine is implemented to drive the Simulink® solver according to the CFL condition. The pressure, temperature and mass flow at 0.14 m before intake valve are given in figs. 6.2 to 6.4

1.1. Results

Results are shown in figs. 6.2 to 6.4 for speeds of 2000, 4000 and 6000 RPM. As previously mentioned, GT-Power is used to get the theoretical reference results.

The valve's opening will initiate a mass flow towards the cylinder and a decrease in the local pressure. After the valve's closure, the initiated wave will travel back and forth until the next valve opening. Due to the simplicity of the system, all differences will be linked to the models analyzed.

There is an over estimation in the mass flow and pressure for both CE-SE ($\Delta x = 40\,mm$, $\alpha = 2$ and $CFL = 0.8$) and MTF ($\Delta x = 40\,mm$). The main reason is primarily the treatment of the boundary conditions and the interface with GT-Power. The numerical scheme CE-SE has been shown to be mass conservative using shock-tube simulations, but can have a small off-set relative to the real mass content.

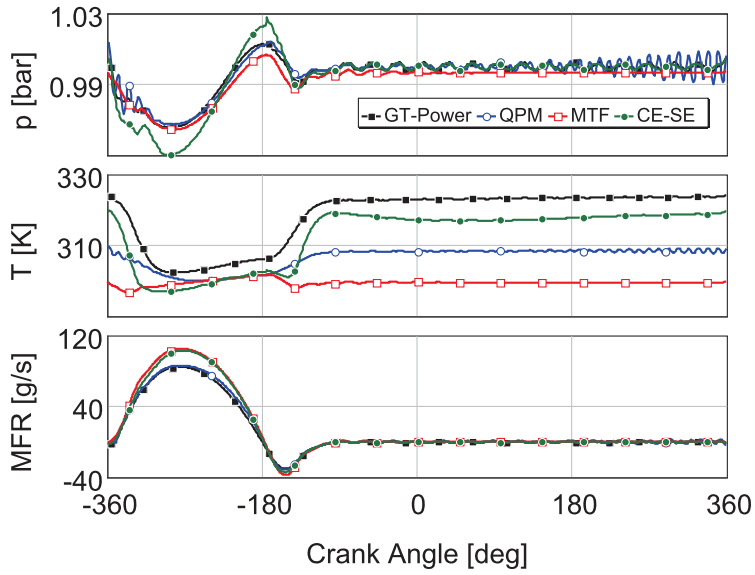

Fig. 6.2.: Predicted pressure, temperature and mass flow rate for 2000 RPM for the 1-Cylinder engine

The main differences observed are in the temperature, which has an impact on the wave propagation speed. This difference is constant for the MTF regardless of the rotational speed. This can be expected, since the MTF is based on the conservation of mass and momentum only, hence the effect of the non-homentropic flow is more apparent. Although in this case no geometry variations were considered, friction and heat transfer were present.

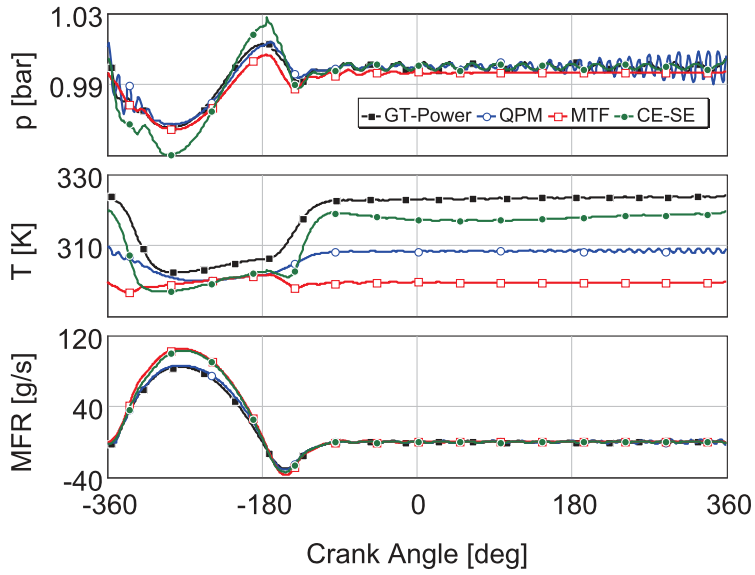

Fig. 6.3.: Predicted pressure, temperature and mass flow rate for 4000 RPM for the 1-Cylinder engine

This over estimation is also observed in the pulsation frequency. An over estimated temperature results in an overestimated speed of sound. This will result in a higher pulsating frequency.

Despite its simplicity, the quasi-propagatory model reproduces almost the same results as the full models, except for high frequency pressure fluctuations. The pulsation frequency seems to be well fitted using the QPM. However, in this case the duct length has been multiplied by a coefficient to obtain the correct pulsating frequency and optimized for higher speeds. This virtual length is dependent on the operational speed, and for this reason, for a speed of 2000 RPM, this length is smaller than the effective length, which results in higher frequencies when the intake valve is closed. Only one branch has been used.

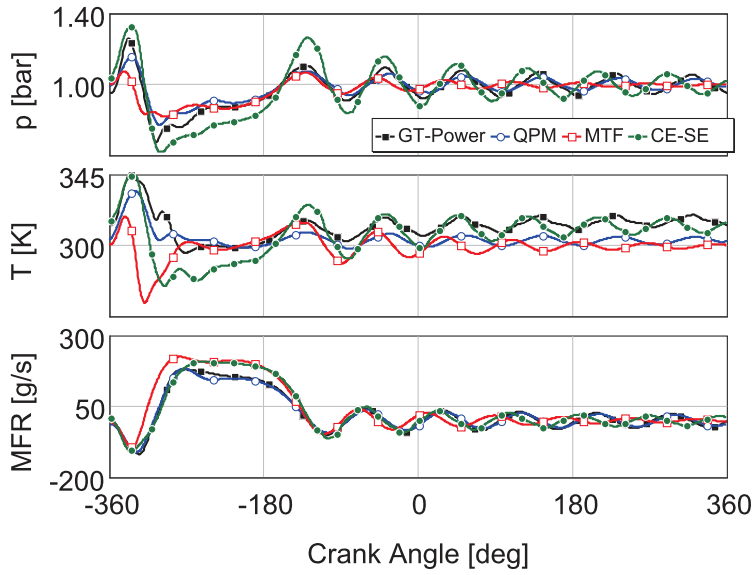

Fig. 6.4.: Predicted pressure, temperature and mass flow rate for 6000 RPM for the 1-Cylinder engine

All three methods show a good accuracy for the different operation points considered which will be confirmed within the next section as well. Using a space discretization of 40 mm for the CE-SE and MTF, and one branch for the QPM, the calculation time of the different approaches has been normalized with respect to CE-SE and is given in fig. 6.5.

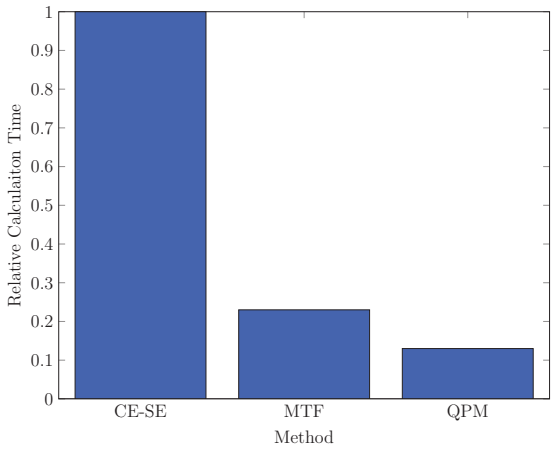

Fig. 6.5.: Relative calculation time

2. Validation of Ducts Models on the 2-Cylinder Engine

Similar to the previous test case, the former models have been applied using Simulink / GT-Power co-simulation in order to simulate a test made upon the intake system of a two cylinder turbocharged engine.

The complex geometry between the compressor and air cooler (fig. 6.7) has been modeled in Simulink. This geometry contains different bends and materials but has been approximated as one single pipe to reduce the computational time. For an accurate reference, the detailed geometry has been considered in GT-Power. In this work, two types of test benches have been used, and are briefly described in the following:

2.1. The Experimental Setup

Model validation tests were performed at the Robert Bosch GmbH engine test cells. The experiments were conducted on a 2 cylinder 1.2 liter standard production turbocharged diesel engine. A dynamometer coupled to the engine using a compliant shaft can be controlled to impose a specific load torque on the engine.

Both crank angle resolved measurements of pressure, temperature, mass flow and rotational speeds.

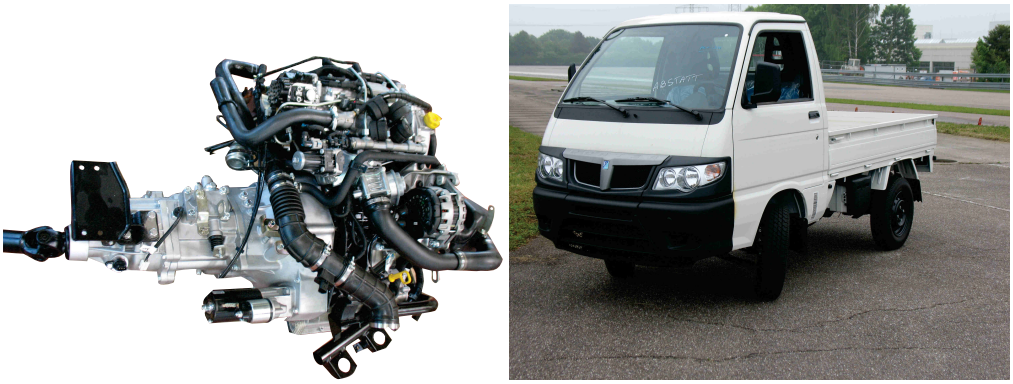

Fig. 6.6.: Engine test bench

Table 6.1.: Geometric characteristics of the two cylinder diesel engine

Cylinders	2 Inline
Displacement	1.2L
Bore x Stroke	87x101mm
Compression	17.5:1
Valves	4/Cylinder

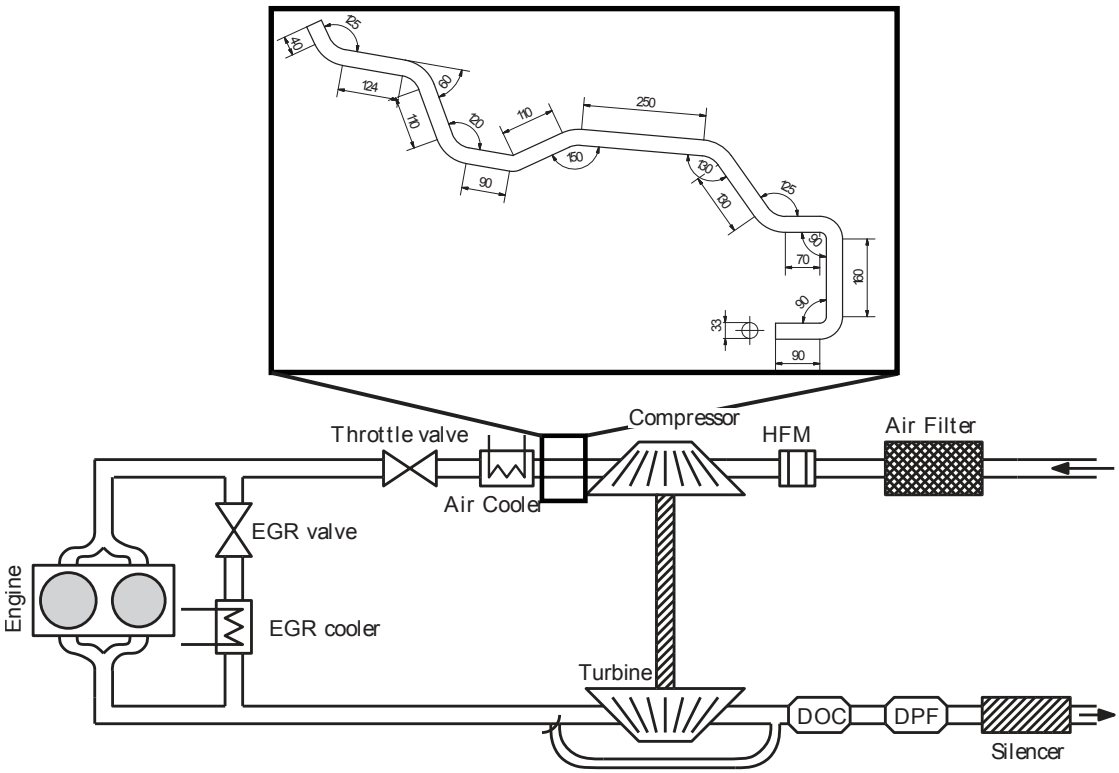

Fig. 6.7.: Schematic of the air system

2.2. Results

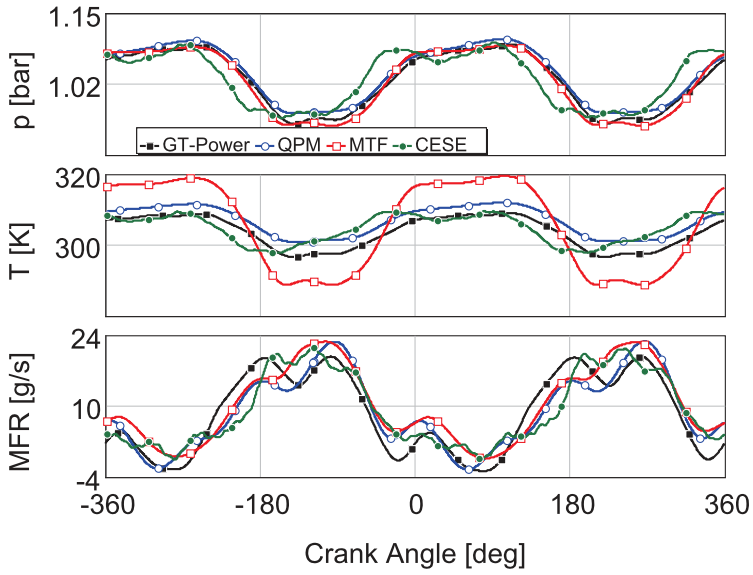

Fig. 6.8.: Predicted pressure, temperature and mass flow rate for 1500 RPM for the 2-Cylinder Diesel engine

In this case, results from three rotational engine speeds will be compared in detail and the filling estimation error is then presented for the different speeds up to 4500 RPM (maximum allowed speed) and constant injection.

- The wave motion in the intake path has been predicted fairly well by CE-SE ($\alpha = 2$ and CFL=0.95) and QPM (one branch). The MTF still suffers the energy conservation which results in a difference of ≈ 20°C and 0.15 bar by 4500 RPM.
- Despite the fact that the geometry was taken as a straight pipe, the QPM does not lack any accuracy compared to the one dimensional models. In this case, only one branch has been used.

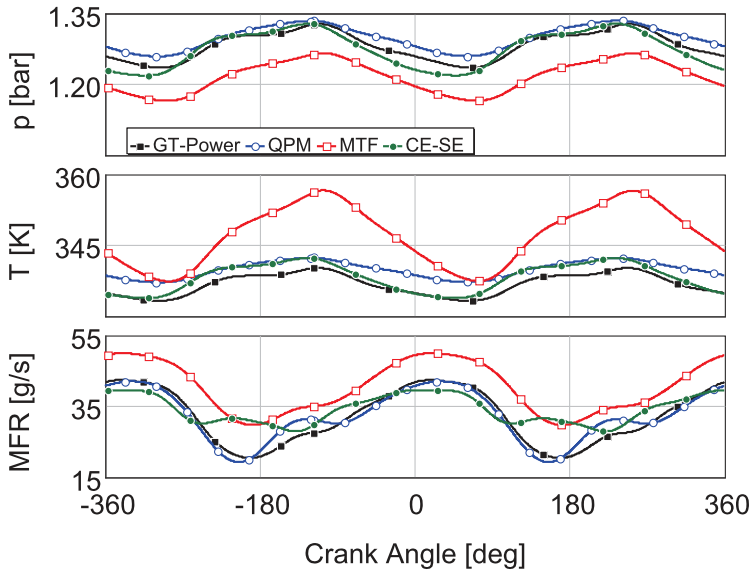

Fig. 6.9.: Predicted pressure, temperature and mass flow rate for 3000 RPM for the 2-Cylinder Diesel engine

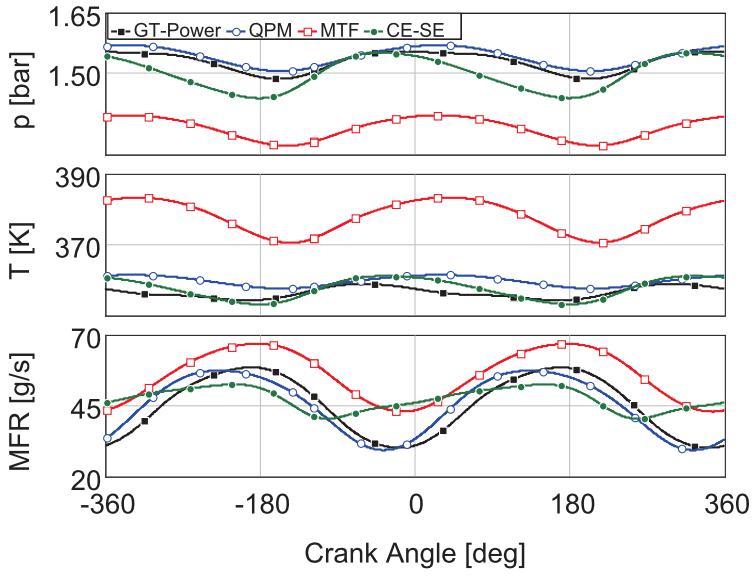

Fig. 6.10.: Predicted pressure, temperature and mass flow rate for 4500 RPM for the 2-Cylinder Diesel engine

- Considering the results shown in figs. 6.8 to 6.10, the integrated mass flow error given in fig. 6.11 and taking into consideration that no calibration has been used, both CE-SE and QPM provide relative error less than $\pm 10\%$ except for rotational speed equal to 1500 RPM

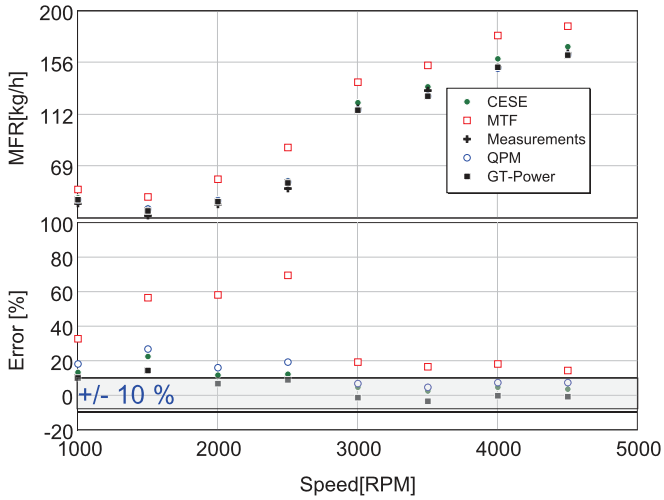

Fig. 6.11.: Measured and predicted mass flow rate

This can be due to several reasons such as the non-predictive combustion model or even the calibration at this specific rotational speed.

It is clear that the QPM, being a lumped parameter model requires a higher calibration effort, while neglecting the energy conservation in the MTF results in important errors in the estimation of the mass flow rate.

In order to validate an overall air system simulation, the previously presented modeling approaches are used to simulate the flow in an entire air system of the 2-cylinder diesel engine. In general, a modern diesel engine will consist of these essential components: cylinders, intake- and exhaust manifold, turbocharger (including compressor and turbine), exhaust gas recirculation system, inter-cooler, catalytic converter and diesel particulate filter.

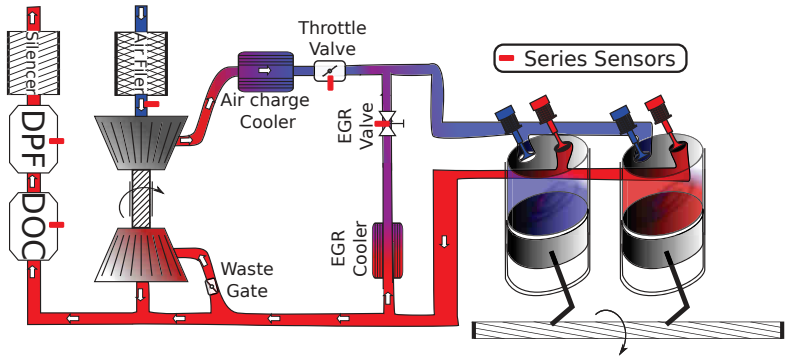

Fig. 6.12.: Air system and exhaust gas after-treatment for a two-cylinder in-line diesel engine

As shown in fig. 6.12, the filtered ambient air is, at first, aspired into the radial compressor of the turbocharger, and leaves with an increased pressure. Afterwards, the compressed air is cooled through the inter-cooler and then pumped into the intake manifold, where its mass flow rate is manipulated by a throttle valve. In the intake manifold, the fresh air is mixed with the recirculated exhausted gas (in case of an open EGR valve or a back flow through the intake valve). After that, the mixture is aspired through diverse manifold branches into the individual cylinders, burned in the combustion chamber, and discharged into the exhaust manifold. Besides the part of recirculated gas, the rest of the burned gas enters the turbine, impelling the continuous rotation of the entire turbocharger. Eventually, after a series of post-processing in the catalytic converter and DPF, gas is discharged back to the environment.

In current ECUs, the model for the pipe flow between arbitrary two components was established on the basis of a null-dimensional, or in other words, lumped-parameter approach. In fact, a common Emptying-Filling Capacity Model was implemented which could only calculate approximately the lumped variation of the gas state of a duct, but it is not able to reflect the variations of gas states in different spatial positions of the duct. Furthermore, this model can concentrate on holding the conservation of mass and energy, nevertheless, neglecting inevitably the other conservation law of momentum. As a consequence, the wave actions of engine flow, or more specifically, the propagation of the pressure, and temperature waves between the boundaries of the duct could not be effectively captured by this Emptying-Filling Model.

3. Waves in the Intake and Exhaust Manifolds

In the previous section, the different modeling approaches have been compared to measurements and reference results from a virtual engine. It was clear that the model accuracy is proportional to model complexity. Filling and Emptying models are not capable of building waves effects. On the other hand, they required minimum computational power. This can be used if waves effects can be neglected at specific engine

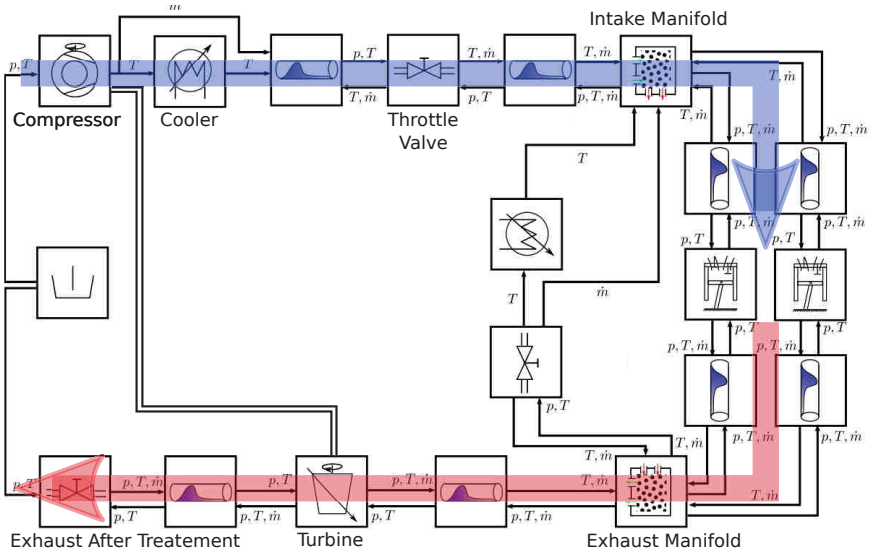

Fig. 6.13.: Schematic diagram of gas system modeling in engine simulation

ducts. It is thus necessary to investigate the necessity of modeling waves based on the measurements.

Keeping the cylinder breathing as final aim, let us observe pressure profiles at the intake and exhaust manifold.

Figure 6.15 shows the pressure and valves opening profiles at the manifold for three different engine operation points.

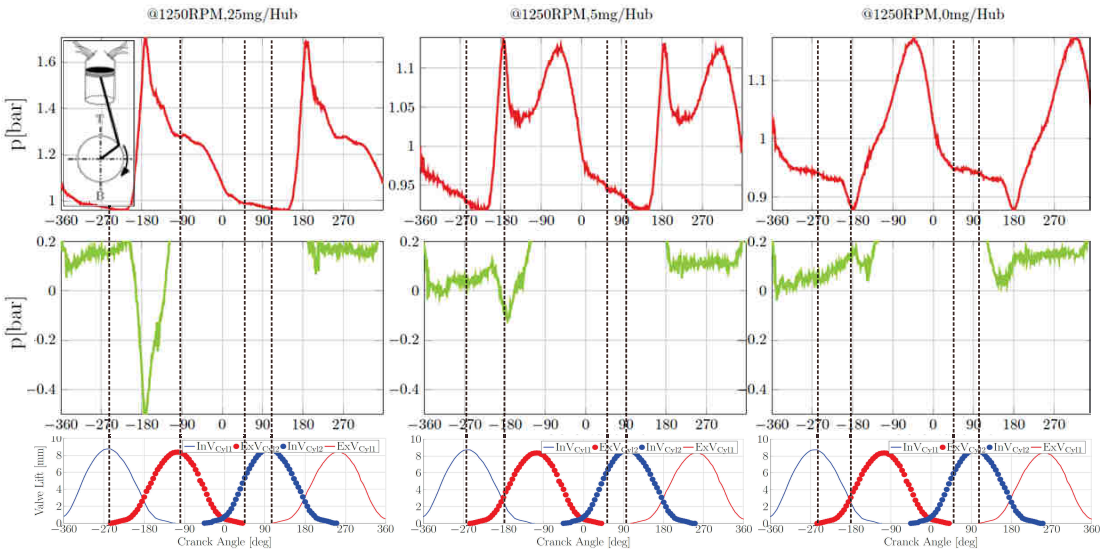

Fig. 6.14.: Pressure sensitivity at exhaust manifold

Consider the upper left subplot at 1250 RPM and 25 mg/cylinder. At around -270 CA, the exhaust valve of cylinder 1 opens. This will lead to an increase in the exhaust manifold pressure until the pressure reaches its maximum at -180 CA. Due to the high pressure difference across the exhaust valves ($p_{cyl} >> p_{exh}$), the flow across the exhaust valves reaches quickly a high speed. Combined to the increasing cylinder volume, this will lead to sharp decrease in cylinder pressure.

Starting from -180, the cylinder volume will decrease, leading to an increase in cylinder pressure, some local back flow will take place across the exhaust valve. Due to this and/or gas flowing through the turbine and EGR-valve, the pressure in the exhaust manifold will decrease almost until next opening of the exhaust valve in the following working cycle. It is clear that in this case, no waves phenomena (such as reflections) can be observed and pressure profile is defined simply through the Filling and Emptying (f & E) of the exhaust manifold.

Operation point at 1250 RPM and 5 mg/cylinder confirms that the F& E is dominant along the exhaust manifold. The same behavior is observed between -270 CA and -180 CA. However, due to the lower injection quantity compared to the previous operation point, the flow will reach a lower maximum leading to more remaining gas quantity in the cylinder. The piston upward movement starting from -180 CA, will generate a new positive pressure difference across the exhaust valve. This will trigger a positive mass flow leading to the second peak pressure signal (around -45 CA). Afterwards, most of the mass is released from the cylinder and the exhaust manifold pressure will decrease until the next exhaust phase. Once again, the F& E phenomena is dominant.

Without injection (third operation point), a very low in-cylinder pressure is observed leading to a small positive mass flow across the exhaust valve. This later is not high enough to compensate the flow leaving the exhaust manifold (mainly due to turbine rotation) leading to a first decrease in exhaust manifold pressure.

Starting from -180 CA, the decreasing cylinder valve will lead to a higher mass flow and hence the observed increase in exhaust pressure manifolds.

These three operation points can be said to represent the different exhaust pressure behavior for the complete engine operation map.

It will be shown in the Overall Simulation Section that modeling the exhaust manifold using only concentrated parameter models will be enough to simulate the previous effects while keeping the calculation power to its minimum.

The pressure profile at the intake manifold, on the other hand, observes more dominant wave effects. Figure 6.14 shows the intake manifold pressure at three different operation points. It is clear that in addition to the F& E effects, reflected waves are super-imposed on the main pressure wave. Even if the air charge cooler and EGR coolers act as filters, reflections from throttle valve (sudden area changes), moving intake valves (partially open or closed ends) and the intake manifold geometry generate apparent reflected waves.

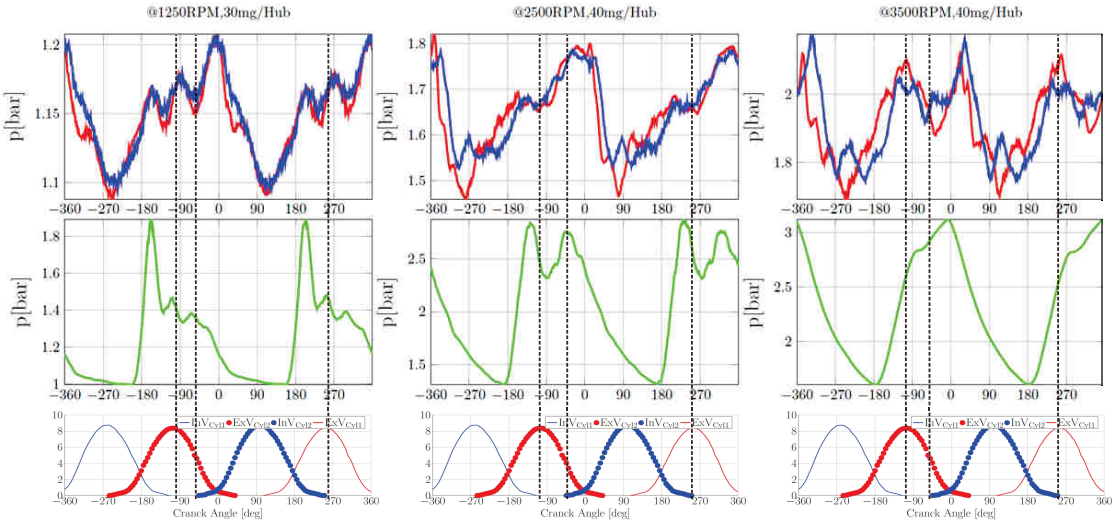

Fig. 6.15.: Pressure sensitivity at intake manifold

4. Intake Manifold Modeling Using the QPM

In this context, the one-dimensional duct flow model or Quasi-Propagatory-Model seems to be a necessary supplement for the engine simulation, because they not only specify the spatial differences of the gas state over the duct, but also theoretically take all the conservation laws into account.

The number of branches (or capacities) for the QPM can only be defined iteratively based on the required accuracy. For the flow in the intake manifold, the flow is usually separated by more than one manifold branch. As to evaluate the boundary conditions at the common border of the branches, i.e. at the duct junction, a generic capacity model is introduced. For the intake manifold, the capacity model is capable of specifying the upstream conditions of the QPM. The composition of branch and capacity models is illustrated in fig. 6.16.

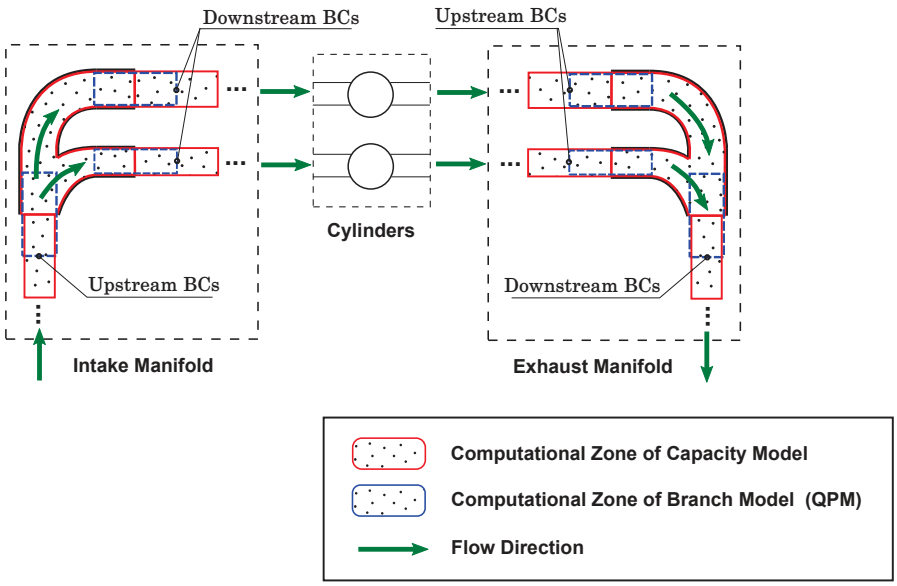

Fig. 6.16.: Modeling of the intake and exhaust manifolds by branches and capacities

In order to reveal this withdraw evidently, a simulation was made where a single capacity model was imposed at the place of the intake and exhaust manifolds, as well as the other ducts in the engine (see fig. 6.13).

4.1. Single Operation Point Test

In this simulation, all the existing capacity models in the simulation have been replaced with the implemented 1D CE-SE, quasi Quasi-Propagatory and F&E Models. An identical configuration of simulation parameters has been conducted in order to guarantee a proper comparison.

For the 1D numerical model, the CE-SE scheme is applied to the simulation in order to ensure simultaneously the accuracy and stability of the solution. On the other hand, for the Quasi-Propagatory-Model, the branch and capacity models are properly combined with the adjacent valves in order to reflect the real geometry of the pipes or the sections of pipe junction.

In this case, no variable valve timing was considered. Thus the inlet and exhaust valves would open and close at a fixed sequence. Hence, the effective flow area of both the inlet and exhaust valves would vary as a function the crank angle[1]. For the engine in hand, the dynamics of the effective valve orifice area is shown in fig. 6.17.

[1]The crank angle refers to the angle of rotation of a crankshaft. It is measured from the highest position of a piston (or named as top dead center). When the piston reaches its lowest position (or known as bottom dead center), the crank angle will be ± 180 deg

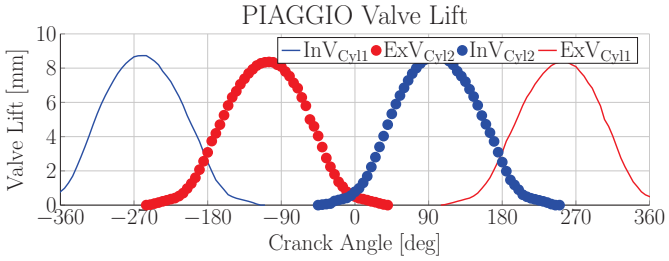

Fig. 6.17.: The dynamics of the orifice area of inlet and exhaust valves

The results for the experimental validation of different numerical models are shown in figs. 6.18 to 6.21

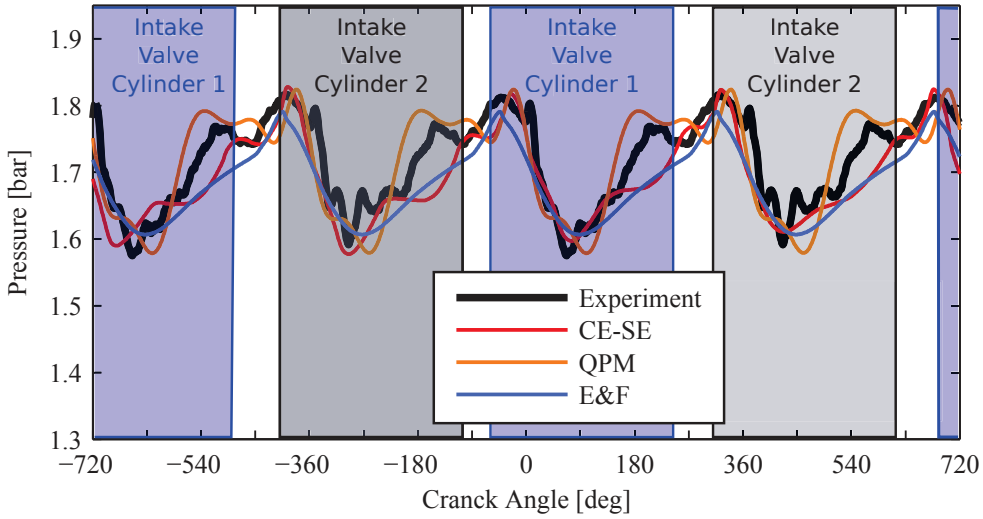

Fig. 6.18.: Experimental validation of different numerical models: Pressure in engine intake manifold (2000 rpm)

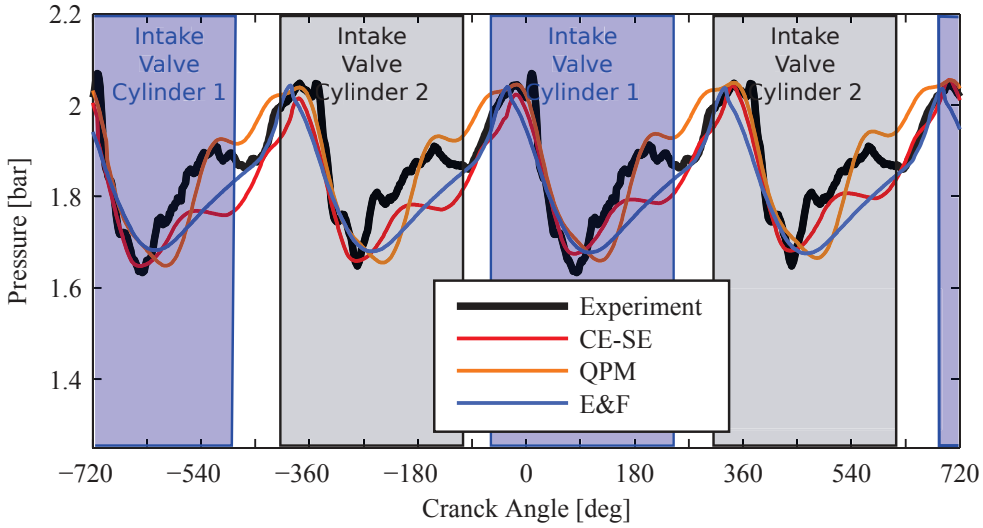

Fig. 6.19.: Experimental validation of different numerical models: Pressure in engine intake manifold (2500 rpm)

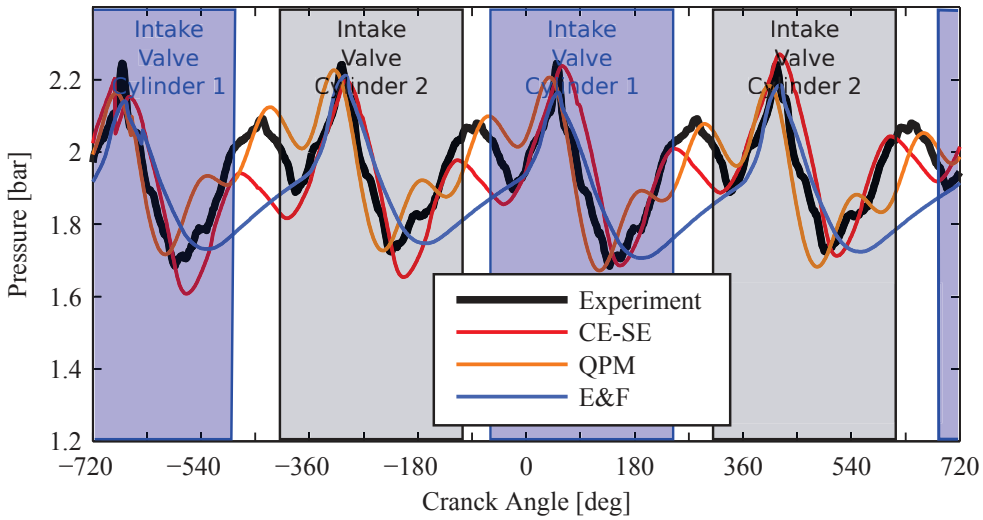

Fig. 6.20.: Experimental validation of different numerical models: Pressure in engine intake manifold (3000 rpm)

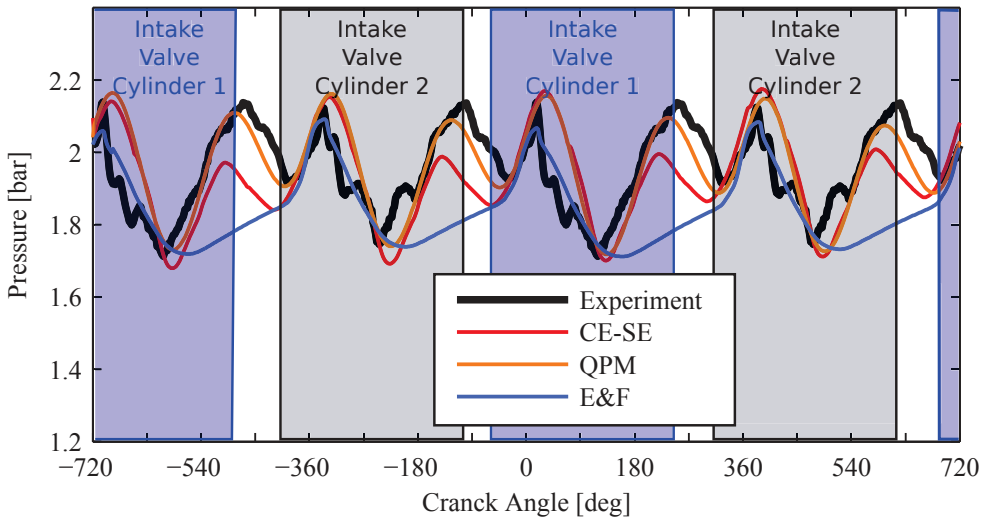

Fig. 6.21.: Experimental validation of different numerical models: Pressure in engine intake manifold (3500 rpm)

Clearly, the single capacity model shows a smooth approximation in following the pressure variation arising from the dynamics of the valves. This phenomenon was presented as the main resonance of pressure profile. But, it was not capable of capturing the high-frequency pressure pulsations, which is caused by the specific wave actions such as reflection at the boundaries, superposition of successive waves. This confirms the analysis presented previously in section 3.

As shown in the figures, compared to the E&F model, the results of 1D numerical model and the QPM presented a much more satisfactory correspondence with the measured data. The pulsation phenomena in the pressure profiles resulting from the propagation and reflection of the pressure waves are acceptably reproduced in the simulation. However, the magnitudes of these pulsations, especially the high-frequency ones, are sometimes not precisely represented by either of them. The pressures in the intake manifold are often underestimated by means or overestimated by means of QPM. The possible reasons are as follows:

1. There may exist deviation in estimating the geometrical parameters of the manifold branches (Length, Variation of Cross-section area, ...) from the real situation.
2. The bent section and the sudden-flow-area-variation section in the intake manifold can particularly lead to an energy loss and a local wave reflection. Since the geometry of the model is assumed as a straight duct, possibly with a gentle flow-area-change, this phenomenon can not be well simulated without considering much more complicated models.
3. Complicated aspiration processes from the intake manifold can not be entirely translated into the one-dimensional flow problem. The local eddies have a

considerable influence on the flow, which can be only evaluated in a higher-dimensional flow analysis.

In contrast with the 1D numerical models, the most attractive highlight brought by the QPM is that it enormously shortens the calculation time without sacrificing too much precision in pressure prediction. For example, a single replacement of 1D numerical model with the QPM will accelerate the computation in at least six times, which only loses an ignorable accuracy of about 0.2%. The comprehensive comparison between the 1D duct flow models is given as follows:

Models	**Average Relative Computation Time [-]**	**Average Relative Computation Errors [%]**
Emptying and Filling Capacity Model	1	7.1
CE-SE ($v = 0.9$)	13.9	3.3
Quasi-Propagatory Model	2.1	3.5

5. Over All Engine Map Validation

It is clear that the QPM provides a good compromise between accuracy and computational complexity. We will assess this modeling approach over an entire engine operation range. The engine operation points are given in fig. 6.22.

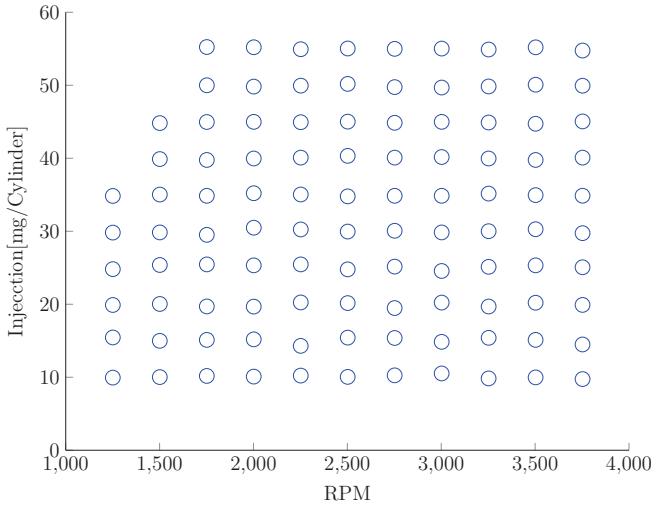

Fig. 6.22.: Engine operation points

Even for a single operation point, the engine can be considered in steady-state (in terms of mean energy and injection), gas dynamics will remain apparent. This dynamics (due

to valves movement) if modeled properly will lead to a proper estimation of engine breathing also during transients.

To correlate the operation points to the set of the subplots, the later in fig. 6.23 and fig. 6.24 is mapped one-to-one.

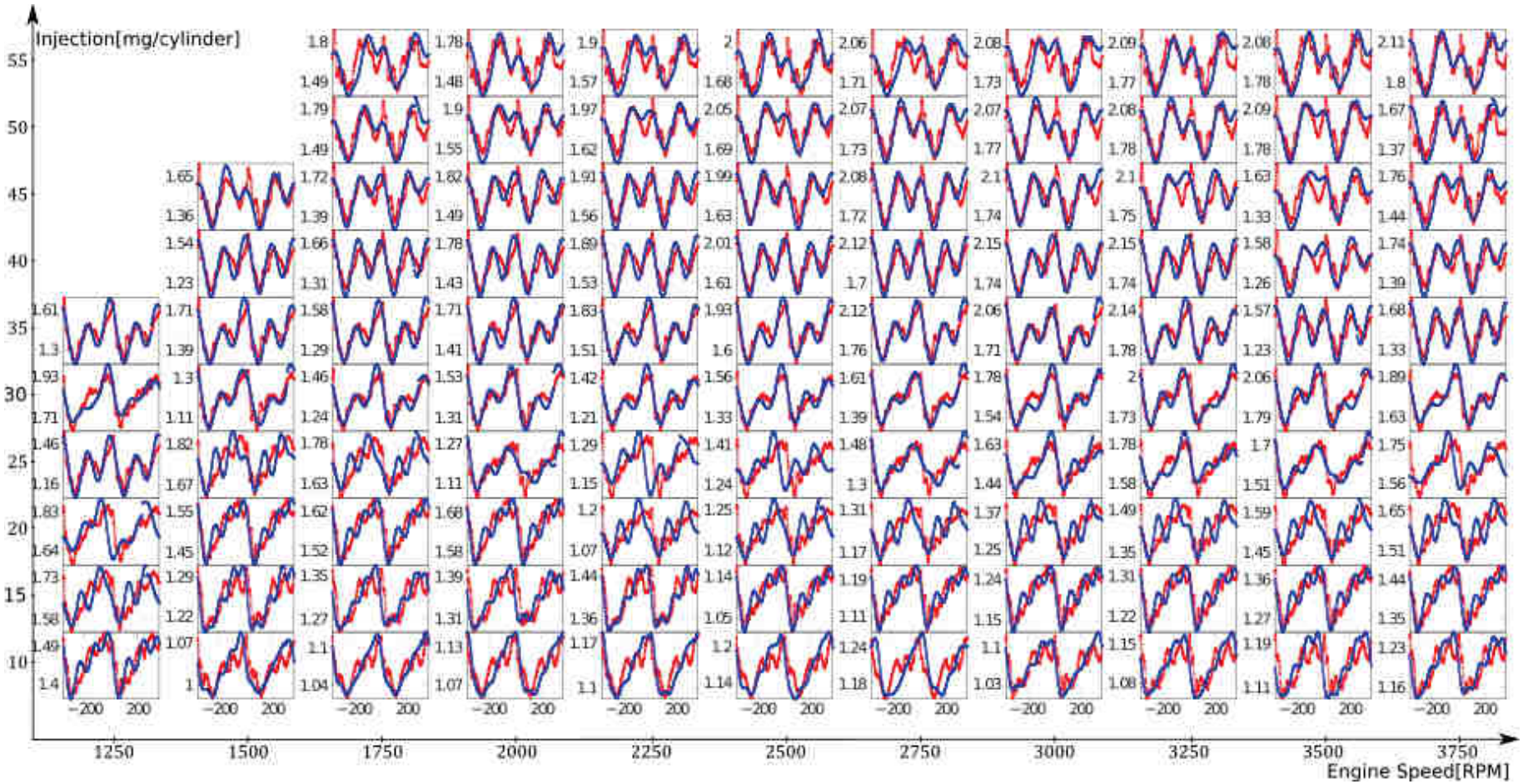

Fig. 6.23.: Simulation (blue) Vs measurements (red) of the intake manifold pressure

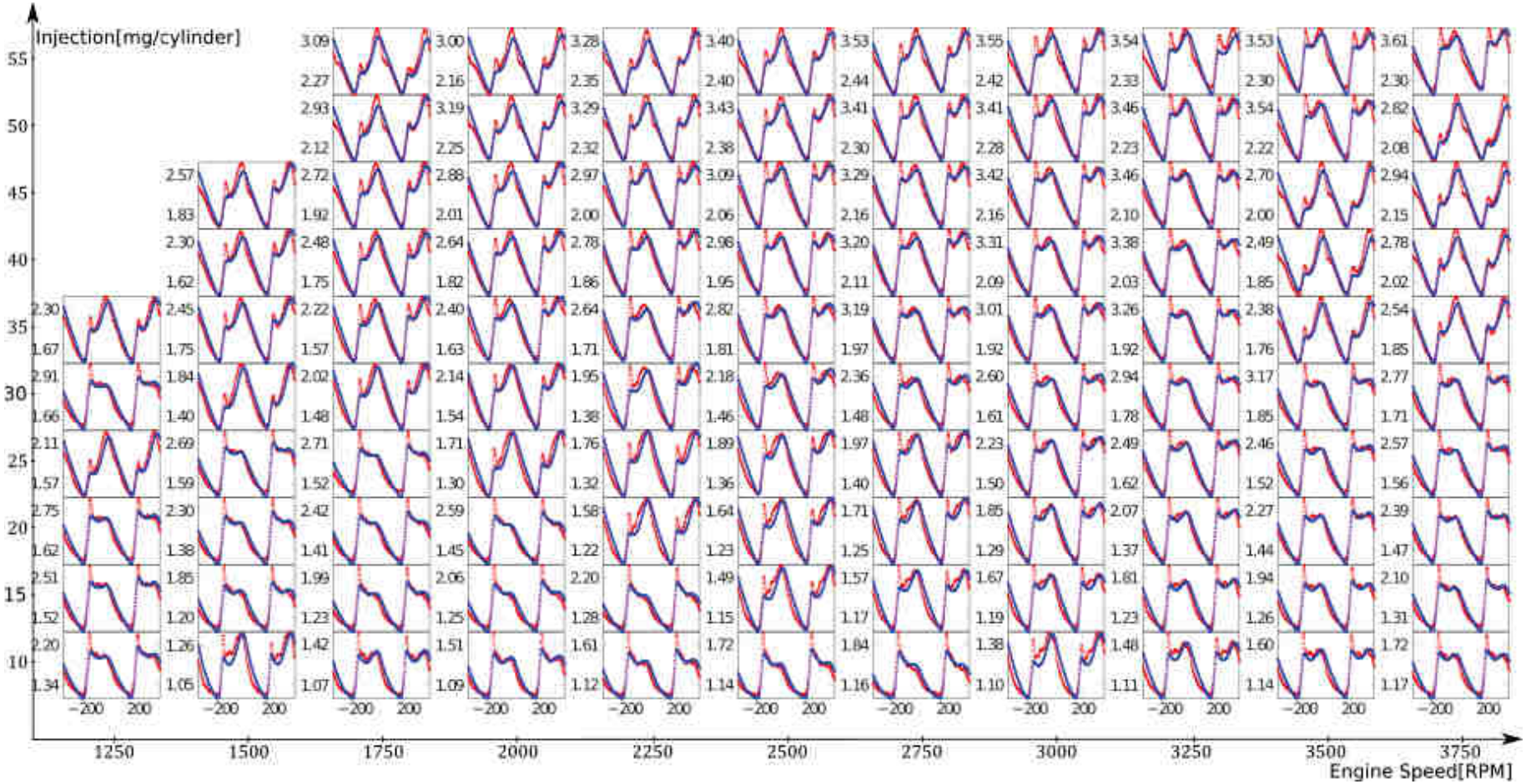

Fig. 6.24.: Simulation (blue) Vs measurements (red) of the exhaust manifold pressure

For the intake manifold, the model accuracy varies depending on the injection and engine speed. The model reaches a very good accuracy for operation points higher than 25 mg/cylinder. However, some phase shifts are observed at some operation points such as (1750 RPM).

The accuracy is very reduced for low speeds and injections. This is due to the number of branches considered. Ideally, the number of branches/capacities is calibrated to match gas dynamics. For this simulation, only one branch has been considered. Due to the low injection, the turbocharger speed is reduced (waste gate position always open), leading to a low mass flow. The QPM capacities will observe a slow filling and emptying flow which will dominate the gas momentum modeled using the branch sub-model.

Generally speaking, it is clear that the mean simulated pressure matches well the measured one.

The trapped mass per cylinder is now considered to evaluate the simulation accuracy. Because no direct measurement of this quantity is available, we will consider measured mass flow at the air system entry with a hypothesis of equal distribution between the two cylinders.

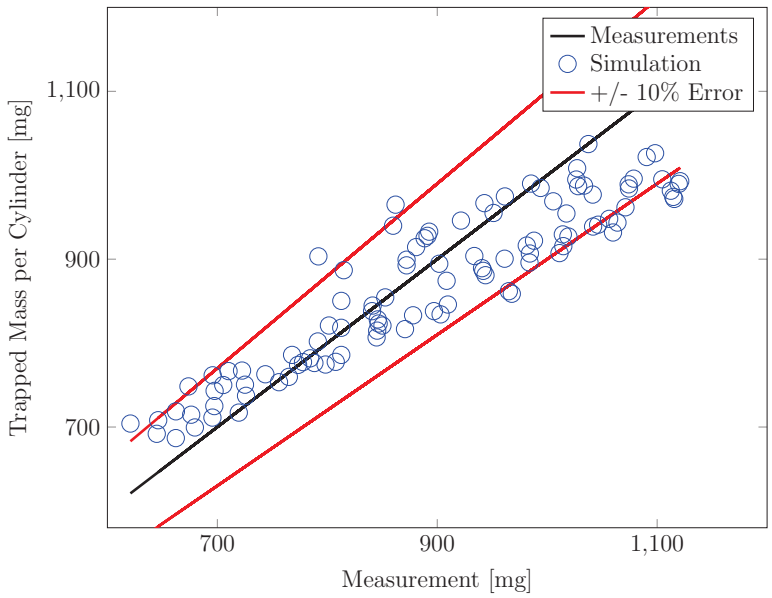

Fig. 6.25.: Comparison between measured and trapped mass per cylinder

It is important to note that no specific calibration has been performed to match the measurements. Flow through valves such as the throttle valve, EGR-valve, intake and exhaust valves have been measured on dedicated test benches and used to calculate flow coefficients. This helped avoid the use of volumetric efficiency for the cylinders.

6. Conclusion

To complete the simple numerical validation in chapters , thus chapter presented the validation of flow models under engine like conditions

First, a virtual single cylinder engine was used to assess the accuracy of the models. Only the intake path was simulated whereas the rest of the system was modeled using the commercial tool GT-Power. This gave the possibility to relate all differences to the simulated intake path. The simulation accuracy was proportional to the models complexity. However, the QPM gave the best compromise between precision and calculation effort. These results have been confirmed again on a 2-cylinder diesel engine using the same simulation principle.

The measurements were then used to extract some knowledge on flow complexity along intake and exhaust paths. It was deduced that filling and emptying phenomena are dominant along the exhaust path. On the other hand, wave phenomena are crucial for flow simulation. This motivated the use of a hybrid model based on the QPM along the intake path and F&E along the exhaust ducts.

This was used to build a complete air system and compared to measurements. Pressure pulsations were reproduced with varying accuracy for the complete engine operation map.

CONCLUSION

Gas flow impact on air system dynamics and hence on combustion products, i.e. emissions, has imposed itself strongly due to the dynamics content in new test drive cycles such as the WLTC. This makes current real-time 0D models less reliable as they rely on stationary measured look up tables. In addition, wave phenomena and gas inertial effects are inherently neglected. This makes the estimation of the flow into and from the cylinder inaccurate.

A methodology to proposed reproduce wave effects along the internal combustion engine ducts was presented in this work. The idea relies on combining both lumped parameter and quasi-one-dimensional models.

This combination gives the possibility to take inertial effects of gas dynamics while avoiding the heavy computational cost of the 1D modeling approach.

The first part investigated one-dimensional numerical schemes, with the aim of evaluating them with respect to real-time applications. Four different numerical schemes have been tested and have shown clear discrepancies in accuracy and stability. Even though the augmented Lax-Wandroff with total variation diminishing algorithm was able to produce accurate simulation results, it suffered from a very high calculation effort.

As long as 1D models are concerned, the Conservation Element-Solution Element scheme was found to be the best in terms of compromise between accuracy and computational power. However, being still too slow for a real-time application, it was necessary to use a reduced order model. Thus, the CE-SE has served as a good reference for further numerical validations.

The Quasi-Propagatory model was the best candidate to model waves with less computational power. It was found to be able to reduce the calculation effort by 80% with a penalty of only 0.2% on the accuracy for some investigated engine operation points.

For the sake of a complete air system simulation, it was necessary to address valves,

turbochargers and coolers modeling. To have an accurate boost pressure estimation, more focus was put on the compressor to provide a better extinction of manufacturer data maps. A physics based model was presented based on [55]. Results have also shown a better interpretation and extrapolation ability.

To assess the overall simulation, a complete air system of a diesel engine was simulated for every single operation point. The QPM was used along the intake path whereas the lumped parameters (filling and emptying) models, along the exhaust path. This configuration was chosen based on the analysis of pressure profiles at the intake and exhaust manifolds, and proved to be satisfactory in terms of accuracy and calculation effort.

Future Developments

The following future work directions have been identified:

- The QPM has proved to be efficient in terms of accuracy and calculation effort for simple engine ducts. The natural extension is to investigate this approach for complex geometries such as compressors and turbines. This will give the possibility to detect surge phenomena without complex CFD simulations.
- Future ECUs will provide the possibility to resolve sub-problems simultaneously on different cores. It is thus necessary to investigate the parallelization of the CE-SE and QPM approaches.
- The Taylor approximation of the heat transfer model used in the compressor modeling in chapter 5 produces some inaccuracies when the mass flow tends towards zero. This approximation was used to simplify the model but has to be extended to increase model accuracy.

CONCLUSION (FRENCH)

L'impact de la dynamique des gaz sur la chaine d'air et de ce faite sur les produits de combustion (les émissions polluantes) s'est fortement imposé, en raison de l'impact de la dynamique des gaz dans les nouveaux cycles d'essais d'homologation automobile tels que le WLTC.

En effet, les modèles temps réel 0D actuels sont moins fiables car ils reposent sur les cartographies mesurées sur des points de fonctionnements stationnaires. En outre, les phénomènes d'onde et les effets inertiels des gaz sont intrinsèquement négligés. Ce qui rend l'estimation des flux entrant et sortant du cylindre imprécise. Une méthodologie pour reproduire efficacement les effets d'ondes le long des conduites de moteurs à combustion interne a été présentée dans ce travail.

L'idée est basée sur la combinaison des modèles à paramètres concentrés et les modèles quasi unidimensionnels. Cette combinaison donne la possibilité de prendre en considération les effets d'inertie et la dynamique des gaz, tout en évitant un coÃ»t plus élevé en temps de calcul du à l'approche de modélisation 1D. La première partie de ce travail été consacrée aux schémas numériques à une dimension, dans le but de les évaluer par rapport à des applications temps réel. Par la suite, quatre schémas numériques différents ont été testés et ont montrés des différences majeures dans la précision et la stabilité. MÃªme si le schéma Lax-Wandroff étendu par le correcteur de flux "Variation Total décroissante, TVD" était capable de produire des résultats de simulation précis, il était malheureusement caractérisé par un temps de calcul plus lourd. Le schéma Conservation Elément-Solution Elément (CE-SE) a prouvé Ãªtre le meilleur en termes de compromis précision et puissance de calcul. Cependant, il souffrait d'une importante lenteur pour les applications temps réel, il était nécessaire ainsi d'utiliser un modèle à ordre réduit. Ainsi le CE-SE a servi comme une bonne référence pour plus de validations numériques.

Le modèle "Quasi-Propagatory" était le meilleur candidat pour modéliser les ondes avec une plus grande économie en ce qui concerne la puissance de calcul. Il a été

remarqué que ce modèle est capable de réduire les efforts de calcul de 80

Pour avoir un traitement de conditions aux limites plus représentif, divers cas ont également été présentés brièvement. Et pour avoir une meilleure estimation de la pression de suralimentation, on s'est intéressé plus particulièrement au compresseur. Un modèle physique a été présenté en se basant sur les travaux de Martin et al. [55]. Les résultats ont également montré une meilleure capacité d'interpolation et d'extrapolation. Pour évaluer la simulation globale, un système d'air complet d'un moteur diesel a été simulé pour chaque point opérationnel. Le QPM a été utilisé le long de la voie d'admission, tandis que les modèles à paramètres concentrés, ont été utilisés le long du trajet d'échappement.

Cette configuration a été choisie sur la base d'une analyse des profils de pression dans les collecteurs d'admission et d'échappement, elle a prouvée Ã^{a}tre satisfaisante en termes de précisions et le temps de calcul. Il a été remarqué que l'application des modèles à paramètres concentrés produit des résultats satisfaisant le long de la conduite d'échappement, tout en réduisant le temps de calcul et en décrivant les phénomènes d'ondes à l'entrée des soupapes d'admission.

Perspective et voies de développements :

Des pistes pour l'amélioration de ce travail de thèse ont été identifiées afin d'améliorer et de généraliser l'utilisation des méthodes développées dans cette thèse :

- Le QPM a prouvé son efficacité en termes d'exactitude et de temps de calcul par rapport aux modèles 1D, en ce qui concerne la simulation d'une simple tubulure. L'extension de cette méthode consiste à son utilisation pour décrire des géométries complexes telles que le compresseur. Ce qui permettra la possibilité de prendre les ondes en considération et de détecter le retour de flux sans Ã^{a}tre obligé d'utiliser les modèles 3D.
- Les nouvelles générations de calculateurs donneront la possibilité de résoudre les problèmes sous-jacents en utilisant différents noyaux de processeurs. La continuité logique de ce travail conduira à la parallélisation du QPM et la CE-SE dans le cas des moteurs à combustion.
- L'approximation de Taylor des pertes de chaleurs dans le chapitre 5 produit des erreurs numériques quand le débit de masse traversant le compresseur tend vers zéro. Il est donc important d'étudier d'autres modèles pour améliorer l'exactitude de l'algorithme.

APPENDIX A

HYPERBOLICITY

Definition 0.1. The following is a system of s first order partial differential equations for s unknown $\vec{u} = (u_1, \ldots, u_s)$, $\vec{u} = \vec{u}(\vec{x}, t)$, where $\vec{x} \in \mathbb{R}^d$:

$:(*) \quad \frac{\partial \vec{u}}{\partial t} + \sum_{j=1}^{d} \frac{\partial}{\partial x_j} \vec{f^j}(\vec{u}) = 0,$

where $\vec{f^j} \in C^1(\mathbb{R}^s, \mathbb{R}^s), j = 1, \ldots, d$ are once continuously differentiable functions, nonlinear in general.

Next, for each $\vec{f^j}$ a matrix $s \times s$ is defined

$$A^j := \begin{pmatrix} \frac{\partial f_1^j}{\partial u_1} & \cdots & \frac{\partial f_1^j}{\partial u_s} \\ \vdots & \ddots & \vdots \\ \frac{\partial f_s^j}{\partial u_1} & \cdots & \frac{\partial f_s^j}{\partial u_s} \end{pmatrix}, \text{ for } j = 1, \ldots, d.$$

The system $(*)$ is "'hyperbolic"' if for all $\alpha_1, \ldots, \alpha_d \in \mathbb{R}$ the matrix $A := \alpha_1 A^1 + \cdots + \alpha_d A^d$ has only real eigenvalues and is diagonalizable.

If the matrix A has "n" "distinct" real eigenvalues, it follows that it's diagonalizable. In this case the system $(*)$ is called "'strictly hyperbolic"'.

If the matrix A is symmetric, it follows that it's diagonalizable and the eigenvalues are real. In this case the system $(*)$ is called "'symmetric hyperbolic"'.

The homogeneous portion of the governing equations 2.35, is

$$\frac{\partial \mathbf{W}}{\partial t} + \frac{\partial \mathbf{F}(\mathbf{W})}{\partial x} = 0 \tag{A.1}$$

This system of equations can be written as

$$\frac{\partial \mathbf{W}}{\partial t} + \mathbf{A}\frac{\partial \mathbf{W}}{\partial x} = 0 \tag{A.2}$$

where **A** is a 3x3 matrix. The equations can be expressed more explicitly as

$$\frac{\partial W_1}{\partial t} + A_{11}\frac{\partial W_1}{\partial x} + A_{12}\frac{\partial W_2}{\partial x} + A_{13}\frac{\partial W_3}{\partial x} = 0 \tag{A.3}$$

$$\frac{\partial W_1}{\partial t} + A_{21}\frac{\partial W_1}{\partial x} + A_{22}\frac{\partial W_2}{\partial x} + A_{23}\frac{\partial W_3}{\partial x} = 0 \tag{A.4}$$

$$\frac{\partial W_1}{\partial t} + A_{31}\frac{\partial W_1}{\partial x} + 32\frac{\partial W_2}{\partial x} + 33\frac{\partial W_3}{\partial x} = 0 \tag{A.5}$$

$$\mathbf{A} = \begin{bmatrix} 0 & 1 & 0 \\ (\gamma-3)\frac{u^2}{3} & (3-\gamma)u & \gamma-1 \\ (\gamma-1)\frac{u^3}{2} - \frac{ua^2}{\gamma-1} & \frac{a^2}{\gamma-1} - \frac{u^2}{2}(2\gamma-3) & \gamma u \end{bmatrix} \tag{A.6}$$

The eigen valuues, λ_k, and corresponding right eigen vectors, $\mathbf{e_k}$, of **A** are:

$$\lambda_1 = u + a, \qquad \mathbf{e_1} = \begin{bmatrix} 1 \\ u+a \\ \frac{a^2}{\gamma-1} + \frac{u^2}{2} + ua \end{bmatrix} \tag{A.7}$$

$$\lambda_2 = u - a, \qquad \mathbf{e_2} = \begin{bmatrix} 1 \\ u-a \\ \frac{a^2}{\gamma-1} + \frac{u^2}{2} - ua \end{bmatrix} \tag{A.8}$$

$$\lambda_3 = u, \qquad \mathbf{e_3} = \begin{bmatrix} 1 \\ u \\ \frac{u^2}{2} \end{bmatrix} \tag{A.9}$$

Since the eigen values are real and the eigen vectors are linearly independent (none of the vectors can be represented as a linear combination of the others) the system of equations given in equation A.2 is said to be *hyperbolic*. A hyperbolic set of equations associated with propagating waves so the behavior of a physical system described by such as equation set will be dominated by wave-like phenomena; the eigen values, λ_k, of the system are the propagation speeds of the waves.

1. Lax-Wendroff Schemes

Since the 1950s, a lot of investigations have been done in the field of FDM for the simulation of one-dimensional unsteady flow. The most famous and significant achievements were made by Lax and Friedrich in [70] and [71] as well as their colleague Wendroff in [37] and [72], who developed a number of discretization techniques for the finite difference method in their cooperation, such as Lax-Friedrich method and Lax-Wendroff method, and brought them successfully into the computation of fluid dynamics for pipes.

Reformulating the equation (2.33) with these three symbolic vectors,

$$\mathbf{W} = \begin{bmatrix} \rho \\ \rho u \\ \rho e_0 \end{bmatrix}, \mathbf{F}(\mathbf{W}) = \begin{bmatrix} \rho u \\ \rho u^2 + p \\ \rho u h_0 \end{bmatrix}, \mathbf{C}(\mathbf{W}) = \begin{bmatrix} \rho u \\ \rho u^2 \\ \rho u h_0 \end{bmatrix} \frac{d(\ln F)}{dx} + \begin{bmatrix} 0 \\ \rho G \\ -\rho q \end{bmatrix} \tag{A.10}$$

it becomes

$$\frac{\partial \mathbf{W}}{\partial t} + \frac{\partial \mathbf{F}(\mathbf{W})}{\partial x} + \mathbf{C}(\mathbf{W}) = 0 \tag{A.11}$$

The integral form of the equation over the time and space will be then:

$$\int_t \int_x \left(\frac{\partial \mathbf{W}}{\partial t} + \frac{\partial \mathbf{F}(\mathbf{W})}{\partial x} + \mathbf{C}(\mathbf{W}) \right) \mathrm{d}x\mathrm{d}t = 0 \tag{A.12}$$

Significantly, the symbolic vector for flux $\mathbf{F}$ is a function of the fluid properties vector $\mathbf{W}$, which can be described as the algebraic operation of the elements in $\mathbf{F}$:

$$\begin{aligned} \mathbf{F}_1 &= \rho u = \mathbf{W}_2 \\ \mathbf{F}_2 &= \rho u^2 + p = \frac{(\rho u)^2}{\rho} + \rho R_{spec} \cdot \frac{e_0 - \frac{1}{2}u^2}{c_v} = \frac{\mathbf{W}_2^2}{\mathbf{W}_1} + (\gamma - 1)\left(\mathbf{W}_3 - \frac{1}{2}\frac{\mathbf{W}_2^2}{\mathbf{W}_1} \right) \\ \mathbf{F}_3 &= \rho u h_0 = u(\rho e_0 + \rho \cdot \frac{p}{\rho}) = \frac{\mathbf{W}_2}{\mathbf{W}_1}\left(\mathbf{W}_3 + (\gamma - 1)\left(\mathbf{W}_3 - \frac{1}{2}\frac{\mathbf{W}_2^2}{\mathbf{W}_1} \right) \right) \end{aligned} \tag{A.13}$$

Eventually, the simplification leads to:

$$\begin{aligned} \mathbf{F}_1 &= \mathbf{W}_2 \\ \mathbf{F}_2 &= \frac{3-\gamma}{2}\frac{\mathbf{W}_2\mathbf{W}_3}{\mathbf{W}_1} + (\gamma - 1)\mathbf{W}_3 \\ \mathbf{F}_3 &= \gamma\frac{\mathbf{W}_2\mathbf{W}_3}{\mathbf{W}_1} - \frac{\gamma - 1}{2}\frac{\mathbf{W}_2^3}{\mathbf{W}_1^2} \end{aligned} \tag{A.14}$$

where the subscripts $1, 2, 3$ refer to the 1^{st}, 2^{nd} and 3^{rd} component of the vector $\mathbf{W}$, $\mathbf{F}$

or $\mathbf{C}$ Likewise, it is also possible to express the vector of non-homogeneous terms $\mathbf{C}$ with $\mathbf{W}$

$$\begin{aligned}
\mathbf{C}_1 &= \mathbf{W}_2 \cdot \frac{d(\ln F)}{dx} \\
\mathbf{C}_2 &= \frac{\mathbf{W}_2^2}{\mathbf{W}_1} \cdot \frac{d(\ln F)}{dx} + \frac{2f}{D} \cdot \mathbf{W}_2 \cdot \left|\frac{\mathbf{W}_2}{\mathbf{W}_1}\right| \\
\mathbf{C}_3 &= \left(\gamma \frac{\mathbf{W}_2 \mathbf{W}_3}{\mathbf{W}_1} - \frac{\gamma - 1}{2} \frac{\mathbf{W}_2^3}{\mathbf{W}_1^2}\right) \cdot \frac{d(\ln F)}{dx} - \frac{\delta \dot{Q}}{F}
\end{aligned} \tag{A.15}$$

The proposed equation (A.14) manifests no dependence on geometrical factors but only on the properties of the fluid, when the investigated fluid behaves like an ideal gas. However, in contrast to the evaluation of $\mathbf{F}$, the non-homogeneous term involves several relevant properties from geometry and boundary of the control volume, such as the variation of cross-section area and friction factor. Since this function establishes a unique and determined relationship between $\mathbf{F}$ and $\mathbf{W}$ as well as $\mathbf{C}$ and $\mathbf{W}$, it is always possible to calculate $\mathbf{F}(x_0, t_0)$ and $\mathbf{C}(x_0, t_0)$ after obtaining the vector of fluid property $\mathbf{W}(x_0, t_0)$ at the same point.

1.1. Lax-Wendroff Two-Step Scheme

Another numerical scheme involving the algebraic operation from only two levels of time t^n, t^{n+1} is introduced to take charge of the primary calculation. At the very beginning of the iterations, as long as the value of $\mathbf{W}^2$ is calculated by a primary-step scheme with regard to the initial condition $\mathbf{W}^1$, the mid-point leapfrog method can be applied to obtain the $\mathbf{W}^3$ with a review of $\mathbf{W}^1$ and $\mathbf{W}^2$.

A simplest prototype of such a numerical approach is called two-step Lax-Wendroff (Richtmyer) method [73], which processes a second-order precision. The Lax-Friedrichs method is responsible for the primary step of the two-step approach by establishing a space-centered difference about the gird point $[i\Delta x, n\Delta t]$, while the mid-point leapfrog scheme is in charge of the subsequent step of every iteration with building a time-centered difference about the grid point $[i\Delta x, (n+1)\Delta t]$. Applying the Lax-Friedrichs method to evaluate the half mesh points $\left[(i \pm \frac{1}{2})\Delta x, (n + \frac{1}{2})\Delta t\right]$ gives:

$$\begin{cases}
\mathbf{W}_{i+1/2}^{n+1/2} = \frac{1}{2}\left[\mathbf{W}_{i+1}^n + \mathbf{W}_i^n\right] - \frac{\Delta t}{2\Delta x}\left[\mathbf{F}_{i+1}^n - \mathbf{F}_i^n\right] + \mathbf{C}_{i+1/2}^n \Delta t \\
\mathbf{W}_{i-1/2}^{n+1/2} = \frac{1}{2}\left[\mathbf{W}_i^n + \mathbf{W}_{i-1}^n\right] - \frac{\Delta t}{2\Delta x}\left[\mathbf{F}_i^n - \mathbf{F}_{i-1}^n\right] + \mathbf{C}_{i-1/2}^n \Delta t
\end{cases} \tag{A.16}$$

The vector of flux $\mathbf{F}$ at the point $\left[(i \pm \frac{1}{2})\Delta x, (n + \frac{1}{2})\Delta t\right]$ can be exactly evaluated from the corresponding vector $\mathbf{W}$ with respect to the explicit relationship which has been

demonstrated in equation (A.14).

$$\begin{cases} \mathbf{F}_{i+1/2}^{n+1/2} = \mathbf{F}(\mathbf{W}_{i+1/2}^{n+1/2}) \\ \mathbf{F}_{i-1/2}^{n+1/2} = \mathbf{F}(\mathbf{W}_{i-1/2}^{n+1/2}) \end{cases} \tag{A.17}$$

However, as described in equation (A.16), the evaluation for $\mathbf{W}$ requires additionally a reliable estimate of source terms $\mathbf{C}_{i+1/2}^{n}$, $\mathbf{C}_{i-1/2}^{n}$, which is located at the half mesh points. A common manipulation for that is replacing the term by the average of the surrounding points. Expanding $\mathbf{C}(x+\Delta x,t)$ and $\mathbf{C}(x,t)$ in form of the Taylor Polynomial respectively about the mesh point $[x-\frac{1}{2}\Delta x,t]$ and $[x+\frac{1}{2}\Delta x,t]$ results in:

$$\begin{aligned} \mathbf{C}(x+\Delta x,t) = \mathbf{C}(x+\frac{1}{2}\Delta x,t) + \frac{\partial \mathbf{C}}{\partial x}(x+\frac{1}{2}\Delta x,t)\cdot\frac{1}{2}\Delta x \\ +\frac{1}{2}\frac{\partial^2 \mathbf{C}}{\partial x^2}\cdot\left(\frac{1}{2}\Delta x\right)^2 + \mathbf{O}(\Delta x^3) \\ \mathbf{C}(x,t) = \mathbf{C}(x+\frac{1}{2}\Delta x,t) - \frac{\partial \mathbf{C}}{\partial x}(x+\frac{1}{2}\Delta x,t)\cdot\frac{1}{2}\Delta x \\ +\frac{1}{2}\frac{\partial^2 \mathbf{C}}{\partial x^2}\cdot\left(\frac{1}{2}\Delta x\right)^2 + \mathbf{O}(\Delta x^3) \end{aligned} \tag{A.18}$$

Apparently, $\mathbf{C}(x+\frac{1}{2}\Delta x,t)$ can be approximated by averaging $\mathbf{C}(x+\Delta x,t)$ and $\mathbf{C}(x-\Delta x,t)$ and ignoring the high-order term of Δx:

$$\mathbf{C}_{i+1/2}^{n} = \mathbf{C}(x+\frac{1}{2}\Delta x,t) = \frac{1}{2}\left[\mathbf{C}(x+\Delta x,t)+\mathbf{C}(x,t)\right] + \mathbf{O}(\Delta x^2) \tag{A.19}$$

Likewise,

$$\mathbf{C}_{i-1/2}^{n} = \mathbf{C}(x-\frac{1}{2}\Delta x,t) = \frac{1}{2}\left[\mathbf{C}(x,t)+\mathbf{C}(x-\Delta x,t)\right] + \mathbf{O}(\Delta x^2) \tag{A.20}$$

Subsequently, as the second step of two-step Lax-Wendroff scheme, the leapfrog method is utilized over another half-mesh interval to present the advance of the vector $\mathbf{W}$ from $n+\frac{1}{2}$ to $n+1$.

$$\mathbf{W}_{i}^{n+1} = \mathbf{W}_{i}^{n} - \frac{\Delta t}{\Delta x}\left(\mathbf{F}_{i+1/2}^{n+1/2} - \mathbf{F}_{i-1/2}^{n+1/2}\right) + \frac{1}{2}\mathbf{C}_{i}^{n+1/2}\Delta t + \mathbf{O}(\Delta x^2) \tag{A.21}$$

where $\mathbf{C}_{i}^{n+1/2}$ is estimated as

$$\mathbf{C}_{i}^{n+1/2} = \frac{1}{2}(\mathbf{C}_{i+1/2}^{n+1/2} + \mathbf{C}_{i-1/2}^{n+1/2}) \tag{A.22}$$

Imposing this scheme on the linear advection equation enables an integration of two

steps

$$w_i^{n+1} = w_i^n - \frac{v}{2}\left(w_{i+1}^n - w_{i-1}^n\right) + \frac{v^2}{2}\left(w_{i+1}^n - 2w_i^n + w_{i-1}^n\right) \tag{A.23}$$

Assuming $\Delta w_{i+1/2}^n = w_{i+1}^n - w_i^n$ and $\Delta w_{i-1/2}^n = w_i^n - w_{i-1}^n$ leads to

$$w_i^{n+1} = w_i^n - \frac{v}{2}\left(\Delta w_{i+1/2}^n + \Delta w_{i-1/2}^n\right) + \frac{v^2}{2}\left(\Delta w_{i+1/2}^n - \Delta w_{i-1/2}^n\right) \tag{A.24}$$

A schematic of the computational stencil in shown in figure A.1.

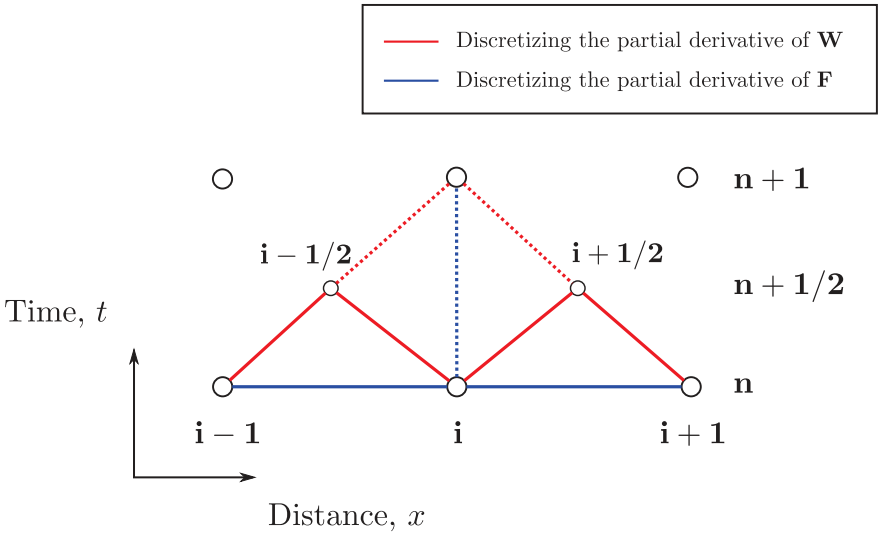

Fig. A.1.: Computational stencil of two-step Lax-Wendroff scheme

1.2. Lax-Wendroff 2-step with TVD

It is well-known, and as a consequence of Godunov's theorem, that finite difference schemes which have constant coefficients and are greater than first-order accuracy, such as the Lax-Wendroff method, produce local instabilities around shock waves and contact surfaces. This oscillatory behavior is nonphysical and is known as the Gibbs phenomenon. The classical approach to preventing oscillations was to introduce artificial viscosity into the solution, so called because it was added explicitly to the "viscosity" which is inherent in the numerical schemes. This palliative tended to smear the shocks and contact surfaces and, with large discontinuities, often failed completely. In addition, the same amount of damping, usually problem dependent, was applied indiscriminately across the whole solution domain.In the 1970s the Flux-Corrected Transport (FCT) technique was developed by Boris and Book [74, 75]. This approach attempts to apply sufficient global diffusion to the solution to eradicate nonphysical

oscillations, and then cancels it out with equal anti-diffusion in locations where it is not required. The criterion for this selectivity is incorporated in the nonlinear flux limiter; the magnitude of the anti-diffusion depends on the values of the solution from point to point. The total variation of the solution is then bounded by that of the initial data. It can be shown that the Lax-Wendroff scheme, as defined in Equation 2.62, is not TVD Sweby [76]. Harten [40] established criteria for three-point difference schemes to be TVD, and Sweby [76] used the concept of the "flux limiter" to construct TVD schemes which are second-order accurate. Davis [77] took the general form of the upwind TVD schemes analysed by Sweby and modified it in such a way as to render it independent of the direction of wave propagation. This approach essentially involved appending to the Lax-Wendroff scheme a nonlinear term which discerns precisely the correct amount of artificial viscosity required at each mesh point to prevent the occurrence of spurious oscillations. The resulting five-point scheme has the simplification of not being upwind biased, and is therefore easily implemented in existing Lax-Wendroff or MacCormack codes. A brief prescription of the method is given below. The two-step Lax-Wendroff method can be rendered in TVD form by appending, after the second step[50], the term:[50]

2. Total Diminishing Variation Scheme

The classical Two-Step Lax-Wendroff method, which is mentioned in section 1.1, cannot match the expectation of well-resolved solutions because it may raise oscillatory profiles at discontinuities.

As the forerunners, Godunov [78], Toro [79] and Roe [80] proposed a diversity of non-oscillatory solutions for the governing equations. The only flaw of these schemes is that the spatial accuracy is confined within the first-order. In this context, it is desired to introduce the so-called high-resolution scheme which is able to retain a satisfactory resolution without generating a spurious oscillation at discontinuities. Toro [79] interpreted the criterion of such numerical schemes in his work:

- No new local extremum is created as the time advances.
- The absolute value of the local extrema (including the minimal and maximal) must not decrease as the time advances.

In this context, Sweby has suggested a mathematical limitation for w_i^{n+1} which is sufficient to fulfill the both properties described above. This criterion, taking into account the values of the center cells w_i^n and the surrounding ones w_{i-1}^n and w_{i+1}^n, artificially gives rise to preventing the scheme from producing of a new local peak and suppressing the magnitude of any existing local peaks.

$$\min\{w_{i-1}^n, w_i^n, w_{i+1}^n\} \leq w_i^{n+1} \leq \max\{w_{i-1}^n, w_i^n, w_{i+1}^n\} \tag{A.25}$$

The other criterion raised by Sweby follows the principle of monotonicity preservation.

Assume a scheme can be written as:

$$w_i^{n+1} = \mathrm{G}^n \left(w_{i-k}^n, \cdots, w_i^n, \cdots, w_{i+l}^n \right) \tag{A.26}$$

where w_{i-k}^n, ... , w_{i+l}^n are the values of the surrounding cells from w_i^n. The scheme is called monotone if and only if it is an increasing function of all its arguments, which means mathematically

$$\frac{\partial \mathrm{G}}{\partial w_j} \geq 0, j = i-k, \cdots, i, \cdots, i+l \tag{A.27}$$

Moreover, in case the w^n is monotonic, the scheme remains monotonicity preserving if and only if w_i^{n+1} inherits the monotonic property from w_i^n as well. Unquestionably, the artificial oscillations fails to agree with anyone of these criteria. However, it was declared by Sweby [81] that it is not always simple and unconditional to recognize immediately if a numerical scheme can meet the requirements of criteria above.

A generally acceptable approach to defining these limitations mathematically was conceptually introduced by Ami Harten [82]. It was named as **Total Variation Diminishing** (abbr. **TVD**) Scheme. In the discrete case, the total variation refers to the sum of all the absolute differences between the adjacent cells in the calculation domain.

$$\mathrm{TV}(w^n) = \sum_i \left| w_{i+1}^n - w_i^n \right| \tag{A.28}$$

It can be also described in a continuous form:

$$\mathrm{TV}(w) = \int_0^L \left| \frac{\partial w}{\partial x} \right| dx \tag{A.29}$$

where L is the length of pipe. As the time advances, the total variation $TV(w)$ will increase in case either a new local peak is brought into the solutions, which gives rise to the spurious oscillations, or the absolute value of the current extrema grows. Thus, the only criterion from the TVD Scheme is that, for the discrete case, the new total variation of the solutions $\mathrm{TV}(w^{n+1})$ must be diminished as time advances

$$\textbf{TVD Criterion: } \mathrm{TV}(w^{n+1}) \leq \mathrm{TV}(w^n) \tag{A.30}$$

The characteristic of TVD assures the maintenance of the monotonicity as well, satisfying validly the third rule of non-oscillatory solutions which is mentioned previously. In addition, it was also implied by Winterbone's work [24] that a non-linear scheme, which consists of a series of variable coefficients, is second-order accurate when the TVD condition is achieved. Therefore, it creates the necessity for numerical schemes to be non-linear to prevent the production of local oscillations at discontinuities. Considering the general form of a non-linear scheme for the linear advection equation:

$$w_i^{n+1} = w_i^n - C_{i-1/2}^n \Delta w_{i-1/2}^n + D_{i+1/2}^n \Delta w_{i+1/2}^n \tag{A.31}$$

where the values of coefficients $C_{i-1/2}^n$ and $D_{i+1/2}^n$ rely respectively on the values of $w_{i-1/2}^n$ and $w_{i+1/2}^n$. As defined in equation (A.28), the total variation at the time level $n+1$ will be

$$\begin{aligned} TV(w_i^{n+1}) &= \sum_i \left| w_{i+1}^n - w_i^n \right| \\ &\leq \sum_i \left| (1 - C_{i+1/2}^n - D_{i+1/2}^n) \Delta w_{i+1/2}^n \right| + \left| C_{i-1/2}^n \Delta w_{i-1/2}^n \right| + \left| D_{i+3/2}^n \Delta w_{i+3/2}^n \right| \end{aligned} \tag{A.32}$$

where $i = 0, 1, 2..., I-1$. If the following conditions for the coefficients can be simultaneously guaranteed

$$\begin{aligned} C_{i-1/2}^n &\geq 0 \\ D_{i+3/2}^n &\geq 0 \\ 1 - C_{i+1/2}^n - D_{i+1/2}^n &\geq 0 \\ C_{-1/2}^n = D_{I+1/2}^n &= 0 \end{aligned} \tag{A.33}$$

Then the inequality (A.32) is developed further

$$\begin{aligned} TV(w_i^{n+1}) &\leq \sum_i \left| (1 - C_{i+1/2}^n - D_{i+1/2}^n) \Delta w_{i+1/2}^n \right| + \left| C_{i-1/2}^n \Delta w_{i-1/2}^n \right| + \left| D_{i+3/2}^n \Delta w_{i+1/2}^n \right| \\ &= \sum_i (1 - C_{i+1/2}^n - D_{i+1/2}^n) \left| \Delta w_{i+1/2}^n \right| + C_{i-1/2}^n \left| \Delta w_{i-1/2}^n \right| + D_{i+3/2}^n \left| \Delta w_{i+3/2}^n \right| \\ &= (1 - C_{1/2}^n - D_{1/2}^n) \left| \Delta w_{1/2}^n \right| + C_{-1/2}^n \left| \Delta w_{-1/2}^n \right| + D_{3/2}^n \left| \Delta w_{3/2}^n \right| \\ &+ (1 - C_{3/2}^n - D_{3/2}^n) \left| \Delta w_{3/2}^n \right| + C_{1/2}^n \left| \Delta w_{1/2}^n \right| + D_{5/2}^n \left| \Delta w_{5/2}^n \right| \\ &+ (1 - C_{5/2}^n - D_{5/2}^n) \left| \Delta w_{5/2}^n \right| + C_{3/2}^n \left| \Delta w_{3/2}^n \right| + D_{7/2}^n \left| \Delta w_{7/2}^n \right| \\ &..... \\ &+ (1 - C_{I-3/2}^n - D_{I-3/2}^n) \left| \Delta w_{I-3/2}^n \right| + C_{I-5/2}^n \left| \Delta w_{I-5/2}^n \right| + D_{I-1/2}^n \left| \Delta w_{I-1/2}^n \right| \\ &+ (1 - C_{I-1/2}^n - D_{I-1/2}^n) \left| \Delta w_{I-1/2}^n \right| + C_{I-3/2}^n \left| \Delta w_{I-3/2}^n \right| + D_{I+1/2}^n \left| \Delta w_{I+1/2}^n \right| \\ &= \left(\sum_i \left| w_{i+1}^n - w_i^n \right| \right) - D_{1/2}^n \left| \Delta w_{1/2}^n \right| - C_{I-1/2}^n \left| \Delta w_{I-1/2}^n \right| \leq \sum_i \left| w_{i+1}^n - w_i^n \right| = TV(w_i^n) \end{aligned} \tag{A.34}$$

Therefore, the essential restrictions for achieving total variation diminishing are exactly

the ones enumerated in (A.33). It must be emphasized that supposing the coefficients $C^n_{i-1/2}$ and $D^n_{i+1/2}$ are totally independent from the physical quantity w, the statement will be reduced to a linear scheme, giving rise to an artificial oscillation again.

The TVD criteria are also capable of determining whether an existing scheme may solve the numerical problems without oscillation. As a representative example, a test is made for the two-step Lax-Wendroff scheme. Reshaping the linear advection equations of the method (A.23) into the form of (A.31) gives

$$w_i^{n+1} = w_i^n - (\frac{1}{2}v + \frac{1}{2}v^2) \cdot \Delta w^n_{i-1/2} + (-\frac{1}{2}v + \frac{1}{2}v^2) \cdot \Delta w^n_{i+1/2} \tag{A.35}$$

where the restrictions for $C_{i-1/2}$ and $D_{i+1/2}$ embody in:

$$\begin{aligned} C_{i-1/2} &= \frac{1}{2}v + \frac{1}{2}v^2 && \geq 0 \\ D_{i+1/2} &= -\frac{1}{2}v + \frac{1}{2}v^2 && \geq 0 \\ C_{i-1/2} + D_{i+1/2} &= \frac{1}{2}v + \frac{1}{2}v^2 - \frac{1}{2}v + \frac{1}{2}v^2 && \leq 1 \end{aligned} \tag{A.36}$$

the solution of which is exclusively

$$v = 1 \tag{A.37}$$

which consequently causes the invariability of physical quantity w.

$$w_i^{n+1} = w_i^n \tag{A.38}$$

In this critical case, although the scheme obviously keeps the iteration from generation or growth of a local extremum, the convection resulting from the relative motion of the fluid particles will be restricted to zero in the global flow domain, which is unfortunately not in accord with the actual case.

In this context, several recent approaches from Chakravarthy and Osher[83], Harten[82], van Leer[84] and etc., were oriented to reconstruct the scheme of two-step Lax-Wendroff by means of redefining and non-linearizing its coefficients with respect to the TVD criteria. Besides that, Toro[79] and LeVeque[85] involved the theory into the system of non-linear equations, more specifically, the Euler Equations.

2.1. TVD scheme in a single direction

Of a great significance, Sweby [76] has introduced a basic approach of flux limiter to restraint the magnitude of the anti-diffusive flux term. The complete evolution of the function for flux limiter was implemented upon the linear advection equation in a single direction of propagation ($c > 0$). Reconstructing Lax-Wendroff scheme (A.24) in

the following expression

$$w_i^{n+1} = w_i^n - v\Delta w_{i-1/2}^n - \frac{1}{2}v(1-v)\Delta_-(\Delta w_{i+1/2}^n) \tag{A.39}$$

where Δ_- symbolizes

$$\Delta_-(\Delta w_{i+1/2}^n) = (\Delta w_{i+1/2}^n - \Delta w_{i-1/2}^n) = (w_{i+1}^n - w_i^n) - (w_i^n - w_{i-1}^n) \tag{A.40}$$

Sweby [76] pointed out the scheme (A.39) can be thought as a combination of the first-order upwind scheme for the positive propagation $(c > 0)$

$$w_i^{n+1} = w_i^n - v\Delta w_{i-1/2}^n \tag{A.41}$$

and the rest term:

$$-\frac{1}{2}v(1-v)\Delta_-(\Delta w_{i+1/2}^n) \tag{A.42}$$

Godunov has proved in his thesis [78] that the first-order upwind scheme (A.41), which refers equivalently to the first part of the equation (A.39), behaves unconditionally robustly, no matter what data for w is given. That reveals evidently that the occurrence of the spurious oscillation will not be the outcome from the first-order upwind scheme, but only from the term (A.42). This term was designated as an anti-diffusive one since it acts as a resistance to the diffusion of the quantity w. Apparently, the essential treatment to prevent the scheme from oscillation is to constraint the contribution of the anti-diffusive term. A so-called flux limiter ϕ is designed to fulfill the mission. The application of the flux limiter is found at

$$w_i^{n+1} = w_i^n - v\Delta w_{i-1/2}^n - \frac{1}{2}v(1-v)\Delta_-(\phi_i\Delta w_{i+1/2}^n) \tag{A.43}$$

Unlike the coefficient of a linear scheme, the flux limiter ϕ is a data-dependent function, which forces the scheme to be non-linear. Moreover, the evaluation of every limiter ϕ_i must be closely associated with the profiles of local solutions. If a continuous profile is obtained around the cell $i\Delta x$, it means the solved data in that surroundings is smooth enough so that a factitious interfere for limiting the anti-diffusive term will be less necessary, thus, a close-to-one flux limiter is supposed to be predicted in order to approach a quasi-second-order-accurate two-step Lax-Wendroff scheme. On the contrary, if a high-discontinuous data is detected, a close-to-zero flux limiter has to be employed for approaching a quasi-first-order-accurate upwind-like scheme in order to yield a non-oscillatory profile by introducing a sufficient dissipation. The prediction of ϕ_i for the data profiles between extreme smoothness and extreme roughness ranges logically from $(0, 1)$.

Significantly, van Leer suggested that a non-negative flux limiter is supposed to be a

function of the ratio of consecutive gradients of the data r_i.

$$\phi_i = \phi(r_i) = \phi(\frac{\Delta^n_{i-1/2}}{\Delta^n_{i+1/2}}) \tag{A.44}$$

As revealed previously, shrinking the flux limiter will although help stabilize the scheme, it sacrifices the numerical accuracy in the meanwhile. An optimal approach to evaluating the limiter function ϕ_i is, thereby, to achieve a large limiter as possible, where the constraint of TVD conditions is valid. Then the full expansion for the equation is:

$$w^{n+1}_i = w^n_i - v\Delta w^n_{i-1/2} - \frac{1}{2}v(1-v)(\phi_i \Delta w^n_{i+1/2} - \phi_{i-1}\Delta w^n_{i-1/2}) \tag{A.45}$$

The equation (A.45) can be rearranged as a statement agreeing with the first-order upwind scheme, in order to make up a stable form in terms of the principle of TVD.

$$w^{n+1}_i = w^n_i - \left[v + \frac{1}{2}v(1-v)\frac{\phi_i \Delta w^n_{i+1/2} - \phi_{i-1}\Delta w^n_{i-1/2}}{\Delta w_{i-1/2}}\right] \cdot \Delta w^n_{i-1/2} \tag{A.46}$$

With respect to the description of r_i, the equation (A.46) is reduced to

$$w^{n+1}_i = w^n_i - \left[v + \frac{1}{2}v(1-v)\left(\frac{\phi_i}{r_i} - \phi_{i-1}\right)\right] \cdot \Delta w^n_{i-1/2} \tag{A.47}$$

If expressing the coefficient $C^n_{i-1/2}$ as

$$C^n_{i-1/2} = v + \frac{1}{2}v(1-v)\left(\frac{\phi_i}{r_i} - \phi_{i-1}\right), \tag{A.48}$$

the other one $D^n_{i+1/2}$ can simply vanish

$$D^n_{i+1/2} = 0 \tag{A.49}$$

According to the limitation for $C^n_{i-1/2}$ and $D^n_{i+1/2}$ from (A.33),

$$0 \leq v + \frac{1}{2}v(1-v)\left(\frac{\phi_i}{r_i} - \phi_{i-1}\right) \leq 1 \tag{A.50}$$

With regard to the CFL condition which states $|v| \leq 1$ should be satisfied,

$$-\frac{2}{1-v} \leq \frac{\phi_i}{r_i} - \phi_{i-1} \leq \frac{2}{v} \tag{A.51}$$

Furthermore, a full validity of the inequality can be obtained only if

$$\left|\frac{\phi_i}{r_i} - \phi_{i-1}\right| \leq 2 \tag{A.52}$$

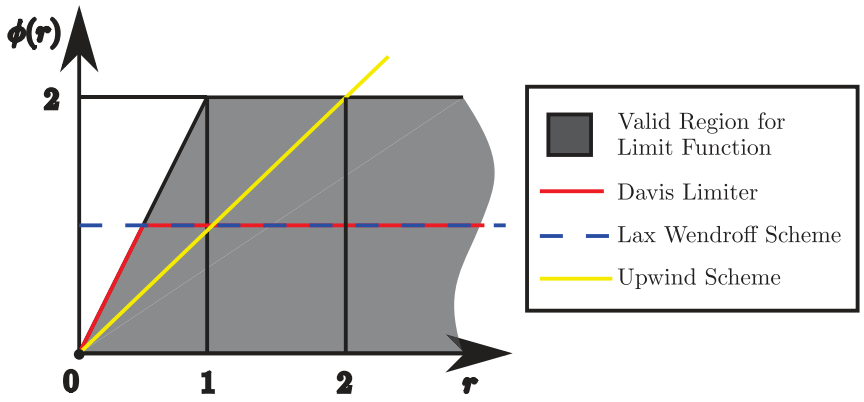

Fig. A.2.: Valid zone of flux limiter indicated by the TVD criterion

since the flux limiter is defined as a non-negative number, separate constraints can be imposed for estimating $\frac{\phi(r)}{r}$ and $\phi(r)$

$$\phi(r) \in [0,2], \frac{\phi(r)}{r} \in [0,2] \tag{A.53}$$

The valid region for evaluating the relationship between the data-dependent parameter r_i and the limiter function $\phi(r)$ is shown in figure A.2 and table A.1.

Flux Limiter	Function
Davis Limiter	$\phi < \frac{1}{2}, r < \frac{1}{2}$ $\phi = 1, r \geq \frac{1}{2}$
Upwind Scheme	$\phi = r$
Lax Wendroff Scheme	$\phi = 1$

Table A.1.: Mathematical expressions of different flux limiters

2.2. Symmetric TVD scheme

In the previous discussion for evaluating the flux limiters, only the situation for positive linear advection $(c > 0)$ was taken into account. Obviously, if the propagation speed remains negative $(c < 0)$, the evolution of the flux limiter function must be reorganized to adapt to the new upwind direction. Instead of (A.39), the Lax Wendroff scheme in this circumstance will be then transformed into:

$$w_i^{n+1} = w_i^n - v\Delta w_{i+1/2}^n - \frac{1}{2}v(1+v)\Delta_+(\Delta w_{i-1/2}^n) \tag{A.54}$$

where comparably, the first part of the expression, $w_i^{n+1} = w_i^n - v\Delta w_{i+1/2}^n$ is equivalent to upwind scheme of negative propagation ($c < 0$). The symbolic term $\Delta_+(\Delta w_{i-1/2}^n)$ refers to the difference between the local variations of the consecutive cells, formally,

$$\Delta_+(\Delta w_{i-1/2}^n) = \Delta w_{i-1/2}^n - \Delta w_{i+1/2}^n \tag{A.55}$$

Analogically, adding a flux limiter into the scheme to prevent it from any possible oscillations at discontinuities

$$w_i^{n+1} = w_i^n - v\Delta w_{i+1/2}^n - \frac{1}{2}v(1+v)\Delta_+\left(\phi_i(r_i)\Delta w_{i-1/2}^n\right) \tag{A.56}$$

The flux limiter is conventionally defined as a function of the ratio r_i between the upwind gradient (numerator) and downwind one (denominator) of the solutions. Thereby, the formulation of r_i for the advection equation in a negative propagation speed must distinguish from the one in a positive propagation speed.

$$r_i = \frac{\Delta w_{i+1/2}^n}{\Delta w_{i-1/2}^n} \tag{A.57}$$

Regarding the general form of a non-linear scheme (A.31) and , the two coefficients $C_{i-1/2}^n$ and $D_{i+1/2}^n$ will currently represent

$$\begin{aligned} C_{i-1/2}^n &= 0 \\ D_{i+1/2}^n &= -v - \frac{1}{2}v(1+v)\frac{\Delta_+(\Delta w_{i-1/2}^n)}{\Delta w_{i+1/2}^n} \\ &= -v\left\{1 + \frac{1}{2}(1+v)\frac{\phi_i\Delta w_{i-1/2}^n - \phi_{i+1}\Delta w_{i+1/2}^n}{\Delta w_{i+1/2}^n}\right\} \\ &= -v\left\{1 + \frac{1}{2}(1+v)\left[\frac{\phi_i}{r_i} - \phi_{i+1}\right]\right\} \end{aligned} \tag{A.58}$$

Fortunately, the valid range of ϕ obtained from the TVD criteria remains the same as the one in case of $c < 0$, which is stated in equation (A.53). However, it can be noticed that some differences have appeared in implementing the TVD scheme on positive- and negative-traveling-speed advection equations, such as in formulating the coefficient $C_{i-1/2}^n$ and $D_{i+1/2}^n$. Therefore, two distinguished statements for TVD scheme have to be given to cover all the possibilities ($c > 0$ and $c < 0$). Undoubtedly, it will arise the inconveniences of determining the direction of upwind before conducting a numerical calculation.

In 1987, Davis [86] put forward a symmetric TVD approach Lax-Wendroff scheme as to remove the necessity for ascertaining the propagating direction. In addition, a term generating a local artificial dissipation is appended to the Lax-Wendroff scheme in

order to ensure the nonoccurence of the local spurious oscillations at discontinuities. The magnitude of the artificial dissipation is yet precisely controlled so that the scheme will not scarifies too much accuracy for holding the TVD criteria.

Davis suggested the dissipative term should take the forms

$$\begin{cases} G^{+}_{i+1/2}(r^{+}_{i})\Delta w^{n}_{i+1/2} - G^{+}_{i-1/2}(r^{+}_{i-1})\Delta w^{n}_{i-1/2}\,, & c>0 \\ G^{-}_{i+1/2}(r^{-}_{i+1})\Delta w^{n}_{i+1/2} - G^{-}_{i-1/2}(r^{-}_{i})\Delta w^{n}_{i-1/2}, & c<0 \end{cases} \tag{A.59}$$

The script "+" refers to the appended term for $c>0$, while conversely "-" refers to the one for $c<0$. The ratio of consecutive gradients for these two situation is

$$r^{+}_{i} = \frac{\Delta w^{n}_{i-1/2}}{\Delta w^{n}_{i+1/2}},\; r^{-}_{i} = \frac{\Delta w^{n}_{i-1/2}}{\Delta w^{n}_{i+1/2}} \tag{A.60}$$

Adding them respectively into the (A.24) gives

$$w^{n+1}_{i} = \begin{cases} w^{n}_{i} - \left\{ v\left[1+\frac{1}{2}(1-v)\left(\frac{1}{r^{+}_{i}}-1\right)\right] - \left[\frac{G^{+}_{i+1/2}}{r^{+}_{i}} - G^{+}_{i-1/2}\right]\right\}\Delta w^{n}_{i-1/2}, & c>0 \\ w^{n}_{i} + \left\{ -v\left[1+\frac{1}{2}(1+v)\left(\frac{1}{r^{-}_{i}}-1\right)\right] - \left[\frac{G^{-}_{i-1/2}}{r^{-}_{i}} - G^{-}_{i+1/2}\right]\right\}\Delta w^{n}_{i+1/2}, & c<0 \end{cases} \tag{A.61}$$

Evidently, the coefficients $C^{n}_{i-1/2}$ and $D^{n}_{i+1/2}$ can be indicated from these relationships above.

$$c>0: \begin{cases} \left(C^{n}_{i-1/2}\right)^{+} = v\left[1+\frac{1}{2}(1-v)\left(\frac{1}{r^{+}_{i}}-1\right)\right] - \left[\frac{G^{+}_{i+1/2}}{r^{+}_{i}} - G^{+}_{i-1/2}\right] \\ \left(D^{n}_{i+1/2}\right)^{+} = 0 \end{cases} \tag{A.62}$$

$$c<0: \begin{cases} \left(C^{n}_{i-1/2}\right)^{-} = 0 \\ \left(D^{n}_{i+1/2}\right)^{-} = -v\left[1+\frac{1}{2}(1+v)\left(\frac{1}{r^{-}_{i}}-1\right)\right] - \left[\frac{G^{-}_{i-1/2}}{r^{-}_{i}} - G^{-}_{i+1/2}\right] \end{cases} \tag{A.63}$$

Making a comparison between the specified coefficients $C^{n}_{i-1/2}$ and $D^{n}_{i+1/2}$ by the TVD criteria in (A.48), (A.49) and (A.58) with those from the assumptions of Davis in (A.62)

and (A.63), the coefficients G^+ and G^- included in the dissipative terms will denote

$$c>0:\begin{cases} G^+_{i+1/2}(r^+_i)=\dfrac{v}{2}(1-v)[1-\phi(r^+_i)] \\ G^+_{i-1/2}(r^+_{i-1})=\dfrac{v}{2}(1-v)[1-\phi(r^+_{i-1})] \end{cases} \tag{A.64}$$

$$c<0:\begin{cases} G^-_{i+1/2}(r^-_{i+1})=-\dfrac{v}{2}(1+v)[1-\phi(r^-_{i+1})] \\ G^-_{i-1/2}(r^-_i)=-\dfrac{v}{2}(1+v)[1-\phi(r^-_i)] \end{cases} \tag{A.65}$$

These two statements can be patched together into the equation (A.24),

$$\begin{aligned} w^{n+1}_i = w^n_i - \frac{v}{2}\left(\Delta w^n_{i+1/2}+\Delta w^n_{i-1/2}\right)+\frac{v^2}{2}\left(\Delta w^n_{i+1/2}-\Delta w^n_{i-1/2}\right) \\ +\left(G^+_{i+1/2}(r^+_i)+G^-_{i+1/2}(r^-_{i+1})\right)\Delta w^n_{i+1/2} \\ -\left(G^+_{i-1/2}(r^+_{i-1})+G^-_{i-1/2}(r^-_i)\right)\Delta w^n_{i-1/2} \end{aligned} \tag{A.66}$$

if only the G^+ terms vanish when propagation speed is negative $a<0$, and so do the G^- terms under $a>0$.

$$G^+_{i+1/2}(r^+_i)=\begin{cases} \dfrac{v}{2}(1-v)[1-\phi(r^+_i)] & c>0 \\ 0 & c<0 \end{cases} \tag{A.67}$$

$$G^+_{i-1/2}(r^+_{i-1})=\begin{cases} \dfrac{v}{2}(1-v)[1-\phi(r^+_{i-1})] & c>0 \\ 0 & c<0 \end{cases} \tag{A.68}$$

$$G^-_{i+1/2}(r^-_{i+1})=\begin{cases} 0 & c>0 \\ -\dfrac{v}{2}(1+v)[1-\phi(r^-_{i+1})] & c<0 \end{cases} \tag{A.69}$$

$$G^-_{i-1/2}(r^-_i)=\begin{cases} 0 & c>0 \\ -\dfrac{v}{2}(1+v)[1-\phi(r^-_i)] & c<0 \end{cases} \tag{A.70}$$

Obviously, the coefficient functions (A.67) and (A.69) are symmetrical about the axis $c=0$, and so are the functions (A.68) and (A.70). Therefore, it is very reasonable to introduce simply a uniform expression for the $G^+_{i+1/2}$ and $G^-_{i+1/2}$ as well as for $G^+_{i-1/2}$ and $G^-_{i-1/2}$, so that it will be not required anymore to determinate whether $a>0$ or $a<0$ and then select appropriate expressions for G from (A.67) to (A.70). The approach

is implemented in [77].
Assuming $G^{\pm}_{i+1/2}$ and $G^{\pm}_{i-1/2}$ have the following forms

$$\begin{aligned} G^{\pm}_{i+1/2} &= \frac{|v|}{2}(1-|v|)[1-\phi(r^{\pm}_{i})] \\ G^{\pm}_{i-1/2} &= \frac{|v|}{2}(1-|v|)[1-\phi(r^{\pm}_{i+1})] \end{aligned} \tag{A.71}$$

where some additional restrictions for the flux limiter $\phi(r^{\pm})$ are required to guarantee the validity of the transition from (A.67) $\sim$ (A.70) to (A.71)

$$\begin{cases} \phi(r^{-}_{i}) = 1 & \text{for } c > 0 \\ \phi(r^{+}_{i}) = 1 & \text{for } c < 0 \end{cases} \tag{A.72}$$

2.3. Application of TVD Scheme on Vectorized H-PDE

The evolution of single-direction or symmetric TVD scheme based on the linear advection equation can both be applied to the vectorized non-linear hyperbolic equation, which is stated in (A.11). Removing the source term $\mathbf{C}(\mathbf{W})$ from the equation gives:

$$\frac{\partial \mathbf{W}}{\partial t} + \frac{\partial \mathbf{F}(\mathbf{W})}{\partial x} = 0 \tag{A.73}$$

Considering the chain rule of partial derivative brings about

$$\frac{\partial \mathbf{W}}{\partial t} + \frac{\mathrm{d}\mathbf{F}(\mathbf{W})}{\mathrm{d}\mathbf{W}} \cdot \frac{\partial \mathbf{W}}{\partial x} = 0 \tag{A.74}$$

If proposing a Jacobian matrix $\mathbf{A}$ which represents

$$\mathbf{A}(\mathbf{W}) = \frac{\mathrm{d}\mathbf{F}(\mathbf{W})}{\mathrm{d}\mathbf{W}} \tag{A.75}$$

then the equation (A.73) becomes

$$\frac{\partial \mathbf{W}}{\partial t} + \mathbf{A}\frac{\partial \mathbf{W}}{\partial x} = 0 \tag{A.76}$$

Expanding the vector $\mathbf{W}$ in form of second-order-accurate Taylor series gives

$$\mathbf{W^{n+1}} = \mathbf{W^{n}} + \frac{\partial \mathbf{W}}{\partial t}\Delta t + \frac{1}{2}\frac{\partial^2 \mathbf{W}}{\partial t^2}(\Delta t)^2 \tag{A.77}$$

As shown in the equation above, it is necessary to specify the involved partial derivatives $\frac{\partial \mathbf{W}}{\partial t}$ and $\frac{\partial^2 \mathbf{W}}{\partial t^2}$ before evaluating $\mathbf{W^{n+1}}$. If the matrix $\mathbf{A}$ is given as a constant, the

equation (A.76) implies

$$\frac{\partial \mathbf{W}}{\partial t} = -\mathbf{A}\frac{\partial \mathbf{W}}{\partial x} \tag{A.78}$$

and

$$\frac{\partial^2 \mathbf{W}}{\partial t^2} = \frac{\partial}{\partial t}\left(\frac{\partial \mathbf{W}}{\partial t}\right) = \frac{\partial}{\partial t}\left(-\mathbf{A}\frac{\partial \mathbf{W}}{\partial x}\right) = -\mathbf{A}\frac{\partial}{\partial x}\left(\frac{\partial \mathbf{W}}{\partial t}\right) = \mathbf{A}^2\frac{\partial^2 \mathbf{W}}{\partial x} \tag{A.79}$$

Then, the issue is converted into the determination of the derivatives $\frac{\partial \mathbf{W}}{\partial x}$ and $\frac{\partial^2 \mathbf{W}}{\partial x^2}$. Expanding the $\mathbf{W}$ at $(n\Delta t, (i+1)\Delta x)$ and $(n\Delta t, (i-1)\Delta x)$ with regard to Taylor series gives

$$\begin{aligned}
\mathbf{W}(x+\Delta x) &= \mathbf{W}(x) + \frac{\partial \mathbf{W}}{\partial x}\Delta x + \frac{1}{2}\frac{\partial \mathbf{W}^2}{\partial^2 x}\Delta x^2 + \mathbf{O}(\Delta x^3)\cdots\cdots(1) \\
\mathbf{W}(x-\Delta x) &= \mathbf{W}(x) - \frac{\partial \mathbf{W}}{\partial x}\Delta x + \frac{1}{2}\frac{\partial \mathbf{W}^2}{\partial^2 x}\Delta x^2 + \mathbf{O}(\Delta x^3)\cdots\cdots(2)
\end{aligned} \tag{A.80}$$

Omitting the high-order terms of Δx, then $\frac{\partial \mathbf{W}}{\partial x}$ is derived by $(1)-(2)$, while the other one $\frac{\partial^2 \mathbf{W}}{\partial x^2}$ can be calculated from $(1)+(2)$.

$$\begin{aligned}
\frac{\partial \mathbf{W}}{\partial x} &= \frac{\mathbf{W}(x+\Delta x) - \mathbf{W}(x-\Delta x)}{2\Delta x} \\
\frac{\partial^2 \mathbf{W}}{\partial x^2} &= \frac{\mathbf{W}(x+\Delta x) - 2\mathbf{W}(x) + \mathbf{W}(x-\Delta x)}{\Delta x}
\end{aligned} \tag{A.81}$$

Substituting these partial derivatives into (A.77) with regard to the evolutions (A.78), (A.79) and (A.81) gives rise to the vectorized Lax-Wendroff method:

$$\mathbf{W}_i^{n+1} = \mathbf{W}_i^n - \frac{1}{2}\frac{\Delta t}{\Delta x}\mathbf{A}\left(\mathbf{W}_{i+1}^n - \mathbf{W}_{i-1}^n\right) + \frac{1}{2}\left(\frac{\Delta t}{\Delta x}\right)^2 \mathbf{A}^2\left(\mathbf{W}_{i+1}^n - 2\mathbf{W}_i^n + \mathbf{W}_{i-1}^n\right) \tag{A.82}$$

In case the physical quantity $\mathbf{W}$ equals a null vector, then in view of (A.13), the flux term will be forced to be a zero vector as well.

$$\mathbf{W} = [0,0,0]^{\mathrm{T}} \Rightarrow \mathbf{F}(\mathbf{W}) = [0,0,0]^{\mathrm{T}} \tag{A.83}$$

On the other hand, since the Jacobin matrix $\mathbf{A} = \frac{\mathrm{d}\mathbf{F}}{\mathrm{d}\mathbf{W}}$ is assumed to be invariable, it can be inferred from the particular condition (A.83) that the $\mathbf{F}$ should be proportional to the $\mathbf{W}$

$$\mathbf{F}(\mathbf{W}) = \mathbf{A}\mathbf{W} \tag{A.84}$$

Replacing this proportional correlation (A.84) into (A.82), the equation can be simplified to

$$\mathbf{W}_i^{n+1} = \mathbf{W}_i^n - \frac{\Delta t}{\Delta x}\mathbf{A}\left\{\frac{1}{2}\left[\mathbf{W}_{i+1}^n - \mathbf{W}_{i-1}^n\right] - \frac{1}{2}\frac{\Delta t}{\Delta x}\left[\mathbf{F}_{i+1}^n - 2\mathbf{F}_i^n + \mathbf{F}_{i-1}^n\right]\right\} \tag{A.85}$$

Applying the Lax-Friedrichs scheme over half-cell intervals on the equation (A.85) gives (see (A.16) but neglect the source term $\mathbf{C}$),

$$\begin{aligned}\mathbf{W}_i^{n+1} &= \mathbf{W}_i^n - \frac{\Delta t}{\Delta x}\mathbf{A}\left(\mathbf{W}_{i+1/2}^{n+1/2} - \mathbf{W}_{i-1/2}^{n+1/2}\right) \\ &= \mathbf{W}_i^n - \frac{\Delta t}{\Delta x}\left(\mathbf{F}_{i+1/2}^{n+1/2} - \mathbf{F}_{i-1/2}^{n+1/2}\right)\end{aligned} \tag{A.86}$$

Therefore, the equation (A.82) is mathematically in accord with the the Two-Step Lax-Wendroff scheme described in the previous section, where a constant matrix $\mathbf{A}$ needs to be premised. Based on the vectorization of Lax-Wendroff scheme, Davis developed a Lax-Wendroff-method-based TVD scheme in a vectorial form. As long as the square matrix $\mathbf{A}_{m\times m}$ possesses real eigenvalues and correspondingly a full set of right eigenvectors, one of which is linearly independent from one another, then there exists a matrix $\mathbf{P}_{m\times m}$ containing all the right eigenvectors of $\mathbf{A}$: $\lambda_1, \lambda_2 \cdots \lambda_m$, which enables the transformation

$$\mathbf{P}^{-1}\mathbf{A}\mathbf{P} = \mathbf{E} \tag{A.87}$$

where $\mathbf{E}$ is a diagonal matrix involving all the eigenvalues of the matrix $\mathbf{A}$.

$$\mathbf{E} = \begin{bmatrix} \lambda_1 & 0 & \cdots & 0 \\ 0 & \lambda_2 & & \vdots \\ \vdots & & \ddots & 0 \\ 0 & \cdots & 0 & \lambda_m \end{bmatrix} \tag{A.88}$$

Multiplying the hyperbolic equation (A.78) by the $\mathbf{P}$ on the left side:

$$\begin{aligned} & \mathbf{P}^{-1}\frac{\partial \mathbf{W}}{\partial x} + \mathbf{P}^{-1}\mathbf{A}\frac{\partial \mathbf{W}}{\partial x} = 0 \\ \Rightarrow \quad & \frac{\partial\left(\mathbf{P}^{-1}\mathbf{W}\right)}{\partial x} + \mathbf{P}^{-1}\mathbf{A}\mathbf{P}\frac{\partial\left(\mathbf{P}^{-1}\mathbf{W}\right)}{\partial x} = 0 \\ \Rightarrow \quad & \frac{\partial \mathbf{V}}{\partial x} + \mathbf{E}\frac{\partial \mathbf{V}}{\partial x} = 0 \end{aligned} \tag{A.89}$$

where the matrix $\mathbf{V}_{m\times m}$ represents

$$\mathbf{V} = \mathbf{P}^{-1}\mathbf{W} \tag{A.90}$$

Applying the scalar TVD scheme from (A.66) to (A.90) and replacing the variable w, Courant number v and the coefficients $G^{\pm}$ respectively with the matrices $\mathbf{V}$, $\mathbf{v}$, $\mathbf{G}$ yields

$$\begin{aligned}\mathbf{V}_i^{n+1} = \mathbf{V}_i^n - \frac{\mathbf{v}}{2}\left(\mathbf{V}_{i+1}^n - \mathbf{V}_{i-1}^n\right) + \frac{\mathbf{v}^2}{2}\left(\mathbf{V}_{i+1}^n - 2\mathbf{V}_i^n + \mathbf{V}_{i-1}^n\right) \\ + \left(\mathbf{G}_{i+1/2}^{+}(r_i^{+}) + \mathbf{G}_{i+1/2}^{-}(r_{i+1}^{-})\right)\Delta\mathbf{V}_{i+1/2}^n \\ - \left(\mathbf{G}_{i-1/2}^{+}(r_{i-1}^{+}) + \mathbf{G}_{i-1/2}^{-}(r_i^{-})\right)\Delta\mathbf{V}_{i-1/2}^n\end{aligned} \tag{A.91}$$

where the matrix $\mathbf{v}$ denotes

$$\mathbf{v} = \mathbf{E}\frac{\Delta t}{\Delta x} = \mathbf{P}^{-1}\mathbf{A}\mathbf{P}\frac{\Delta t}{\Delta x} \tag{A.92}$$

With regard to the definition of $\mathbf{V}$, there exists

$$\mathbf{P}\mathbf{V} = \mathbf{P}(\mathbf{P}^{-1}\mathbf{W}) = \mathbf{W} \tag{A.93}$$

Hence, multiply equation (A.91) by $\mathbf{P}$ and substitute $\mathbf{v}$ with (A.92), gaining the equation in terms of the original variables.

$$\begin{aligned}\mathbf{W}_i^{n+1} = \mathbf{W}_i^n - \frac{1}{2}\frac{\Delta t}{\Delta x}\mathbf{A}\left(\mathbf{W}_{i+1}^n - \mathbf{W}_{i-1}^n\right) + \frac{1}{2}\left(\frac{\Delta t}{\Delta x}\right)^2\mathbf{A}^2\left(\mathbf{W}_{i+1}^n - 2\mathbf{W}_i^n + \mathbf{W}_{i-1}^n\right) \\ + \mathbf{P}\left(\mathbf{G}_{i+1/2}^{+}(r_i^{+}) + \mathbf{G}_{i+1/2}^{-}(r_{i+1}^{-})\right)\mathbf{P}^{-1}\Delta\mathbf{W}_{i+1/2}^n \\ - \mathbf{P}\left(\mathbf{G}_{i-1/2}^{+}(r_{i-1}^{+}) + \mathbf{G}_{i-1/2}^{-}(r_i^{-})\right)\mathbf{P}^{-1}\Delta\mathbf{W}_{i-1/2}^n\end{aligned} \tag{A.94}$$

Obviously, the first row of equation (A.94) is exactly in accord with the vectorized Lax-Wendroff scheme in (A.82). The only remaining problem of this scheme is to cope with the complicated coefficients in the dissipative terms.

$$\mathbf{P}\left(\mathbf{G}_{i+1/2}^{+}(r_i^{+}) + \mathbf{G}_{i+1/2}^{-}(r_{i+1}^{-})\right)\mathbf{P}^{-1}, \mathbf{P}\left(\mathbf{G}_{i-1/2}^{+}(r_{i-1}^{+}) + \mathbf{G}_{i-1/2}^{-}(r_i^{-})\right)\mathbf{P}^{-1} \tag{A.95}$$

The calculation of these terms requires the determination of the matrices $\mathbf{P}$ and $\mathbf{P}^{-1}$ as well as the direction of upwind in advance. Davis [77] provided a simplified approach of this scheme in order to remove these demands. The $\mathbf{G}^{\pm}$ can be evaluated approximately as the product of the diagonal matrices $\bar{\mathbf{G}}^{\pm}$ and the unit matrix $\mathbf{I}$:

$$\mathbf{G}^{\pm}(r) = \bar{\mathbf{G}}^{\pm}(r)\mathbf{I} \tag{A.96}$$

then

$$\mathbf{P}\mathbf{G}^{\pm}(r)\mathbf{P}^{-1} = \mathbf{P}\left(\bar{\mathbf{G}}^{\pm}(r)\mathbf{I}\right)\mathbf{P}^{-1} = \bar{\mathbf{G}}^{\pm}(r)\left(\mathbf{P}\mathbf{I}\mathbf{P}^{-1}\right) = \bar{\mathbf{G}}^{\pm}(r) \tag{A.97}$$

Hence, the dissipative terms in equation (A.94) are reduced to

$$\left(\bar{\mathbf{G}}^{+}_{i+1/2}(r^{+}_{i}) + \bar{\mathbf{G}}^{-}_{i+1/2}(r^{-}_{i+1})\right)\Delta\mathbf{W}^{n}_{i+1/2} - \left(\bar{\mathbf{G}}^{+}_{i-1/2}(r^{+}_{i-1}) + \bar{\mathbf{G}}^{-}_{i-1/2}(r^{-}_{i})\right)\Delta\mathbf{W}^{n}_{i-1/2} \tag{A.98}$$

The scalar ratio of consecutive gradients $r^{\pm}$ is defined as

$$\begin{cases} r^{+}_{i} = \dfrac{[\Delta\mathbf{W}^{n}_{i-1/2}, \Delta\mathbf{W}^{n}_{i+1/2}]}{[\Delta\mathbf{W}^{n}_{i+1/2}, \Delta\mathbf{W}^{n}_{i+1/2}]} \\ r^{-}_{i} = \dfrac{[\Delta\mathbf{W}^{n}_{i-1/2}, \Delta\mathbf{W}^{n}_{i+1/2}]}{[\Delta\mathbf{W}^{n}_{i-1/2}, \Delta\mathbf{W}^{n}_{i-1/2}]} \end{cases} \tag{A.99}$$

where the $[\cdots, \cdots]$ denotes the usual inner product. To give a more intuitive image of the expressions for $r^{\pm}$, expanding one of them r^{+}_{i} as an instance:

$$\begin{aligned} r^{+}_{i} &= \frac{\Delta\mathbf{W}^{n}_{i-1/2}\{1\}\Delta\mathbf{W}^{n}_{i+1/2}\{1\} + \Delta\mathbf{W}^{n}_{i-1/2}\{2\}\Delta\mathbf{W}^{n}_{i+1/2}\{2\} + \Delta\mathbf{W}^{n}_{i-1/2}\{3\}\Delta\mathbf{W}^{n}_{i+1/2}\{3\}}{\left[\Delta\mathbf{W}^{n}_{i-1/2}\{1\}\right]^{2} + \left[\Delta\mathbf{W}^{n}_{i-1/2}\{2\}\right]^{2} + \left[\Delta\mathbf{W}^{n}_{i-1/2}\{3\}\right]^{2}} \\ &= \frac{r^{+}_{i}\{1\}\left[\Delta\mathbf{W}^{n}_{i-1/2}\{1\}\right]^{2} + r^{+}_{i}\{2\}\left[\Delta\mathbf{W}^{n}_{i-1/2}\{2\}\right]^{2} + r^{+}_{i}\{3\}\left[\Delta\mathbf{W}^{n}_{i-1/2}\{3\}\right]^{2}}{\left[\Delta\mathbf{W}^{n}_{i-1/2}\{1\}\right]^{2} + \left[\Delta\mathbf{W}^{n}_{i-1/2}\{2\}\right]^{2} + \left[\Delta\mathbf{W}^{n}_{i-1/2}\{3\}\right]^{2}} \end{aligned} \tag{A.100}$$

where $\Delta\mathbf{W}^{+}_{i}\{k\}$ refers to the k^{th} element ($k = 1, 2, 3$) in the $\Delta\mathbf{W}^{+}_{i}$. Similarly to the definition of $r^{\pm}$ for linear advection equations, the parameter $r^{+}_{i}\{k\}$ represents

$$r^{+}_{i}\{k\} = \frac{\mathbf{W}^{n}_{i-1/2}\{k\}}{\mathbf{W}^{n}_{i+1/2}\{k\}} \tag{A.101}$$

Thereby, these definitions for $r^{\pm}_{i}$ in (A.100) can be explained as the weighted averages of the ratio $r^{\pm}_{i}\{1\}$, $r^{\pm}_{i}\{2\}$ and $r^{\pm}_{i}\{3\}$. In addition, the scalar functions of $\bar{\mathbf{G}}$ are specified as

$$\bar{\mathbf{G}}^{\pm}(r^{\pm}) = \frac{1}{2}C(v)[1 - \phi(r^{\pm})] \tag{A.102}$$

where the Courant number v is suggested to be data-dependent

$$v = \max\{|\lambda_1|, |\lambda_2|, \cdots, |\lambda_n|\} \cdot \frac{\Delta t}{\Delta x} \tag{A.103}$$

Davis indicated the non-negative function $C(v)$ can be chosen as follows

$$C(v) = \begin{cases} v(1-v), & v < 0.5 \\ 0.25, & v \geq 0.5 \end{cases} \tag{A.104}$$

Assuming the $\mathbf{W}$ is a 1×1 matrix, or more precisely, a scalar, then the issue is downsized to be one-dimensional. In that case, comparing the equation (A.76) with the linear advection equation, the main coefficients $\mathbf{A}$, $\mathbf{P}$ and $\mathbf{E}$ can be scaled as:

$$\mathbf{A} = a, \quad \mathbf{P} = \mathbf{P}^{-1} = 1, \quad \mathbf{E} = \lambda_1 = \mathbf{P}^{-1}\mathbf{A}\mathbf{P} = \mathbf{A} \tag{A.105}$$

The relationship $\lambda_1 = a$ can be inferred from the evolutions above. Particularly for $v < 0.5$, it makes the $\bar{\mathbf{G}}^{\pm}$ takes the same form as $G^{\pm}$ provided by (A.71). But instead of a unified modeling for $G^{\pm}$ in (A.71), this scheme specifies a constant value for $C(v)$ for $v > 0.5$ in order to avoid an extraordinarily large Courant number v evaluated by (A.103). For instance, a extreme case $v > 1$ will lead to the appearance of a negative $C(v)$, when keeping on using the expression of $C(v)$ for $v < 0.5$.

At last, the flux limiter occurred in equation (A.102), which was selected by Davis in [77], takes the form

$$\phi(r) = \begin{cases} \min\{2r, 1\}, & r \geq 0 \\ 0, & r < 0 \end{cases} \tag{A.106}$$

Owing to the equivalence of vectorized Lax-Wendroff scheme (A.82) and Two-Step Lax-Wendroff scheme (A.86), the symmetrical TVD scheme derived from the former can be simply applied to the latter as well. By attaching the artificial dissipative terms to the second-step calculation of Two-Step Lax-Wendroff method, a new algorithm holding the TVD property is obtained.

$$\begin{aligned} \mathbf{W}_i^{n+1} = \mathbf{W}_i^n - \frac{\Delta t}{\Delta x}\left(\mathbf{F}_{i+1/2}^{n+1/2} - \mathbf{F}_{i-1/2}^{n+1/2}\right) \\ + \left(\bar{\mathbf{G}}_{i+1/2}^{+}(r_i^{+}) + \bar{\mathbf{G}}_{i+1/2}^{-}(r_{i+1}^{-})\right)\Delta\mathbf{W}_{i+1/2}^{n} \\ - \left(\bar{\mathbf{G}}_{i-1/2}^{+}(r_{i-1}^{+}) + \bar{\mathbf{G}}_{i-1/2}^{-}(r_i^{-})\right)\Delta\mathbf{W}_{i-1/2}^{n} \end{aligned} \tag{A.107}$$

The spurious oscillations generated by the Lax-Wendroff scheme are caused by numerical dispersion which arises from the presence of third-order derivatives in the truncation error of the scheme. This dispersion causes high-frequency components to travel slower than the main component of a waveform. Discontinuities contain a significant contribution from high-frequency components and these separate out (disperse) from the main wave as it propagates, thus forming spurious oscillations. The addition of the term A.98 to the Lax-Wendroff algorithm represents an attempt to introduce sufficient local nonlinear dissipation to eradicate any oscillations where they occur. It is clear that the term A.98 is dissipative since it constitutes a second difference

with positive coefficients; essentially it is a dissipation term based on the theory of TVD schemes and it does not contain any free parameters

Consequently, TVD schemes for the computation of weak solutions of the nonlinear problem 2.36 have been developed according to the following guidelines:

- Design a scheme so that its linearized version is L2-stable.
- Add numerical dissipation to damp oscillations and to control "nonlinear instabilities".

Since the addition of numerical dissipation brings about loss of information, the designer of such numerical schemes finds himself in a position where he has to compromise accuracy to achieve stability, or vice versa[87].

3. Stability Analysis of the Numerical Schemes

In the previous sections, the derivation of diverse numerical approaches in the framework of FDM have been discussed. As mentioned at the beginning of this chapter, the stability of the numerical schemes is subject to the numerical errors, among which the round-off errors play a dominant role. Generically, a finite difference scheme is stable only if the round-off errors originated at one time level of the computation will not lead to the enlargement of them at the following time levels. If they attenuate with time and finally dissolve, the finite difference scheme is considered as a stable one. Otherwise, it is deemed to be unstable.

It is possible to check the stability of numerical methods through a simple but effective tool: **von Neumann Stability Analysis** (abbr. **VNSA**). The basic assumptions for performing this method are as followed[88]:

- The influences of the boundaries are not involved into consideration.
- The coefficients included in the difference equations vary so slowly with space and time that they can be treated as constants. Hence, the linear equations are preferable to this method.

To illustrate the procedure intuitively, take the 1D FTCS linear advection equation as instance

$$w_i^{n+1} = w_i^n - \frac{v}{2}(w_{i+1}^n - w_{i-1}^n) \tag{A.108}$$

If the exact solutions of the PDE is assumed as $\hat{w}$, then the equality is still valid for $\hat{w}$.

$$\hat{w}_i^{n+1} = \hat{w}_i^n - \frac{v}{2}(\hat{w}_{i+1}^n - \hat{w}_{i-1}^n) \tag{A.109}$$

Subtracting (A.109) from (A.108) obtains:

$$\epsilon_i^{n+1} = \epsilon_i^n - \frac{v}{2}(\epsilon_{i+1}^n - \epsilon_{i-1}^n) \tag{A.110}$$

where ϵ_i^n is defined as the error between the calculated approximation of the number w_i^n and its exact mathematical value $\hat{w}_i^n$.

$$\epsilon_i^{n+1} = w_i^n - \hat{w}_i^n \tag{A.111}$$

It is suggested that the variation of the error in space can be expanded in a Fouries series which contains a limited number of terms. The errors in the interval L at the time level n can be interpreted as the superposition of its components from every grid point, which is formally expressed as:

$$\epsilon^n(x) = \sum_{m=1}^{M} A_m^n e^{ik_m x} \tag{A.112}$$

where M is the total amount of the cells distributed in the interval L and the A_m denotes the amplitude of the error component from the cell m, which is a complex number. k_m is named as the wave number referring to

$$k_m = \frac{\pi m}{L} \tag{A.113}$$

The error component from the cell m is specified as

$$\epsilon_m = A_m^n e^{ik_m x} \tag{A.114}$$

Mathematically, if the error $\epsilon^n(x)$ decays in the next time level $n+1$, it leads to the inequality

$$|\epsilon^n(x)| < \left|\epsilon^{n+1}(x)\right| \tag{A.115}$$

hence, according to (A.112) and (A.114)

$$\left|\sum_{m=1}^{M} \epsilon_m\right| < \left|\sum_{m=1}^{M} \epsilon_m^{n+1}\right| \tag{A.116}$$

Then the sufficient condition for the validity of the inequality is that each error component from cell $m = 1, 2, 3..., M$ must be diminished at the following calculation step.

$$|\epsilon_m^n| < \left|\epsilon_m^{n+1}\right| \Leftrightarrow \left|A_m^n e^{ik_m x}\right| < \left|A_m^{n+1} e^{ik_m x}\right| \Leftrightarrow |A_m^n| < \left|A_m^{n+1}\right| \tag{A.117}$$

or in a brief criterion

$$|\xi_m| < 1 \tag{A.118}$$

where the complex number ξ_m is called amplification factor indicating the ratio of the

errors from two successive time levels n, $n+1$ at the cell m.

$$\xi_m = \frac{A_m^{n+1}}{A_m^n} \tag{A.119}$$

Formulating the error term for the FTCS difference equation (A.110) with equation (A.114) gives

$$A_m^{n+1} = A_m^n e^{ik_m x} - \frac{v}{2}\left[A_m^n e^{ik_m(x+\Delta x)} - A_m^n e^{ik_m(x-\Delta x)}\right] \tag{A.120}$$

After rearrangement

$$\begin{aligned} \xi_m &= 1 - \frac{v}{2}\left[e^{ik_m(x+\Delta x)} - e^{ik_m(x-\Delta x)}\right] \\ &= 1 - iv\sin(k_m\Delta x), \end{aligned} \tag{A.121}$$

the modulus $|\xi_m|$ is then

$$|\xi_m| = \sqrt{|\xi_m|^2} = \sqrt{\xi_m\bar{\xi}_m} = \sqrt{1 + v^2\sin^2(k_m\Delta x)} \geq 1 \tag{A.122}$$

Therefore, the FTCS scheme is proved to be unstable in any condition. By reason of this property, the scheme will not generate acceptable results so that it is scarcely employed in the numerical calculation of flow problems.

Such a criterion from von Neumann stability analysis is also applicable for the stability investigation of other numerical schemes. The amplification factor ξ_m of the Lax-Friedrichs scheme is expressed as:

$$|\xi_m| = \sqrt{1 - (1 - v^2)\sin^2(k_m\Delta x)} \tag{A.123}$$

Obviously, the equation (A.117) can be completely satisfied only if the condition

$$|v| \leq 1 \tag{A.124}$$

is guaranteed. This criterion is called **Courant-Friedrichs-Lewy stability condition** (abbr. **CFL condition**), which is obedient to the constraints imposed by VNSA. From the angle of mathematics, the CFL condition does not allow the dependence area of the solution from numerical calculation smaller than the one from physics (see figure A.3).

From the other viewing point, it ensures the information of physical quantities cannot be transmitted longer than the interval of a cell Δx in a single time step Δt. On the contrary, when the propagation distance of the physical information in Δt exceeds the mesh length Δx ,

$$|c|\,\Delta t > \Delta x \tag{A.125}$$

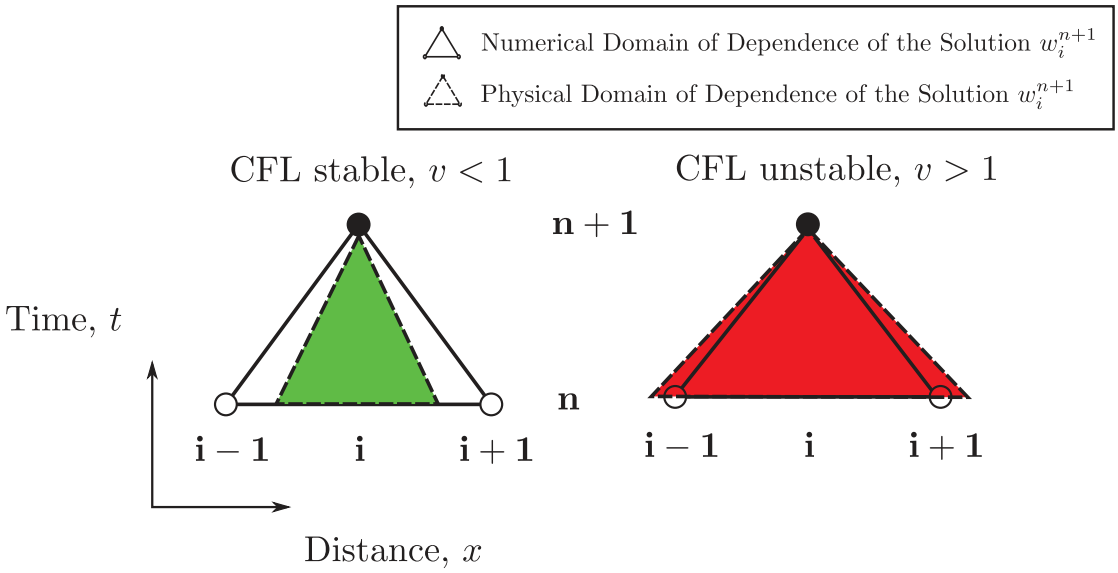

Fig. A.3.: Stencil of CFL stable and unstable selection of Courant Number v

the stability of the scheme must be damaged since the numerical error ϵ will grow with time. However, it must be underlined that the CFL condition is only a necessary but not sufficient criterion for the stability of the numerical schemes. As demonstrated in the evolution of the amplification factor ξ_m for the FTCS scheme, even if the Courant number v is less than the unity, the scheme still remains unstable.

Performing the VNSA on the Leapfrog scheme yields

$$A_m^{n+1} e^{ik_m x} = A_m^{n-1} e^{ik_m x} - v\left[A_m e^{ik_m(x+\Delta x)} - A_m e^{ik_m(x-\Delta x)}\right] \tag{A.126}$$

If a homogenous amplification of consecutive errors over two time levels is assumed,

$$\frac{A_m^{n+1}}{A_m^n} = \frac{A_m^n}{A_m^{n+1}} \tag{A.127}$$

then for any $|v| < 1$, the value of the amplification factor ξ_m is

$$\xi_m = \pm\sqrt{1 - v^2 \sin^2(k_m \Delta x)} - iv \sin(k_m \Delta x) \tag{A.128}$$

and thus,

$$|\xi_m| = \sqrt{1 - v^2 \sin^2(k_m \Delta x) + (v \sin(k_m \Delta x))^2} = 1 \tag{A.129}$$

Therefore, since neither the dissipation or the enlargement of the amplitude can be observed in this case, the Leapfrog scheme can achieve a neutral stability as long as the CFL condition is satisfied. However, this scheme may suffer from the stability problems

when the amplification is not equally distributed over the two time level.

Applying VNSA to the Lax-Wendroff scheme obtains

$$\xi_m = 1 - v^2(1 - \cos(k_m \Delta x)) - iv \sin(k_m \Delta x) \tag{A.130}$$

so that the modulus of the amplification factor is

$$|\xi_m| = \sqrt{1 - v^2(1 - v^2)\sin^2(k_m \Delta x)} \tag{A.131}$$

From the expression it is inferred that the valid zone of Courant number for the stability of scheme is $|v| \leq 1$ as well.

With respect to the general expression of TVD schemes in (A.31), the error equation will take the form as

$$\epsilon_m^{n+1} = (1 - C - D)\epsilon_m^n + C\epsilon_{m+1}^n + D\epsilon_{m-1}^n \tag{A.132}$$

where the coefficients C and D must satisfy

$$\begin{cases} 0 \leq C \leq 1 \\ 0 \leq D \leq 1 \\ 0 \leq C + D \leq 1 \end{cases} \tag{A.133}$$

as to hold the TVD properties permanently. The amplification factor ξ_m of the scheme will be then:

$$\xi_m = (1 - C - D) + Ce^{-ik_m \Delta x} + De^{ik_m \Delta x} \tag{A.134}$$

According to constraints in equation (A.133), the squared modulus of ξ_m will be

$$\begin{aligned} |\xi_m|^2 &\leq |1 - C - D|^2 + |C|^2 + |D|^2 \\ &\leq (1 - C - D) + C + D = 1 \end{aligned} \tag{A.135}$$

thus proving the numerical stability of any TVD schemes.

APPENDIX B

BOUNDARY CONDITIONS

1. Standard Boundary Conditions

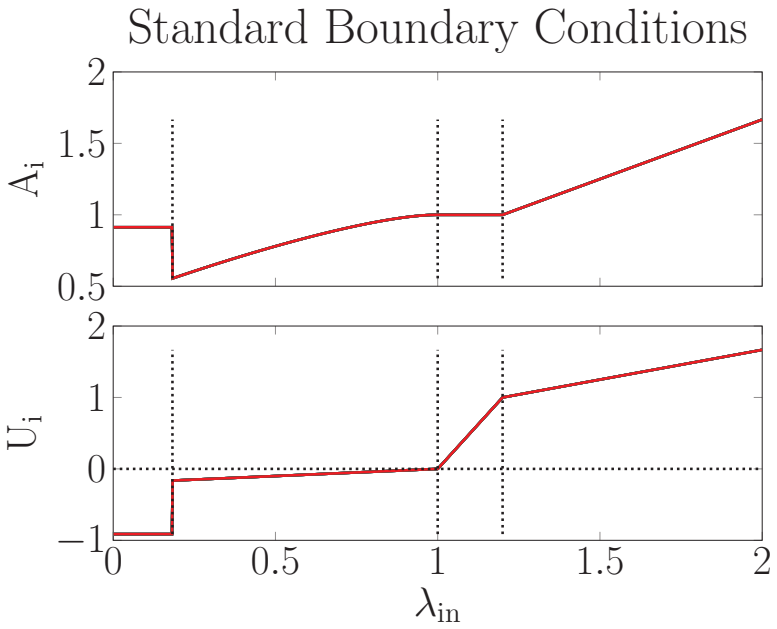

Fig. B.1.: Nondimensional sound of speed and fluid velocity for closed and open ends

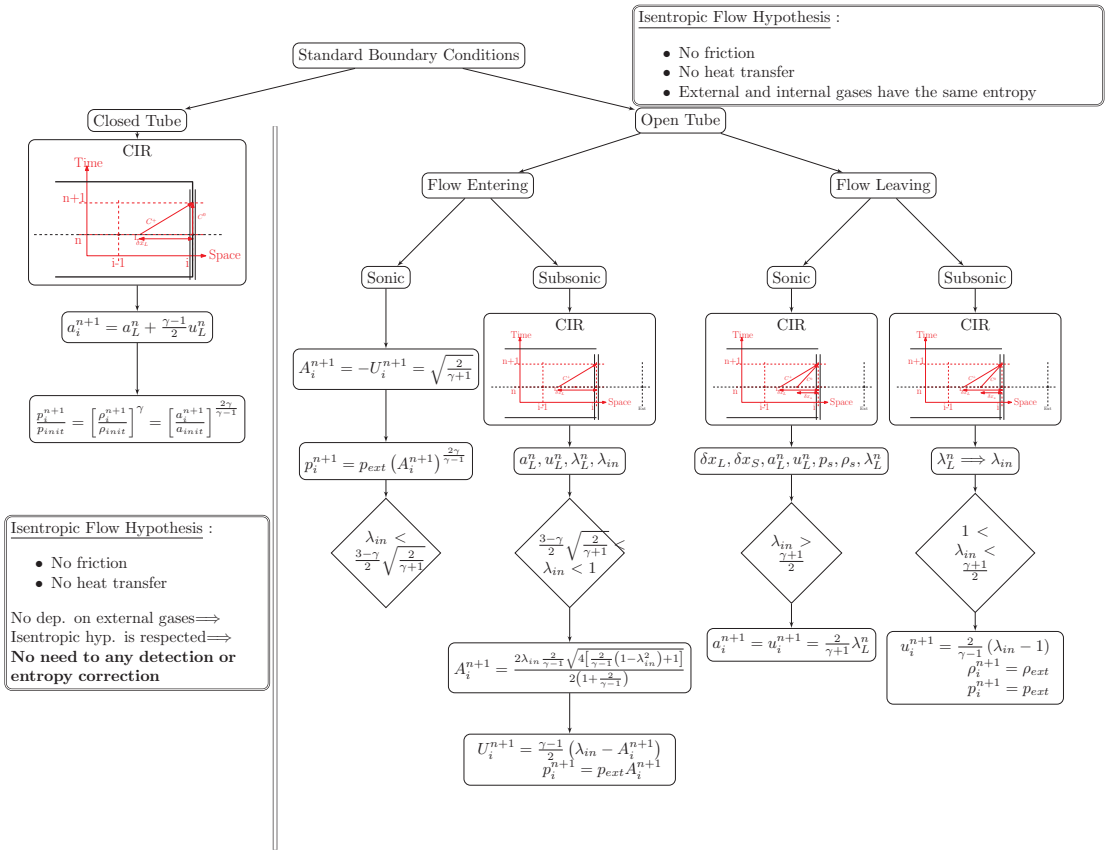

Fig. B.2.: Standard boundary conditions Treatement algorithm

2. Partially Open Boundary

The way in which waves are transmitted by, or reflected from, a partially open boundary is a function of the area ratio of the hole to the pipe: the nozzle area ratio is denoted by

$$\phi = \frac{F_t}{F} \tag{B.1}$$

The main parameters defining flow through a partially open end to a reservoir are shown in the Fig. B.3, both on a physical and a speed of sound-entropy ($a-s$) diagram. The flow can be either sonic or subsonic, and in the latter case the pressure p_b (no allowance is made for the pressure recovery). The effective area ratio of the nozzle should be used and account must be taken of the coefficient of discharge, C_d, when evaluating ϕ.

The continuity and energy equations can be applied to the nozzle arrangement and a relationship between the non-dimensional speed of sound A and the non-dimensional

particle velocity in the pipe, U, and the area ratio, ϕ, is derived: the derivation is base on Benson. For non-homentropic flow, the non-dimensional parameters are defined as

$$A = \frac{a}{a_{ref}}, \qquad U = \frac{u}{a_{ref}}, \qquad A_t = \frac{a_t}{a_{ref}}, \qquad \phi = \frac{F_t}{F}, \qquad U_t = \frac{u_t}{a_{ref}} \tag{B.2}$$

where the suffix t refers to the throat. However a_{ref} need no longer be on the same isentrope as the general speed of sound, a, and the reference is not necessarily p_t, the throat pressure for subsonic flwo. The entropy diagrams for the subsonic and sonic flow are shown in Fig. B.3.

The basic conservation equations for the flow through the nozzle are :
energy

$$a_0^2 = a^2 + \frac{\gamma - 1}{2}u^2 = a_t^2 + \frac{\gamma - 1}{2}u_t^2 \tag{B.3}$$

continuity

$$\rho u F = \rho_t u_t F_t \tag{B.4}$$

isentropic flow

$$\frac{\rho}{\rho_t} = (\frac{a}{a_t})^{\frac{2}{\gamma-1}} = (\frac{A}{A_t})^{\frac{2}{\gamma-1}} \tag{B.5}$$

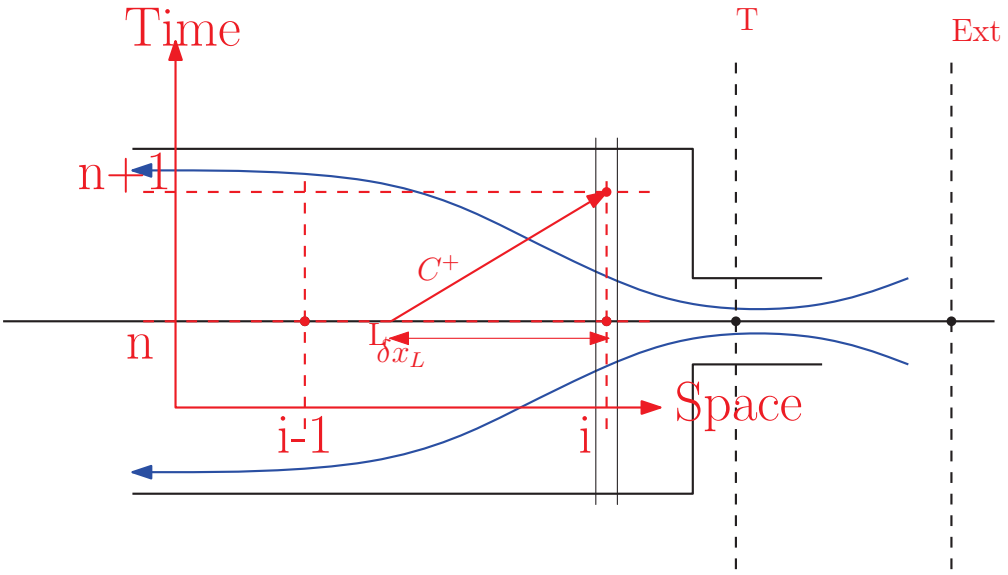

Fig. B.3.: The sudden area change with CIR

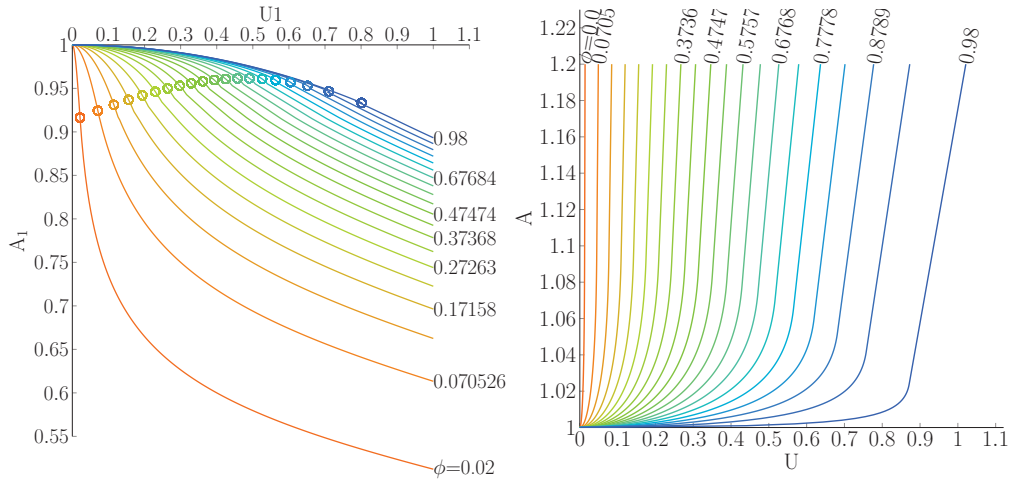

(a) Inflow

(b) Outflow

Fig. B.4.: Boundary charts for flow trough a partially open end

Dividing equation B.3 by a_{ref} gives the following non-dimensional energy equation:

$$A_0^2 = A^2 + \frac{\gamma - 1}{2} U^2 = A_t^2 + \frac{\gamma - 1}{2} U_t^2 \tag{B.6}$$

and combining equations B.4, B.5, and B.6 gives, after rearrangement,

$$\left(\frac{U}{A_t}\right)^2 = \frac{\frac{2}{\gamma-1}\left(\left(\frac{A}{A_t}\right)^2 - 1\right)}{\left(\frac{1}{\phi^2}\left(\frac{A}{A_t}\right)^{\frac{4}{\gamma-1}} - 1\right)} \tag{B.7}$$

From this equation it is possible to evaluate the non-dimensional particle velocity based on the instantaneous speed of sound and the nozzle area ratio. To use this information in a computer program it is better to relate λ_{in} and λ_{out}, and this can be achieved by manipulating the equation defining the boundary. The development of these equations may be referred to in Benson [26].

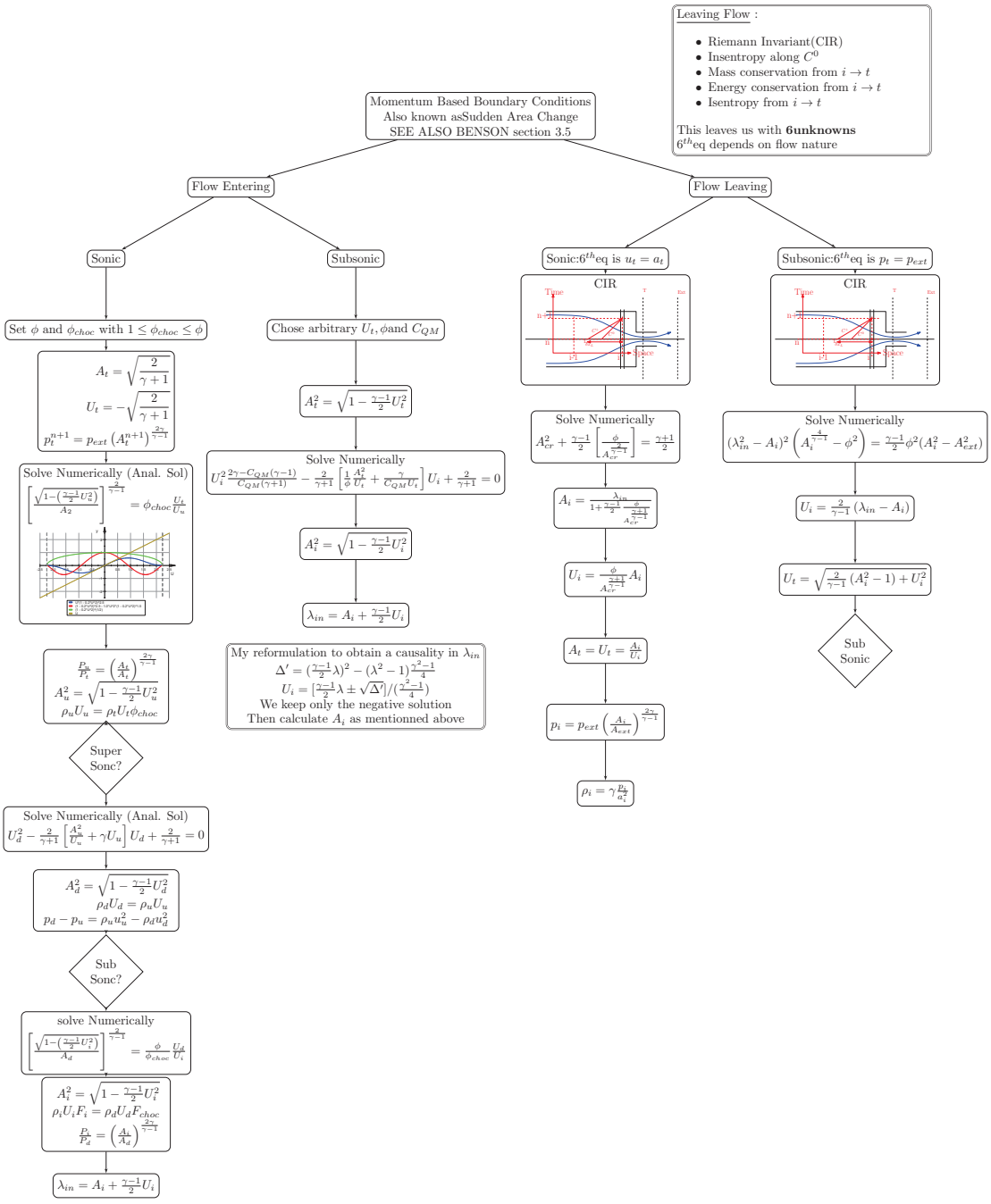

Fig. B.5.: An example of BC Solution

APPENDIX C

THE METHOD OF TRANSFER FUNCTION

Following an electrical analogy between voltage-speed of sound, and current-fluid velocity, Cipollone and Pinamonti [5] developed a new formulation for the solution of the 1-D advected wave equation in the Laplace Domain and is known as the Method of Transfer Function(MTF).

The combination of the mass and momentum equations gives.

$$\begin{array}{l} \frac{\partial^2 a(x,t)}{\partial t^2} + 2u(x,t)\frac{\partial^2 a(x,t)}{\partial x \partial t} + \left[u^2(x,t) - a^2(x,t)\right]\frac{\partial^2 a(x,t)}{\partial^2 x^2} = 0 \\ \frac{\partial^2 u(x,t)}{\partial t^2} + 2u(x,t)\frac{\partial^2 u(x,t)}{\partial x \partial t} + \left[u^2(x,t) - a^2(x,t)\right]\frac{\partial^2 u(x,t)}{\partial^2 x^2} = 0 \end{array} \tag{C.1}$$

Equation C.1 solely is applied if source terms are neglected. This can be overcome through the introduction of a third state variable (entropy) which introduces a correction for the estimated progressive and regressive speed of sound taking into account friction and heat transfer effects.

Solving and linearizing for the progressive and regressive speed of sound $a^{\pm}$ in the Laplace Domain gives the following solution:

$$a^{\pm}(x,s) = a^{\pm}(x,s)e^{-\frac{s\Delta x}{c^{\pm}}} + \Delta a_s^{\pm} + \Delta a_{\Omega}^{\pm} \tag{C.2}$$

Where $\Delta a_s^{\pm}$ and $\Delta a_{\Omega}^{\pm}$ represent the correction for a non-homentropic flow and area variation respectively. The entropy was taken as the summation of the transported

entropy and produced one and is calculated as follows:

$$\begin{aligned} S(x,s) =& S(s \pm \Delta x, s) e^{-s\frac{\Delta x}{u_0}} \\ &+ \frac{\gamma R}{a_0^2} (q_0 + u_0 F_0) \frac{1}{s} \left(1 - e^{-s\frac{\Delta x}{u_0}}\right) \end{aligned} \tag{C.3}$$

To overcome the time delay operators which depend on the local value of the speed of sound and fluid velocity, a fixed step solution can be obtained through linear interpolations of adjacent nodes based on the zone of influence as shown in fig. C.1.

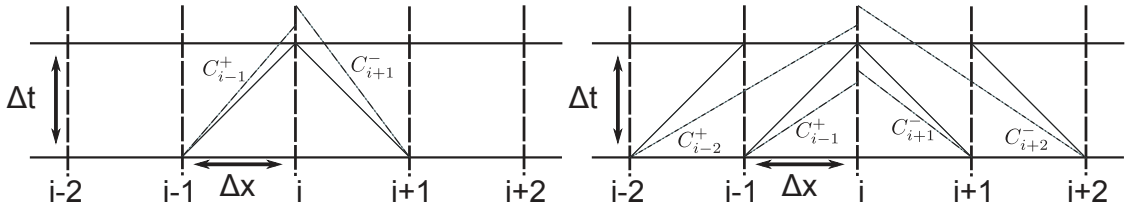

(a) Zone of influence (b) Zone of influence 2

Fig. C.1.: Zone of influence of the method of transfer function

If the point $(i, n+1)$ lies within the zone of influence of the adjacent nodes $(i-1, n)$ and $(i+1, n)$ (fig. C.1a), then:

$$a^+|_i^{n+1} = K^+|_i^n \cdot a^+|_i^n + K^+|_{i-1}^n \cdot a^+|_{i-1}^n \tag{C.4}$$

$$a^-|_i^{n+1} = K^-|_i^n \cdot a^-|_i^n + K^-|_{i+1}^n \cdot a|_{i+1}^n \tag{C.5}$$

If the point $(i, n+1)$ lies outside the zone of influence of the adjacent nodes $(n, i \pm \Delta x)$, the second adjacent nodes are to be used (fig. C.1b), and eqs. (C.4) and (C.5) become:

$$a^+|_i^{n+1} = K^+|_{i-1}^n \cdot a^+|_{i-1}^n + K^+|_{i-2}^n \cdot a^+|_{i-2}^n \tag{C.6}$$

$$a^-|_i^{n+1} = K^-|_{i+1}^n \cdot a^-|_{i+1}^n + K^-|_{i+2}^n \cdot a|_{i+2}^n \tag{C.7}$$

This will improve the range of validity but will not reduce the computational time, as numerical speed will have to satisfy the strictest CFL condition and will remain unchanged over simulation time.

The correction terms in eq. (C.2) can then be calculated as:

$$\begin{aligned}\Delta a_s^{\pm} = &[S(x,t) - S(x,t-\Delta t)] \cdot \left(-\frac{a_B}{4c_v}\right) \\ &+ \frac{S(x,t) - S(x \pm \Delta x, t)}{\Delta x} \cdot \left(\pm\frac{a_B^2}{4c_v} - \frac{a_B \cdot u_B}{4c_v}\right) \Delta t \\ &\mp \frac{\gamma - 1}{4} F \Delta t\end{aligned} \tag{C.8}$$

$$\Delta a_{\Omega}^{\pm} = -a_B u_B \frac{\gamma - 1}{4} \frac{1}{\Omega_m} \frac{\Omega_A - \Omega_B}{\Delta x} \Delta t \tag{C.9}$$

It will be observed in the results and experimental validation section, that neglecting the energy conservation will result in a error in the calculated temperature, which will affect the wave transport.

NOMENCLATURE

Abbreviations

1,2,3D One,Two,Three Dimensional Models

1D One Dimensional

A/F Air-to-Fuel ratio

CE-SE Conservation Element-Solution Element

CFD Computational Fluid Dynamics

CO Carbon Monoxide

DOC HydroCarbon

DPF Diesel Particulate Filter

ECU Electronic Control Unit

EGR Exhaust Gas Recirculation

FCT Flux-Corrected Transport

FEM Finite Element Method

H-PDEs Hyperbolic Partial Differential Equations

HC Hydrocarbon

ICCT International Council on Clean Transportation

ICE Internal Combustion Engine

IDI Combustion Indirect Combustion

LDVs Light-Duty Vehicles

MOC Method of characteristics

MV Mean Value

MVEM Mean Value Engine Model

NEDC New European Driving Cycle

NO2 Nitrogen Oxide

OBD On Board Diagnostics

ODE Ordinary Differential Equation

OEM Original Equipment Manufacturer

PDE Partial Differential Equation

QPM Quasi Propagatory Model

RDE Real Driving Emission

SCR Selective Catalytic Reduction

TA Type Approval

TVD Total Variation Diminishing

TWC Three Way Catalyst

VVT Variable Valve Timing

WLTC Worldwide harmonized Light vehicles Test Cycle

Greek Symbols

α	Heat transfer coefficient	W/m^2 K
β	Riemann Invariant	-
β_2	Geometrical blade angle	deg
Δ	Variation	-
η	Efficiency	-
γ	Heat capacity ratio	-
λ	Riemann Invariant	-

ϕ	Dimensionless flow rate	-
Π	Compressor pressure ratio	-
ψ	Dimensionless head parameter	-
ρ	Density	kg/m^3
σ	Tuning parameter	-
τ	Torque	Nm
τ_w	Shear stress	Pa
τ_{ij}	Viscous stress component perpendicular to i-axis, and parallel to j-axis	Pa

Mathematical Symbols

$\dot{m}$	Mass flow rate	kg/s
$\dot{W}_c$	Compressor power	W
Π_{crit}	Critical pressure ratio	
A	Tuning parameter	-
a	Local speed of sounds	m/s
a_i	Tuning parameter	-
A_{Pipe}	Pipe cross section	m^2
B	Tuning parameter	-
b_i	Tuning parameter	-
C	Tuning parameter	-
c_p	Heat capacity at constant pressure	J/kg K
c_v	Heat capacity at constant speed	
Cst	Constant	kg/s
D	Pipe diameter	m
e	specific internal energy	J/Kg K
f	Friction coefficient	-
h	specific enthalpy	J/Kg K
k	Tuning parameter	-

N	Rotational speed	RPM
p	Pressure	bar
r	Radius	m
R_{spec}	Specific gas constant	$JKg^{-}K^{-}$
Re_L	Reynolds number	-
s	Entropy	J/kg K
S_{rot}	Outflow cross section	m^2
T	Temperature	K
u	Particle velocity	m/s
u	Tangential speed	m/s
u	fluid speed	m/s
V	Volume	m^3
V_{r2}	Radial flow velocity	m/s
W	Work	J
x_f	Tuning parameter	-
MFR	Mass Flow Rate	g/s

Subscripts

01	Total conditions at compressor entry
02	Total condition at compressor exit
1	Stagnation conditions at compressor entry
2	Stagnation condition at compressor exit
Cyl	Cylinder
$d0$	Initial condition downstream
em	Exhaust manifold
f	Work/parameter related to friction
HL	Heat Losses
I	Incidence

im	Intake manifold
OL	Overall losses
out	Compressor output
ref	Reference Value
$u0$	Initial condition upstream
a	Air
c	Compressor
c,corr	Compressor, Corrected value

Superscripts

$*$	At minimum incidence losses
$+$	Progressive wave
$-$	Regressive wave

BIBLIOGRAPHY

[1] Stephanie, S., Marcello, C., Yann, G., Augusto, D. T., Gianluca, M., and Angelo, O. Modeling wave action effects in ice air path systems comparison of numerical and systems dynamics approaches. *International Journal of Engine Research (IMech)-SAGE*, 2012.

[2] Denga, H., Jianga, M., and Huanga, C.-Q. New spatial basis functions for the model reduction of nonlinear distributed parameter systems. *Journal of Process Control*, 22, 2012.

[3] Vladimir, D., Rob, R., and Mikhail, Z. An extended krylov subspace model-order reduction technique to simulate wave propagation in unbounded domains. *Journal of Computational Physics*, 2014.

[4] Cipollone, R. and Sciarretta, A. The quasi-propagatory model : A new approach for describing transient phenomena in engine manifolds. *SAE International*, (2001-01-0579), 2001. doi: 10.4271/2001-01-0579.

[5] Cipollone, R. and Pinamonti, Silvio, S. Homentropic subsonic in engine ducts: New theoretical procedure and experimental validation. *6th World Conference on Experimental Heat Transfer, Fluid Mechanics, and Thermodynamics*, 2005.

[6] Cipollone, R., Martella, L., Scarpone, L., and Valente, R. A new modeling to predict the fluid dynamic transient phenomena in ice ducts. *SAE International*, 2008. doi: 10.4271/2008-01-2389.

[7] Meddahi, F., Charlet, A., Chamaillard, Y., Fleck, C., and Groedde, S. Modeling waves in ice ducts: Comparison of 1d and low order models. *SAE International*, (2015-24-2386), 2015. doi: 10.4271/2015-24-2386.

[8] *Wave-RT user's Manual.*

[9] European emissions standards. https://en.wikipedia.org/wiki/European_emission_standards.

[10] Reducing co2 emissions from passenger cars. http://ec.europa.eu/clima/policies/transport/vehicles/cars/index_en.

[11] Global passenger vehicle standards. http://www.theicct.org/info-tools/global-passenger-vehicle-standards,.

[12] Global pv standards chart library. http://www.theicct.org/global-pv-standards-chart-library,.

[13] Weiss, M., Bonnel, P., Hummel, R., Provenza, A., and Manfredi, U. On-road emissions of light-duty vehicles in europe. *Environ. Sci. Technol.*, 2011. ISSN 1520-5851. doi: 10.1021/es2008424. URL http://dx.doi.org/10.1021/es2008424.

[14] The wltp: How a new test procedure for cars will affect fuel consumption values in the eu. http://www.theicct.org/sites/default/files/publications/ICCT_WLTP_EffectEU_20141029.pdf.

[15] Heywood, J. B. *Internal combustion engine fundamentals*, volume 930. Mcgraw-hill New York, 1988.

[16] Bargende, M. Zukunft der motorprozessrechnung und 1d-simulation. *MTZ Motorenentwicklung*, 2014.

[17] Chalet, D., Mahe, A., Migaut, J., and Hetet, J. Multifrequency modeling of unsteady flows in the inlet manifold of an ice. *Proc. IMechE*, 226 Part D: J. Automobile Engineering, 2011.

[18] Chalet, D., Mahé, A., Hétet, J.-F., and Migaud, J. A new modeling approach of pressure waves at the inlet of internal combustion engines. *Journal of Thermal Science*, 2011. doi: 10.1007/s11630-011-0455-8.

[19] Bodin, O. Numerical computations of internal combustion engine related transonic and unsteady flows. Technical report, Royal Institute of Technology. KTH Mechanics .SE-100 44 Stockholm, Sweden, 2009.

[20] Chang, S.-C. The method of space time conservation element and solution element_a new approach for solving the navier stokes and euler equations.pdf. *Journal of Computational Physics*, 1995.

[21] Arnau, J. M., Romero, J. V., and Rosell, M. D. Treatment of geometry source terms in ce-se method to improve the mass conservation property in tapered ducts of internal combustion engines. *4to Congreso Internacional, 2do Congreso Nacional de Métodos Numéricos en Ingeniería y Ciencias Aplicadas*, 2007.

[22] Guzzella, L. and Onder, C. *Introduction to modeling and control of internal combustion engine systems*. Springer Science & Business Media, 2009.

[23] Mancini, G., Asprion, J., Cavina, N., Onder, C., and Guzzella, L. Dynamic feedforward control of a diesel engine based on optimal transient compensation maps. *Energies*. doi: 10.3390/en7085400.

[24] Winterbone, D. and Pearson, R. *Theory of engine manifold design*. Professional Engieering Publishing, 2000.

[25] Serrano, J., Climent, H., Piqueras, P., and García-Afonso, O. Analysis of shock capturing methods for chemical species transport in unsteady compressible flow. *Mathematical and Computer Modeling*, 57(7-8):1751–1759, 2011.

[26] Benson, R. S. *The thermodynamics and gas dynamics of internal-combustion engines*, volume Volume I. Clarendon Press. Oxford, 1982.

[27] Kuzmin, D. *A Guide to numerical methods for transport equations*. Friedrich-Alexander-Universität. Erlangen-Nürnberg, 2010.

[28] Courant, R.and Friedrichs, K. . and Lewy, H. Über die partiellen differenzengleichungen der mathematischen physik. *Mathematische Annalen*, 1928.

[29] Hughes, T., Engel, G., Mazzei, L., and Larson, M. The continuous galerkin method is locally conservative. *Journal of Computational Physics*, 2000.

[30] Hughes, T. and G.N.Wells. Conservation properties for the galerkin and stabilised forms of the advection-diffusion and incompressible navier-stokes equations. *Computer Methods in Applied Mechanics and Engineering*, 194, 2005.

[31] Chalet, D. and Chesse, P. Fluid dynamic modeling of junctions in internal combustion engine inlet and exhaust systems. *Journal of Thermal Science*, 19, 2010.

[32] Peters, B. and Gosman, A, D. Numerical simulation of unsteady flows in engine intake manifolds. *SAE*, (930609), 1993.

[33] Jenny, E. L'écoulement transitoirc unidimensionnel et l'influence du frottement, des apport de chaleur et des variations de section. *Revue Brown Boveri*, 1950.

[34] Benson, R.Sand Garg, R. and Woollatt, D. A numerical solution of unsteady flow problems. *International Journal of Mechanical Sciences*, 1964.

[35] Briz, G. and Giannattasio, P. Applicatione dello schema numerico "conservation element- solution element" al calcolo del flusso non stazionario nei condotti dei motort a c.i. 1993.

[36] Winterbone, D. and Pearson, R. Numerical simulation of intake and exhaust aows in a highspeed multi-cylindcr petrol engine using the lax-wendroff method. *Proc. lnt. Corif. on Computers in Engine Teclmology, IMechE*, 1991.

[37] Lax, P, D. and Wendroff, B. Systems of conservation laws. *Communications on Pure and Applied Mathematics*, 1960.

[38] Onorati, a., Perotti, M., and Rebay, S. Modeling one-dimensional unsteady flows in ducts: Symmetric finite difference schemes versus galerkin discontinuous finite element methods. *International Journal of Mechanical Sciences*, 39(11):1213–1236, 1997. ISSN 00207403. doi: 10.1016/S0020-7403(97)00014-3.

[39] Corberán, J. and Gascón, M, L. Tvd schemes for the calculation of flow in pipes of variable cross-section. *Mathl. Comput. Modeling*, 21(3):85–92, 1995.

[40] Harten, A. High resolution schemes for hyperbolic conservation laws. *Journal of Computational Physics*, 1982.

[41] Chang, S. and To, W, M. A brief description of a new numerical framework for solving conservation laws:the method of space time conservation element solution element. *13th International Conference on Numerical Methods in Fluid Dynamics*, 1992.

[42] Onorati, A. and Ferrari, G. Modeling of 1-D unsteady flows in i.c. engine pipe systems: numerical methods and transport of chemical species. 1998. doi: 10.4271/980782.

[43] Siavashi, M., Pourafshary, P., and Raisee, M. Application of space-time conservation element and solution element method in streamline simulation. *Journal of Petroleum Science and Engineering*, 96-97, 2012.

[44] Zhang, Z.-C., Yu, S., and Chang, S.-C. A space-time conservation element and solution element method for solving the two- and three-dimensional unsteady euler equations using quadrilateral and hexahedral meshes. *Journal of Computational Physics*, 175:168–199, 2002.

[45] Richtmyer, R. D. A survey of difference methods for non-steady fluid dynamics. *National Center for Atmospheric Research, Colorado*, 1962.

[46] Onorati, A., Cerri, T., Ceccarani, M., and Cacciatore, D. Experimental analysis and 1d thermo-fluid dynamic simulation of a high performance lamborghini v10 s . i . engine experimental analysis and 1d thermo-fluid dynamic simulation of a high performance lamborghini v10 s . i . engine. *SAE*, (2005-24-081), 2005.

[47] Bassett, M. D., Pearson, R. J., Fleming, N. P., and Winterbone, D. E. A multi- pipe junction model for one- dimensional gas- dynamic simulations. *SAE*, 2003.

[48] Zuecrow, M. and Hoffman, J. *Gas dynamics*. JOHN WILEY & SONS, INC., 1976.

[49] Benson, R. Numerical solution of one dimensional non-steady flow with supersonic and subsonic flows and heat transfer. *International Journal of Mechanical Sciences*, 1972.

[50] Pearson, R. and Winterbone, D. Calculating the effects of variations in composition on wave propagation in gases. *International Journal of Mechanical Sciences*, 35, 1993.

[51] Grondin, O., Stobart, R., Chafouk, H., and Maquet, J. Modeling the compression ignition engine for control : Review and future trends. (2004-01-0423), 2004. doi: 10.4271/2004-01-0423.

[52] Jensen, J.-P., Kristensen, S. C., Houbak, N., and Hendricks, E. Mean value modeling of a small turbocharged diesel engine. *SAE International*, (910070), 1991.

[53] MÃ$\frac{1}{4}$ller, M., Hendricks, E., and Sorenson, S. C. Mean value modeling of turbocharged spark ignition engines. *SAE International*, Feb 1998. doi: 10.4271/980784.

[54] Moraal, P. and Kolmanovsky, I. Turbocharger modeling for automotive control applications. *SAE International*, (1999-01-0908), 1999. doi: 10.4271/1999-01-0908.

[55] Martin, G., Talon, V., Peuchant, T., Higelin, P., and Charlet, A. Physics based diesel turbocharger model for control purposes. *SAE International*, (2009-24-0123), Sept. 2009. doi: 10.4271/2009-24-0123.

[56] Martin, G., Talon, V., Higelin, P., Charlet, A., and Caillol, C. Implementing turbomachinery physics into data map-based turbocharger models. *SAE International*, (2009-01-0310), 2009. doi: 10.4271/2009-01-0310.

[57] Hendricks, e., Chevalier, A., Jensen, M., Sorenson, S., Trumpy, D., and Asik, J. Modeling of the intake manifold filling dynamics.pdf. *SAE*, (960037), 1996.

[58] Alan, H. and O'Brien, W. A three-dimensional turbine engine analysis compressor code for steady-state inlet distortion. *Journal of Turbomachinery*, 1997.

[59] Macek, J., Vávra, J., and Vítek, O. 1-d model of radial turbocharger turbine calibrated by experiments. *SAE International*, (2002-01-0377), 2002. doi: 10.4271/2002-01-0377.

[60] Piscaglia, F., Onorati, A., Marelli, S., and Capobianco, M. Unsteady behavior in turbocharger turbines : Experimental analysis and numerical simulation. *SAE International*, (2007-24-0081), 2007. doi: 10.4271/2007-24-0081.

[61] Léonard, O. and Adam, O. A quasi-one-dimensional cfd model for multistage turbomachines. *Journal of Thermal Science*, 17(1):7–20, Mar. 2008. doi: 10.1007/s11630-008-0007-z.

[62] Japikse, D. Turbomachinery performance modeling. *SAE International*, (2009-01-0307), 2009. doi: 10.4271/2009-01-0307.

[63] Bozza, F. and De Bellis, V. Steady and unsteady modeling of turbocharger compressors for automotive engines. *SAE International*, (2010-01-1536), 2010. doi: 10.4271/2010-01-1536.

[64] Bozza, F. and De Bellis, V. Map-based and 1d simulation of a turbocharger compressor in surging operation. *SAE International*, (2011-24-0126), 2011. doi: 10.4271/2011-24-0126.

[65] Dowell, P. G. and Akehurst, S. Advanced mapping techniques for radial compressor for use in real-time engine models. *SAE International*, (2010-01-1227), 2010. doi: 10.4271/2010-01-1227.

[66] El Hadef, J., Colin, G., Chamaillard, Y., and Talon, V. Physical-based algorithms for interpolation and extrapolation of turbocharger data maps. *SAE International*, 2012. doi: 10.4271/2012-01-0434.

[67] Shaaban, S. *Experimental investigation and extended simulation of turbocharger non-adiabatic performance*. PhD thesis, Universität Hannover, 2004.

[68] Hanlon, P. *Compressor handbook*. McGRAW-HILL, 2001.

[69] Watson, N. and Janota, Marian, S. *Turbocharging the internal combustion engine*. The Macmillan Press LTD, 1982.

[70] Lax, P. Weak solutions of nonlinear hyperbolic equations and their numerical computation. *Communications on Pure and Applied Mathamtics*, 1954.

[71] Lax, P. D. *Hyperbolic systems of conservation laws and the mathematical theory of shock waves*, volume 11. SIAM, 1973.

[72] Lax, P. D. and Wendroff, B. Difference schemes for hyperbolic equations with high order of accuracy. *Communications on pure and applied mathematics*, 17(3): 381–398, 1964.

[73] Richtmyer, R. D. *A survey of difference methods for non-steady fluid dynamics*. Number 63. National Center for Atmospheric Research, 1963.

[74] Boris, J. and Book, D. Flux-corrected transport i. *Journal of Computational Physics*, 1973.

[75] Book, D., Boris, J., and Hain, K. Flux-corrected transport ii. *Journal of Computational Physics*, 1975.

[76] Sweby, P. High resolution schemes using flux limiters for hyperbolic conservation laws. *SIAM Journal on Numerical Analysis*, 1984.

[77] Davis, S. Tvd finite-difference schemes and artificial viscosity. *NASA CR*, 1984.

[78] Godunov, S. K. A difference method for numerical calculation of discontinuous solutions of the equations of hydrodynamics. *Matematicheskii Sbornik*, 89(3): 271–306, 1959.

[79] Toro, E. F. *Riemann solvers and numerical methods for fluid dynamics: a practical introduction*. Springer Science & Business Media, 2009.

[80] Roe, P. L. Approximate riemann solvers, parameter vectors, and difference schemes. *Journal of computational physics*, 43(2):357–372, 1981.

[81] Sweby, P. K. Flux limited schemes for conservation laws, upwind methods in cfd. *SERC CFD Community Club Collaborative Computational Project 22*, 1992.

[82] Harten, A. High resolution schemes for hyperbolic conservation laws. *Journal of computational physics*, 49(3):357–393, 1983.

[83] Osher, S. and Chakravarthy, S. High resolution schemes and the entropy condition. *SIAM Journal on Numerical Analysis*, 21(5):955–984, 1984.

[84] Van Leer, B. Towards the ultimate conservative difference scheme. v. a second-order sequel to godunov's method. *Journal of computational Physics*, 32(1):101–136, 1979.

[85] LeVeque, R. J. and Le Veque, R. J. *Numerical methods for conservation laws*, volume 132. Springer, 1992.

[86] Davis, S. F. A simplified tvd finite difference scheme via artificial viscosity. *SIAM journal on scientific and statistical computing*, 8(1):1–18, 1987.

[87] Harten, A. On a class of high resolution total variation diminishing stable finite difference schemes. Technical report, New York University, 1982.

[88] Crank, J. and Nicolson, P. A practical method for numerical evaluation of solutions of partial differential equations of the heat-conduction type. In *Mathematical Proceedings of the Cambridge Philosophical Society*, volume 43, pages 50–67. Cambridge Univ Press, 1947.

Farouq Meddahi

Contribution à la Modélisation Temps-Réel de la Chaîne d'Air dédiée à l'Estimation du Remplissage

L'impact de la dynamique des gaz sur la chaine d'air s'est imposé fortement en raison du contenu de la dynamique dans les nouveaux cycles de test automobile tels que le WLTC. Cela rend les modèles 0D actuels moins fiables car ils reposent sur plusieurs positions sur les cartographies mesurées sur des points de fonctionnements stationnaires. En outre, les phénomènes d'onde et les effets inertiels des gaz sont intrinsèquement négligés.

Une méthodologie pour reproduire efficacement les effets d'ondes le long des conduites de moteurs à combustion interne a été présentée dans ce travail. L'idée est basée sur la combinaison des modèles à paramètres concentrés et les modèles quasi-unidimensionnels. Cette combinaison donne la possibilité de prendre les effets d'inertie de la dynamique des gaz tout en évitant le coût lourd de calcul de l'approche de modélisation 1D.

La première partie s'est intéressée aux schémas numériques à une dimension, dans le but de les évaluer par rapport aux temps de calcul, d'exactitude et de définir une bonne référence pour davantage validations numériques pour les modèles réduits. Le modèle « quasi-Propagatory » était le meilleur candidat pour modéliser les ondes avec moins de puissance de calcul.

Pour avoir une propre estimation de la pression de suralimentation, on s'est intéressé plus particulièrement au compresseur. Un modèle physique a été présenté on se basant sur les travaux de Martin et al. [55]. Finalement, les développements sont validés expérimentalement sur tous les points de fonctionnement du moteur.

Mots clés : Moteur, Simulation et Modélisation, Turbocompresseur

Contribution to Real-Time Air System Modeling Dedicated to Trapped Mass Estimation

Gas dynamics impact on air system dynamics and hence on combustion products, i.e. emissions, has imposed itself strongly due to the dynamics content in new test drive cycles such as the WLTC. This makes current real-time 0D models less reliable as they rely on stationary measured look up tables. In addition, wave phenomena and gas inertial effects are inherently neglected. This makes the estimation of the flow into and from the cylinder inaccurate.

A methodology to efficiently reproduce wave effects along the internal combustion engine ducts was presented in this work. The idea relies on combining both lumped parameter and quasi-one-dimensional models. This combination gives the possibility to take inertial effects of gas dynamics while avoiding the heavy computational cost of the 1D modeling approach.

The first part investigated one-dimensional numerical schemes, with the aim of evaluating them with respect to real-time applications and defining a good reference for further numerical validations for the low order models. The Quasi-Propagatory model was the best candidate to model waves with less computational power.

To have a proper boost pressure estimation, more focus was on the compressor. A physics based model was presented based on [55]. Results have also shown a better interpretation and extrapolation ability. Finally, the developments have been validated experimentally using the complete engine operation map.

Keywords: Engine, Simulation and Modeling, Turbocharger.

UNIVERSITE D'ORLEANS

Laboratoire PRISME
8 rue Léonard de Vinci
45072 Orléans cedex
FRANCE

BOSCH
Invented for life